Higgs boson phenomenology beyond the Standard Model

Solen Le Corre

N° d'ordre NNT : 2018LYSE1028

THÈSE DE DOCTORAT DE L'UNIVERSITÉ DE LYON
opérée au sein de
l'Université Claude Bernard Lyon 1

École Doctorale ED52
de Physique et d'Astrophysique

Spécialité de doctorat : Physique Théorique / Physique des Particules

Soutenue publiquement le 13 Mars 2018, par :
Solen Le Corre

Higgs boson phenomenology beyond the Standard Model

Devant le jury composé de :

Mme G. Bélanger	Rapporteure
M. G. Moreau	Rapporteur
Mme S. Gascon Shotkin	Présidente du Jury
Mme F. N. Mahmoudi	Examinatrice
M. A. Djouadi	Examinateur
M. U. Ellwanger	Examinateur
M. A. Deandrea	Directeur de thèse
M. A. Arbey	Co-directeur de thèse

Résumé

Suite à la découverte du boson de Higgs en Juin 2012 au Large Hadron Collider, l'accélérateur de particules situé à la frontière franco-suisse, l'étude du secteur scalaire des particules élémentaires a connu un regain d'intérêt. En particulier, le boson de Higgs étant une particule clef au sein du Modèle Standard des particules, les expérimentateurs étudient ses propriétés avec beaucoup de soin.

Le Modèle Standard, dont le but est de décrire les interactions entre particules élémentaires, n'est cependant pas une théorie complète. En effet, en plus de quelques problèmes d'ordre théorique, certains phénomènes observés expérimentalement ne peuvent pas être expliqués par ce modèle. Les théoriciens en physique des particules cherchent donc à établir une nouvelle théorie venant le compléter et permettant d'expliquer pleinement les observations expérimentales.

Ma thèse est axée sur l'étude du secteur scalaire de modèles au-delà du Modèle Standard des particules. J'ai plus particulièrement travaillé sur un modèle à deux doublets de Higgs – modèle purement effectif mais qui peut être inclus dans d'autres théories plus abouties – ainsi que sur un modèle construit comme une combinaison entre les théories déjà très proches de techicouleur et de Higgs composites, et ce dans le cas particulier d'une brisure de symétrie $SU(4) \to Sp(4)$. J'ai étudié ce dernier modèle d'un point de vue effectif mais la théorie complète est capable de pallier un certain nombre des limitations du Modèle Standard.

Chacun de ces modèles inclut un secteur scalaire plus riche que celui du Modèle Standard et contient au moins une particule pouvant être assimilée au boson de Higgs découvert au LHC.

J'ai réalisé l'étude phénoménologique de chacun de ces modèles et les ai confrontés à des contraintes tant théoriques qu'expérimentales – en particulier celles obtenues grâce aux études les plus récentes, portant sur le boson de Higgs et sur de potentielles particules scalaires additionnelles, réalisées par les équipes du LHC. Cela m'a permis de contraindre les paramètres libres des modèles et en particulier de restreindre les valeurs possibles pour la masse des autres particules scalaires, permettant de mieux cibler les zones où ces nouvelles particules, si elles existent, pourraient être détectées au LHC.

Notons également que les deux théories sur lesquelles j'ai travaillé ne sont toujours pas exclues par les contraintes expérimentales les plus récentes.

Mots clefs :

Boson de Higgs, phénoménologie, LHC, scalaire, Higgs lourd, Higgs léger, Higgs chargé.

Summary

Following the discovery of the Higgs boson in June 2012 at the Large Hadron Collider, the particle collider located beneath the France-Switzerland border, interest in the study of the scalar sector in elementary particle physics significantly increased. In particular, as the Higgs boson plays a very special role in the Standard Model of particle physics, experimentalists study its properties with great care.

The goal of the Standard Model is to describe the interactions between elementary particles. However the theory is not quite complete. Indeed, in addition to some purely theoretical problems, a number of experimental observations cannot be explained by the Standard Model. Theorists are therefore looking for a more comprehensive theory able to fully explain the observations.

This thesis is based on the study of the scalar sector of two different extensions of the Standard Model of particle physics. I have worked on the Two-Higgs Doublet Model – this model is purely effective but can be included in more comprehensive theories – as well as on a model based on a combination of Technicolor and Composite Higgs theories in the framework of the $SU(4) \to Sp(4)$ symmetry breaking pattern. I studied the latter *via* an effective approach but the full theory is able to get rid of some of the pitfalls of the Standard Model.

These two models include a scalar sector that is richer than the one found in the Standard Model and contain at least one particle which can be assimilated to the Higgs boson discovered at the LHC.

I performed a phenomenological study for these two models and tested them against both theoretical and experimental constraints. In particular I used the latest studies on the 125 GeV Higgs boson and on possible additional scalars performed by the ATLAS and CMS collaborations. The application of all these constraints drastically reduced the available parameter space of the two models. In particular it narrowed the possible mass range of the additional scalars, allowing to know more accurately where to search them experimentally in order to prove or rule out their possible existence.

As of today the two theories I worked on are still not excluded by the latest experimental data.

Key words:

Higgs boson, phenomenology, LHC, scalar particle, heavy Higgs, light Higgs, charged Higgs.

Remerciements

J'aimerais remercier l'équipe de physique théorique de l'IPNL, tout d'abord Aldo Deandrea et Alexandre Arbey pour m'avoir accepté en thèse sous leur direction, Giacomo Cacciapaglia pour son aide discrète mais efficace durant ces trois années et Dany Davesne pour son humour défrisant et toute l'aide administrative qu'il m'a apportée.

J'aimerais également remercier Suzanne Gascon et Morgan Lethuillier de l'équipe CMS pour m'avoir proposé un projet commun entre nos deux groupes qui m'a permis d'amorcer véritablement ma thèse.

Je remercie également les autres doctorants sans qui ces trois années de thèse auraient été bien moins agréables : Pierre, Bertrand, Glenn, Lucille et les autres de l'équipe du midi, Emeline pour les pauses thé trop vite avortées, ainsi qu'Anne-Laure, notamment pour son aide sur le déchiffrage de codes. Et, enfin et surtout, Nicolas qui, outre son humour particulier qui a bien souvent su me dérider, m'a tant de fois débloqué durant ma thèse grâce à ses explications lumineuses et ses références bibliographiques pertinentes que je ne saurais lui dire suffisamment merci.

Je remercie également l'équipe enseignante avec qui j'ai travaillé durant ces trois ans : Houmani El Mamouni pour m'avoir, année après année, laissé la liberté de prendre plus de responsabilités au sein de son UE, Floriane Poignant pour l'aide et la collaboration lors de notre toute première année d'enseignement, Sonia Fleck, d'une aide inestimable et qui abat un travail titanesque pour l'UE, Sylvain Monnier avec qui j'ai eu le plaisir de construire et développer les "mini-projets", ainsi que toute l'équipe du café pédagogique pour les discussions animées des vendredis après-midi.

Un grand merci également à mon frère Julien qui a sacrifié ses vacances de Noël pour relire consciencieusement mon manuscrit et traquer les fautes d'anglais et les tournures de phrases trop "à la française".

Je remercie également mes jury, en particulier mes rapporteurs Geneviève Bélanger et Grégory Moreau pour avoir accepté de lire et corriger mon manuscrit, et Suzanne Gascon pour avoir présidé le jury lors de ma soutenance.

Je remercie enfin Romain, pour avoir été présent durant ces trois ans, et pour m'avoir soutenu, supporté et, surtout, attendu.

Contents

Introduction

In 2012 the Large Hadron Collider (LHC), a circular particle collider located beneath the France-Switzerland border, publicly announced the discovery of a new particle with properties very similar to the ones predicted by the Standard Model (SM) of particle physics for a Higgs boson with a mass of around 125 GeV. The discovery of this long-awaited particle represented a new evidence in favor of the SM.

The SM of particle physics is a theory describing the interactions of elementary particles through the exchange of other particles, called gauge bosons. It has been developed since the beginning of the XIX$^{\text{th}}$ century and has been tested against experimental observations since then.

All the SM predictions are very well reproduced by experiments. However some observations cannot be explained by the SM. Hence, although very accurate, the model does not account for every phenomenon occurring at the level of particle physics and thus needs to be modified or completed.

Experimentalists are tracking down every deviation between experimental results and theoretical predictions in order to bring to light new discrepancies which can help elaborate a new, more comprehensive theory, whereas theorists are developing new models said to be beyond the Standard Model (BSM) which encompass the SM as a substructure or as an effective part.

The development of BSM theories is greatly helped by the meticulous study of the newly discovered Higgs boson. Its properties are very close to the ones predicted by the SM but divergences may appear. Moreover the precise determination of its properties helps constrain the BSM theories in a highly effective way.

As the Higgs boson was the first elementary particle ever discovered, the study of the scalar sector of particle physics increased drastically since its discovery. Experiments are looking for possible additional scalars both neutral or charged, allowing a better check of the scalar sector of BSM theories.

During my thesis I worked on the scalar sector linked to the Higgs boson in two distinct theory frameworks.

The first one is an effective theory called Two-Higgs Doublet Model (2HDM). This model contains the usual particles of the SM but includes two electroweak Higgs doublets instead of one. It results in the appearance of three neutral scalars – one of which can be assimilated to the 125 GeV Higgs boson – and two charged scalars.

This model has six free parameters, *i.e.* six independent parameters whose numerical value is not fixed either by theory or experiment. I compared this theory against different constraints coming from both theoretical requirements and experimental observations in order to reduce the available parameter space. In particular I used the latest results published by the ATLAS and CMS collaborations on both 125 GeV Higgs studies and limits on other scalar particles – lighter or heavier, neutral or charged. These constraints greatly reduce the available parameter

space but the model is still allowed.

The second theory I worked on is a model based on a combination of Technicolor and Composite Higgs theories. This model, called Fundamental Composite Dynamics (FCD), assumes that a new strongly coupled gauge interaction exists at high energy. Additional gauge bosons and elementary fermions are introduced. At low energy the new fermions condense and break the initial flavor symmetry.

Many condensates appear, the same way as the mesons and baryons in QCD after chiral symmetry breaking. Among them at least one has the same quantum numbers as the Higgs boson discovered at the LHC. The lightest one is chosen to be the *condensate Higgs candidate*.

The breaking also produces Goldstone bosons, which can acquire a small mass due to explicit symmetry breaking terms arising in the theory. Depending on the symmetry breaking pattern some of the Goldstone bosons can make appropriate Higgs candidates.

Hence both the Goldstone boson candidate(s) and the condensate candidate mix together to give rise to the "real" 125 GeV Higgs boson.

As the phenomenological study of such FCD model is strongly dependent on the chosen symmetry breaking pattern, I focused on the specific case where an initial $SU(4)$ flavor symmetry is broken down to an $Sp(4)$ symmetry. This pattern is the minimal one, with three new scalars arising from the breaking: two (pseudo-)Goldstone bosons – a scalar and a pseudoscalar – and a scalar condensate. I performed the phenomenological study of these three particles and compared the properties of the model with theoretical and experimental constraints. As in the 2HDM case, the constraints allow an important reducing of the available parameter space without ruling out the model.

In the first part of this thesis I will briefly remind the historical development of particle physics before summarizing the current mathematical development of the Standard Model. Then I will introduce the physics of the Higgs boson and the experimental measurement of its properties and show how they can be used in order to constrain extensions of the Standard Model.

In a second part I will expose my work on the Two-Higgs Doublet Model. I will introduce briefly the model, with its particle content and its free parameters, and list the different constraints used in my analysis. Then, as there are two possible Higgs candidates in 2HDM – either the light scalar called h or the heavier scalar H – I will perform my analysis in two different frameworks: in the first one I will assume that the heavy Higgs boson H is the 125 GeV Higgs boson discovered at the LHC, and in the second that the light Higgs boson h is the 125 GeV Higgs boson. In the first hypothesis I will focus on the possibility of detecting the light scalar h whose mass is less than 125 GeV. In the second one I will work in the alignment limit, that is, assume that the couplings of the 125 GeV Higgs boson are similar to those of the SM Higgs boson within 1% of uncertainty.

In a third part I will present my work on the FCD model, first introducing the concepts of Technicolor and Composite Higgs theories and showing how they can be combine. Second I will perform a phenomenological study on the three scalars emerging in the $SU(4) \to Sp(4)$ symmetry breaking pattern, looking at the efficiency of the different selected constraints to reduce the parameter space.

Finally I will conclude on the global work presented in this thesis.

Part I:

Introduction to particle and Higgs physics

Particle physics was born slightly more than a century ago. It is a recent field still in expansion. Since its beginning many elementary particles have been discovered. But particle physics is not only the inventory of existing elementary particles but also the search for a theory explaining their behaviors and interactions.

The theory of particle physics has evolved quickly and has given birth to a complete theory of elementary particle interactions called the Standard Model of particle physics. In this model, one particle, called the Higgs boson, plays a very special role as it is involved in the process which generates mass to all the other known particles. The Higgs boson was predicted in 1964 but has only been discovered in 2012 at the LHC. As it was the only particle predicted by the Standard Model left to be discovered, and due to its key role within the theory, its discovery was highly celebrated in the physics community.

In this introduction we will first remind the historical construction of the Standard Model and its current mathematical form. In the second chapter we will expose the history of the discovery of the Higgs boson, its production and decay modes at the LHC. Finally we will discuss how we can make use of experimental data to constrain theories beyond the Standard Model.

1 The Standard Model of particle physics

1.1 Historical introduction

The Standard Model of particle physics (SM) is a theory describing the behavior of the elementary particles – or rather the behavior of particles that we currently believe to be elementary. In the following I will remind some of the major steps leading to the establishment of the SM. More details on this historical development can be found in [1, 2, 3, 4, 5].

1.1.1 The beginning of particle physics

The development of particle physics, and especially the construction of the SM, was spread over several decades. It probably began with the discovery of the electron by J.J. Thomson in 1897. Studying cathode rays emitted by hot filament, he showed that these rays were made of very light charged particles which he called *corpuscles* and which were later renamed electrons. The first elementary particle had been discovered.

Following this discovery Thomson emitted the hypothesis that atoms contain electrons. At that time the notion of atoms, as chemical elements, was well known, and Mendeleev's periodic table well established, but the composition of such objects was still unknown. Thomson proposed a "plump model": electrons, negatively charged, are suspended in a heavy positively charged paste, like plums in a pudding. The atom as a whole is therefore globally electrically neutral, in agreement with experiments.

In 1909 Rutherford lead an experiment to probe the atomic structure and test Thomson's model. For this he fired a beam of α particles – *i.e.* ionized helium – at a thin sheet of gold foil and observed the distribution of outgoing particles. If Thomson's model was true the α particles, positively charged, would have been barely deflected by the gold atoms. However he observed that, although most of the beam was not deflected at all, some particles were significantly deviated. Such a deviation was not consistent with Thomson's model. The only viable explanation was that the positive charges and the main mass of the gold atoms were gathered in the center of the atom, as a nucleus, and that the electrons were "orbiting" around it.

After this great discovery Rutherford called *proton* the nucleus of the hydrogen atom, giving a name to what was regarded at that time as a new elementary particle and a new fundamental piece of the particle jigsaw puzzle.

However this model – protons positively charged inside the nucleus and electrons orbiting around – was not completely convincing for different reasons.

One of them was that, following the understanding of forces already known, protons should not have been able to stay together in the nucleus. At that time the only forces we knew of were gravity and electromagnetism, and the latter imposes the repulsion of two positively – or two

negatively – charged particles, making *a priori* the existence of atoms impossible. This problem was solved many years later with the development of Quantum ChromoDynamics (QCD).

Another problem was the evolution of atomic weights: Helium, with two electrons – and hence two protons in order to ensure atom's neutrality – should have weighted twice as much as the Hydrogen atom. However experiment found a mass four times as much as the Hydrogen mass; and the same issue occurred for heavier nucleus. The answer appeared in 1932 when Chadwick discovered a new neutral particle with a mass similar to the proton's: the *neutron*. This new particle, as the second component of the nucleus, solved the problem of missing mass.

1.1.2 The photon

During the same period theorists were struggling with the notion of photon. At the beginning of the 1900s light was considered as electromagnetic waves and the old theory of light being a bunch of particles proposed by Newton had long been abandoned.

However Einstein's theory of photoelectric effect, based on Planck's theory of *quanta*, was reintroducing the notion of photon. He postulated that light carries a certain amount of energy $E = h\nu$, with h the Planck's constant and ν the wave frequency. When light hits a metal plate, the whole energy is transmitted to electrons inside the plate, which can then be dislodged and emitted. Then the energy of the outgoing electrons depends only on the frequency of the incoming wave and not at all on the beam intensity. Einstein's theory was in agreement with experiments already performed but theorists did not like it because it looked too much like a particle theory of light.

Precise experimental measurements on photoelectric effects were lead in 1916 by Millikan, who wanted to refute Einstein's theory. However his results confirmed very precisely Einstein's predictions and even lead to the precise measurement of Planck's constant h. Yet Einstein's point of view that light was quantized was still poorly accepted by the community.

It is finally the experiment conducted by Compton in 1923 on light scattering and the perfect agreement between experimental results and Einstein's theory that lead to the general acceptance of the particle theory of light and the notion of *photon*.

1.1.3 Antiparticles and the beginning of QED

In the beginning of the 1930s we were aware of four particles that we believed to be elementary, *i.e.* with no substructure: the electron, the proton, the neutron and the photon. As we knew that electrons and photons were interacting together, as in the photoelectric effect, some physicists – such as Fermi, Pauli, Heisenberg or Born, among others – intended to propose a theory, called Quantum ElectroDynamics (QED), describing these interactions.

The development of QED was largely based on Dirac's work. In 1927 he proposed what is called the *Dirac equation*, a relativistic formula describing the behavior of massive spin-$\frac{1}{2}$ particles. However his formula predicted that the states could have negative energy down to minus infinity. As the stable state of a particle is supposed to be the one of lowest energy, the electron should de-excitate infinitely to lower energy states, radiating in the process an infinite amount of energy.

In order to avoid this issue Dirac assumed that the negative energy states were already filled by an infinite "sea" of electrons. Due to Pauli's exclusion principle the "physical" electrons could not de-excitate to negative energy states and were therefore confined to positive ones. Then a hole in the sea, *i.e.* a lack of electron with a specific *negative* energy, was interpreted as the presence of a real particle with *positive* energy and charge.

Dirac's theory stayed marginal until the discovery by Anderson in 1931 of a new particle having the same mass as the electron but with positive charge: the *positron*. This discovery was the first step to prove Dirac's theory. However many physicists were uncomfortable with the idea of an infinite sea of electrons and, despite the discovery of the positron, were still skeptical.

Feynman and Stueckelberg reinterpreted the Dirac equation in the 1940s, introducing, instead of holes and negative energies, the existence of a real new particle with positive energy called *antiparticle*. The discomfort about the hole theory hence disappeared and the idea that, for each particle following Dirac's equation, there was another one, the *antiparticle*, with the same mass but with opposite charge, began to be accepted.

Other antiparticles were discovered subsequently, such as the antiproton in 1955 and the antineutron in 1956 but the discovery of the positron by itself ensured the success of Dirac's theory and validated the notion of antiparticles.

At the same time, and based on Dirac's studies, many physicists tried to develop the QED formalism. This approach was really innovative: in a classical point of view, two electric charges produce an electro-magnetic field; this field is responsible for the action at a distance between the two particles. In QED, the interaction is made through the exchange of a mediator particle, or *gauge boson*, the photon. This concept is generalizable to other interactions, such as the weak or strong interactions as we will see in the following. The notion of mediator is really a key idea in the development of particle physics and later theories of new interactions tried to use this idea.

The development of QED encountered many issues but led to a rather satisfying formulation, called renormalization theory, which was found independently by three different physicists at the end of the 1940s: Feynman, Schwinger and Tomonaga. As it described only interactions between electrons and photons and did not include other particles already known at that time it was still far from a standard model of all particle physics, but the development of QED had made a major step in this direction.

1.1.4 The cosmic ray turmoil and the development of the quark model

Since the discovery of the proton and the neutron, the question of how these particles hold together was still open. We needed a new force strong enough to overcome the repulsive electric force but with a sufficiently short range to not have any influence on everyday life, unlike electromagnetism or gravity.

Based on the development of QED and the idea of particles mediating the interactions, Yukawa proposed in 1934 a model in which a new attractive force, called strong interaction, was binding together protons and neutrons. Assuming that the range of this interaction was of the order of the nucleus size, he derived that the mediator needed to be massive and quite heavy – of the order of 300 times the mass of the electrons, or about a sixth of the mass of the proton, that is, around 150 MeV.

At the same time, physicists studying cosmic rays – flux of particles coming from the universe and crossing Earth's atmosphere – discovered a bunch of new particles. The first ones, the muon μ and the pion π, were discovered in 1937 but fully identified only in 1947. The heaviest one, the pion, had properties very similar to the particle predicted by Yukawa. Physicists called it a *meson*, as its was "middle-weighted" compared to electrons and protons; the muon, as the electron, was set in the *lepton* category due to their low mass, whereas the proton and neutron were set in the *baryon* category.

Was it the end of the story? We had a set of particles; electrons, muons, protons, neutrons

and their antiparticles, and the mediators of two interactions: the photon for electroweak interaction and the pion for strong interaction.

However a great number of new particles were discovered starting from 1947 by studying cosmic rays: the neutral kaon K^0 in 1947, the charged kaon K^+ in 1949, and many others that extended the meson category – which was no longer made exclusively of "middle-weighted" particles. From 1950 onwards heavy baryons were also discovered. Two years later the first modern accelerator, the Brookhaven Cosmotron, was constructed, allowing the production and the study of these "strange" particles in a laboratory instead of relying only on cosmic rays. The number of supposedly elementary particles suddenly blew up during that period and no theory was able to explain such phenomenon.

These new particles were called "strange" not only because they were unexpected but also because they had a very short rate of creation, typically of the order of 10^{-23} s, and a much slower decay rate of the order of 10^{-10} s, which pointed toward two different types of interactions at the origin of the creation and decay phenomena. At the beginning of the 1900s physicists were aware of only two forces: electroweak and gravitational interactions. By the 1950s it seemed that there were two additional ones, called strong and weak interactions.

A first attempt to explain theoretically the appearance of new particles was made by Gell-Mann and Nishijima in 1953, introducing the notion of strangeness – a new conserved quantum number. In 1961, Gell-Mann proposed a new method to classify these particles inside baryon or meson categories, called the Eightfold way. This method still did not explain how the strong interaction works but was nonetheless able to predict the existence of still-undiscovered particles. This was the case for instance for the particle called *omega-minus*, predicted by Gell-Mann and discovered experimentally in 1964.

In 1964, intending to explain the mechanism of the strong interaction, Gell-Mann and Zweig proposed independently to introduce three new elementary particles, the *quarks*, called respectively up (u), with electric charge $+\frac{2}{3}e$, and down (d) and strange (s), both with electric charge $-\frac{1}{3}e$. According to their theory, each baryon was composed of three quarks, each antibaryon of three antiquarks and each meson of a quark and an antiquark. Thus the crowd of new particles was not fundamental ones but bigger structures built from three elementary constituents.

Greenberg added to the theory the existence of three colors: blue, red and green. Each quark carries a color and each baryon and meson is assumed to be "white". For baryons, it means that the three quarks gather the three colors, one for each quark; for mesons it means that the quark carries a color – *e.g.* blue – and the antiquark carries its anticolor – here, anti-blue.

Nambu and Han introduced colored gauge bosons known as *gluons* as mediator of the strong interaction, hence completing the theory and forming the basis of the future Quantum Chromodynamic (QCD).

This theory accounted very well for the observed mesons and baryons but the main pitfall was that no quarks had been observed so far.

In the late 1960s, an experiment was lead at SLAC to probe the structure of the proton in the same way as Rutherford did for the atom. Again the experiment showed a substructure inside the proton, providing a good support to the quark model; however physicists were still very skeptical as experiments were not able to produce isolated quarks. Some of them suggested that the interaction could be confining, forcing quarks to stay inside mesons and baryons and explaining why experiments were not able to catch any free quark. However these explanations were not very satisfactory as the confinement hypothesis was not based on any realistic mechanism.

1.1.5 Beta decays and electroweak unification

Before continuing the story of QCD we need to come back to the 1930s and to the problem of beta decay.

This decay is a radioactive phenomenon known since the end of the 1890s and characterized independently in 1913 by Soddy and Fajans. It corresponds to the decay of a mother nucleus A into a daughter nucleus B and an electron. The nucleus B has the particularity of being the element located one place to the right of A in the periodic table. In more modern notations the beta decay corresponds naively to the equation:

$$n \to p + e^-$$

In a two-body decay the energy of each daughter particle is fixed. However it was observed experimentally that, in the case of a beta decay, the energy of the resulting electron could vary inside a continuous range, suggesting that at least one additional daughter particle was produced during the decay without being detected.

This assumption was first made by Pauli and later by Fermi who proposed a full theory of beta decay. The third daughter particle, called *neutrino*, was assumed to be neutral and to interact very weakly with matter. As was the case for the positron, this new particle was detected experimentally some years later, in the mid-1950s, confirming that the beta decay mechanism follows the equation:

$$n \to p + e^- + \bar{\nu}_e \tag{1.1}$$

The existence of a neutrino associated with each lepton – an electron-neutrino ν_e, a muon-neutrino ν_μ and, later, a tau-neutrino ν_τ – was experimentally demonstrated in 1962 at Brookhaven.

After the discovery in the cosmic rays of new particles interacting weakly, as the electron and the neutrino, the theory of beta decay was generalized to the theory of weak interactions. However Fermi's theory was valid only at low energy and physicists knew that a full theory of weak interactions, as for QED, was needed to contain new particles mediating the interaction.

Relying on the work of Yang and Mills on non-abelian Gauge theory published in 1954, Glashow proposed in 1961 a model of weak interaction containing three gauge bosons: W^+, W^- and Z^0. He also proposed to add the photon to the theory, hence developing a unification of electromagnetism and weak interactions.

However, unlike the photon, the $W^\pm$ and Z^0 bosons needed to be massive in order to account for the short range of the weak interaction, but no viable mechanism producing such additional mass terms correctly was known at that time.

It is only in 1964 that three independant groups – Englert and Brout, Higgs and Guralnik, Hagen and Kibble – proposed a way to make the weak bosons massive. This mechanism is nowadays denoted shortly as the Higgs mechanism.

In 1967, following this discovery, Weinberg and Salam combined Glashow's model and the Higgs mechanism to formulate the electroweak theory, one of the main pieces of the current SM. A young scientist, 't Hooft, proved in 1971 the renormalizability of the theory. Then the entire physics of leptons was formulated.

The $W^\pm$ and Z^0 bosons predicted by the electroweak theory were discovered in 1983 at CERN, extending the set of experimental discoveries in agreement with SM predictions.

1.1.6 Quark model: the November revolution

After the electroweak theory was established, some physicists intended to enlarge it, including not only leptons – as electrons, muons or neutrinos – but also quarks. At that time, as we

have already said, the quark model was considering only three different quark flavors: u, d and s. However, with this quark flavor configuration, the electroweak theory predicts what is called Flavor Changing Neutral Currents (FCNC): interactions at tree or loop level allowing a modification of flavor with no variation of the electric charge. However this phenomenon was not – or barely – observed experimentally. This is the case for instance for the $K^0 - \bar{K}^0$ transition which is observed experimentally although very small. The tree-level phenomenon (see left panel of figure 1.1) would produce too large a $K^0 - \bar{K}^0$ transition compared to experimental measurements and hence would need to be theoretically suppressed – which is the case in the SM – whereas the transition at loop level (right panel of figure 1.1) produces small FCNC consistent with experimental results.

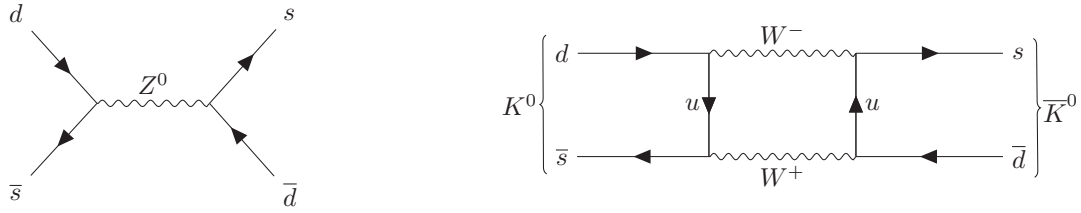

FIGURE 1.1: $K^0 - \bar{K}^0$ transition in the three-quark flavor scheme at both tree level (left panel) and one-loop level (right panel).

In order to suppress these processes theoretically Glashow, Iliopoulos and Maiani proposed in 1970 to introduce a new quark, the *charm* c with electric charge $+\frac{2}{3}e$. This new particle, beside suppressing FCNC at tree level and reducing them drastically at loop level, provided an additional symmetry between particles when included in the model. Indeed in the lepton sector, particles can be stored by pairs: (ν_e, e^-), (ν_μ, μ), (ν_τ, τ). The c quark can be viewed as a heavy cousin of the u quark; then one can store the quark sector into two different pairs: (u,d) and (c,s).

Even with the theoretical success of the FCNC deletion due to the use of the new quark, this proposal was not recognized before the events of 1974. That year two experimental teams published in November the discovery of a new particle: the J/ψ. It was an electrically neutral meson and very heavy whose lifetime was very long as compared to other hadrons in the same mass range, then probably relying on new physics. Physicists intensively discussed this discovery and it was finally the quark model, which interpreted the J/ψ particle as the $c\bar{c}$ meson, that won the debate. Since then, the quark model became the common explanation of the existence of multiple mesons and baryons.

Experiments kept on discovering new particles. In 1975 the tau lepton, belonging to the third generation of leptons, was discovered, providing the hint of the existence of a third generation of quarks. In 1977 a new heavy meson was discovered and proved the existence of the bottom quark b, heavier equivalent of the strange or the down quarks. In 1979 the DESY experiment discovered the gluon, gauge boson of the strong interaction. The top quark t, last quark predicted by the theory in order to complete the third generation of quarks, was only discovered in 1995 at the Tevatron, hence completing the SM fermion spectrum.

1.1.7 Final piece: the Higgs boson

By the end of the 1980s the SM of particle physics was well established: physicists had constructed a model for the strong and electroweak forces which, together, formed the SM. The

gauge bosons mediating the interactions – namely the $W^{\pm}$, Z^0 and γ for the electroweak part, and the gluon g for the strong part – were all discovered and we were aware of three generations of quarks and leptons. Physicists kept testing the model against experimental data and, over the years, found an astonishing agreement between theory and experiment. However one last piece was missing: the Higgs boson.

This boson is a piece of the theoretical mechanism required to provide a mass to the $W^{\pm}$ and Z^0 bosons and to all fermions. But its mass is barely constrained by theory and its lifetime is too short to be detected directly, making its experimental discovery a very difficult challenge.

After decades of searches during which the Higgs boson was still hiding, the two main collaborations at CERN based on the ATLAS and CMS detectors finally made the discovery in 2012, providing the evidence of a new neutral scalar particle with a mass of around 125 GeV and with properties very similar to the ones predicted by the SM [6, 7].

Experiments are still studying the Higgs boson and physics around it, measuring its properties with very high accuracy, testing their adequacy with the SM predictions.

But this is not the end of the story: some experiments performed during the last decades have shed light on phenomena not described at all by the SM (see section 1.3). The work of theorists is then to modify or to complete the current SM in order to account for these phenomena. In the meantime experimentalists work hard to get ever more precise measurements to detect discrepancies between the SM predictions and the experimental data and probe higher and higher energies in order to, maybe, discover new particles.

1.2 Structure of the Standard Model

1.2.1 Particle content and symmetries

The Standard Model of particle physics is a gauge theory based on the symmetry group $G_{SM} = SU(3)_c \times SU(2)_L \times U(1)_Y$. This theory is able to describe three of the four known interactions: the strong (through $SU(3)_c$) and the electroweak interactions gathering electromagnetism and weak interactions (through $SU(2)_L \times U(1)_Y$).

The theory contains a set of elementary particles which is split into two groups: the fermions, with spin-$\frac{1}{2}$, which are the basic components of all matter from which we are made, and the bosons, with integer spin – spin-0 for the Higgs boson, spin-1 for the other bosons – which are the mediators of the interactions. Figure 1.2 summarizes all the particle content of the model.

1.2.1.1 *Bosons*

Most of the known bosons are *gauge* bosons (see fourth column of figure 1.2), that is, particles being a mediator of a specific interaction.

The different interactions, with their mediators, range of action and relative intensity, are summarized in table 1.1.

Gluons g are the mediators of the strong interaction, described by Quantum ChromoDynamics (QCD) based on the $SU(3)_c$ non-abelian gauge group. This force binds quarks together in order to form hadrons (protons, neutrons, pions...). It is also responsible for the nucleus cohesion, allowing protons to stay together despite the electromagnetic repulsion. The mass

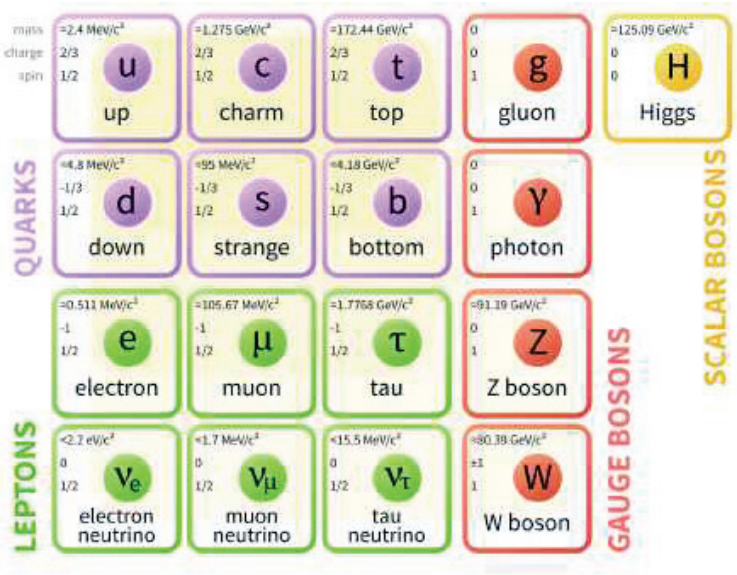

FIGURE 1.2: Particle content of the Standard Model of particle physics.

of common objects around us is mainly generated by the binding energy resulting from this interaction.

$W^{\pm}$ and Z^0 bosons are the mediators of the weak interaction, described as a part of the electroweak interaction based on the $SU(2)_L \times U(1)_Y$ gauge group. This interaction is responsible for radioactive β-decays.

Photons γ are the mediators of the electromagnetic interaction which is, with gravity, the only force we are directly sensitive to in everyday life. Besides binding electrons with nuclei, hence allowing the stability of all matter we are made of, photons, as elementary constituents of light, are essential in most of our daily life, from the microwave to warm up food to telecommunication, including our ability to see.

The Higgs boson h plays a very unique role as it takes part in the Higgs mechanism which gives mass to the elementary particles. Discovered in 2012 at the Large Hadron Collider (LHC), a circular accelerator located beneath the France-Switzerland border, it was, for more than fourty years, the last particle predicted by the SM yet undiscovered. Due to its key role inside the SM theory, its discovery was hoped for and much anticipated. Hence the experimental proof of its existence was celebrated all around the world.

Interaction	**Mediator**	**Relative intensity at 10^{-18} m**	**Range (m)**
Strong	gluons g	25	10^{-15}
Electromagnetic	photons γ	1	∞
Weak	$W^{\pm}$, Z^0	0.8	10^{-18}
Gravitation	gravitons ?	10^{-41}	∞

TABLE 1.1: The four fundamental interactions. Ranges have been taken from [8].

1.2.1.2 *Fermions*

Fermions are split into two categories: quarks and leptons. Leptons are only sensitive to the electroweak interaction whereas quarks are sensitive to both the strong and the electroweak interactions. They are sorted in three generations, each one corresponding to a column in figure 1.2.

Quarks, bound together with gluons, form heavier structures called hadrons. These hadrons are split into two categories: mesons – pions, kaons... – with integer spin, composed of two valence quarks – one quark and one antiquark –, and baryons – protons, neutrons... – with half-integer spin, composed of three valence quarks – three quarks or three antiquarks.

Quarks and leptons – especially the first generation including up and down quarks and electrons – are the building blocks of all matter we are made of (see figure 1.3). Indeed matter is made up of molecules, themselves composed of atoms. Atoms contain a nucleus made of protons and neutrons constituted by gluons and up and down quarks – *uud* and *udd* respectively. Around the nucleus electrons are "orbiting".

Atoms stay stable thanks to the strong force, which binds protons and neutrons together inside the nucleus, and the electromagnetic interaction which links electrons, negatively charged, to the positively charged nucleus. Finally atoms interact with each other mostly *via* the electromagnetic interaction, creating bigger structures.

The two other generations of quarks – forming heavy baryons and mesons – and leptons, if not present in ordinary matter, can be found in specific phenomena such as cosmic rays – beams of very energetic particles coming from space and hitting Earth's atmosphere – or can be created in particle accelerators.

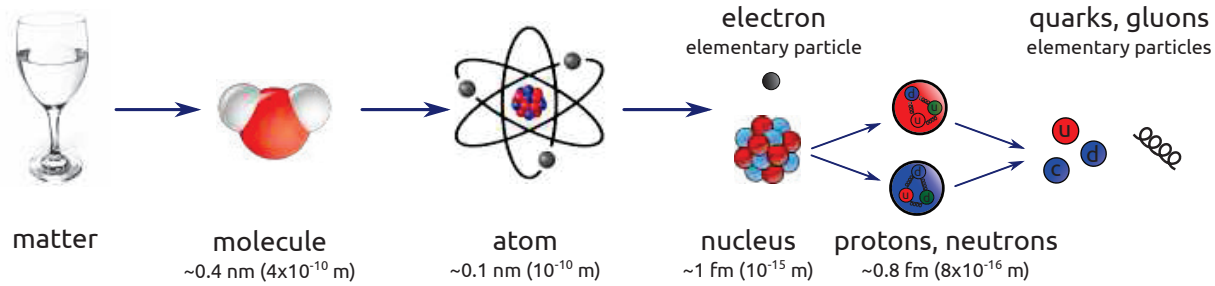

FIGURE 1.3: Quarks, gluons and electrons as building blocks of matter.

1.2.2 LAGRANGIAN FORMULATION

The mathematical formulation of the SM is based on Quantum Field Theory (QFT) where each particle is associated with a space-time dependent field $\psi(\vec{r}, t)$. Particles and their interactions are described through a Lagrangian $\mathcal{L}$, which can be split into different sectors:

$$\mathcal{L}_{SM} = \mathcal{L}_{fermions} + \mathcal{L}_{bosons} + \mathcal{L}_{Higgs} + \mathcal{L}_{Yukawa} \tag{1.2}$$

Each field $\psi(\vec{r}, t)$ will transform in a specific way under the global symmetry $G_{SM} = SU(3)_c \times SU(2)_L \times U(1)_Y$. The quantum numbers of the SM particles associated with the G_{SM} transformations are summarized in table 1.2. In particular, the electric charge of each particle – which is the quantum number associated with the $U(1)_{em}$ symmetry included

in the $SU(2)_L \times U(1)_Y$ symmetry – can be computed from I_3 and Q_Y, the quantum numbers associated with $SU(2)_L$ and $U(1)_Y$ respectively: $Q_{em} = I_3 + \frac{Q_Y}{2}$.

Particle type	**Particle content**	$\boldsymbol{SU(3)_c}$	$\boldsymbol{SU(2)_L}$	$\boldsymbol{I_3}$	$\boldsymbol{Q_Y}$ $\boldsymbol{(U(1)_Y)}$	$\boldsymbol{Q_{em}}$ $\boldsymbol{(U(1)_{em})}$
Quarks	$Q_L = \begin{pmatrix} u_L \\ d_L \end{pmatrix}$	**3**	**2**	+1/2 -1/2	1/3	+2/3 -1/3
	u_R	$\bar{\mathbf{3}}$	**1**	0	-4/3	-2/3
	d_R				2/3	1/3
Leptons	$L_L = \begin{pmatrix} \nu_L \\ e_l \end{pmatrix}$	**1**	**2**	+1/2 -1/2	-1	0 -1
	e_R	**1**	**1**	0	2	+1
Gauge bosons	g	**8**	**1**	0	0	0
	Z^0, $W^\pm$	**1**	**3**	0, ±1	0	0, ±1
(spin 1)	γ	**1**	**1**	0	0	0
Higgs doublet (spin 0)	$H = \begin{pmatrix} G^+ \\ \frac{h+iG^0+v}{\sqrt{2}} \end{pmatrix}$	**1**	**2**	+1/2 -1/2	+1	+1 0

TABLE 1.2: Particles quantum numbers under the gauge symmetry G_{SM}.

As we assume the theory to be invariant under G_{SM}, the Lagrangian $\mathcal{L}_{SM}$ needs to be globally and locally invariant under any transformation of G_{SM}. We will see in the following how this condition can be imposed. The discussion below is based on [2, 9].

1.2.2.1 *Fermionic sector* $\mathcal{L}_{fermions}$

A spin-$\frac{1}{2}$ particle with mass m can be represented by a four-component Dirac spinor ψ, which can also be decomposed into two Weyl spinors ψ_L and ψ_R:

$$\psi = \begin{pmatrix} \psi_L \\ \psi_R \end{pmatrix}, \qquad \psi_L \equiv P_L\psi, \qquad \psi_R \equiv P_R\psi \tag{1.3}$$

with the projectors $P_L \equiv \frac{1-\gamma^5}{2}$, $P_R \equiv \frac{1+\gamma^5}{2}$ and γ^5 the fifth Dirac matrix (see Appendix A).

The Lagrangian associated with a Dirac field writes:

$$\mathcal{L} = \underbrace{i\bar{\psi}\gamma^\mu\partial_\mu\psi}_{\text{kinetic term}} - \underbrace{m\bar{\psi}\psi}_{\text{mass term}} \tag{1.4}$$

with $\bar{\psi} = \psi^\dagger\gamma^0$ and γ_μ, $\mu = \{0, 1, 2, 3\}$, the Dirac matrices (see Appendix A).

However this Lagrangian encounters two pitfalls. First, there is no local invariance under a $U(1)$ symmetry – and, *a fortiori*, uner G_{SM}. Indeed, if we assume the Dirac spinors to transform under some *global* $U(1)$ symmetry with generator Q such that $\psi \xrightarrow{U(1)} e^{i\alpha Q}\psi$, then the Lagrangian $\mathcal{L}$ is invariant under $U(1)$. However this is no longer true for a *local* transformation $\psi \xrightarrow{U(1)} e^{i\alpha(x)Q}\psi$:

$$\mathcal{L} \xrightarrow{U(1)} \mathcal{L}' = \underbrace{i\bar{\psi}\gamma^\mu\partial_\mu\psi - m\bar{\psi}\psi}_{=\mathcal{L}} - \bar{\psi}\gamma^\mu\left(\partial_\mu\alpha(x)\right)Q\psi \neq \mathcal{L} \tag{1.5}$$

In order to preserve local invariance one needs to replace the partial derivative ∂_μ by a covariant derivative D_μ defined such that:

$$D_\mu \psi \xrightarrow{U(1)} e^{i\alpha(x)Q} D_\mu \psi \tag{1.6}$$

For this, one needs to introduce a gauge field, denoted A_μ, linked to the covariant derivative and transforming not trivially inder a local $U(1)$ transformation:

$$D_\mu \equiv \partial_\mu + ieQA_\mu, \qquad A_\mu \xrightarrow{U(1)} A_\mu - \frac{1}{e}\partial_\mu \alpha(x) \tag{1.7}$$

where e will be interpreted as the coupling strength of the interaction mediated by the A_μ field.

In order to make the field A_μ physical one needs also to add a kinetic term. The only possible gauge-invariant and renormalizable term writes:

$$\mathcal{L}_{kin} = -\frac{1}{4} F_{\mu\nu} F^{\mu\nu}, \qquad F_{\mu\nu} \equiv \partial_\mu A_\nu - \partial_\nu A_\mu \tag{1.8}$$

Notice that a mass term for A_μ would break the $U(1)$ symmetry. In order to preserve the $U(1)$ symmetry in the whole Lagrangian the gauge field has to be massless.

We can now rewrite the Lagrangian (1.4) in a locally invariant form:

$$\mathcal{L} = i\bar{\psi}\gamma^\mu D_\mu \psi - m\bar{\psi}\psi - \frac{1}{4} F_{\mu\nu} F^{\mu\nu} \tag{1.9}$$

$$= \underbrace{i\bar{\psi}\gamma^\mu \partial_\mu \psi}_{\text{fermion kinetic term}} - \underbrace{m\bar{\psi}\psi}_{\text{mass term}} - \underbrace{eQ\bar{\psi}\gamma^\mu A_\mu \psi}_{\text{interaction term}} \underbrace{- \frac{1}{4} F_{\mu\nu} F^{\mu\nu}}_{\text{gauge boson kinetic term}} \tag{1.10}$$

Hence, the Lagrangian contains a kinetic term for both the fermion ψ and the gauge field A_μ. In addition, an interaction term between the fermion and the gauge field has appeared.

We can easily generalize this process to a generic symmetry group G instead of $U(1)$. Then we can conclude that requiring local invariance under some specific symmetry group G imposes the apparition of an associated gauge field $\tilde{G}_\mu$ and of an interaction term between the Dirac fermions and the gauge field.

This method can be applied to the whole G_{SM} symmetry, introducing the appropriate gauge fields and kinetic terms for the strong and electroweak sectors (see equations (1.20) and (1.21)): we can introduce the gauge field B_μ associated with the hypercharge $U(1)_Y$, the three gauge fields W^a_μ, $a = \{1, 2, 3\}$, associated with the isospin $SU(2)_L$, and the eight gauge fields G^A_μ, $A = \{1, ..., 8\}$, associated with the strong interaction $SU(3)_c$.

Taking the example of a left-quark spinor $\psi = Q_L$, the field will transform under G_{SM} as (cf. table 1.2):

$$\psi \xrightarrow{G_{SM}} e^{i(\alpha(x)Q_Y/2 + \beta_a(x)\tau^a + \delta_A(x)T^A)} \psi \tag{1.11}$$

with $\tau^a = \frac{\sigma^a}{2}$, $T^A = \frac{\lambda^A}{2}$, σ^a the Pauli matrices and λ^A the Gell-Mann matrices (see Appendix A). The matrices τ^a and T^A obey the following relations:

$$[\tau^a, \tau^b] = \epsilon^{abc}\tau^c, \qquad [T^A, T^B] = f^{ABC}T^C \tag{1.12}$$

with ϵ^{abc} the total antisymmetric tensor. ϵ^{abc} and f^{ABC} are called the structure constants of the $SU(2)$ and $SU(3)$ symmetry group respectively.

Using transformation (1.11) and following the method described above for the $U(1)$ case, one can define the covariant derivative associated with the transformation (1.11) and the field transformations:

$$\begin{gathered} D_\mu \equiv \partial_\mu + ig'\frac{Q_Y B_\mu}{2} + ig\tau_a W_\mu^a + ig_s T_A G_\mu^A \\ B_\mu \xrightarrow{G_{SM}} B_\mu - \frac{1}{g'}\partial_\mu \alpha(x), \qquad W_\mu^a \xrightarrow{G_{SM}} W_\mu^a - \frac{1}{g}\partial_\mu \beta^a(x) + \underbrace{\epsilon^{abc}\beta_b(x)W_{c\mu}}_{\text{non-abelian term}} \\ G_\mu^A \xrightarrow{G_{SM}} G_\mu^A - \frac{1}{gs}\partial_\mu \gamma^A(x) + \underbrace{f^{ABC}\gamma_B(x)G_{C\mu}}_{\text{non-abelian term}} \end{gathered} \tag{1.13}$$

with g', g and g_s the coupling strengths associated with the hypercharge, isospin and strong interaction respectively. The third terms in the transformation of the W_μ^a and G_μ^A fields is due to the non-abelian nature of the $SU(2)$ and $SU(3)$ groups and are required to ensure local invariance.

Using these definitions and inserting them in (1.4), one can check that local gauge invariance under a G_{SM} transformation is now well preserved for the kinetic term.

It is important to notice that the exact definition of the covariant derivative tightly depends on the quantum numbers of the Dirac spinor considered. The above equations are valid for a SM left-quark spinor Q_L. The covariant derivative for the other SM particles are listed in equation (1.20).

The second pitfall of Lagrangian (1.4) is that, in the case where ψ_L and ψ_R do not transform in the same way under a specific group symmetry, then the mass term is not invariant under the symmetry considered. This is the case for the SM fermions which transform under $SU(2)_L$ as a doublet for the left component and as a singlet for the right one. One can show this issue by explicitly rewriting the Lagrangian (1.4) in terms of the Weyl spinors:

$$\mathcal{L} = (\bar{\psi_L} + \bar{\psi_R})(i\gamma^\mu\partial_\mu - m)(\psi_L + \psi_R) \tag{1.14}$$

Using some properties of the Dirac matrices:

$$\{\gamma^5, \gamma^\mu\} = 0, \qquad (\gamma^5)^2 = \mathbb{1}_4 \tag{1.15}$$

one can easily show the following relations:

$$P_L P_R = P_R P_L = 0, \qquad P_L P_L = P_L, \qquad P_R P_R = P_R \tag{1.16}$$

$$P_L\gamma^\mu P_L = P_R\gamma^\mu P_R = 0, \qquad P_L\gamma^\mu P_R = \gamma^\mu P_R, \qquad P_R\gamma^\mu P_L = \gamma^\mu P_L \tag{1.17}$$

We then deduce that the only non-zero terms in the Lagrangian (1.14) write:

$$\mathcal{L} = i\bar{\psi_L}\gamma^\mu\partial_\mu\psi_L + i\bar{\psi_R}\gamma^\mu\partial_\mu\psi_R - m(\bar{\psi_L}\psi_R + \bar{\psi_R}\psi_L) \tag{1.18}$$

Considering the SM case, the left and right components do not transform in the same way under $G_{SM} = SU(3)_c \times SU(2)_L \times U(1)_Y$ (see table 1.2). Then, although the kinetic

term is still invariant under G_{SM}, this is no longer true for the mass term. As local gauge invariance under G_{SM} is required, the fermionic mass term cannot appear in the Lagrangian. However, as we observe experimentally that fermions are massive, we need to introduce another mechanism, called Higgs mechanism, in order to give fermions a mass (see section 1.2.2.3).

Based on the above argumentation one can write the fermionic part of the SM Lagrangian:

$$\begin{aligned}\mathcal{L}_{fermions} = &\sum_{i=1}^{3}(\bar{L}_{i,L}\gamma^\mu D_\mu L_{i,L} + \bar{e}_{i,R}\gamma^\mu D_\mu e_{i,R}) \\ &+ (\bar{Q}_{i,L}\gamma^\mu D_\mu Q_{i,L} + \bar{u}_{i,R}\gamma^\mu D_\mu u_{i,R} + \bar{d}_{i,R}\gamma^\mu D_\mu d_{i,R})\end{aligned} \tag{1.19}$$

with i indexing the three generations of fermions. The covariant derivatives are defined as:

$$\begin{aligned}D_\mu L_{L,i} &= (\partial_\mu + igW^a_\mu\tau_a + ig'\frac{B_\mu Q_Y}{2})L_{L,i} \\ D_\mu e_{R,i} &= (\partial_\mu + ig'\frac{B_\mu Q_Y}{2})e_{R,i} \\ D_\mu Q_{L,i} &= (\partial_\mu + ig_sG^A_\mu T_A + igW^a_\mu\tau_a + ig'\frac{B_\mu Q_Y}{2})Q_{L,i} \\ D_\mu u_{R,i} &= (\partial_\mu + ig_sG^A_\mu T_A + ig'\frac{B_\mu Q_Y}{2})u_{R,i} \\ D_\mu d_{R,i} &= (\partial_\mu + ig_sG^A_\mu T_A + ig'\frac{B_\mu Q_Y}{2})d_{R,i}\end{aligned} \tag{1.20}$$

with, as above, B_μ, W^a_μ, $a = \{1,2,3\}$ and G^A_μ, $A = \{1,...,8\}$ the gauge fields associated with the hypercharge symmetry group $U(1)_Y$, the isospin symmetry group $SU(2)_L$ and the color symmetry group associated with the strong interaction $SU(3)_c$ respectively. The g', g and g_s constants are their respective coupling strengths.

1.2.2.2 *Bosonic sector* $\mathcal{L}_{bosons}$

The bosonic part of the SM Lagrangian corresponds to the gauge bosons kinetic terms as constructed in equation (1.8). Following the discussion developed in the previous section one can write the appropriate Lagrangian:

$$\mathcal{L}_{bosons} = -\frac{1}{4}B_{\mu\nu}B^{\mu\nu} - \frac{1}{4}W^a_{\mu\nu}W^{a\ \mu\nu} - \frac{1}{4}G^A_{\mu\nu}G^{A\ \mu\nu} \tag{1.21}$$

with the kinetic term:

$$\begin{aligned}B_{\mu\nu} &= \partial_\mu B_\nu - \partial_\nu B_\mu \\ W^a_{\mu\nu} &= \partial_\mu W^a_\nu - \partial_\nu W^a_\mu - g\epsilon^{abc}W^b_\mu W^c_\nu \\ G^A_{\mu\nu} &= \partial_\mu G^A_\nu - \partial_\nu G^A_\mu - g_s f^{ABC}G^B_\mu G^C_\nu\end{aligned} \tag{1.22}$$

As for equation (1.13), the third term in $W^a_{\mu\nu}$ and $G^A_{\mu\nu}$ comes from the non-abelian nature of the $SU(2)$ and $SU(3)$ symmetry groups.

1.2.2.3 *Higgs sector $\mathcal{L}_{Higgs}$ – one-Higgs doublet model*

In the two previous paragraphs we have introduced kinetic terms for both fermions and gauge bosons and have established interaction terms between the two. However, as we have shown explicitly for the fermion sector, we are not able to add a mass term for both fermions and gauge bosons which is suitably locally invariant under G_{SM}.

As we measure experimentally that the fermions and the $W^{\pm}$ and Z^0 gauge bosons are massive, the SM theory needs to introduce an appropriate mechanism to generate mass terms for these particles.

The solution to this problem has been found by R. Brout, F. Englert and P. Higgs in 1964 and is now known as the "Higgs mechanism". But before exposing how it works we must introduce first the notion of spontaneous symmetry breaking.

◦ Spontaneous symmetry breaking principle

Let's consider the following Lagrangian for a real scalar field ϕ:

$$\mathcal{L} = \underbrace{\frac{1}{2}\partial_\mu\phi\partial^\mu\phi}_{\text{kinetic term}} - \underbrace{\left(\frac{1}{2}\mu^2\phi^2 + \frac{1}{4}\lambda\phi^4\right)}_{=\,\mathrm{V}(\phi),\ \text{potential term}} \tag{1.23}$$

with $\lambda > 0$ in order to have a potential bounded from below and thus ensure the existence of a minimum. This Lagrangian is symmetric under the parity transformation:

$$P : \phi \to -\phi \tag{1.24}$$

In the case where $\mu^2 > 0$, the above Lagrangian corresponds to the usual Lagrangian for a massive real scalar field with mass $m = \mu$. The ground state – or vacuum – *i.e.* the state corresponding to the minimum of energy, corresponds to the minimum of the potential $V(\phi)$ and, in the case $\mu^2 > 0$, is the trivial solution $\phi = 0$:

$$\frac{dV}{d\phi} = 0 \Leftrightarrow \mu^2\phi + \lambda\phi^3 = 0 \tag{1.25}$$

$$\Leftrightarrow \phi(\mu^2 + \lambda\phi^2) = 0 \tag{1.26}$$

$$\Rightarrow \phi = 0 \tag{1.27}$$

The left panel of figure 1.4 shows the shape of the potential in the case $\mu^2 > 0$.

However if we consider that $\mu^2 < 0$ then the potential has three extrema:

$$\frac{dV}{d\phi} = 0 \Leftrightarrow \begin{cases} \phi = 0 \\ \phi = \pm\sqrt{\frac{-\mu^2}{\lambda}} \end{cases} \tag{1.28}$$

Then the minima occur at $\phi_{min} = \pm\sqrt{\frac{-\mu^2}{\lambda}}$ and the trivial vacuum obtained in the previous case becomes unstable (see right plot of figure 1.4). Hence, perturbation theory cannot be performed at $\phi = 0$ as the perturbation series in ϕ will not converge; we need therefore to proceed to a change of variable in order to work around one of the real minima. Choosing arbitrarily one of the ground states, we define:

$$\phi \equiv \eta + v, \qquad v = \sqrt{\frac{-\mu^2}{\lambda}} \tag{1.29}$$

The η field corresponds to fluctuations around the ground state $\phi_{min} = v$, with v called the *vacuum expectation value* (vev).

Rewriting Lagrangian (1.23) in terms of η, we obtain:

$$\mathcal{L} = \underbrace{\frac{1}{2}\partial_\mu\eta\partial^\mu\eta}_{\text{kinetic term}} - \underbrace{\lambda v^2\eta^2}_{\text{mass term}} - \lambda v\eta^3 - \frac{1}{4}\lambda\eta^4 + \frac{1}{4}\lambda v^4 \tag{1.30}$$

The case where $\mu < 0$, which at first glance seemed unphysical, finally corresponds to the Lagrangian of a massive scalar particle η with mass $m = \sqrt{2\lambda v^2}$.

We can note however that the initial symmetry $P : \phi \to -\phi$ is not valid anymore for η due to the presence of the η^3 term. This phenomenon is called **spontaneous symmetry breaking**: the initial symmetry is broken without the intervention of any external term.

Note that the other way to break a symmetry, called *explicit symmetry breaking*, has already been illustrated when working on the fermionic sector of the Lagrangian: the mass term $m\bar{\psi}_L\psi_R$ is not invariant under a transformation of $SU(2)_L$; then adding this term in the Lagrangian explicitly breaks the $SU(2)_L$ symmetry.

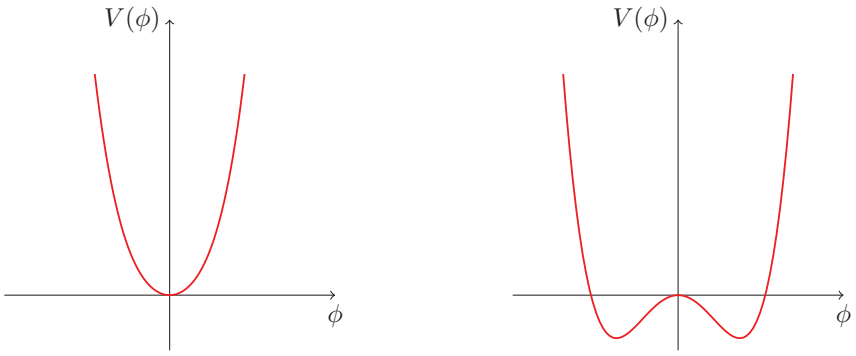

FIGURE 1.4: Shape of the potential $V(\phi) = \frac{1}{2}\mu^2\phi^2 + \frac{1}{4}\lambda\phi^4$ in the case where $\mu^2 > 0$ (left) and $\mu^2 < 0$ (right). In the second case, the trivial extremum $\phi = 0$ becomes unstable and the true minima are at $\phi_{min} = \pm\sqrt{\frac{-\mu^2}{\lambda}}$.

The mechanism of spontaneous symmetry breaking seen above can easily be generalized to a continuous symmetry using this time a complex scalar field $\phi = \frac{1}{\sqrt{2}}(\phi_1 + i\phi_2)$. Then the initial Lagrangian writes:

$$\mathcal{L} = (\partial_\mu\phi)^\dagger(\partial^\mu\phi) - (\mu^2\phi^\dagger\phi + \lambda(\phi^\dagger\phi)^2) \tag{1.31}$$

This time the Lagrangian is globally invariant under a $U(1)$ symmetry: $\phi \xrightarrow{U(1)} e^{i\alpha Q}\phi$.

As above, if $\mu^2 < 0$ the potential will have non-trivial minima:

$$\frac{\partial V}{\partial\phi} \Leftrightarrow \begin{cases} \phi = 0 \\ |\phi|^2 = -\frac{\mu^2}{2\lambda} \equiv \frac{v^2}{2} \end{cases} \tag{1.32}$$

Thus we have an infinity of minima parametrized by an angle θ:

$$\phi_{min} = \frac{v}{\sqrt{2}}e^{i\theta} \tag{1.33}$$

In order to be able to conduct perturbative calculations we need to pick one specific minimum, say $\phi_{min} = \frac{v}{\sqrt{2}}$, that is $\phi_{1,min} = v$, $\phi_{2,min} = 0$ and then perform a change of variables:

$$\phi_1 = v + \eta, \qquad \phi_2 = \xi, \qquad \phi = \frac{1}{\sqrt{2}}(v + \eta + i\xi) \tag{1.34}$$

As above, the fields η and ξ correspond to excitations around the vacuum ϕ_{min}.

Rewriting the Lagrangian in terms of η and ξ we obtain:

$$\mathcal{L} = \left[\underbrace{\frac{1}{2}\partial_\mu\eta\partial^\mu\eta}_{\text{kinetic term}} - \underbrace{\lambda v^2\eta^2}_{\text{mass term}}\right] + \left[\underbrace{\frac{1}{2}\partial_\mu\xi\partial^\mu\xi}_{\text{kinetic term}}\right] - \left[\lambda v(\eta^3 + \eta\xi^2) + \frac{1}{4}\lambda(\eta^4 + \xi^4 + 2\eta^2\xi^2)\right] + \frac{1}{4}\lambda v^4 \tag{1.35}$$

In addition to the interaction terms between η and ξ, we can see that both fields have a kinetic term. However only the η field acquires a mass $m = \sqrt{2\lambda v^2}$ whereas the ξ field remains massless. This kind of field ξ is called a Goldstone Boson. Note that, according to the Goldstone theorem, a spontaneous symmetry breaking generates a number of Goldstone bosons – *i.e.* additional massless fields – equal to the number of broken generators of the initial symmetry group G. Here, the $U(1)$ symmetry group is one-dimensional and is entirely broken. Hence there is only one Goldstone boson.

◦ The Higgs mechanism

We are still left with the problem of generating mass for the gauge bosons. This is the role of the Higgs mechanism that we will present in this section.

The Higgs mechanism is based on the notions of both spontaneous symmetry breaking and local gauge invariance. As seen in the paragraph on the fermionic part of the SM Lagrangian, imposing local gauge invariance under a specific G group requires the replacement of the partial derivatives ∂_μ by the appropriate covariant derivative D_μ. We will develop in the following the formalism of the Higgs mechanism in the case of a $U(1)$ symmetry associated with a gauge field A_μ but it is generalizable to any symmetry group G.

Making the following replacement in (1.31):

$$\partial_\mu \to D_\mu = \partial_\mu + ieQA_\mu \tag{1.36}$$

and then doing the change of variables $\phi = \frac{1}{\sqrt{2}}(v + \eta + i\xi)$ in order to work near the chosen minimum, the Lagrangian becomes:

$$\begin{aligned}\mathcal{L} = &\left[\frac{1}{2}\partial_\mu\eta\partial^\mu\eta - \lambda v^2\eta^2\right] + \left[\frac{1}{2}\partial_\mu\xi\partial^\mu\xi\right] \\ &- \left[\lambda v(\eta^3 + \eta\xi^2) + \frac{1}{4}\lambda(\eta^4 + \xi^4 + 2\eta^2\xi^2)\right] + \frac{1}{4}\lambda v^4 \\ &+ \underbrace{eQvA_\mu\partial^\mu\xi + e^2Q^2vA_\mu A^\mu\eta + eQA_\mu(\eta\partial^\mu\xi - \xi\partial^\mu\eta) + \frac{1}{2}e^2Q^2(\eta^2 + \xi^2)(A_\mu A^\mu)}_{\text{interaction terms}} \\ &+ \underbrace{\frac{1}{2}e^2Q^2v^2A_\mu A^\mu}_{\text{gauge boson mass term}} - \underbrace{\frac{1}{4}F_{\mu\nu}F^{\mu\nu}}_{\text{kinetic term}}\end{aligned} \tag{1.37}$$

The first two lines are identical to the Lagrangian obtained after spontaneous symmetry breaking (see equation (1.35)).

The third line corresponds to interaction terms between the gauge field A_μ and the fields η and ξ.

In the fourth line, in addition to the kinetic term for the gauge field A_μ that we have added by hand in order to make the field physical, there is also the appearance of a mass term that emerges naturally after symmetry breaking. The field A_μ is then massive, with a mass $m = evQ$.

However the term $A_\mu \partial^\mu \xi$ present in the interaction terms is embarrassing: it means that the gauge field A_μ can turn into the scalar field ξ, that is, that the fields are not well defined, allowing a mixing between the two. In fact, this problem can be solved by a simple redefinition of ϕ in the initial Lagrangian (1.31), which was initially invariant under a $U(1)$ transformation. We redefine the field in the following way:

$$\phi \xrightarrow{U(1)} \phi' \equiv \frac{1}{\sqrt{2}}(\phi'_1 + i\phi'_2) = \phi e^{i\theta}, \qquad \theta = -\tan^{-1}(\frac{\phi_2}{\phi_1}) \tag{1.38}$$

such that $\phi'_2 = 0$ and ϕ' is real. Following the same step as above, that is, introducing the covariant derivative in equation (1.31) and doing the change of variable $\phi' = \frac{1}{\sqrt{2}}(v + \eta)$, the field ξ is totally eliminated from equation (1.37):

$$\begin{aligned}\mathcal{L} = &\left[\frac{1}{2}\partial_\mu\eta\partial^\mu\eta - \lambda v^2\eta^2\right] - \left[\lambda v\eta^3 + \frac{1}{4}\lambda\eta^4\right] + \frac{1}{4}\lambda v^4 \\ &+e^2vQ^2\eta(A_\mu A^\mu) + \frac{1}{2}e^2Q^2\eta^2(A_\mu A^\mu) \\ &+\frac{1}{2}e^2Q^2v^2A_\mu A^\mu - \frac{1}{4}F_{\mu\nu}F^{\mu\nu}\end{aligned} \tag{1.39}$$

This transformation can be better understood when counting the number of degrees of freedom: a massless vector field A_μ carries only two degrees of freedom. When it acquires a mass it gains one additional degree of freedom. This is only possible if it "absorbs" the one contained into the massless field ξ. The Goldstone boson then plays the role of the longitudinal part of the field A_μ and, with the appropriate choice of gauge for the initial symmetry G – *i.e.*, in the above example, with the appropriate choice of θ – the Goldstone boson disappears from the equations.

The Higgs mechanism can then be summarized by the following steps:

- Define the Higgs Lagrangian $\mathcal{L} = (\partial_\mu\phi)^\dagger(\partial^\mu\phi) - (\mu^2\phi^\dagger\phi + \lambda(\phi^\dagger\phi)^2)$;
- Impose local gauge invariance under a given symmetry group G in the Lagrangian by replacing partial derivatives ∂_μ with the appropriate covariant derivatives D_μ;
- Choose an arbitrary ground state ϕ_{min} with a vev v and do a change of variables in order to work around it;
- Eliminate the additional Goldstone bosons if necessary by choosing an appropriate gauge.

◦ Lagrangian of the SM Higgs sector

In the case of the SM, as we want to generate mass for $W^\pm$ and Z^0 gauge bosons only, we need to break the $SU(2)_L \times U(1)_Y$ symmetry but still preserve the $U(1)_{em}$ group symmetry

associated with the electromagnetic interaction – and hence with the photon γ. We thus use a complex scalar field ϕ which is a doublet of $SU(2)_L$ with hypercharge $Y = 1$. We can write:

$$\phi = \frac{1}{\sqrt{2}} \begin{pmatrix} \phi_1^+ + i\phi_2^+ \\ \phi_1^0 + i\phi_2^0 \end{pmatrix} \tag{1.40}$$

with ϕ_1^+, ϕ_2^+ charged scalar fields and ϕ_1^0, ϕ_2^0 neutral scalar fields.

Then the Lagrangian of the Higgs sector writes:

$$\mathcal{L}_{Higgs} = (D_\mu\phi)^\dagger(D^\mu\phi) - (\mu^2\phi^\dagger\phi + \lambda(\phi^\dagger\phi)^2), \qquad D_\mu = \partial_\mu + igW_\mu^a\tau^a + ig'\frac{B_\mu}{2} \tag{1.41}$$

Taking $\mu^2 < 0$, the $SU(2)_L \times U(1)_Y$ symmetry breaks spontaneously down to a $U(1)$ symmetry. As we want the photon to be massless we choose a neutral ground state that preserves the $U(1)_{em}$ symmetry:

$$\phi_{min} = \frac{1}{\sqrt{2}} \begin{pmatrix} 0 \\ v \end{pmatrix} \tag{1.42}$$

As $SU(2)_L \times U(1)_Y$ is 3+1=4 dimensional and $U(1)_{em}$ is one-dimensional, we are left, according to the Goldstone theorem, with three Goldstone bosons.

With the appropriate gauge choice, the three Goldstone bosons are "eaten" by the $W^\pm$ and Z^0 gauge bosons which acquire a mass whereas the photon remains massless. We are then left with the field:

$$\phi = \frac{1}{\sqrt{2}} \begin{pmatrix} 0 \\ v + h \end{pmatrix} \tag{1.43}$$

with h a massive neutral scalar field with $m = \sqrt{2\lambda v^2}$ called the Higgs boson.

◦ Computing the mass of the gauge bosons

The last step in the Higgs mechanism is to compute the mass of the physical gauge bosons $W^\pm$, Z^0. For that we need to bring out from the Lagrangian mass terms of the form:

$$m_W^2 W_\mu^+ W^{-\mu}, \qquad \frac{1}{2}m_Z^2 Z_\mu^0 Z^{0\mu} \tag{1.44}$$

These terms are hidden in the kinetic term $(D_\mu\phi)^\dagger(D^\mu\phi)$ of equation (1.41), where the gauge fields W_μ^a, $a = \{1, 2, 3\}$ and B_μ are included in the covariant derivative D_μ. Developing only the part of the kinetic term containing gauge fields and substituting ϕ by the vacuum ϕ_{min} one finds:

$$\begin{aligned} \left| \left(igW_\mu^a\tau_a + ig'\frac{B_\mu}{2} \right) \phi_{min} \right|^2 &= \left| \begin{pmatrix} ig\frac{W_\mu^3}{2} + ig'\frac{B_\mu}{2} & ig\frac{W_\mu^1 - iW_\mu^2}{2} \\ ig\frac{W_\mu^1 + iW_\mu^2}{2} & -ig\frac{W_\mu^3}{2} + ig'\frac{B_\mu}{2} \end{pmatrix} \begin{pmatrix} 0 \\ \frac{v}{\sqrt{2}} \end{pmatrix} \right|^2 \\ &= \frac{1}{8}v^2g^2 \left(W_\mu^1 - iW_\mu^2 \right) \left(W^{1\mu} + iW^{2\mu} \right) \\ &\quad + \frac{1}{8}v^2 \left(g'B_\mu - gW_\mu^3 \right) \left(g'B^\mu - gW^{3\mu} \right) \end{aligned} \tag{1.45}$$

From equation (1.45) one can clearly see that the fields W^a_μ and B_μ are not mass eigenstates. After diagonalisation and proper normalization we deduce the expression of the mass eigenstates $W^\pm_\mu$, Z^0_μ and A_μ:

$$W^+_\mu = \frac{W^1_\mu - iW^2_\mu}{\sqrt{2}}, \qquad W^+_\mu = \frac{W^1_\mu + iW^2_\mu}{\sqrt{2}}, \tag{1.46}$$

$$Z^0_\mu = \frac{g'B_\mu - gW^3_\mu}{\sqrt{g^2+g'^2}}, \qquad A_\mu = \frac{g'B_\mu + gW^3_\mu}{\sqrt{g^2+g'^2}}, \tag{1.47}$$

Re-injecting these expressions into equation (1.45) and comparing to equation (1.44), we deduce the mass of the gauge bosons:

$$m_{W^\pm} = \frac{vg}{2}, \qquad m_{Z^0} = \frac{v}{2}\sqrt{g^2+g'^2}, \qquad m_\gamma = 0 \tag{1.48}$$

As expected we find that the $W^\pm$ and Z^0 are massive whereas the photon remains massless.

1.2.2.4 *Yukawa sector* $\mathcal{L}_{Yukawa}$

As for the gauge bosons, a mass term of the form $m\bar{\psi}_L\psi_R$ breaks explicitly the $SU(2)_L$ symmetry. However we can construct a gauge invariant term based on the Higgs doublet ϕ:

$$\mathcal{L}_{Yukawa} = \sum_{i,j=1}^{3} -y^l_{ij}\bar{L}_{i,L}\phi\ e_{j,R}\ - y^d_{ij}\bar{Q}_{i,L}\phi\ d_{j,R}\ - y^u_{ij}\bar{Q}_{i,L}\tilde{\phi}\ u_{j,R}\ + h.c. \tag{1.49}$$

with i,j indexing the three generations of fermions, $L_{i,L} = \begin{pmatrix}\nu_{i,L}\\ e_{i,L}\end{pmatrix}$, $Q_{i,L} = \begin{pmatrix}u_{i,L}\\ d_{i,L}\end{pmatrix}$ as defined in table 1.2, y_{ij} the 3×3 coupling matrices of the fermions to the Higgs doublet ϕ, which we will call Yukawa matrices, and $\tilde{\phi} = i\sigma^2\phi^*$ the Higgs doublet charge conjugate, with σ^2 the second Pauli matrix (see Appendix A).

Notice that the third term is needed in order to give mass to the up-type quarks, as we will see just below.

After symmetry breaking we need to replace the Higgs doublet by its correct expression:

$$\phi = \frac{1}{\sqrt{2}}\begin{pmatrix}0\\ v+h\end{pmatrix}, \qquad \tilde{\phi} = \frac{1}{\sqrt{2}}\begin{pmatrix}v+h\\ 0\end{pmatrix} \tag{1.50}$$

Equation (1.49) becomes:

$$\mathcal{L}_{Yukawa} = \sum_{i,j=1}^{3} -\frac{y^l_{i,j}}{\sqrt{2}}(v+h)\bar{e}_{i,L}e_{j,R}\ - \frac{y^d_{i,j}}{\sqrt{2}}(v+h)\bar{d}_{i,L}d_{j,R} \tag{1.51}$$

$$- \frac{y^u_{i,j}}{\sqrt{2}}(v+h)\bar{u}_{i,L}u_{j,R}\ + h.c \tag{1.52}$$

The mass terms are of the form $\mathcal{M}^f_{i,j} = \frac{y^f_{i,j}v}{\sqrt{2}}$. In order to get the mass eigenstates one needs to diagonalize the $\mathcal{M}^f_{i,j}$ matrices – or, equivalently, the $y^f_{i,j}$ matrices – *via* a unitary

transformation in the generation space:

$$\begin{aligned}
\tilde{L}'_{L,R} \equiv \begin{pmatrix} e_1 \\ e_2 \\ e_3 \end{pmatrix}_{L,R} &= A_{L,R} \begin{pmatrix} e^m \\ \mu^m \\ \tau^m \end{pmatrix}_{L,R} \equiv A_{L,R}\ \tilde{L}_{L,R}, \\
\tilde{U}'_{L,R} \equiv \begin{pmatrix} u_1 \\ u_2 \\ u_3 \end{pmatrix}_{L,R} &= B_{L,R} \begin{pmatrix} u^m \\ c^m \\ t^m \end{pmatrix}_{L,R} \equiv B_{L,R}\ \tilde{U}_{L,R}, \\
\tilde{D}'_{L,R} \equiv \begin{pmatrix} d_1 \\ d_2 \\ d_3 \end{pmatrix}_{L,R} &= C_{L,R} \begin{pmatrix} d^m \\ s^m \\ b^m \end{pmatrix}_{L,R} \equiv C_{L,R}\ \tilde{D}_{L,R}
\end{aligned} \tag{1.53}$$

where e^m, μ^m, τ^m, u^m, d^m, c^m, s^m, t^m, b^m are the mass eigenstates and $A_{L,R}$, $B_{L,R}$ and $C_{L,R}$ are six unitary matrices such that:

$$\begin{aligned}
A_L^\dagger \mathcal{M}^l A_R &= \begin{pmatrix} m_e & 0 & 0 \\ 0 & m_\mu & 0 \\ 0 & 0 & m_\tau \end{pmatrix} = \frac{v}{\sqrt{2}} \begin{pmatrix} y_e & 0 & 0 \\ 0 & y_\mu & 0 \\ 0 & 0 & y_\tau \end{pmatrix}, \\
B_L^\dagger \mathcal{M}^u B_R &= \begin{pmatrix} m_u & 0 & 0 \\ 0 & m_c & 0 \\ 0 & 0 & m_t \end{pmatrix} = \frac{v}{\sqrt{2}} \begin{pmatrix} y_u & 0 & 0 \\ 0 & y_c & 0 \\ 0 & 0 & y_t \end{pmatrix}, \\
C_L^\dagger \mathcal{M}^d C_R &= \begin{pmatrix} m_d & 0 & 0 \\ 0 & m_s & 0 \\ 0 & 0 & m_b \end{pmatrix} = \frac{v}{\sqrt{2}} \begin{pmatrix} y_d & 0 & 0 \\ 0 & y_s & 0 \\ 0 & 0 & y_b \end{pmatrix}
\end{aligned} \tag{1.54}$$

Then the Yukawa Lagrangian becomes:

$$\begin{aligned}
\mathcal{L}_{Yukawa} = \sum_{i=1}^{3} & -\frac{y_i^l}{\sqrt{2}}(v+h)\bar{e}_{i,L}^m e_{i,R}^m \ - \frac{y_i^d}{\sqrt{2}}(v+h)\bar{d}_{i,L}^m d_{i,R}^m \\
& - \frac{y_i^u}{\sqrt{2}}(v+h)\bar{u}_{i,L}^m u_{i,R}^m \ + h.c
\end{aligned} \tag{1.55}$$

with e_i^m, u_i^m and d_i^m corresponding to the three generations of mass eigenstates defined above.

We deduce the fermion masses and the couplings between fermions and the Higgs boson:

$$m_f = \frac{y_f v}{\sqrt{2}}, \qquad C_{hf\bar{f}} = \frac{y_f}{\sqrt{2}} = \frac{m_f}{v} \tag{1.56}$$

However, as y_f are free parameters in the SM, the masses are not fixed at all by the model and thus cannot be predicted. We then have to rely on experimental data to know the value of the fermion masses (see table 1.3).

◦ The CKM matrix

The unitary transformations defined in equations (1.53), though useful to go to the mass eigenstates basis, is problematic when looking at weak interactions with the $W^\pm$ boson, called

m_e	m_μ	m_τ	m_u	m_d	m_s	$\bar{m}_c(\bar{m}_c)$	$\bar{m}_b(\bar{m}_b)$	m_t
0.51	105.66	177.682	2.2	4.7	96	1.28×10^3	4.18×10^3	174.2×10^3

TABLE 1.3: Masses of the SM fermions in MeV. The quark masses are taken in the $\overline{MS}$ scheme except for the top mass taken as the pole mass. Data taken from [10].

charged currents, in the quark sector as it breaks the link between up- and down-type quarks of a same generation.

Developing the fermion Lagrangian (1.19) one find the charged current part for the quark sector:

$$-\mathcal{L}_{cc}^{\text{quark}} \supset \frac{g}{2\sqrt{2}}\left[\bar{\tilde{U}}'_L\gamma^\mu(1-\gamma_5)\tilde{D}'_L W_\mu^+ + h.c.\right] \tag{1.57}$$

Rewriting this equation in terms of the mass eigenstates one finds:

$$\begin{aligned}-\mathcal{L}_{cc}^{\text{quark}} \supset& \frac{g}{2\sqrt{2}}\left[\bar{\tilde{U}}_L\gamma^\mu(1-\gamma_5)B_L^\dagger C_L\tilde{D}_L W_\mu^+ + h.c.\right]\\ =& \frac{g}{2\sqrt{2}}\left[\sum_{i,j=1}^{3}\bar{u}_{i,L}^m\gamma^\mu(1-\gamma_5)V_{ij}^{CKM}d_{j,L}^m W_\mu^+ + h.c.\right]\end{aligned} \tag{1.58}$$

with $V^{CKM} \equiv B_L^\dagger C_L$, called the Cabibbo-Kobayashi-Maskawa (CKM) matrix, and u_i^m, d_j^m the quark mass eigenstates.

Equation (1.58) shows that the quark mass eigenstates u_i^m, d_i^m are not eigenstates of the weak interactions. Then the charged currents perform not only an interchange between up-type and down-type quarks of a same generation, but also an interchange between two different generations (see for instance figure 1.5).

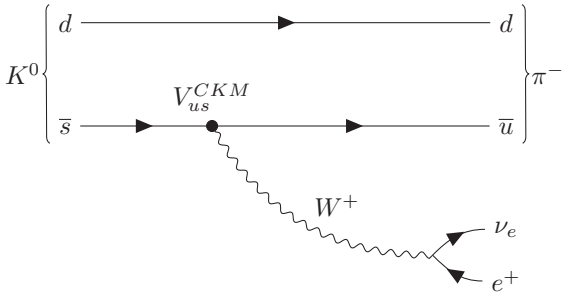

FIGURE 1.5: $K^0 \to \pi^- e^+ \nu_e$ decay made possible by the CKM matrix.

Note that we can show, because of CP-conservation required by the Lagrangian and because of the definition of V^{CKM}, that the CKM-matrix is real and unitary.

In the case of neutral currents the interaction does not change as it involves couplings with

two up-type quarks or two down-type quarks:

$$\begin{aligned} -\mathcal{L}_{nc} \supset & -\frac{g}{4c_W}\left[\bar{\tilde{U}}'_L\gamma^\mu\left(I_3 - s_W^2 Q_{em} - \gamma_5\right)\tilde{U}'_L Z^0_\mu\right] \\ = & -\frac{g}{4c_W}\left[\bar{\tilde{U}}_L\gamma^\mu\left(I_3 - s_W^2 Q_{em} - \gamma_5\right)B_L^\dagger B_L\tilde{U}_L Z^0_\mu\right] \\ = & -\frac{g}{4c_W}\left[\sum_{i,j=1}^{3}\bar{u}^m_{i,L}\gamma^\mu\left(I_3 - s_W^2 Q_{em} - \gamma_5\right)u^m_{i,L}Z^0_\mu\right] \end{aligned} \tag{1.59}$$

with $s_W \equiv \sin\theta_W$ and Q_{em} the electric charge of the particle considered.

Hence, there is no interchange at tree level between two different generations of up-type or down-type quarks. This result is well verified by experiments.

Note that, in the lepton sector, as the neutrinos are massless in the SM, the unitary matrix A_L can be reabsorbed by an arbitrary redefinition of the vector $\tilde{N}' \equiv \begin{pmatrix}\nu_1\\ \nu_2\\ \nu_3\end{pmatrix} = A_L \begin{pmatrix}\nu_e^m\\ \nu_\mu^m\\ \nu_\tau^m\end{pmatrix}$. Hence, as long as the neutrinos are massless, the charged and neutral currents in the lepton sector occur only with particles of a same generation. However if the neutrinos are assumed to be massive – which is the case experimentally, see section 1.3 – one needs to introduce the Pontecorvo-Maki-Nakagawa-Sakata (PMNS) matrix which is the equivalent of the CKM matrix in the lepton sector, allowing charged currents between different generations of leptons.

1.3 The limitations of the Standard Model

The SM has known many successes during and after its final elaboration. It was able to predict the existence of particles such as the charm and top quarks or the $W^\pm$ and Z^0 bosons which were discovered some years later.

Current experiments are measuring the values of the SM parameters with a very high accuracy, searching for a deviation from theoretical predictions. As the experiments are ever more accurate, the theoretical measurements need to include higher-order computation – at next-to-leading order or beyond. However theoretical and experimental measurements of the SM parameters are in very good agreement (see figure 1.6), confirming the success of the SM.

The final discovery of the Higgs boson in 2012, forty eight years after its prediction by R. Brout, F. Englert, P. Higgs and others, marked the SM apogee. Now all the SM particles have been discovered and there is still no hint of new unknown particles. However different issues, both in theoretical and experimental aspects, point toward the existence of physics beyond the SM. Some of them are summarized below.

◦ Theoretical issues

Gravitation: The first and the most obvious pitfall is that SM does not include the fourth fundamental force, gravity. Although many theorists are working on the problem to reconcile strong and electroweak interactions with general relativity, much work has to be done before obtaining a full theory.

Hierarchy problem: Another theoretical problem is called the *hierarchy problem* and gathers several aspects.

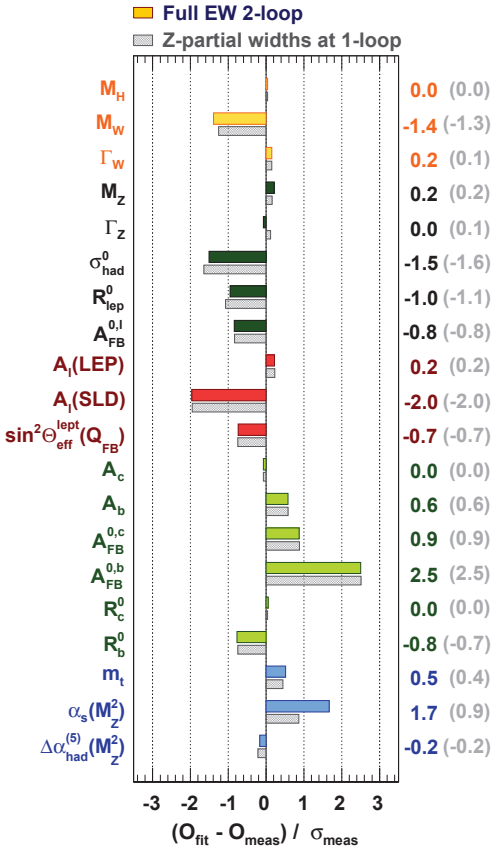

FIGURE 1.6: Comparison of the results of the theoretical fit with direct measurments in units of the experimental uncertainty. Figure taken from [11].

First, the SM does not explain the wide difference between the intensities of the four fundamental interactions. Moreover, although it includes three generations of fermions, there is no mechanism explaining the huge splitting of masses we observe experimentally (see table 1.3). As the masses are generated after the electroweak symmetry breaking that occurs at scale v, one can expect that all fermion masses are of order v. However only the top mass ($m_t \simeq \frac{v}{\sqrt{2}}$) verifies this assumption. Instead, fermion masses spread out over a large range of values: from 0.51 MeV for the electron to 1776.82 MeV for the tau in the lepton sector, and from 2.2 MeV for the up quark to 174.2 GeV for the top quark in the quark sector, that is, a variation of more than three – for the lepton sector – and almost five – for the quark sector – orders of magnitude.

The last aspect that the hierarchy problem covers is the corrections to the Higgs mass. Although its bare mass m_h appears in the SM Lagrangian, one needs to add radiative corrections at next-to-leading order (NLO) or beyond to account for finer processes (see figure 1.7). Computing these corrections at NLO, one finds [12]:

$$\Delta m_h^2 \propto \frac{\alpha}{\pi}\left[\frac{3}{4}\left(m_W^2 + m_Z^2 + m_h^2\right) - \sum_f m_f^2\right]\left(\frac{\Lambda^2}{m_W^2}\right) \tag{1.60}$$

with Λ an energy cut-off which is assumed to tend to infinity.

The main contribution comes from the fermionic sector, especially from the top quark, where the corrections grow quadratically with the fermion mass. If we choose a specific value for the cut-off Λ, say the Planck mass scale $M_P = 2.435 \times 10^{18}$ GeV, then the Higgs mass should be of order $m_h \sim 10^{16}$ GeV, which is not coherent with the very light Higgs mass of 125 GeV measured experimentally. Again, there is no way in the SM theory to cancel these huge corrections in order to get a light Higgs boson in agreement with experiment.

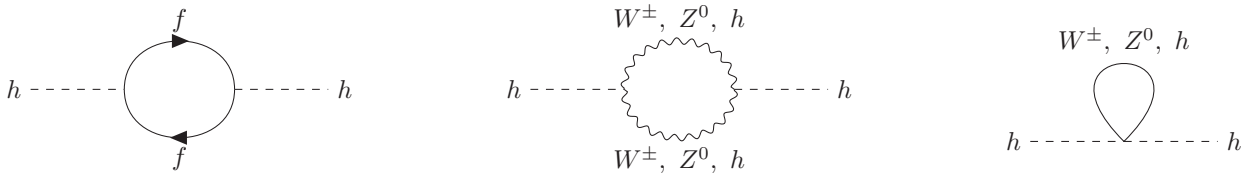

FIGURE 1.7: One-loop corrections to the Higgs mass.

◦ EXPERIMENTAL ISSUES

Beyond the theoretical issues, experiments have discovered phenomena that were not predicted nor explained by the SM, bringing new evidence that the SM is not a complete theory. Examples of such experimental issues are presented below.

The Dark Matter (DM) problem [13]: One of the first times the Dark Matter term appeared was in 1933, when Swiss astrophysicist Fritz Zwicky measured the velocity dispersion of the Coma cluster. He deduced the dynamical mass $M_{\mathcal{D}}$ of the cluster that he compared to its luminous mass $M_{\mathcal{L}}$, that is, to the mass inferred from the amount of luminosity emitted by the cluster. He discovered that the dynamical mass was four hundred times larger than the luminous one, which could mean that there were invisible matter inside the cluster.

This result was not taken into account by the community at that time, partly because of the great uncertainties of the measurements. It is only in the 70s that the problem came back to the point, when American astronomer Vera Rubin studied the rotation curve of galaxies. Looking at the galaxy velocity as a function of the distance to the center r, it appears that, instead of decreasing as $\frac{1}{\sqrt{r}}$ as predicted by Newton's laws, the velocity remains broadly constant (see figure 1.8). One possible explanation of this phenomenon was that galaxies are immersed in a huge halo of invisible matter, called Dark Matter.

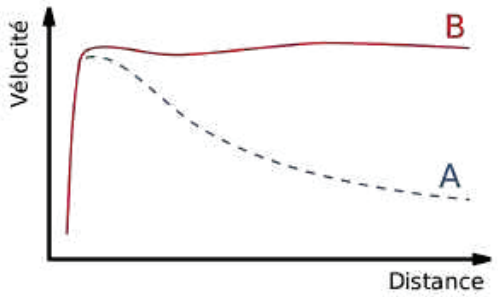

FIGURE 1.8: Galaxy velocity as a function of the distance to the center. The dashed blue curve represents the theoretical prediction based on Newton's laws if the whole mass of the galaxy is gathered in a small radius. The solid red curve is what is experimentally observed.

Other later experiments supported the theory of DM, such as the study of gravitational lenses, which highlights that the distribution of mass inside clusters is significantly different from the distribution of luminous matter, or the study of the cosmological microwave background by WMAP and Planck experiments which confirms the existence of 26.6% of non-baryonic matter in the total amount of energy in the Universe (against 4.9% for ordinary matter [14]).

Nowadays the existence of DM is rather well established; however its nature is still mysterious. Many theories had proposed different candidates (white dwarfs or brown dwarfs, light neutrinos...) but most of them are now ruled out. The currently most popular theory is the Weakly Interactive Massive Particle (WIMP), which gathers numerous candidates proposed by particle physicists. The WIMP (or other DM candidates) needs to follow some requirements coming from experiment: it needs to be a non-relativistic particle – hence, sufficiently massive to be so – to be stable in order to be still observed nowadays in the Universe, to be neutral in order to be insensitive to electromagnetic interaction, to interact very weakly with ordinary matter – else it would have been already detected – and have a relic density – *i.e.* a current stable density – compatible with the Planck measurements. However, except for these points, little is known about these particles.

Many experiments are currently working on the direct or indirect detection of DM.

Direct detection consists of measuring precisely the nuclear recoil due to the elastic scattering of a WIMP on a SM nucleus. However, as the WIMPs are assumed to interact very weakly with ordinary matter, these experiments need to get rid of numerous sources of noise such as solar muons and neutrons.

Direct detection then provides upper limits on the WIMP diffusion cross-section as a function of its mass. The main actors in this field are Xenon-1T or LUX for the study of heavy WIMP – masses above $\sim$10 GeV – and CDMS or EDELWEISS for the low-mass range – below $\sim$10 GeV.

Indirect detection consists of measuring the particle content of cosmic beams reaching Earth and comparing the experimental data to theoretical predictions. As two particles of DM can annihilate and give birth to SM particles, an excess in the experimental flux of incoming SM particles can be interpreted as a DM contribution.

The major actors in this field are AMS-02, Fermi-LAT and HESS. The first experiment is searching for excesses in the detected flux of particles such as positrons or anti-protons. However some sources of astroparticles, such as pulsars, are not well known; in addition the propagation of particles inside the galaxy suffers from many uncertainties, making it difficult to interpret an excess in the data as a clear proof of a DM contribution.

The last two experiments focus on the detection of gamma rays coming from the center of the galaxy or from other specific galaxies. The advantage of gamma rays is that they propagate in a straight line, getting rid of most of the propagation problem cited above. However there are still uncertainties due to the modeling of the DM halo.

Both experiments are able to put upper limits on the DM annihilation cross-section as a function of its mass.

So far none of these experiments, through either direct or indirect searches, have found a clear hint of DM; but, similarly to the Higgs hunting, it may take several decades before discovery.

The neutrino mass [15]: In the late 60s an experiment lead by Davis and Bahcall was conducted to count the number of electron-neutrinos emitted by the Sun and reaching the earth. However the experiment detected only one third of the expected rate. This unexpected

deficit was called the solar neutrino problem.

Other experiments such as Super-Kamiokande in 1998, which provided the first model-independent evidence of neutrino oscillations, and later KamLAND, Solar Neutrino or Minos experiments, confirmed this discrepancy between theory and experiment which could not be explained by large uncertainties.

We will illustrate this discovery by giving some details on the Solar Neutrino Experiment (SNO), turned on in 1999 and off in 2006, and which also provided the proof of neutrino oscillations. Using a tank of 1000 tons of heavy water, this experiment was able to count both the number of solar electron-neutrinos and the total number of solar neutrinos reaching Earth.

They measured that the total flux of solar neutrinos reaching Earth totally agreed with the SM theoretical flux of electron-neutrinos emitted by the sun, whereas the flux of electron-neutrinos on Earth corresponded to one third of the measured total flux of neutrinos. This means that the electron-neutrinos emitted by the sun are "converted" during their travel into muon- or tau-neutrinos. The total flux of neutrinos is therefore constant but some electron-neutrinos oscillate into another flavor of neutrino, leading to the decrease of the effective electron-neutrino flux.

This oscillation is theoretically possible only if neutrinos have masses - albeit very small - which is not predicted at all by the SM.

Many experiments are currently running to detect neutrino oscillations and to measure the mass difference between the three neutrinos – as the value of their mass is not directly measurable – such as KamLAND and Super-Kamiokande in Japan, MINOS+ near Chicago – shut down in 2016 – or OPERA, between Switzerland and Italy. However the theoretical explanation beyond the SM to account for massive neutrinos is still under study. The most successful theory is probably the seesaw mechanism [16], which introduces right-handed neutrinos ν_R in order to generate low mass for the left-handed SM neutrinos ν_L, but with ν_R sufficiently heavy to explain why they have not been detected yet.

Baryon asymmetry [17]: In the early Universe the Big Bang should have produced an equal amount of matter and antimatter. However our present Universe seems to be essentially made of matter. Some theories suggest that there could exist galaxies made of anti-matter, but current observations seem to refute these assumptions. We then say that there is a matter-antimatter asymmetry – or a baryon asymmetry.

However, as particle physics processes involving both particles and antiparticles create or destroy them by pair, the initial equal amount of matter and anti-matter should have been preserved since the Big Bang, giving rise to a cohabitation of matter and anti-matter or a total annihilation between the two. The current observations of our Universe tend to show that, at one point of its expansion, a mechanism would have allowed an asymmetry between the number of particles and antiparticles – maybe a very small difference, but sufficient to preserve some matter from annihilation.

If the SM predicts a small CP-violation in the baryon sector, which is necessary to explain a baryon asymmetry, it is not large enough to be fully responsible of the current matter-antimatter asymmetry. Many theories beyond the SM (BSM) are developed in order to answer this question, but only a few are experimentally testable. One, amongst others, is the theory of sterile neutrinos, introduced via the seesaw mechanism, which could explain the observed baryon asymmetry.

2 The Higgs boson

2.1 History of the Higgs boson discovery

The Higgs boson has been introduced in the SM theory as a way to give mass to gauge bosons and fermions. Since then many experiments have been searching for it using particle colliders.

There are basically two main types of colliders: linear ones, where a beam of particles is sent on a target, and circular ones, where two beams of particles are spinning in opposite directions inside a ring. In the first case the detector is placed at the level of the target; in the second case, it is located around a specific position of the beam.

In both types of colliders the beam of particles is accelerated using an electromagnetic field and can be deflected from its straight path by a magnetic field.

The advantage of a circular collider is that the beam can reach higher energies – depending on the number of revolutions inside the ring – than in a linear one which is limited by its total length. Then a circular collider is able to produce heavier particles. However a spinning charged particle will radiate energy, which causes energy losses. Hence, the process or the specific particle one wants to study will determine the required shape of the accelerator and the nature of the beam particles.

In their search for the Higgs boson, physicists are confronted with two main issues. As the Higgs boson has a very short lifetime, we can only observe its decay products and not the Higgs boson itself. Designing an appropriate detector is then a difficult task as it needs to be sensitive to several different particles. Moreover, as the theory did not predict the Higgs mass, experimenters needed to probe a large range of possible masses, which explains why the search of the Higgs boson took almost fifty years.

The history of the discovery of the Higgs boson is quickly summarized in the following sections. For more details, see for instance [18].

2.1.1 The beginning of the hunt – 1980s

In the 1980s different accelerators began to search for the Higgs boson. As they were not very powerful, the mass range they probed was very low – of the order of a few GeV.

During this period, a first signal was detected by the DORIS electron-positron circular accelerator, at DESY in Germany. They studied the decay of the upsilon meson Υ ($b\bar{b}$) into a Higgs boson and a photon following the Feynman diagrams of figure (2.1).

The excess in the data was found by the collaboration in 1984, with a significance of 5σ at a mass of 8.32 GeV, which is generally considered as a discovery. However the CUSB Collaboration at CESR of Cornwell University, which were working on the same decay on their

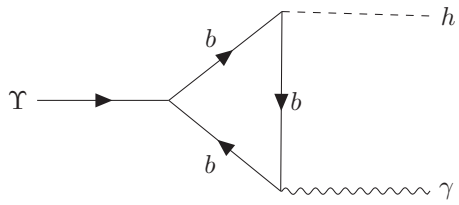

FIGURE 2.1: Decay of an upsilon meson into a Higgs boson and a photon studied at DORIS accelerator.

own accelerator, did not confirm this excess. Even more, the 5σ excess in DORIS results vanished by itself after acquiring more data. This false discovery is a good example illustrating the necessity of always being very careful with excesses appearing in the data and of always cross-checking the results.

Other experiments were also working on the Higgs search, such as the SINDRUM collaboration which worked on a proton cyclotron and looked at the process $\pi^+ \to e^+\nu_e h$ or the CLEO collaboration, also at CESR and looking at $B \to Kh$. However the Higgs boson was still hiding and the different collaborations could only give a lower bound on the Higgs mass: $m_h > 9$ GeV.

2.1.2 The Large Electron Positron (LEP) – 1989-2000

With its 27 km in circumference, the LEP was the largest electron-positron collider ever constructed. It was designed to reach 100 GeV per beam, which corresponds to an energy of 200 GeV in the center of mass. There were four detectors searching for the Higgs boson around the ring: ALEPH, DELPHI, L3 and OPAL.

The searches at LEP were conducted in two stages, called LEP1 and LEP2. In both of them, the search was conducted on a process where the electron and the positron produced a Z^0 boson – on-shell for LEP1, off-shell for LEP2 – which decayed into a Higgs boson and an off-shell or on-shell Z^0 boson (see figure (2.2)).

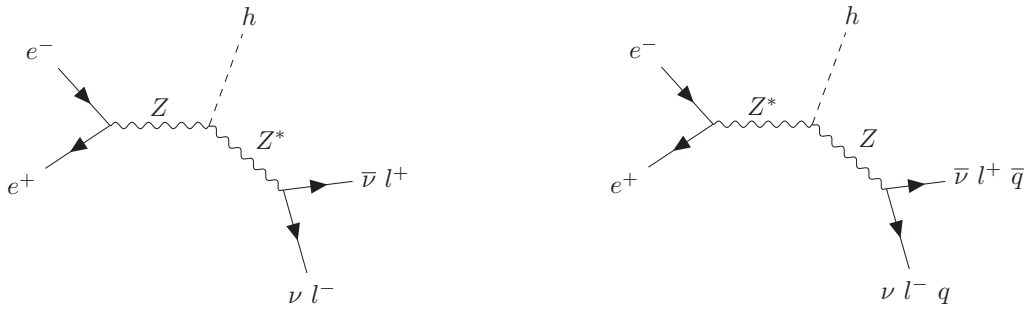

FIGURE 2.2: Processes studied at LEP1 (left) and LEP2 (right). The l symbol stands for both electrons and muons.

- LEP1 – 1989-1995

The first phase was conducted at a center of mass energy of 91.18 GeV, corresponding to the mass of the Z^0 boson. This specific energy allowed the massive production of Z^0 bosons and hence the increase of the number of interesting events (see left panel of figure (2.2)). In addition to the Higgs boson search, this phase allowed physicists to perform precise tests of the SM.

As no excess appeared in the data during this phase, the LEP excluded a SM Higgs particle with a mass up to $m_h = 65$ GeV.

- LEP2 – 1995-2000

In the second phase the accelerator was pushed to its designed energy of 200 GeV in the center of mass. This time the electron-positron collisions were able to create off-shell Z^0 bosons (see right panel of figure (2.2)).

As there were no evidence of a new particle by the year 1999, the LEP was upgraded in order to reach an energy of 209 GeV in the center of mass. After the upgrade some excesses with low significance began to appear in the data at masses around 110-120 GeV. However, despite these exciting signs, the LEP did not obtain additional running time and had to shut down at the beginning of November 2000. It was however able to exclude a SM Higgs particle with a mass up to 107.9 GeV.

2.1.3 The Tevatron – 1987-2011

Once the LEP was shut down the Tevatron took over the Higgs search. Situated near Chicago, it was a proton-antiproton collider of 1 km in diameter reaching a center of mass energy of 1.96 TeV. The experiments were led by two detectors: CDF and DØ.

Although no evidence of the Higgs boson was found during its operation period, the Tevatron succeeded in excluding large possible SM Higgs mass regions. In 2012, at the end of its run, it had ruled out the existence of a SM Higgs boson with a mass between 100 GeV and 103 GeV and between 147 GeV and 180 GeV. Moreover, some 3σ excesses had appeared in the data between 115 GeV and 140 GeV, maybe a first hint of the particle which would be detected during the same year at the LHC.

Unfortunately the luminosity was not sufficient to detect the Higgs boson with more accuracy. The accelerator was finally shut down in 2011, after 24 years of operation.

2.1.4 The Large Hadron Collider (LHC) – 2008-2035?

The LHC is a circular proton-proton collider located beneath the France-Switzerland border and is currently the largest and more powerful particle collider in the world. It was built in the same tunnel as the LEP, its predecessor.

Designed to reach a center of mass energy up to 14 TeV, it was first launched at half of its maximum energy from 2010 to 2011. In 2012 the energy went up to 8 TeV in the center of mass and was finally increased in 2015 up to 13 TeV.

Four detectors are placed around the ring: ATLAS, CMS, ALICE and LHCb (see figure (2.3)); but only the first two focus their studies on the Higgs search.

The choice of the type of particles spinning in a circular collider is crucial and highly depends on what we want to study. A spinning particle will radiate an energy $\Delta E \propto \frac{E_{beam}^4}{m^4 R}$ with E_{beam} the energy of the beam particle, R the accelerator radius and m the mass of the beam particle. Then, as probing higher mass regions than LEP did requires a higher E_{beam}, one has to use heavier beam particles, such as protons, in order to limit the energy lost by radiation.

The choice of using proton-proton instead of electron-positron beams at the LHC leads to additional difficulties: as protons are composite objects, the collision involves two elements of their substructure – either quark-quark, gluon-gluon or gluon-quark collisions. Each of these

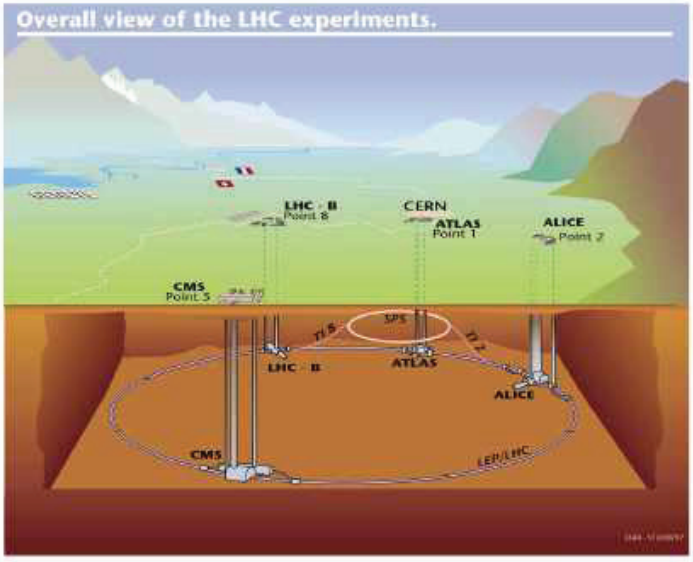

FIGURE 2.3: Drawing of the LHC structure with the different detectors around the main ring. The two detectors studying the Higgs boson properties are CMS and ATLAS.

collisions owns an unknown fraction of the total momentum of the two incoming protons – contrary to the electron-positron accelerators where the momentum is precisely known. Hence, this makes the study of the outgoing particles and jets even more difficult.

Using a proton-proton circular collider instead of a proton-antiproton one is technically more difficult since, in the first case, two particles with identical charge need to spin in opposite directions. It then requires two different tubes, one for each spinning direction, so that each proton is bathed in its specific magnetic field with opposite directions. However the reachable luminosity, *i.e.* the number of events by unit of time divided by the cross-section, is higher in a proton-proton collider than a proton-antiproton one, hence the advantage of the LHC compared to Tevatron.

After a proton-proton collision, many particles are created – potentially including Higgs bosons – which can themselves decay. The work of the ATLAS and CMS detectors is then to identify the resulting particles coming from the collisions using multiple layers of complementary detectors (see for instance the different slices of the CMS detector represented in figure (2.4)) and to measure their energy, charge and direction. Then one needs to reconstruct each event, that is, determine for each collision occurring inside the detector the chain of events, from the initial colliding particles to the different daughter particles and their own decays, observed in the detector.

The beginning of the LHC did not go well because an electric fault a few days after its start forced to shut down the accelerator for more than a year. However the beam was restarted in November 2009 and data collection could finally start.

The Higgs search was performed in three main decay channels (see section 2.2.2): $H \to WW$, $H \to ZZ \to 4l$ and $H \to \gamma\gamma$. By the summer of 2011 a first indication of a new particle was observed by both ATLAS and CMS in the channel $H \to WW$ at a mass of 145 GeV and 120 GeV respectively; the excess was around 2σ, so not sufficient to claim a discovery, but this first hint created excitement in the scientific community.

Excesses in the two other decay channels $H \to ZZ \to 4l$ and $H \to \gamma\gamma$ started to appear in

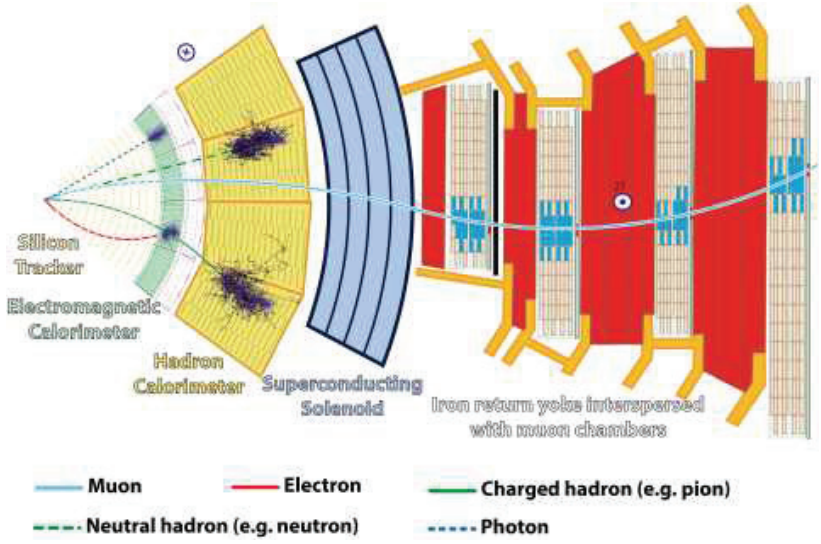

FIGURE 2.4: Slice of CMS detector with the different detector layers [19]. The path of different particle types is symbolized by the colored lines. The silicon tracker, bathed in a magnetic field, allows the distinction between neutral, positively charged and negatively charged particle. Then, depending on its nature, the particle will create a shower in a specific detector – in the electromagnetic calorimeter for the photons and the electrons, in the hadron calorimeter for the hadrons – allowing their precise identification.

the following months. However, in order to avoid any bias, the two experiments continued to accumulate data before analyzing them and revealing them publicly.

On July 4, 2012, CERN organized a special symposium presenting the ATLAS and CMS results on the Higgs search. Both experiments presented data with an excess of 5σ for ATLAS [6] and 4.9σ for CMS [7] located at a mass of $m_h = 126.5$ GeV and 125 GeV respectively, that was sufficiently high to claim the discovery of a new particle (see for instance figure (2.5)).

Additional studies lead by the two collaborations confirmed the scalar nature of the new particle, as expected by the SM, and measured its properties with accuracy, showing that the particle discovered at the LHC had a behavior very similar to the SM Higgs boson (see for instance figure (2.6)). Hence, the discovery of the Higgs particle is a brillant example of the success of the SM.

Figures (2.5) and (2.6) illustrate the Higgs boson discovery.

In the left panel of figure (2.5), the search is performed by the CMS collaboration in the $h \to \gamma\gamma$ decay channel [7]. The black dots represent the number of events – number of detected photon pairs supposed to be produced by a unique particle of mass $m_{\gamma\gamma}$, called invariant mass – over the number of signal plus background – the background being photon pairs not originating from a unique particle – as a function of the invariant mass $m_{\gamma\gamma}$. The theoretical rate, computed in the SM framework without Higgs boson, is represented by the red dashed line. The experimental data around $m_{\gamma\gamma} \simeq 125$ GeV is clearly above the theoretical expectation. This excess of events is a sign of the presence of an unknown particle, later interpreted as the Higgs boson, decaying into a pair of photons.

In the right panel of figure (2.5), the local p-value (see Appendix B) coming from the combination of the search in the $h \to \gamma\gamma$ and $h \to ZZ$ decay channels by the CMS collaboration is shown as a function of the new particle mass m_H [7]. The p-value represents the probability,

depending on the invariant mass m_H and under the hypothesis that no new particle exists, for a signal rate higher than the one measured experimentally to occur. In concrete terms, the lower the p-value, the higher the probability that the excess corresponds to a new unknown particle. In the plot, the combined p-value, represented by the solid black line, is really low around $m_H = 125$ GeV. It corresponds to a 5σ excess, that is, there is a 99.99994% chance that the excess is due to a new unknown particle. This plot is clearly a proof of the existence of a new particle, later assimilated to the Higgs boson.

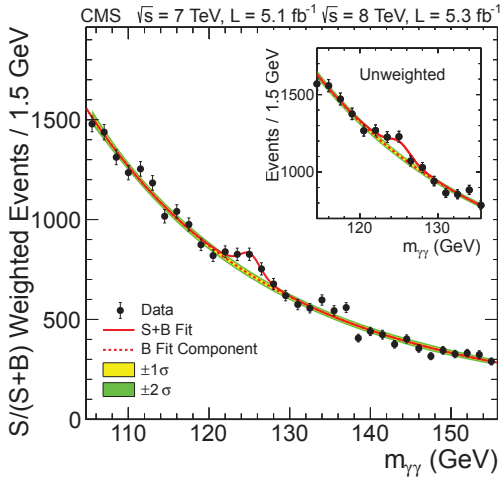

(A) Plot from CMS analysis [7] showing the number of signal events over signal plus background events as a function of the invariant mass $m_{\gamma\gamma}$ in the $\gamma\gamma$ channel. The black dots are the experimental data and have to be compared with the theoretical expected rate without SM Higgs boson (red dashed line). The experimental data clearly show an excess of events around 125 GeV, sign of a new unknown particle decaying into two photons.

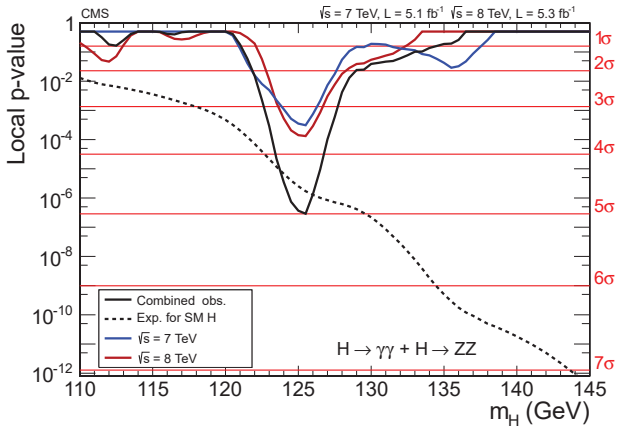

(B) Plot from CMS analysis [7] showing the combination from the $\gamma\gamma$ and ZZ channels of the experimental local p-value – the probability for a background fluctuation to be at least as large as the observed events – depending on the mass of the hypothetical new resonance. The lower the p-value, the most likely the new resonance exists.

FIGURE 2.5: Plots originating from the first CMS paper following the Higgs discovery [7]. The two plots, in two different manners, are proofs of the new particle existence.

Some properties of the new particle are shown in figure (2.6), coming from an ATLAS analysis following the Higgs discovery [6]. It shows the value of the signal strength μ (see section 2.2.3 for more details) with 1σ uncertainty for the different decay channels $h \to bb$, $h \to \tau\tau$, $h \to WW$, $h \to \gamma\gamma$ and $h \to ZZ$. The signal strength measures the deviation between the new particle properties and those expected for a SM Higgs boson. If $\mu = 1$, then the properties are the same as in the SM; else they are different. We can see that the signal strength's central value is close to 1 and that the value $\mu = 1$ is inside the 2σ uncertainty for all five decay channels, showing that the new particle's properties are very close to those of the SM Higgs boson.

At the end of LHC Run I, ATLAS and CMS collaborations combined their data in order to constrain the Higgs boson's properties as accurately as possible [20, 21]. The Higgs boson's mass was therefore fixed at $m_h = 125.09 \pm 0.21 \pm 0.11$ GeV. We will use this value as the Higgs mass for the following of this thesis.

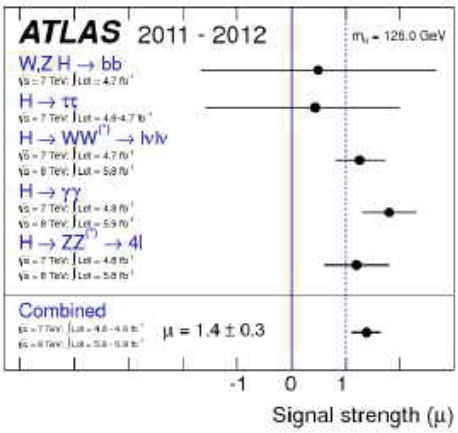

FIGURE 2.6: Signal strength $\mu = \frac{\sigma^{\text{exp}}(pp \to H \to XX)}{\sigma^{\text{SM}}(pp \to H \to XX)}$ of the discovered particle for different decay channels $XX = \{bb,\ \tau\tau,\ WW,\ ZZ,\ \gamma\gamma\}$. The signal strength is equal to 1 if the properties of the new particle correspond to those of the SM Higgs boson. The Higgs boson discovered at LHC is then very similar to the SM Higgs boson. Plot originating from the first ATLAS paper following the Higgs discovery [6].

2.2 Higgs boson production and decay at the LHC

2.2.1 Production at the LHC

The production of a particle – and in particular of the SM Higgs boson – in an accelerator depends on the particles used in the beams.

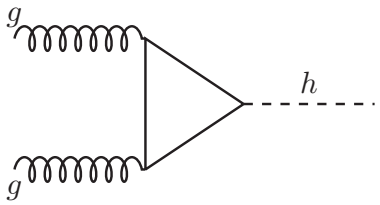

(A) Gluon fusion production (ggF)

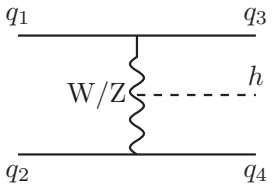

(B) Vector boson fusion production (VBF)

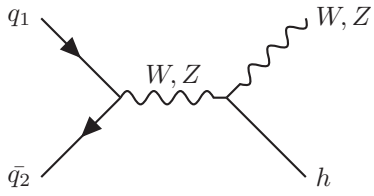

(C) Associated production with vector boson (VH)

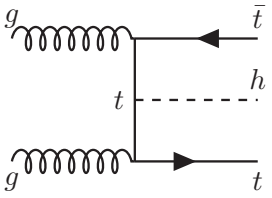

(D) Associated production with top quarks (ttH)

FIGURE 2.7: Four main production channels of the SM Higgs boson at the LHC.

At the LHC – a proton-proton collider – there are four main Higgs boson production modes, called gluon fusion (ggF), vector boson fusion (VBF), associated production with a vector boson (VH) and associated production with heavy quarks (tth, bbh). The Feynman diagram

associated with these different production modes are summarized in figure (2.7). The value of the theoretical production cross-section for a SM Higgs at 8 TeV depending on its mass is shown in the left panel of figure (2.8).

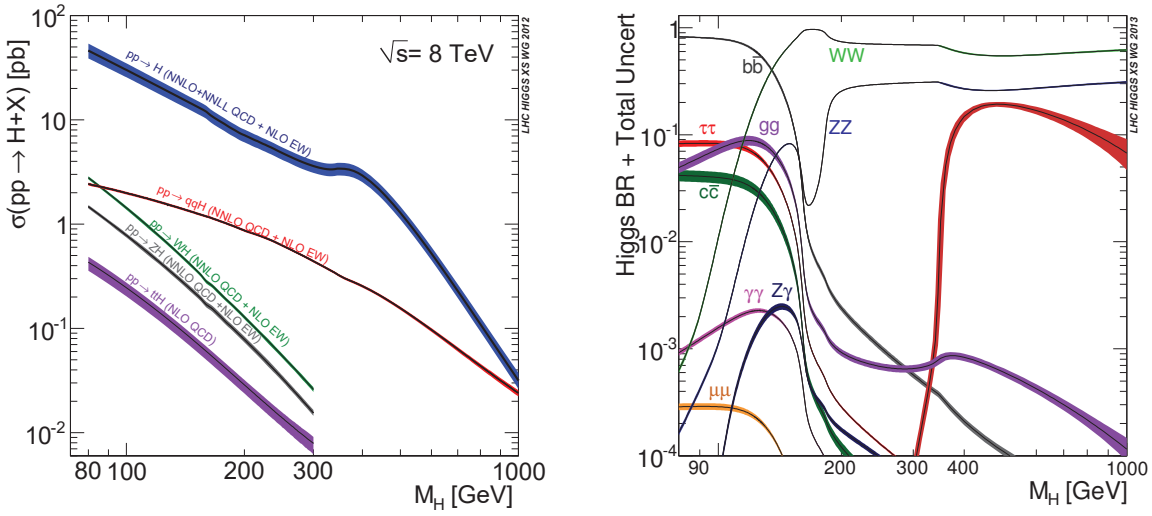

FIGURE 2.8: Production cross-section at 8 TeV (left) and branching ratios (right) of the SM Higgs boson for its different decay channels as a function of its mass. Source: [22].

As we can see in the left panel of figure (2.8), the gluon fusion production mode, represented by the blue curve, is the dominant one for the whole range of masses. The other production modes are significantly smaller. Note that the cross-section value for each production mode varies depending on the beam center of mass energy.

The values of the SM Higgs cross-section at the LHC for a beam center of mass energy of $E = 8$ TeV and 13 TeV and for a mass $m_h = 125.09$ GeV are summarized in table 2.1.

Production mode / Energy	ggF (pb)	VBF (pb)	WH (pb)	ZH (pb)	ttH (pb)	bbH (pb)
8 TeV	21.392	1.6	0.7009	0.4199	0.1326	0.2015
13 TeV	48.517	3.779	1.369	0.8824	0.5065	0.4863

TABLE 2.1: Theoretical values of the production cross-section at the LHC for a SM Higgs boson with a mass of $m_h = 125.09$ GeV. The values are given for a center of mass energy of 8 TeV and 13 TeV. The gluon fusion cross-section is computed at N3LO; the other cross-sections are computed at NNLO [23].

2.2.2 SM HIGGS BOSON DECAYS

Once a SM Higgs boson is produced it decays very quickly into other particles. It is these daugther particles that ATLAS and CMS detectors need to identify in order to characterize the Higgs boson.

The SM predicts the value of the decay width $\Gamma_{h\to XX}$ of a SM Higgs boson into a specific decay channel XX ($XX = WW$, ZZ, $\gamma\gamma$...) as a function of its mass. Then one can compute

the branching ratio (BR) of each decay channel as a function of the Higgs mass:

$$BR^{SM}_{h\to XX}(m_h) \equiv \frac{\Gamma^{SM}_{h\to XX}(m_h)}{\Gamma^{SM}_{tot}(m_h)} \tag{2.1}$$

with $\Gamma^{SM}_{tot}(m_h)$ the total width of a SM Higgs boson with mass m_h.

The branching ratios of the SM Higgs boson as a function of its mass are represented in the right panel of figure (2.8).

Contrary to the production modes, where the gluon fusion production stays dominant for the whole range of mass, the main decay channel varies with the mass of the Higgs boson. At $m_h = 125.09$ GeV, which corresponds to the mass of the Higgs boson discovered at the LHC, the SM Higgs boson decays mainly into $b\bar{b}$. The WW decay is the next significant channel whereas the $\gamma\gamma$ channel is one of the lowest contributions.

ATLAS and CMS collaborations perform their studies in five specific decay channels: WW, ZZ, $\gamma\gamma$, $\tau\tau$ and bb. The values of the BR for a SM Higgs boson at $m_h = 125.09$ GeV for these five decay channels are summarized in table 2.2.

	WW	ZZ	$\gamma\gamma$	$\tau\tau$	bb	Total decay width (GeV)
BR	0.2152	0.02641	0.002270	0.06256	0.5809	4.100×10^{-3}

TABLE 2.2: BR values for a SM Higgs boson at $m_h = 125.09$ GeV [23].

Although the decay into two photons has a low branching ratio value, this channel has very little background – that is, very few SM events that can be taken to be a $H \to \gamma\gamma$ decay event. Moreover both ATLAS and CMS detectors can identify photons very clearly and measure their energy precisely, which allows with very high accuracy the computation of the mass of the particle – supposedly the Higgs boson – having emitted two photons.

The channel $H \to ZZ \to 4l$, with l standing for e or μ, suffers from a lack of events. However the background of such processes is very well under control and the final particles – four leptons – are very well detected, making it one of the most interesting channels for the discovery, and then the study, of the Higgs boson.

The decay channel $H \to WW$, with at least one of the W decaying leptonically, has the highest branching ratio. However there is at least one neutrino present among the daughter particles. As the neutrino cannot be detected by ATLAS or by CMS detectors, then the total amount of energy implied in the decay cannot be computed. Hence, the Higgs mass cannot be accurately measured in this channel. We then say that the decay process has a low mass resolution.

The last two decay channels of interest, $H \to \tau\tau$ and $H \to b\bar{b}$, are both with a low mass resolution. For the first one, the τ can decay leptonically or hadronically. In both cases there is at least one neutrino, giving rise, as for the WW case, to missing energy.

In the case of $H \to b\bar{b}$, despite the large branching ratio, there is a large background due to QCD production of bottom quarks which covers the signal. Hence, one needs to work only with events issued from associated production with vector boson, which reduces the statistics.

2.2.3 LHC RESULTS: SIGNAL STRENGTH AND UPPER LIMITS

As we have seen in section 2.1.4, a new scalar particle has been discovered in 2012 by the ATLAS and CMS collaborations. The properties of this new particle are quite close to those expected for a SM Higgs boson (see for instance figure (2.6), or [20] for the most recent results

on LHC Run I); that is why it is usually called "the Higgs boson".

The agreement between SM expected properties and experimentally measured properties of the new particle is often computed using the *signal strength*.

The experimental signal strength μ^{exp} of the new particle h in a specific production mode XX and decay channel YY is defined by:

$$\mu^{exp}_{XX\to h\to YY} = \frac{\sigma^{exp}_{XX\to h} \times BR^{exp}_{h\to YY}}{\sigma^{SM}_{XX\to h} \times BR^{SM}_{h\to YY}} \tag{2.2}$$

where the exponent exp stands for experimentally measured quantities and SM for quantities theoretically computed in the SM framework. Hence, the signal strength value is close to one if the new particle's experimentally measured properties are similar to the SM predictions.

Although the Higgs boson detected at the LHC has properties very similar to those of the SM Higgs boson, it is important to measure them ever more accurately, either to discover possible discrepancy between experiment and SM prediction or to constrain BSM theories more precisely. We will see in section 2.3 how we can use precise Higgs boson property measurements to constrain models of new physics.

ATLAS and CMS collaborations supply signal strength values for different production modes and decay channels together with uncertainties at 1σ, or similarly with 68.27% of confidence level (C.L.) – which means there is a 68.27% chance that the signal strength's true value is inside the interval defined by the central value and the uncertainty. The link between n σ and the C.L. value is recalled in table 2.3. For more details about statistics in particle physics, see Appendix B.

$n\sigma$	1	2	3	4	5
C.L. (%)	68.27	95.45	99.73	99.994	99.99994

TABLE 2.3: Link between the uncertainty level – in terms of σ – and the C.L. value.

However, for a given decay channel YY, there are correlations between the different signal strengths which need to be taken into account. That is why the collaborations also provide exclusion limits at 1 and 2σ in the plane $(\mu_{ggh,tth\to YY}, \mu_{VBF,VH\to YY})$ using the method of maximum likelihood.

In most BSM theories, the Higgs couplings to W and Z bosons are rescaled in the same way. Hence, one can easily group the VBF, WH and ZH production modes in a unique signal strength, assuming that there is no correlation between them. The merging of ggF and ttH production modes is more difficult to justify but, as $\sigma_{ttH} \ll \sigma_{ggF}$ (see figure (2.8)) one can safely assume that $\mu_{ggh,tth\to YY} \simeq \mu_{ggh\to YY}$, justifying the merging.

The combined results of ATLAS and CMS collaborations for LHC Run I is shown in figure (2.9). We will see in section 2.3 how we can make use of such plots.

Even though a Higgs boson with properties similar to those of the SM Higgs boson has been discovered, it is still possible that other scalar particles are hidden and still undiscovered. Lots of BSM models predict scalar particles arising through symmetry breaking, in a similar way as in the SM. These additional scalars, charged or neutral, CP-even or CP-odd, will also be called Higgs bosons in the following.

ATLAS and CMS collaborations are also searching for such new scalars. So far there is no hint of new particles in experimental data. However the absence of signal makes it possible to put upper limits on the cross-section of specific processes involving these hypothetical particles.

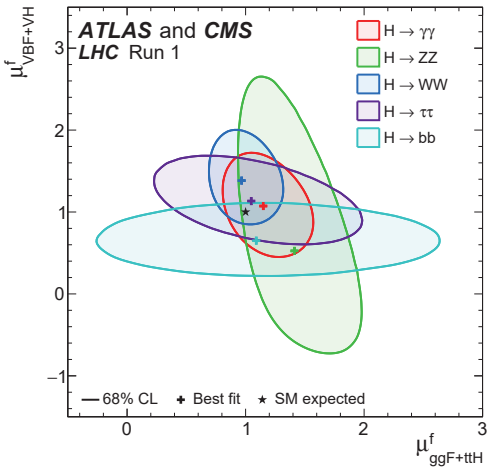

FIGURE 2.9: Exclusion contours at 68% C.L. in the $(\mu_{ggh,tth\to YY}, \mu_{VBF,VH\to YY})$ plane coming from the combination of ATLAS and CMS data for LHC Run I. The five colors correspond to the following five decay channels: $h \to \gamma\gamma$, $h \to ZZ$, $h \to WW$, $h \to \tau\tau$ and $h \to bb$. Plot coming from [20].

A simple example is shown in figure (2.10). The experimental upper limit on the process $gg \to H \to ZZ$, given at 95% C.L. and depending on the mass of a heavy scalar resonance H, is shown as a solid black line. Thus a BSM model predicting a heavy scalar Higgs with a given mass m_H and with a value of $\sigma(gg \to H) \times BR(H \to ZZ)$ above the experimental upper limit at this specific mass m_H is excluded at 95% C.L. Such upper limits are therefore very important in order to constrain models of new physics.

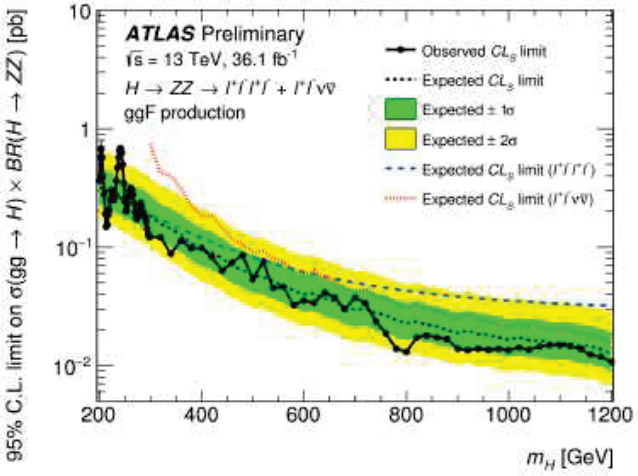

FIGURE 2.10: Upper limit on the process $gg \to H \to ZZ$ depending on the mass of a heavy scalar Higgs H. The dashed black line corresponds to the expected upper limit. The green (yellow) band corresponds to the expected upper limit uncertainty at 1 σ (2 σ). The solid black line corresponds to the observed upper limit obtained by ATLAS collaboration. Plot coming from [24].

2.3 Consequences of LHC results on the 125 GeV Higgs boson

As a Higgs boson has been discovered experimentally, all BSM models need to include a particle with similar properties. Furthermore many BSM models include additional scalars in the Higgs sector. In order to constrain the Higgs sector of such theories optimally one needs to make use of the experimental data probing this sector.

We have seen that ATLAS and CMS collaborations supply two kinds of information on the Higgs sector: constraints on the properties of the 125 GeV Higgs boson experimentally discovered *via* the signal strength, and constraints on other hypothetical Higgs bosons *via* upper limits.

The latter is quite easy to implement if the BSM theory under study is sufficiently predictive. One needs only to compute the cross section of the process considered as a function of the scalar mass in the framework of the BSM theory and check if it is below the experimental upper limit.

The first type of constraint is more difficult to use. We will see below how we can exploit plots such as the one in figure (2.9).

2.3.1 Theoretical signal strength

Considering a theory containing a scalar particle which can be assimilated to the 125 GeV Higgs boson h, one can define the signal strength for a specific production mode XX and decay channel YY as follows:

$$\mu_{XX\to h\to YY} = \frac{\sigma^{BSM}_{XX\to h} \times BR^{BSM}_{h\to YY}}{\sigma^{SM}_{XX\to h} \times BR^{SM}_{h\to YY}} \tag{2.3}$$

where the exponent BSM stands for quantities computed in the framework of a specific BSM theory and SM for quantities computed in the SM framework.

If one is able to compute the cross section $\sigma^{BSM}_{XX\to h}$ and the branching ratio $BR^{BSM}_{h\to YY}$ in the BSM theory framework then, using tabulated SM data to compute the denominator, one can obtain the numerical value of the whole signal strength $\mu_{XX\to h\to YY}$. More details on the computation will be given in the following parts as we work on a specific model.

However, as we have seen in section 2.2.3, there are correlations between the different signal strengths. Hence, comparing one theoretical signal strength value to the experimental one and its uncertainty is too restrictive as correlations are not taken into account.

Working for now with a specific decay channel YY one can take into account the correlations between the signal strengths issued from different production modes, say ggh and tth on one hand and VBF and VH on the other hand, as explained in section 2.2.3. Then, in order to apply the 2D-signal strength constraints, one needs to compute theoretically the pair $(\mu_{ggh,tth\to YY}, \mu_{VBF,VH\to YY})$ and check if the point lies inside the 95% C.L. exclusion contour associated with the YY decay channel. Otherwise, the point is excluded.

In order to perform this check numerically we need to have access to the exclusion contour equation. However we only have access to plots similar to figure (2.9); neither ATLAS nor CMS collaborations supply publicly the likelihood function giving rise to the exclusion contours. Hence, we need to perform some statistical assumptions in order to get back to the initial information.

2.3.2 Extraction of the 1σ exclusion contour

2.3.2.1 *Likelihood and Wilks' theorem*

Note that more details about statistics are given in Appendix B.

The exclusion contours supplied by the ATLAS and CMS collaborations are based on the maximum likelihood or profile likelihood method (see for instance [20] for more details).

The basic method is the following [20, 25, 26]: we consider a likelihood function $\mathcal{L}(\vec{\theta})$ depending on a set of n parameters of interest that we want to determine $\vec{\theta} = (\theta_1, ..., \theta_n)$. Then, according to the maximum likelihood method, an estimate of the true value of the $\vec{\theta}$ parameters is obtained by maximizing the likelihood function. This estimate, denoted $\widehat{\vec{\theta}}$, is also called best fit.

The best fit can be found with a second method providing that the number of independent measurements N is sufficiently high. Indeed, according to Wilks' theorem, for a set of N independent measurements of l physical quantities $\vec{y} = (y_1, ..., y_l)$ which depends theoretically on the n independent parameters of interest $\vec{\theta}$, if $N \to \infty$ then the function $-2\ln\mathcal{L}(\vec{\theta})$ is distributed as a chi-squared function with n degrees of freedom. The hypothesis $N \to \infty$ is also called the *Gaussian approximation*. Then maximizing the profile likelihood $\mathcal{L}(\vec{\theta})$ is equivalent to minimizing the chi-squared function $\chi^2_n(\vec{\theta})$ with n degrees of freedom.

In this approximation one can rewrite the log-likelihood as:

$$\chi^2_n(\vec{\theta}) = -2\ln\mathcal{L}(\vec{\theta}) + C = (\vec{y} - \vec{y}_{bf}(\vec{\theta}))^T \cdot V^{-1} \cdot (\vec{y} - \vec{y}_{bf}(\vec{\theta})) \tag{2.4}$$

with C a constant, $V^{-1} = \begin{pmatrix} a & b \\ b & c \end{pmatrix}$ the inverse of the covariant matrix, $\vec{y}$ the measured physical quantities and $\vec{y}_{bf}(\vec{\theta})$ the corresponding vector of predicted values depending on the parameters $\vec{\theta}$.

Hence, minimizing $\chi^2(\vec{\theta})$ makes it possible to find the best fit values $\widehat{\vec{\theta}}$ and then the associated values $\widehat{\vec{y}}_{bf} = \vec{y}_{bf}(\widehat{\vec{\theta}})$.

2.3.2.2 *Application to the case of signal strengths*

In the case of signal strengths, looking at only one specific decay channel YY, the measured physical quantities are the signal strengths $\mu_{ggh,tth\to YY}$ and $\mu_{VBF,VH\to YY}$, renamed in the following $\mu_{1,Y}$ and $\mu_{2,Y}$ for simplicity. The parameters of interest are the estimates of their true values, denotted $\widehat{\mu}_{1,Y}$ and $\widehat{\mu}_{2,Y}$ respectively. Hence equation (2.4) becomes:

$$\chi^2_2(\widehat{\mu}_{1,Y}, \widehat{\mu}_{2,Y}) = -2\ln\mathcal{L}_Y(\widehat{\mu}_{1,Y}, \widehat{\mu}_{2,Y}) + C = \begin{pmatrix} \mu_{1,Y} - \widehat{\mu}_{1,Y} \\ \mu_{2,Y} - \widehat{\mu}_{2,Y} \end{pmatrix}^T \cdot V^{-1} \cdot \begin{pmatrix} \mu_{1,Y} - \widehat{\mu}_{1,Y} \\ \mu_{2,Y} - \widehat{\mu}_{2,Y} \end{pmatrix} \tag{2.5}$$

Minimizing equation (2.5) makes it possible to obtain the best fit values $\widehat{\mu}_{1,Y}$ and $\widehat{\mu}_{2,Y}$.

Then the confidence region at D% of C.L. – or, equivalently, at $m\sigma$ – on this estimation is given by the contour containing $\mu_{1,Y}$ and $\mu_{2,Y}$ true value with a probability of D%. For a

chi-squared distribution function, this corresponds to the area defined by:

$$\Delta\chi^2(\mu_{1,Y},\mu_{2,Y}) \equiv \chi^2(\mu_{1,Y},\mu_{2,Y}) - \chi^2_{min} < b_2^{m\sigma} \tag{2.6}$$

with χ^2_{min} the minimum value of the chi-squared distribution and $b_2^{m\sigma}$ an upper bound depending on the value of the C.L. – or equivalently on the $m\sigma$ level – and on the number of degrees of freedom n of the chi-squared distribution – here, $n = 2$. The values taken by this upper bound are reminded in table 2.4. The link with the C.L. can be made using table 2.3.

$m\sigma$	n=2	n=3	n=4	n=5	n=6
1	2.30	3.53	4.72	5.89	7.04
2	6.18	8.02	9.72	11.3	12.8
3	11.8	14.2	16.3	18.2	29.1

TABLE 2.4: Value of the upper bound $b_n^{m\sigma}$ depending on the number of degrees of freedom n of the chi-squared function and on the C.L. considered, written in terms of number of σ.

In the Gaussian approximation the contour equation at $m\sigma$ based on the log-likelihood ratio $-2\Delta\ln\mathcal{L}_Y = -2\ln\mathcal{L}_Y - \min(-2\ln\mathcal{L}_Y)$ is then defined by the equation:

$$(\mu_{1,Y} - \widehat{\mu}_{1,Y}, \mu_{2,Y} - \widehat{\mu}_{2,Y}) \cdot \begin{pmatrix} a_Y & b_Y \\ b_Y & c_Y \end{pmatrix} \cdot \begin{pmatrix} \mu_{1,Y} - \widehat{\mu}_{1,Y} \\ \mu_{2,Y} - \widehat{\mu}_{2,Y} \end{pmatrix} = b_2^{m\sigma} \tag{2.7}$$

with $\widehat{\mu}_{1,Y}$, $\widehat{\mu}_{2,Y}$, a_Y, b_Y and c_Y fixed.

In the signal strength plane $(\mu_{1,Y},\mu_{2,Y})$ the exclusion contour, in the Gaussian approximation, is therefore an ellipse defined by five parameters: $\widehat{\mu}_{1,Y}$, $\widehat{\mu}_{2,Y}$, a_Y, b_Y and c_Y, with $(\widehat{\mu}_{1,Y},\widehat{\mu}_{2,Y})$ its center coordinates.

However one needs to be very careful: these results have been derived in the Gaussian approximation, yet public exclusion contours published by ATLAS and CMS were not necessarily obtained using it. In particular, as we will see below, the number of events in the $h \to ZZ$ decay channel is low and the Gaussian approximation is not well verified. But, as the log-likelihood function is not publicly provided, using this approximation is the easiest way to get back to a rough estimate of the log-likelihood.

2.3.2.3 *Extraction of the ellipse parameters*

Even though the ATLAS and CMS collaborations do not provide the ellipse parameters or the log-likelihood function for each decay channel YY considered, the 1σ exclusion contours they supply provide however enough information to derive the ellipse parameters defined above and, hence, an approximation of the log-likelihood function.

After extracting from the plots the numerical values of the pairs $(\mu_{1,Y},\mu_{2,Y})$ for each point of the ellipse at 1σ for a specific decay channel YY, one can obtain, using a simple minimization method, the numerical value of the five ellipse parameters $\widehat{\mu}_{1,Y}$, $\widehat{\mu}_{2,Y}$, a_Y, b_Y and c_Y which generate, via equation (2.7), the ellipse closest to the experimental 1σ exclusion contour.

The ellipse parameters I extracted from 8 TeV data [20] in the decay channels $h \to WW$, ZZ, $\gamma\gamma$, $b\bar{b}$, $\tau\tau$ and 13 TeV data in the decay channels $h \to ZZ$ [27, 28], $h \to \gamma\gamma$ [29, 30], $h \to WW$ [31] (CMS only) and $h \to \tau\tau$ [32] (CMS only) are summarized in table 2.5 and 2.6.

Channel YY	a_Y	b_Y	c_Y	$\widehat{\mu}_{1,Y}$	$\widehat{\mu}_{2,Y}$
WW	24.25	2.524	7.097	0.9950	1.410
ZZ	11.86	1.935	1.086	1.413	0.8074
$\gamma\gamma$	17.36	3.213	6.285	1.180	1.074
bb	1.094	9.283×10^{-3}	11.61	1.182	0.6606
$\tau\tau$	3.716	2.700	9.810	1.093	1.140

TABLE 2.5: Values of the extracted ellipse parameters for the $h \to WW$, ZZ, $\gamma\gamma$, bb, $\tau\tau$ decay channels at 8 TeV from the combined ATLAS and CMS collaborations data [20].

Experiment	Channel YY	a_Y	b_Y	c_Y	$\widehat{\mu}_{1,Y}$	$\widehat{\mu}_{2,Y}$
ATLAS	ZZ	23.8206	1.28247	0.460612	1.15032	4.34646
	$\gamma\gamma$	35.3171	3.37995	3.221	0.803742	2.25022
CMS	ZZ	22.8785	2.5419	1.0565	1.2525	-0.3465
	$\gamma\gamma$	32.4490	4.7594	4.1469	1.2037	1.0642
	WW	11.69	0.8911	1.103	1.029	1.577
	$\tau\tau$	5.093	1.012	8.675	1.401	0.9345

TABLE 2.6: Values of the extracted ellipse parameters for the $h \to ZZ$ and $h \to \gamma\gamma$ decay channels at 13 TeV from both ATLAS [27, 29] and CMS [28, 30] analysis and for the $h \to WW$ [31] and $h \to \tau\tau$ [32] decay channels at 13 TeV from CMS analysis.

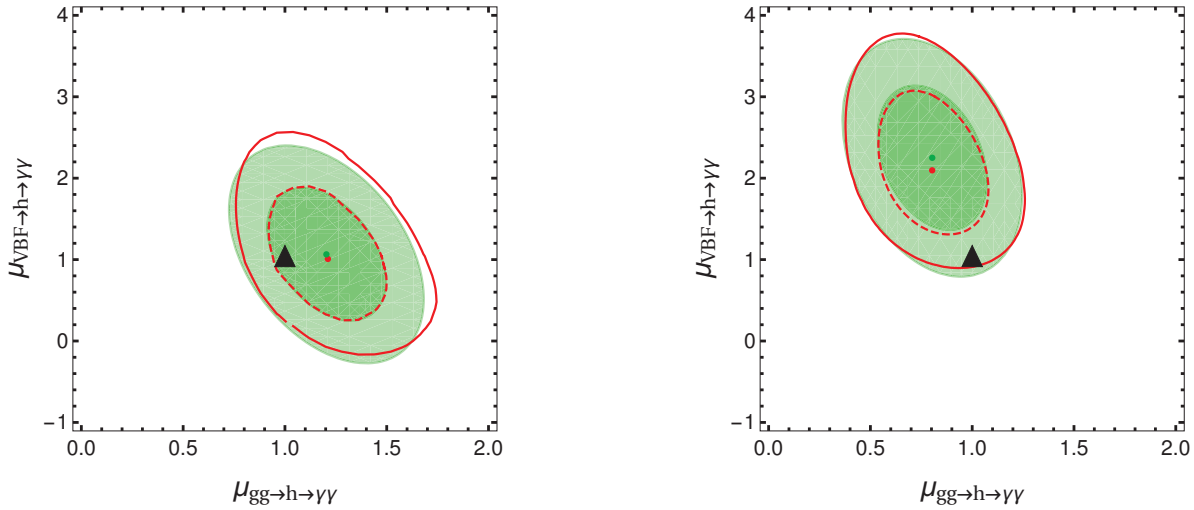

(A) CMS $h \to \gamma\gamma$ decay channel.

(B) ATLAS $h \to \gamma\gamma$ decay channel.

FIGURE 2.11: Experimental exclusions at 1σ (dashed red contour) and 2σ (solid red contour) and reconstructed exclusions with Gaussian approximation at 1σ (dark green) and 2σ (light green) in the signal strength plane for the $h \to \gamma\gamma$ decay channel at 13 TeV by ATLAS [29] (right panel) and CMS [30] (left panel). The red (green) dot represents the experimental (reconstructed) best fit. The triangle corresponds to the signal strength SM value.

Some ATLAS and CMS studies provide also the 2σ exclusion contour, allowing a check of the Gaussian approximation and of the reconstruction method.

The comparison is done for the two decay channels $h \to \gamma\gamma$ (figure (2.11)) and $h \to ZZ$

(figure (2.12)) with both ALTAS (right panel) and CMS (left panel) data at 13 TeV. The dashed red line (solid red line) corresponds to the exclusion contour at 1σ (2σ) given by the collaborations. The green (light green) area corresponds to the reconstructed 1σ (2σ) exclusion zone obtained using the extracted parameters $\widehat{\mu}_{1,Y}$, $\widehat{\mu}_{2,Y}$, a_Y, b_Y and c_Y and equation (2.7). The red (green) dot represents the experimental (reconstructed) best fit. The black triangle corresponds to the SM value. The Gaussian approximation is considered as valid when the reconstructed 1 and 2σ contours fit well with the experimental ones.

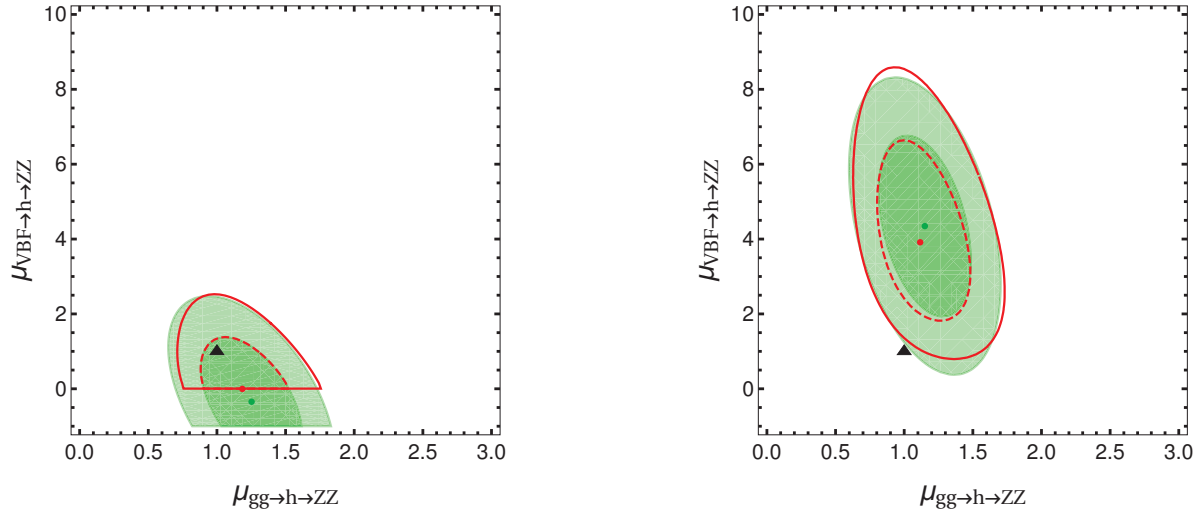

(A) CMS $h \to ZZ$ decay channel.

(B) ATLAS $h \to ZZ$ decay channel.

FIGURE 2.12: Same as figure (2.11) in the $h \to ZZ$ decay channel at 13 TeV using ATLAS [27] (right panel) and CMS [28] (left panel) data.

Reconstructed exclusion areas in the $h \to \gamma\gamma$ decay channel (see figure (2.11)) fit quite well the experimental contours. The reconstructed 2σ exclusion is better in the case of ATLAS than CMS data, but in the two cases the reconstruction is very good.

In the case of the $h \to ZZ$ decay channel (see figure (2.12)), the number of events is lower and hence the Gaussian approximation is less valid. Then the reconstruction, even at 1σ, is less good than in the $h \to \gamma\gamma$ case but it remains a good approximation. The reconstructed 2σ contours, although not in perfect agreement with experimental data, are still good enough to be used as exclusion contours in a posterior analysis.

In the left panel of figure (2.12) experimental exclusion contours are mainly in the negative-$\mu_{VBF,VH\to h\to ZZ}$ region and the reconstructed best fit has a negative $\mu_{VBF,VH\to h\to ZZ}$ value. This is probably due to a lack of events in the $VBF + VH$ production mode in this special decay channel. With more luminosity, exclusion contours should go up and be similar to ATLAS exclusion contours (right panel of figure (2.12)).

However this configuration raises a problem in the exclusion method of theoretical models. Indeed one method is to compute the theoretical signal strength in the $ggh{+}tth$ and $VBF{+}VH$ production modes for a given YY decay channel following equation (2.3) and compare it to the reconstructed exclusion contours at 2σ. Then, if the point $(\mu_{ggh,tth\to YY}, \mu_{VBF,VH\to YY})$ is outside the 2σ contour for one specific decay channel YY, the model is excluded.

However it can happen that the point $(\mu_{ggh,tth\to YY}, \mu_{VBF,VH\to YY})$ is near but outside the exclusion contour for only one specific decay channel YY, and inside the contours for the four

other decay channels under study. With the "decay by decay" method exposed above the model should be excluded. Hence, this method may exclude too many models and is therefore too restrictive.

Another method is to combine the exclusion contours coming from the different decay channels. The statistical method is explained below.

The likelihood for independent measurements can be combined as follows:

$$\mathcal{L}_{tot}(\mu_{1,Y_1}, \mu_{2,Y_1}, \mu_{1,Y_2}, \mu_{2,Y_2}, ...) = \prod_{Y_i} \mathcal{L}_{Y_i}(\mu_{1,Y_i}, \mu_{2,Y_i}) \tag{2.8}$$

Hence, one can construct the $\Delta\chi^2_n$ function defined as:

$$\begin{aligned}\Delta\chi^2_n(\mu_{1,Y_1}, \mu_{2,Y_1}, \mu_{1,Y_2}, \mu_{2,Y_2}, ...) = &- 2\ln\mathcal{L}_{tot}(\mu_{1,Y_1}, \mu_{2,Y_1}, \mu_{1,Y_2}, \mu_{2,Y_2}, ...) \\ &- \min_{\{\mu_{i,Y_j}\}} (-2\ln\mathcal{L}_{tot}(\mu_{1,Y_1}, \mu_{2,Y_1}, \mu_{1,Y_2}, \mu_{2,Y_2}, ...))\end{aligned} \tag{2.9}$$

The function $\Delta\chi^2_n$ is distributed as a chi-squared function with n degrees of freedom, n corresponding to the number of independent parameters in the set of signal strength $\{\mu_{i,Y_j}\}$. Hence, we can define the combined confidence region at 2σ as:

$$\Delta\chi^2_n \leq b^{2\sigma}_n \tag{2.10}$$

Since some of the signal strengths are not independent – for instance $\mu_{1,WW}$ and $\mu_{1,ZZ}$ are linked in many BSM theories – the number of independent parameters n is not necessarily equal to the number of signal strengths involved in the log-likelihood computation. It is important to keep in mind that the parameter n is model-dependent.

This method is less restrictive than the "decay by decay" method as the exclusion is, this time, applied with the total log-likelihood resulting from the combination of all decay channels under study.

We will prefer this latter method in the following. As the complete derivation of the $\Delta\chi^2_n$ function is model-dependent we stop here the discussion on the exclusion method of theoretical models. More details on the derivation of 2σ contours depending on the model under study will be given in the two following parts of this thesis.

Part II:

Two-Higgs Doublet Model

In the previous part we have seen how the Standard Model works and what its strengths and limitations are. We have also highlighted the need to extend this theory to a larger and more complete one.

In this part we will study the Two-Higgs Doublet Model, which corresponds to the Standard Model extended with an additional Higgs doublet. This extension is very simple and does not claim to address all the Standard Model limitations. However many theories beyond the Standard Model have a Higgs sector structure identical to that of the Two-Higgs Doublet Model. Hence, the phenomenology and constraints obtained in the Two-Higgs Doublet Model can be applied to larger and more comprehensive models such as the Minimal Supersymmetric extension of the Standard Model. Hence the importance of the following studies.

In a first chapter we will remind the construction and behavior of the Two-Higgs Doublet Model in a CP-conserving case. Then, as the model contains two CP-even scalars, we will study two different cases: first the case where the heavier CP-even scalar H is assimilated to the 125 GeV Higgs boson discovered at LHC, and second the case where the lightest CP-even scalar h is assimilated to the 125 GeV Higgs boson.

In both cases we will study the influence of theoretical and experimental constraints on the parameter space of the 2HDM. In the $m_H = 125$ GeV hypothesis we will in addition focus on the possible detection of the light Higgs boson h at LHC. In the $m_h = 125$ GeV hypothesis we will work in the particular framework of the alignment limit.

3 Introduction to Two-Higgs Doublet Models

3.1 Motivations of the model

For decades the Higgs boson has been the missing piece of the SM. Its discovery in 2012 by the ATLAS [6] and CMS [7] collaborations brought a great enthusiasm in the particle physics community. However, as we have discussed in chapter 1, the Higgs discovery was not the end of the story: many experimental observations were not predicted by the SM and had to be included in another or bigger theory. Fortunately the discovery of the Higgs boson and the study of its properties have opened new doors for the search of physics beyond the Standard Model.

One idea among others to extend the SM is to enlarge the scalar sector by adding a second Higgs doublet to the initial theory. In such a scenario the two doublets can acquire a vacuum expectation value (vev) and break the electroweak symmetry. Moreover, if the SM contains four real fields – ϕ_1^0, ϕ_2^0, ϕ_1^+ and ϕ_2^+, see equation (1.40) – due to its unique Higgs doublet, the extension with a second Higgs doublet contains a total of eight real fields.

As in the SM, three Goldstone bosons are needed in order to generate the mass of the $W^\pm$ and Z^0 bosons (see section 1.2.2.3). After getting rid of these three degrees of freedom, we are left with five physical fields: two neutral (CP-even) scalar Higgs bosons h and H, one neutral (CP-odd) pseudoscalar Higgs boson A and two charged Higgs bosons $H^\pm$.

This extension, called Two-Higgs Doublet Model (2HDM), although rather simple, allows a more extensive phenomenology in the scalar sector.

It is important to understand that the 2HDM by itself is only an effective theory without UV completion and hence does not solve most of the problems mentioned in section 1.3. However this theory can be a very useful toy model and its development has been motivated by different aspects.

The first one and probably most well known is Supersymmetry – which answers numerous SM problems such as the hierarchy problem and supplies credible DM candidates. Indeed all supersymmetric theories need at least two Higgs doublets in order to give a mass to all fermions and their supersymmetric partners, and to cancel anomalies [33, 34]. More generally, as many BSM theories contain a Higgs sector with two Higgs doublets, the 2HDM is often present as a substructure of such more generic theories.

Another motivation is that the 2HDM, contrary to the SM, is able to produce baryon assymetry using new CP-violating terms [35, 36].

Hence, although the 2HDM is very simple, the study of such a theory makes it possible to constrain bigger and more comprehensive BSM theories and can give clues to understand other models and phenomena.

In this chapter we will first remind the basics of a CP-conserving 2HDM. Second, we will enumerate the different constraints later used in analyses and explain how they are implemented in the special case of a 2HDM. Their practical application will be done in the two following chapters.

3.2 Two-Higgs Doublet Models: some theory

3.2.1 Generic model

A great number of books and articles make a complete theoretical study of the 2HDM (see for instance [37, 38, 39]). The main lines of the theory are reminded below.

The 2HDM takes over the SM Lagrangian and adds a second Higgs doublet ϕ_2 in addition to the original one, here called ϕ_1.

Hence, the theory contains two complex fields ϕ_1 and ϕ_2 with hypercharge one which act as singlets under $SU(3)_c$ and doublets under $SU(2)_L$, exactly as the SM Higgs doublet. Each doublet can acquire a non-zero vev defined by:

$$\langle\phi_1\rangle = \frac{v_1}{\sqrt{2}}, \qquad \langle\phi_2\rangle = \frac{v_2}{\sqrt{2}}, \tag{3.1}$$

$$\sqrt{v_1^2 + v_2^2} \equiv v = 246 \text{ GeV} \tag{3.2}$$

with v the value of the SM vev.

Hence, the two doublets can be written as:

$$\phi_1 = \begin{pmatrix} \phi_1^+ \\ \frac{1}{\sqrt{2}}\left(v_1 + \phi_1^0 + i\eta_1\right) \end{pmatrix}, \qquad \phi_2 = \begin{pmatrix} \phi_2^+ \\ \frac{1}{\sqrt{2}}\left(v_2 + \phi_2^0 + i\eta_2\right) \end{pmatrix} \tag{3.3}$$

with ϕ_i^0, η_i real fields and ϕ_i^+ complex fields.

The most general scalar potential for the 2HDM takes the form [38]:

$$\begin{aligned} V =& m_{11}^2\phi_1^\dagger\phi_1 + m_{22}^2\phi_2^\dagger\phi_2 - \left(m_{12}^2\phi_1^\dagger\phi_2 + \text{h.c.}\right) \\ &+ \frac{\lambda_1}{2}\left(\phi_1^\dagger\phi_1\right)^2 + \frac{\lambda_2}{2}\left(\phi_2^\dagger\phi_2\right)^2 + \lambda_3\left(\phi_1^\dagger\phi_1\right)\left(\phi_2^\dagger\phi_2\right) + \lambda_4\left(\phi_1^\dagger\phi_2\right)\left(\phi_2^\dagger\phi_1\right) \\ &+ \left\{\frac{\lambda_5}{2}\left(\phi_1^\dagger\phi_2\right)^2 + \left[\lambda_6\left(\phi_1^\dagger\phi_1\right) + \lambda_7\left(\phi_2^\dagger\phi_2\right)\right]\left(\phi_1^\dagger\phi_2\right) + \text{h.c.}\right\} \end{aligned} \tag{3.4}$$

with m_{ij}^2 and λ_i complex parameters. However one can simplify this Lagrangian if additional hypotheses are imposed.

As we want to work in the following with well-defined CP-odd and CP-even states one needs to avoid explicit and spontaneous CP-violation. In order to do so, one needs the parameters m_{ij}^2 and λ_i to be real, as well as the vevs v_1 and v_2 to be real and positive [35, 37].

Without any other assumption on the model each doublet ϕ_1 and ϕ_2 couples with all the fermions. Then, by analogy with equation (1.49), the Yukawa interactions take the form [40]:

$$\mathcal{L}_{Yukawa} = \sum_{i=1}^{2}\sum_{j,k=1}^{3} -y_{jk}^{l(i)}\bar{L}_{j,L}\phi_i e_{k,R} - y_{jk}^{d(i)}\bar{Q}_{j,L}\phi_i d_{k,R} - y_{jk}^{u(i)}\bar{Q}_{j,L}\tilde{\phi}_i u_{k,R} + \text{h.c.} \tag{3.5}$$

with $i \in \{1,2\}$ indexing the two Higgs doublets, $j,k \in \{1,2,3\}$ indexing the three generations of fermions, $y^{(i)}$ the 3×3 Yukawa coupling matrices linked to the Higgs doublet ϕ_i and $\tilde{\phi}_i = i\sigma^2\phi_i^*$ the ϕ_i charge conjugate.

After symmetry breaking the Yukawa Lagrangian gives rise to the fermion mass terms. As in the SM case they need to be diagonalized in order to extract the mass eigenstates. However, in the 2HDM case, there are two Yukawa coupling matrices $y_{jk}^{f(1)}$ and $y_{jk}^{f(2)}$ for each fermion type – leptons, up- and down-type quarks – instead of one. In general these two matrices cannot be diagonalized simultaneously. This gives rise to large FCNC mediated by the three neutral Higgs bosons (see for instance figure 3.1).

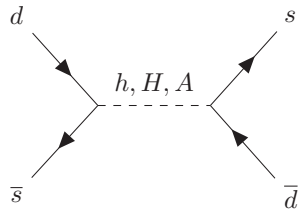

FIGURE 3.1: $K^0 - \bar{K^0}$ at tree level in the 2HDM with FCNC. The h, H and A scalars correspond respectively to the two CP-even and the CP-odd Higgs bosons present in the 2HDM theory.

We know that, experimentally, the FCNC are highly suppressed. Hence, one needs to find a way to eliminate them in 2HDM.

A simple solution to get rid of this problem is to require that all fermions of a given electric charge couple to at most one Higgs doublet, either ϕ_1 or ϕ_2.

This condition is satisfied when introducing a $\mathbb{Z}_2$ symmetry with the two doublets transforming as $(\phi_1, \phi_2) \to (\phi_1, -\phi_2)$ and with the fermion fields transforming as $(f_L, f_R) \to (f_L, \pm f_R)$.

Hence, if a fermion type – say the down-type quarks – transforms as $(d_L, d_R) \to (d_L, +d_R)$ then the only term in the Yukawa Lagrangian respecting the $\mathbb{Z}_2$ symmetry is $-y_{jk}^{d(1)}\bar{Q}_{j,L}\phi_1 d_{k,R}$ and we say that the down-type quarks couple only to ϕ_1.

On the contrary, if they transform as $(d_L, d_R) \to (d_L, -d_R)$ then the only surviving Yukawa term is $-y_{jk}^{d(2)}\bar{Q}_{j,L}\phi_2 d_{k,R}$ and we say that the down-type quarks couple only to ϕ_2.

In both cases, only one of the two Yukawa matrices $y_{jk}^{d(i)}$ now appears in the Yukawa Lagrangian, this for each type of fermions; hence it can be entirely diagonalized and the FCNC similar to the one shown in figure 3.1 are suppressed.

In the following we will always use the $\mathbb{Z}_2$ symmetry solution in order to suppress FCNC.

When applying the $\mathbb{Z}_2$ symmetry, there are only four different ways to couple the three types of fermions to the two Higgs doublets. Each of them has a specific name – Type I, Type II, Flipped type and Lepton-Specific type (see table 3.1 for more details).

It is important to note that the Type II couplings are equivalent to the fermion cou-

	Type I	Type II	Flipped (Type Y)	Lepton-Specific (Type X)
Up-type quark	ϕ_2	ϕ_2	ϕ_2	ϕ_2
Down-type quark	ϕ_2	ϕ_1	ϕ_1	ϕ_2
Leptons	ϕ_2	ϕ_1	ϕ_2	ϕ_1

TABLE 3.1: The four different possible ways to couple the SM fermions to the two Higgs doublets in 2HDM associated with their names.

plings to the two Higgs doublets in the Minimal Supersymmetric Standard Model (MSSM). Hence studying 2HDM Type II can give very useful informations about the MSSM Higgs sector.

As a consequence of the $\mathbb{Z}_2$ symmetry, the coefficients λ_6, λ_7 and m_{12}^2 present in the Higgs potential need to be taken to zero; else the $\mathbb{Z}_2$ symmetry is explicitly broken. However one can allow a soft $\mathbb{Z}_2$-breaking by maintaining $m_{12}^2 \neq 0$.

In the following we will always assume a softly broken $\mathbb{Z}_2$ symmetry, that is, $\lambda_6 = \lambda_7 = 0$ but $m_{12}^2 \neq 0$.

In conclusion, assuming CP-conservation and softly broken $\mathbb{Z}_2$ symmetry, the 2HDM Higgs potential (3.4) can be rewritten as:

$$\begin{aligned} V =& m_{11}^2 \phi_1^\dagger \phi_1 + m_{22}^2 \phi_2^\dagger \phi_2 - \left(m_{12}^2 \phi_1^\dagger \phi_2 + \text{h.c.} \right) \\ &+ \frac{\lambda_1}{2} \left(\phi_1^\dagger \phi_1 \right)^2 + \frac{\lambda_2}{2} \left(\phi_2^\dagger \phi_2 \right)^2 + \lambda_3 \left(\phi_1^\dagger \phi_1 \right) \left(\phi_2^\dagger \phi_2 \right) + \lambda_4 \left(\phi_1^\dagger \phi_2 \right) \left(\phi_2^\dagger \phi_1 \right) \\ &+ \frac{\lambda_5}{2} \left(\phi_1^\dagger \phi_2 \right)^2 + \text{h.c.} \end{aligned} \tag{3.6}$$

with m_{ij}^2 and λ_i real parameters.

The 2HDM Higgs potential has ten degrees of freedom: three real m_{ij}^2, five real λ_i and two real vevs v_1 and v_2. However the two vevs are linked together by equation (3.2) and the minimization of the potential with respect to both ϕ_1 and ϕ_2 leads to two additional conditions, which reduce the number of degrees of freedom.

Hence, the CP-conserving 2HDM with softly broken $\mathbb{Z}_2$ symmetry has seven free parameters.

3.2.2 The Higgs basis and physical basis

The 2HDM Higgs potential can be expressed in different bases which have different physical meanings. The one used in equation (3.6) is called $\mathbb{Z}_2$-basis. Two other possible bases are the *Higgs basis* and the *physical basis*.

3.2.2.1 *The Higgs basis*

In the $\mathbb{Z}_2$-basis, the two doublets ϕ_1 and ϕ_2 acquire a non-zero vev v_1 and v_2 respectively. Using a rotation of angle β one can define two new doublets H_1 and H_2 so that only the first doublet

H_1 acquires a non-zero vev:

$$\begin{pmatrix} H_1 \\ H_2 \end{pmatrix} \equiv \begin{pmatrix} \cos\beta & \sin\beta \\ -\sin\beta & \cos\beta \end{pmatrix} \begin{pmatrix} \phi_1 \\ \phi_2 \end{pmatrix}, \qquad \langle H_1 \rangle = \frac{v}{\sqrt{2}}, \qquad \langle H_2 \rangle = 0 \tag{3.7}$$

Using this definition one can link the vevs v_1 and v_2 to the vev v and the angle β:

$$v_1 = v\cos\beta, \qquad v_2 = v\sin\beta, \qquad \tan\beta = \frac{v_2}{v_1} \tag{3.8}$$

In the CP-conserving case the Higgs basis has the special property of diagonalizing the charged and pseudoscalar sectors. This means that the doublets H_1 and H_2 take the form:

$$H_1 = \begin{pmatrix} G^\pm \\ \frac{1}{\sqrt{2}}\left(h_1^0 + iG^0 + v\right) \end{pmatrix}, \qquad H_2 = \begin{pmatrix} H^\pm \\ \frac{1}{\sqrt{2}}\left(h_2^0 + iA\right) \end{pmatrix} \tag{3.9}$$

with $G^\pm$ and G^0 the Goldstone fields absorbed by the $W^\pm$ and the Z^0 bosons to give them a mass, $H^\pm$ the charged Higgs bosons with mass $m_{H^\pm}$, A the pseudoscalar Higgs boson with mass m_A and h_1^0 and h_2^0 neutral scalar fields which are not mass eigenstates.

3.2.2.2 *The physical basis*

If the Higgs basis allows us to work with the physical charged and pseudoscalar Higgs bosons, the two scalar states h_1^0 and h_2^0 are not mass eigenstates and hence not physical fields.

In order to obtain the scalar mass eigenstates – denoted h and H with, by definition, $m_h < m_H$ – one needs to perform another rotation with angle α.

$$\begin{pmatrix} H \\ h \end{pmatrix} = \begin{pmatrix} \cos\alpha & \sin\alpha \\ -\sin\alpha & \cos\alpha \end{pmatrix} \begin{pmatrix} \phi_1^0 \\ \phi_2^0 \end{pmatrix} = \begin{pmatrix} c_{\beta-\alpha} & -s_{\beta-\alpha} \\ s_{\beta-\alpha} & c_{\beta-\alpha} \end{pmatrix} \begin{pmatrix} h_1^0 \\ h_2^0 \end{pmatrix} \tag{3.10}$$

with $c_{\beta-\alpha} \equiv \cos(\beta-\alpha)$ and $s_{\beta-\alpha} \equiv \sin(\beta-\alpha)$.

This new basis is called the physical basis as we work this time with the five physical Higgs fields h, H, A and $H^\pm$.

Using all the above equations one can show that the seven free parameters of the 2HDM in the $\mathbb{Z}_2$-basis can be converted into the seven free parameters of the physical basis:

$$\lambda_1,\ \lambda_2,\ \lambda_3,\ \lambda_4,\ \lambda_5,\ m_{22}^2,\ m_{12}^2 \tag{3.11}$$

$$\Updownarrow$$

$$m_h,\ m_H,\ m_A,\ m_{H^\pm},\ \tan\beta,\ s_{\beta-\alpha},\ m_{12}^2 \tag{3.12}$$

with m_h the mass of the light scalar h, m_H the mass of the heavy scalar H, m_A the mass of the pseudoscalar A and $m_{H^\pm}$ the mass of the charged Higgs bosons $H^\pm$.

In the following we will work in this basis associated with these seven free parameters.

3.2.3 Scalar and pseudoscalar Higgs couplings

The couplings between the Higgs bosons and the fermions come from the Yukawa terms described in section 3.2.1. Their couplings to the gauge bosons appear, in analogy with the SM,

when developing the 2HDM Higgs kinetic term:

$$\mathcal{L}_{Higgs}^{kinetic} = (D_\mu \phi_1)^\dagger (D^\mu \phi_1) + (D_\mu \phi_2)^\dagger (D^\mu \phi_2), \qquad D_\mu = \partial_\mu + igW_\mu^a \tau^a + ig' \frac{B_\mu}{2} \tag{3.13}$$

and then applying the appropriate transformations defined above in order to express the Lagrangian in terms of the mass eigenstates.

The couplings of the neutral scalar and pseudoscalar Higgs bosons normalized by their SM values are summarized in Table 3.2. Note that the normalization used for the couplings of the pseudoscalar Higgs boson to fermions is taken as $\frac{y^{f(2)}}{\sqrt{2}} = \frac{m_f}{v}$.

		Type I	Type II	Flipped	Lepton-Specific
Up-Type quark	h	$\frac{\cos\alpha}{\sin\beta}$			
	H	$\frac{\sin\alpha}{\sin\beta}$			
	A	$\cot\beta$			
Down-Type quark	h	$\frac{\cos\alpha}{\sin\beta}$	$-\frac{\sin\alpha}{\cos\beta}$	$-\frac{\sin\alpha}{\cos\beta}$	$\frac{\cos\alpha}{\sin\beta}$
	H	$\frac{\sin\alpha}{\sin\beta}$	$\frac{\cos\alpha}{\cos\beta}$	$\frac{\cos\alpha}{\cos\beta}$	$\frac{\sin\alpha}{\sin\beta}$
	A	$\cot\beta$	$\tan\beta$	$\tan\beta$	$\cot\beta$
Lepton	h	$\frac{\cos\alpha}{\sin\beta}$	$-\frac{\sin\alpha}{\cos\beta}$	$\frac{\cos\alpha}{\sin\beta}$	$-\frac{\sin\alpha}{\cos\beta}$
	H	$\frac{\sin\alpha}{\sin\beta}$	$\frac{\cos\alpha}{\cos\beta}$	$\frac{\sin\alpha}{\sin\beta}$	$\frac{\cos\alpha}{\cos\beta}$
	A	$\cot\beta$	$\tan\beta$	$\cot\beta$	$\tan\beta$
WW and ZZ	h	$\sin(\beta-\alpha)$			
	H	$\cos(\beta-\alpha)$			
	A	0			

TABLE 3.2: Tree-level couplings between the neutral Higgs bosons and the gauge bosons and fermions normalized to their SM value for the different 2HDM types.

3.3 Constraints on Two-Higgs Doublet Models

In section 3.2 we have presented the 2HDM framework in which we will work in the following.

We have seen that the model contains, in addition to the usual SM fermions and gauge bosons, five physical Higgs fields: two scalars h and H, a pseudoscalar particle A and two charged Higgs bosons $H^\pm$. The Higgs sector is therefore richer than that of the SM.

We have also seen that the model contains seven free parameters. The ones we will consider in the following are those associated with the physical basis and listed in equation (3.12). Note that, due to the experimental evidence of the existence of a Higgs boson with a mass of 125 GeV, one of the two masses m_h and m_H has to be taken to 125 GeV, leaving only six real free parameters.

However, with six free unconstrained parameters, the theory is not very predictive. It is then important to restrict the parameter space using both theoretical requirements and available experimental results.

We have already mentioned schematically in sections 2.2.3 and 2.3 how we can constrain BSM theories using LHC results. However there are a lot of other theoretical and experimental requirements.

First we will look at purely theoretical constraints – stability, unitarity and perturbativity requirements – then we will consider indirect experimental limitations *via* electroweak precision tests and flavor physics, and finally we will take into account constraints coming from direct searches from LEP and LHC.

3.3.1 Theoretical constraints

We have essentially three theoretical requirements in 2HDM: the stability of the 2HDM Higgs potential, the unitarity of the scattering matrix S and the perturbativity of the calculations.

◦ Stability constraint

As we want the vacuum of the theory to be stable we have to check the **stability of the potential**.

The 2HDM Higgs potential is assumed to be stable if there is no direction in the field space along which the potential tends to minus infinity. In the special case where $\lambda_6 = \lambda_7 = 0$, the necessary and sufficient condition for the vacuum to be bounded from below is that the quartic part of the potential be strictly positive for any value of the fields [37]. This condition can be translated into constraints on the λ_i [37, 41]:

$$\begin{gathered}\lambda_1 \geq 0, \qquad \lambda_2 \geq 0, \qquad \lambda_3 \geq -\sqrt{\lambda_1 \lambda_2}, \\ \lambda_3 + \lambda_4 - |\lambda_5| \geq -\sqrt{\lambda_1 \lambda_2}\end{gathered} \tag{3.14}$$

◦ Unitarity constraint

The theoretical computation of the Higgs-Higgs scattering – and in a general way the computation of identical particle-particle scattering – can lead to arbitrarily high cross-section values for increasing center of mass energy. In order to avoid this problem one has to impose **unitarity constraint** on the scattering matrices, *i.e.* require that the eigenvalues L_i of the tree-level scattering matrices verify [37, 42, 43]:

$$|L_i| < 8\pi \tag{3.15}$$

As the L_i can be expressed as a function of the λ_i – and, *a fortiori*, in terms of the physical basis parameters – this condition adds a constraint on the free parameters.

◦ Perturbativity constraint

As the calculations performed are conducted in a perturbative framework one must make sure that the **perturbativity** of the theory is still satisfied [44]. This condition can be precisely checked by computing higher-order corrections and checking the convergence of the perturbative series. However this task is very difficult to achieve.

Yet one can perform a rough check requiring that the quartic Higgs couplings $C_{h_i h_j h_k h_l}$ are not too high:

$$|C_{h_i h_j h_k h_l}| \leq 4\pi \tag{3.16}$$

These three constraints are checked using the program `2HDMC` v1.7.0 [41] whose behavior will be described in section 3.4.1.2.

3.3.2 Electroweak precision tests

The SM has numerous parameters whose values are not explicitly determined by the model. However, choosing a subset of appropriate parameters and fixing their values allows the determination of the numerical value of all the other SM parameters.

In addition, these parameters are measured experimentally as precisely as possible.

Hence, a consistency check between predicted and measured can be performed [11, 45, 46]. For this, one first need to compute the theoretical value of the chosen subset of parameters using experimental measurements. In the electroweak sector, the theoretical parameters are usually taken as the electric charge e, the Z^0 boson mass m_Z and the weak mixing angle $\sin^2\theta_W$ and their values are obtained using the experimental measurement of the fine structure constant α_e, the Fermi coupling constant G_F and the Z^0 boson mass m_Z. Then the other electroweak parameters are computed theoretically using the above subset and compared to experimental measurements (see for instance figure 1.6).

Theoretical calculations need to be very precise. In particular, they need to include higher-order corrections in order to be as accurate as possible. In the electroweak sector, the largest corrections for two-point functions come from loops arising in the gauge boson propagators. These corrections are called *oblique corrections*.

If new physics beyond the SM exists and contains new particles, as in the 2HDM, then these additional particles can take part in loop phenomena and hence can have a great impact on the theoretical values of the oblique corrections.

This is why M. Peskin and T. Takeuchi developed three parameters, called S, T and U, based on the oblique corrections, in order to highlight the potential influence of new physics [47, 48]. The experimental value of these three parameters can be derived using the electroweak fit described above and their model-dependent theoretical values can be computed using analytical formulas, reminded for instance in [46]. Note that they are constructed such that they are equal to zero in the SM framework.

Hence, the S, T and U parameters, also called *oblique parameters*, are a good experimental tool to detect new physics. However their current experimental value is close to zero, which means that the SM is not questioned by the oblique parameters (see for instance figure 3.2 showing a plot performed by the GFitter collaboration which illustrates the derivation of the experimental S and T values, assuming $U = 0$). Yet they still represent an important constraint that any BSM theory has to verify.

In concrete terms, in order to check the consistency of a given BSM theory with the oblique parameters, one has to compute the theoretical value of the S, T and U parameters in the theory framework. Then, using experimental data reminded in table 3.3, one need to check that the theoretical values of the oblique parameters are in the experimentally allowed region, *i.e.* that the theoretical values S, T and U verify the following equation:

$$\chi^2_{S,T,U}(S,T,U) = \begin{pmatrix} S-\widehat{S} \\ T-\widehat{T} \\ U-\widehat{U} \end{pmatrix}^T \cdot V^{-1} \cdot \begin{pmatrix} S-\widehat{S} \\ T-\widehat{T} \\ U-\widehat{U} \end{pmatrix} < b_3^{2\sigma} \tag{3.17}$$

with $\widehat{S}$, $\widehat{T}$ and $\widehat{U}$ the experimental best fit of the oblique parameters, S, T and U their theoretical values in the 2HDM framework and V^{-1} the inverse of their 3×3 covariant matrix defined by:

$$V_{ij} = C_{ij}\sigma_i\sigma_j, \qquad i,j \in \{1,2,3\} \tag{3.18}$$

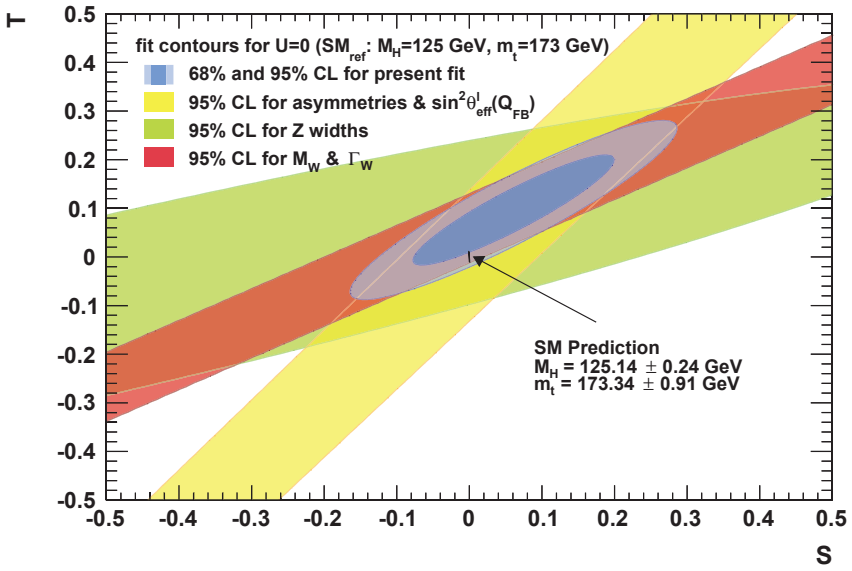

FIGURE 3.2: Constraints on the oblique parameters S and T with U set to zero using all SM observables (in blue). The SM prediction with uncertainties is indicated by the black segment and is still included in the allowed region. Figure taken from [11].

with C the 3×3 correlation matrix between the oblique parameters and σ_i their corresponding uncertainties. All the experimental values are given in table 3.3.

	Experimental best fit	Uncertainty σ_i
$\widehat{S}$	0.05	0.11
$\widehat{T}$	0.09	0.13
$\widehat{U}$	0.01	0.11

$$\mathrm{C}=\begin{array}{c} \begin{matrix} S & T & U \end{matrix} \\ \begin{pmatrix} 1 & 0.90 & -0.59 \\ 0.90 & 1 & -0.83 \\ -0.59 & -0.83 & 1 \end{pmatrix} \end{array} \begin{matrix} S \\ T \\ U \end{matrix}$$

TABLE 3.3: Experimental values of the oblique parameters with 1σ uncertainty and their correlation matrix C [11].

Due to its construction, the S parameter is very sensitive to the presence of new heavy fermions in the BSM theory under study. Therefore it may constrain very strongly theories such as Composite models that we will study in the last part of this thesis.

The T parameter measures the violation of the custodial symmetry, which is a residual symmetry of the Higgs sector. Hence, it will be sensitive to additional Higgs particles present in the model.

Finally the U parameter is only sensitive to changes in the $W^{\pm}$ boson width and hence is generally less constraining than the two other oblique parameters.

The theoretical values of the S, T and U parameters are computed with `2HDMC` in the 2HDM framework. Then the test of the oblique parameters is performed by my own `C++` program using equation (3.17) and the numerical values reminded in table 3.3.

Note that, as S, T and U are model-dependent their check in the 2HDM framework against experimental data is only meaningful in this specific model and is only a broad guideline for

bigger models having two Higgs doublets in their Higgs sector.

3.3.3 Flavor constraints

As we have seen for the oblique parameters, hints of the existence of new particles can be found indirectly *via* processes involving loops of particles. In particular this can happen in some flavor physics processes.

As the BR of such processes are measured experimentally with great accuracy, the computation of the theoretical BR and their comparison to experimental data is an efficient manner to constrain a BSM theory.

The most relevant processes that can contribute to constrain a 2HDM are described below.

3.3.3.1 $B \to X_s\gamma$ *decay*

In the SM the B meson can decay into a photon and a hadron containing a s quark *via* the exchange of a W^- boson and a top quark.

In the 2HDM the charged Higgs boson H^- can take the place of the W^- boson, modifying the BR of the process. Note that this modification depends on the couplings of the charged Higgs bosons to fermions, and hence on the 2HDM type considered. In particular, the $t\bar{b}H^-$ coupling will be enhanced in Type II and Flipped type with respect to Type I and Lepton-Specific type.

The leading-order Feynman diagram for the $b \to s\gamma$ process is shown in figure 3.3.

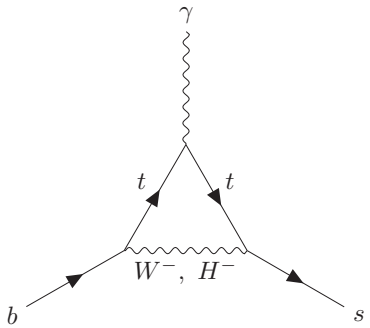

Figure 3.3: Leading-order Feynman diagram of the $b \to s\gamma$ process.

3.3.3.2 $B_s^0 \to \mu^+\mu^-$ *decay*

In the SM the $W^\pm$ and Z^0 bosons take part in the decay process $B_s^0 \to \mu^+\mu^-$. In the 2HDM both the charged Higgs bosons $H^\pm$ and the neutral scalars h and H can contribute to the BR (see figure 3.4).

3.3.3.3 *The isospin asymmetry* Δ_0

The isospin asymmetry for the decay $B \to K^*\gamma$ is defined as:

$$\Delta_0(B \to K^*\gamma) = \frac{\Gamma(\bar{B}^0 \to \bar{K}^{*0}\,\gamma) - \Gamma(B^\pm \to K^{*\pm}\,\gamma)}{\Gamma(\bar{B}^0 \to \bar{K}^{*0}\,\gamma) + \Gamma(B^\pm \to K^{*\pm}\,\gamma)} \tag{3.19}$$

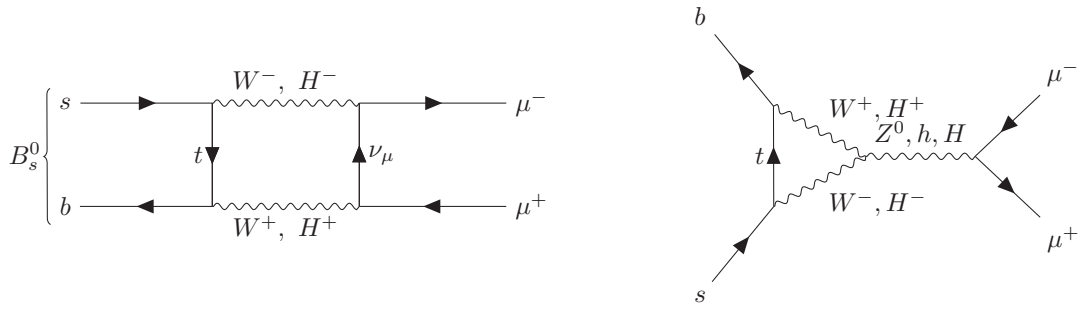

FIGURE 3.4: Leading-order Feynman diagrams of the $B_s^0 \to \mu^+\mu^-$ process.

If the isospin was not a broken symmetry then we would have $\Delta_0(B \to K^*\gamma) = 0$. However, experimentally, this number is non-zero.

The $B \to K^*\gamma$ process involves a $b \to s$ transition as shown in figure 3.3. Then the theoretical value of the isospin is sensitive to the presence of charged Higgs bosons.

3.3.3.4 *Enforcing the constraints*

Experimental values for the three processes enumerated above are written in table 3.4. We computed theoretical values in a 2HDM framework using the program `Superiso` v3.6 [49, 50].

In order to check the validity of the model we need to check that numerical values given by `SuperIso` in the 2HDM framework are consistent with experimental values within two sigma uncertainties – a check that is done in my `C++` program.

However, as `SuperIso` does not evaluate the uncertainties on its computations, we decided to combine the experimental uncertainty σ_{exp} of a specific process with the theoretical uncertainty σ_{th} coming from precise theoretical computation performed in the SM framework and use this combined uncertainty together with the experimental central value to constrain the 2HDM.

Both experimental and theoretical values of the BR processes computed in the SM framework with 1σ uncertainty are summarized in table 3.4. The combined uncertainty σ_{comb} is defined as:

$$\sigma_{comb} = \sqrt{\sigma_{exp}^2 + \sigma_{th}^2} \tag{3.20}$$

In the special case of the process $\bar{B} \to X_s\gamma$ the evaluation of the combined uncertainty is particularly crucial (see section 4.2.3). In order to be as accurate as possible we slightly modify the computation of σ_{comb} for this specific process, rescaling the theoretical uncertainty by the ratio of the BR in the 2HDM framework over the BR in the SM framework:

$$\sigma_{comb} = \sqrt{\sigma_{exp}^2 + \left(\sigma_{th} \times \frac{BR^{2HDM}(\bar{B} \to X_s\gamma)}{BR^{SM}(\bar{B} \to X_s\gamma)}\right)^2} \tag{3.21}$$

Numerical values of the combined uncertainties at 1σ – except for the $\bar{B} \to X_s\gamma$ process which does not have a fixed value – are summarized in table 3.4.

Hence, denoting BR^{exp} the central value of the experimental branching ratios, the model passes the flavor constraints if, for each process, the 2HDM BR check the following relation:

$$BR^{2HDM} \in [BR^{exp} - 2\sigma_{comb}; BR^{exp} + 2\sigma_{comb}] \tag{3.22}$$

Process	Experimental values	Theoretical computation	Combined error at 1σ
$BR(\overline{B} \to X_s\gamma)$	$(3.32 \pm 0.16) \times 10^{-4}$[51]	$(3.36 \pm 0.23) \times 10^{-4}$ [52]	/
$BR(B_s \to \mu^+\mu^-)$	$(2.9 \pm 0.7) \times 10^{-9}$ [53, 54]	$(3.54 \pm 0.27) \times 10^{-9}$ [55]	0.8×10^{-9}
$\Delta_0(B \to K^*\gamma)$	$(5.2 \pm 2.6) \times 10^{-2}$ [10]	$(5.1 \pm 1.5) \times 10^{-2}$ [55]	3.0×10^{-2}

TABLE 3.4: Values of the experimental and theoretical flavor constraints.

3.3.4 LEP constraints

Up to now we have only considered theoretical and indirect constraints on 2HDM. However, we also have accelerator data available to help us constrain the model directly using upper limits, as presented in section 2.2.3.

As mentioned in section 2.1.2, the LEP searched for the SM Higgs boson for many years. Hence, LEP experiments published many upper limits on processes involving possible light scalars, pseudoscalars and charged Higgs bosons – light meaning with a mass below 110 GeV. In particular, it were able to give a lower bound on the charged Higgs mass in a 2HDM scenario: $m_{H^\pm} > 80$ GeV for a Type II and $m_{H^\pm} > 72.5$ GeV if $m_A > 12$ GeV for a Type I [10, 56]. Hence, it is important to take into account LEP results to constrain 2HDM.

In order to do so we used the program `HiggsBounds` v5.1.0 beta [57, 58, 59, 60] which includes, among others, all published LEP analyses. `HiggsBounds` uses the output of `2HDMC` computed for specific values of the free parameters and check the results against LEP experimental data. The result, given as a boolean return value, specifies wether the 2HDM point is excluded at 95% C.L.

3.3.5 LHC constraints

As mentioned in section 2.2.3 LHC analyses give rise to two main ways of constraining BSM theories: the first one is based on the use of direct information on the 125 GeV Higgs boson experimentally discovered and the second one uses upper limits on processes involving hypothetical new particles.

As the methods employed to apply the constraints in the 2HDM framework are quite complex, we will describe them in a specific section.

3.4 Focus on the practical application of LHC constraints

3.4.1 Constraints from the 125 GeV Higgs boson

As a new particle very similar to the SM Higgs boson has been discovered experimentally, all BSM theories need to identify one of their particles to this new boson.

In the 2HDM case, there are two possible candidates: the two neutral scalars h and H with, by convention, $m_h < m_H$.

The choice of the particle identified with the 125 GeV Higgs boson will influence the resulting constraints. Indeed, looking at table 3.2, one can see that if we impose $m_h = 125$ GeV, then the hWW coupling needs to be close to that of the SM, which means that $s_{\beta-\alpha} \sim 1$, hence $c_{\beta-\alpha} \sim 0$. Conversely, if we choose $m_H = 125$ GeV, then we will have $s_{\beta-\alpha} \sim 0$ and $c_{\beta-\alpha} \sim 1$.

In order to impose constraints from the 125 GeV Higgs boson's properties we have already seen in section 2.3 that we can use theoretical signal strengths, computed *via* equation (2.3), together with exclusion contours as shown in figure 2.9.

In order to do so we need to follow these steps:

- We extract the exclusion contours provided by ATLAS and CMS as presented in section 2.3.2.3 and obtain, in the Gaussian approximation and for a given decay channel YY, the analytical expression of the log-likelihood function $-2\ln\mathcal{L}_Y$ depending on the signal strengths $\mu_{ggh,tth\to YY}$ and $\mu_{VBF,VH\to YY}$. The numerical values obtained for the ellipse parameters are summarized in tables 2.5 and 2.6;
- We construct two separate total log-likelihood $-2\ln\mathcal{L}_{tot}$, one with the 8 TeV data and the other with the 13 TeV data. We remind that total log-likelihood can be defined by (see also equation (2.8)):

$$-2\ln\mathcal{L}_{tot}(\mu_{1,Y_1},\mu_{2,Y_1},\mu_{1,Y_2},\mu_{2,Y_2},...)=\sum_{Y_i}-2\ln\mathcal{L}_{Y_i}(\mu_{1,Y_i},\mu_{2,Y_i}) \tag{3.23}$$

  with Y_i the different decay channels considered in ATLAS and CMS studies;
- We identify the n independent parameters generating the different signal strengths μ_{j,Y_i};
- We find the minimum of the total log-likelihood: $\min\limits_{\{\text{indep. param.}\}} -2\ln\mathcal{L}_{tot}$;
- We construct the chi-squared function $\Delta\chi^2_n$ defined as – *cf* equation (2.9):

$$\begin{aligned}\Delta\chi^2_n(\mu_{1,Y_1},\mu_{2,Y_1},\mu_{1,Y_2},\mu_{2,Y_2},...)=&-2\ln\mathcal{L}_{tot}(\mu_{1,Y_1},\mu_{2,Y_1},\mu_{1,Y_2},\mu_{2,Y_2},...)\\&-\min_{\{\text{indep. param.}\}}(-2\ln\mathcal{L}_{tot})\end{aligned} \tag{3.24}$$

  depending on the value of the different signal strengths μ_{j,Y_i};
- We derive, for a given set of the seven free parameters of the 2HDM – reminded in equation (3.12) – the theoretical value of each signal strength μ_{j,Y_i}, deduce the value of $\Delta\chi^2_n$ and compare it to the upper bound $b^{2\sigma}_n$. If $\Delta\chi^2_n > b^{2\sigma}_n$ then the point is excluded at 95% C.L.; else, we say that the point passes the 125 GeV Higgs constraints.

The two main difficulties in this process are first the identification of the independent parameters and the subsequent minimization of the total log-likelihood, and second the computation of the signal strength in the 2HDM framework.

3.4.1.1 *Determination of the independent parameters*

In order to identify the independent parameters generating the signal strengths one needs to look closer to their construction.

We remind that the signal strength for a specific production mode XX and decay channel YY can be written as – see equation (2.3):

$$\mu_{XX\to h_{125}\to YY}=\frac{\sigma^{2HDM}_{XX\to h_{125}}\times BR^{2HDM}_{h_{125}\to YY}}{\sigma^{SM}_{XX\to h_{125}}\times BR^{SM}_{h_{125}\to YY}} \tag{3.25}$$

with h_{125} standing for the 2HDM particle identified with the 125 GeV Higgs boson.

As the couplings of the neutral scalar Higgs bosons to SM particles are simply rescaled with respect to thos of the SM Higgs boson, then, at LO, the values of the 2HDM production

cross-sections and decay widths are approximately equal to those of the SM rescaled by an appropriate factor κ_X, called *scaling factor*, defined as:

$$\kappa_X^2 \equiv \frac{\Gamma^{2HDM}_{h_{125}\to XX}}{\Gamma^{SM}_{h_{125}\to XX}} \tag{3.26}$$

In the following we will call this approximation the *kappa trick*. Hence, one can rewrite equation (3.25) in this approximation as:

$$\begin{aligned}\mu_{XX\to h_{125}\to YY} &= \frac{\kappa_X^2\sigma^{SM}_{XX\to h_{125}}}{\sigma^{SM}_{XX\to h_{125}}} \times \underbrace{\frac{\kappa_Y^2\Gamma^{SM}_{h_{125}\to YY}}{\Gamma^{2HDM}_{tot}}}_{=BR^{2HDM}_{h_{125}\to YY}} \times \underbrace{\frac{\Gamma^{SM}_{tot}}{\Gamma^{SM}_{h_{125}\to YY}}}_{=(BR^{SM}_{h_{125}\to YY})^{-1}} \\ &= \kappa_X^2\kappa_Y^2 \times \frac{\Gamma^{SM}_{tot}}{\Gamma^{2HDM}_{tot}}\end{aligned} \tag{3.27}$$

Note that we have assumed that scaling factors for production and decay are identical at LO.

In the case where Γ^{2HDM}_{tot} does not include any new decay channel – which is the case as long as $m_A > \frac{125}{2}$ GeV and, if $m_H = 125$ GeV, $m_h > \frac{125}{2}$ GeV – then we can rewrite equation (3.27) as:

$$\mu_{XX\to h_{125}\to YY} = \kappa_X^2\kappa_Y^2 \times \frac{1}{\sum\limits_Z \kappa_Z^2 BR^{SM}_{h_{125}\to ZZ}} \tag{3.28}$$

Then finding the dependence of the signal strengths is equivalent to finding the dependence of the scaling factors κ_X.

We can also define *reduced couplings* directly in the Lagrangian as:

$$C_{XX} = \frac{C^{2HDM}_{h_{125}XX}}{C^{SM}_{h_{125}XX}}, \qquad C_{H^+} = C^{2HDM}_{h_{125}H^+H^-}\frac{v}{2m^2_{H^+}} \tag{3.29}$$

with $C^{SM}_{h_{125}XX}$, $C^{2HDM}_{h_{125}XX}$ the coupling between the 125 GeV Higgs boson and two X particles ($XX = W^+W^-, ZZ, \bar{t}t...$) in the SM and 2HDM framework respectively, and $C^{2HDM}_{h_{125}H^+H^-}$ the coupling between the 125 GeV Higgs boson and two charged Higgs bosons defined as:

$$C^{2HDM}_{h_{125}H^+H^-} = \begin{cases} -\frac{1}{2v}\left[\frac{c_{2\beta}}{s_{2\beta}}c_{\beta-\alpha}\left(4m_h^2 - \frac{8m_{12}^2}{s_{2\beta}}\right) + s_{\beta-\alpha}\left(2m_h^2 + 4m^2_{H^+} - \frac{8m_{12}^2}{s_{2\beta}}\right)\right], & m_h = 125 \text{ GeV} \\ \frac{1}{2v}\left[\frac{c_{2\beta}}{s_{2\beta}}s_{\beta-\alpha}\left(4m_H^2 - \frac{8m_{12}^2}{s_{2\beta}}\right) - c_{\beta-\alpha}\left(2m_H^2 + 4m^2_{H^+} - \frac{8m_{12}^2}{s_{2\beta}}\right)\right], & m_H = 125 \text{ GeV} \end{cases} \tag{3.30}$$

with $s_{2\beta} \equiv \sin 2\beta$, $c_{2\beta} \equiv \cos 2\beta$.

At LO one can relate most of the scaling factors to the reduced couplings:

$$\kappa_W^2 = C_{WW}^2, \qquad \kappa_Z^2 = C_{ZZ}^2, \qquad \kappa_f^2 = C_{ff}^2 \tag{3.31}$$

with f standing for a SM fermion.

Looking at the 2HDM couplings reminded in table 3.2 one can see, after some simple mathematical transformations, that the reduced couplings – and hence the scaling factors κ_X – of

the two neutral scalar Higgs bosons to fermions and $W^{\pm}$ and Z^0 bosons depend only on two parameters, namely $s_{\beta-\alpha}$ and $\tan\beta$:

$$h \text{ case: } \begin{cases} C_{tt}^h = \frac{\cos\alpha}{\sin\beta} = s_{\beta-\alpha} + \sqrt{1-s_{\beta-\alpha}^2} \times \frac{1}{\tan\beta}, \\ C_{bb}^h = -\frac{\sin\alpha}{\cos\beta} = s_{\beta-\alpha} - \sqrt{1-s_{\beta-\alpha}^2} \times \tan\beta, \quad \text{(Type II)} \\ C_{WW}^h = C_{ZZ} = s_{\beta-\alpha}. \end{cases} \tag{3.32}$$

$$H \text{ case: } \begin{cases} C_{tt}^H = \frac{\sin\alpha}{\sin\beta} = \sqrt{1-s_{\beta-\alpha}^2} - s_{\beta-\alpha} \times \frac{1}{\tan\beta}, \\ C_{bb}^H = \frac{\cos\alpha}{\cos\beta} = \sqrt{1-s_{\beta-\alpha}^2} + s_{\beta-\alpha} \times \tan\beta, \quad \text{(Type II)} \\ C_{WW}^H = C_{ZZ} = \sqrt{1-s_{\beta-\alpha}^2}. \end{cases} \tag{3.33}$$

However the scaling factors κ_g, κ_γ and $\kappa_{Z\gamma}$, linked to the h_{125} decaying respectively into two gluons, two photons and a photon and a Z^0 boson, appearing in the denominator of equation (3.28), have a more complicated shape as the decays occur through a loop (see figure 3.5 for the Feynman diagram of the $h_{125} \to \gamma\gamma$ decay). As the decay is not reduced to a unique vertex, the scaling factor will be a complex combination of the reduced couplings linked to the different particles running in the loop.

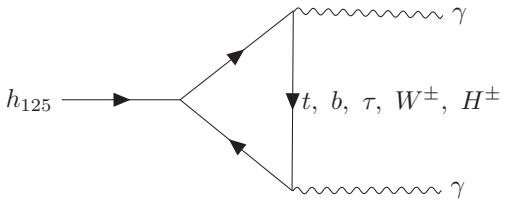

FIGURE 3.5: Feynman diagram of the decay of the 125 GeV Higgs boson into two photons involving a loop of fermions – mainly top quarks – or $W^{\pm}$ bosons. In the 2HDM, the charged Higgs bosons are also involved in the loop.

One can obtain the analytical expression of the scaling factors using the expression of the decay width at LO. Their expressions can be found in Appendix C. Using these formulas one can express the dependence of the scaling factors in terms of the free parameters of the model in order to deduce the minimal set of independent parameters generating them:

$$\kappa_g = f(C_{tt}, C_{bb}, C_{cc}) = f(s_{\beta\alpha}, t_\beta) \tag{3.34}$$

$$\kappa_\gamma = f(C_{tt}, C_{bb}, C_{cc}, C_{\tau\tau}, C_{WW}, C_{H^+}) = f(s_{\beta\alpha}, t_\beta, m_{12}^2, m_{H^+}) \tag{3.35}$$

$$\kappa_{Z\gamma} = f(C_{tt}, C_{bb}, C_{cc}, C_{\tau\tau}, C_{WW}, C_{H^+}) = f(s_{\beta\alpha}, t_\beta, m_{12}^2, m_{H^\pm}) \tag{3.36}$$

This time, in addition to $s_{\beta-\alpha}$ and $\tan\beta$, the scaling factors depend also on m_{12}^2 and $m_{H^\pm}$. This new dependence comes entirely from the presence of the charged Higgs boson in the loop which induces the appearance of a term proportional to the reduced coupling C_{H^+} in the analytical expression of the decay width.

So far we have only looked at the case where $m_A > \frac{125}{2}$ GeV and $m_h > \frac{125}{2}$ GeV.

If $m_A < \frac{125}{2}$ GeV then new decay channels are open: $h_{125} \to AA$ and $h_{125} \to ZA$. Hence equation (3.28) becomes:

$$\mu_{XX\to h_{125}\to YY} = \kappa_X^2 \kappa_Y^2 \times \frac{1}{\frac{\Gamma_{h_{125}\to AA}^{2HDM} + \Gamma_{h_{125}\to ZA}^{2HDM}}{\Gamma_{tot}^{SM}} + \sum_Z \kappa_Z^2 BR_{h_{125}\to ZZ}^{SM}} \tag{3.37}$$

with the value of $\Gamma^{2HDM}_{h_{125}\to AA}$ and $\Gamma^{2HDM}_{h_{125}\to ZA}$ depending on m_A. Therefore the signal strength will depend on five independent parameters this time, namely $s_{\beta-\alpha}$, $\tan\beta$, m^2_{12}, $m_{H^\pm}$ and m_A.

In the area $m_h < \frac{125}{2}$ GeV – and hence $m_H = 125$ GeV – the decays $H \to hh$ and $H \to Zh$ are possible. Hence, following the above discussion, the signal strengths will depend on an additional independent parameter, namely m_h.

In conclusion, in the case where $m_A > \frac{125}{2}$ GeV and $m_h > \frac{125}{2}$ GeV the signal strengths depend on four independent parameters, namely $s_{\beta-\alpha}$, $\tan\beta$, m^2_{12} and $m_{H^\pm}$. It follows that the log-likelihood function depends only on these four parameters and that the resulting $\Delta\chi^2$ function will have four degrees of freedom.

In the case where $m_A < \frac{125}{2}$ GeV and/or $m_h < \frac{125}{2}$ GeV the signal strengths depend also on m_A and/or m_h. Then the log-likelihood function depends on these five or six parameters and the resulting $\Delta\chi^2$ function will have five or six degrees of freedom.

3.4.1.2 *Computation of the signal strengths in the 2HDM framework*

Now that the independent parameters generating the signal strengths in the 2HDM framework have been identified we can search for the minimum of the total log-likelihood function.

The first step is to compute the numerical value of the signal strength for a given set of 2HDM free parameters; then, using equations (2.5) and (3.23), one can compute the numerical value of the total log-likelihood.

For this we used the program `2HDMC` which takes as input numerical values for the seven free parameters of the model and computes, for this specific set of parameters, the numerical values of the couplings, branching ratios and total decay width of the different Higgs bosons in the 2HDM framework. Combining branching ratios and total decay width makes it possible to derive the partial decay widths.

We compute the numerical value of the signal strength using the following formulas:

$$\begin{cases} \mu_{gg\to h_{125}\to YY} = \kappa_g^2 \times \dfrac{BR^{2HDM}_{h_{125}\to YY}}{BR^{SM}_{h_{125}\to YY}}, & \kappa_g^2 \equiv \dfrac{\Gamma^{2HDM}_{h_{125}\to gg}}{\Gamma^{SM}_{h_{125}\to gg}} \\ \mu_{VBF,VH\to h_{125}\to YY} = \kappa_V^2 \times \dfrac{BR^{2HDM}_{h_{125}\to YY}}{BR^{SM}_{h_{125}\to YY}}, & \kappa_V^2 \equiv \begin{cases} s^2_{\beta-\alpha}, & m_h = 125 \text{ GeV} \\ c^2_{\beta-\alpha}, & m_H = 125 \text{ GeV} \end{cases} \end{cases} \tag{3.38}$$

As mentioned above, the numerical values of the branching ratios and partial decay widths in the 2HDM framework are obtained using the program `2HDMC`. The corresponding values in the SM framework are taken from [23] (see also table 2.2).

Using both 2HDM and SM results one can compute the scaling factors κ_g and κ_V numerically and hence the two signal strengths $\mu_{gg\to h_{125}\to YY}$ and $\mu_{VBF,VH\to h_{125}\to YY}$ in a specific decay channel YY following equation (3.38).

Finally, using equations (2.5) and (3.23) one has access to the numerical value of the total log-likelihood $-2\ln\mathcal{L}_{tot}$ for a given set of the free parameters.

3.4.1.3 *Minimization of the log-likelihood*

We have shown in section 3.4.1.2 how to derive the numerical values of the signal strengths and of the total log-likelihood function $-2\ln\mathcal{L}_{tot}$ in the 2HDM framework. The next step is

to compute the minimum of this function. For this we used the program `Minuit2`.

`Minuit2` is a `Root` package which is dedicated to the search of the global minimum of a given function. The user can choose from several minimization methods. Then one needs to supply the program with a function that takes a number `npar` of input parameters and specify if these parameters are fixed to a specific value or if they vary, either freely or inside a given range. For each variable parameter the user needs to provide an initial value inside the search interval.

Once launched, `Minuit2` uses the above information and the selected numerical method to find the minimum of the function.

In our case, the function to be minimized by `Minuit2` is the total log-likelihood function. However, instead of giving an analytical expression of the log-likelihood at LO, which is possible using the formulas reminded in Appendix C but has the drawback of omitting all QCD corrections available in `2HDMC`, we decided to compute it *via* `2HDMC`, as explained in section 3.4.1.2.

For each 2HDM type we performed a minimization of the 8 TeV and 13 TeV total log-likelihood for both 125 GeV Higgs boson candidates h and H in each of the four areas defined by:

$$\mathcal{A}_1 = \{m_A \geq \frac{125}{2}\text{ GeV}, m_h \geq \frac{125}{2}\text{ GeV}\},\ \mathcal{A}_2 = \{m_A < \frac{125}{2}\text{ GeV}, m_h \geq \frac{125}{2}\text{ GeV}\},$$
$$\mathcal{A}_3 = \{m_A \geq \frac{125}{2}\text{ GeV}, m_h < \frac{125}{2}\text{ GeV}\},\ \mathcal{A}_4 = \{m_A < \frac{125}{2}\text{ GeV}, m_h < \frac{125}{2}\text{ GeV}\} \quad (3.39)$$

Note that, in the case where $m_h = 125$ GeV, the last two areas $\mathcal{A}_3$ and $\mathcal{A}_4$ are empty and hence are not considered.

The numerical values of the fixed and free input parameters are summarized in tables 3.5, 3.6 and 3.7.

Fixed parameters	m_h (GeV)	m_H (GeV)	m_A (GeV) $m_A \geq \frac{125}{2}$
Value	125	300	300

TABLE 3.5: Value of the three (two) fixed parameters implemented in `Minuit2` in the case where $m_h = 125$ GeV. In this case, m_A can be fixed – if $m_A \geq \frac{125}{2}$ GeV – or can vary.

Fixed parameters	m_h (GeV) $m_h \geq \frac{125}{2}$	m_H (GeV)	m_A (GeV) $m_A \geq \frac{125}{2}$
Value	80	125	300

TABLE 3.6: Value of the three (two, one) fixed parameters implemented in `Minuit2` in the case where $m_H = 125$ GeV. In this case, m_A can be fixed – if $m_A \geq \frac{125}{2}$ GeV – or can vary and m_h can be fixed – if $m_h \geq \frac{125}{2}$ GeV – or can vary.

Free parameters	$\sin(\beta-\alpha)$	$\tan\beta$	m_{12} (GeV)	m_{H^+} (GeV)	m_h (GeV) $m_h < \frac{125}{2}$	m_A (GeV) $m_A < \frac{125}{2}$
Range of variation	[-1;1]	[0.5;50]	[-2000;2000]	[75; 2000]	[2; 62.5]	[2; 62.5]
Initial value	$\begin{cases}1, & m_h = 125\text{ GeV}\\ 0, & m_H = 125\text{ GeV}\end{cases}$	20	0	1000	30	30

TABLE 3.7: Range of variation of the four (five, six) free parameters and their initial value implemented in `Minuit2`.

The minima of the total log-likelihood functions found by `Minuit2` for all these cases are written in table 3.8 for the 8 TeV data and in table 3.9 for the 13 TeV data.

	$m_h = 125$ GeV				$m_H = 125$ GeV			
Type	I	II	Y	X	I	II	Y	X
$\mathcal{A}_1$	6.01616	3.13212	1.95256	6.01617	6.01613	3.31005	1.95235	5.74596
$\mathcal{A}_2$	6.42363	3.28603	1.87369	8.07468	9.08227	3.30589	2.37654	5.78563
$\mathcal{A}_3$	/	/	/	/	8.09083	3.56058	2.37627	25.6556
$\mathcal{A}_4$	/	/	/	/	6.31839	3.30193	2.40931	23.4568

TABLE 3.8: Minima of the total log-likelihoods at 8 TeV found by `Minuit2` in the four different 2HDM types based on experimental data at 8 TeV [20].

	$m_h = 125$ GeV				$m_H = 125$ GeV			
Type	I	II	Y	X	I	II	Y	X
$\mathcal{A}_1$	17.1627	13.6382	12.6642	17.1628	17.1626	13.6379	12.6641	17.0813
$\mathcal{A}_2$	17.3405	14.529	13.0788	17.7384	17.3196	14.0232	12.6647	17.745
$\mathcal{A}_3$	/	/	/	/	21.4669	16.6657	12.9247	21.385
$\mathcal{A}_4$	/	/	/	/	20.0162	14.0909	13.0214	20.8334

TABLE 3.9: Minima of the total log-likelihood at 13 TeV found by `Minuit2` in the four different 2HDM types. The computation uses the following 13 TeV results: ATLAS analyses on ZZ [27] and $\gamma\gamma$ [29] decay channels and CMS analyses on ZZ [28], $\gamma\gamma$ [30], WW [31] and $\tau\tau$ [32] decay channels.

3.4.1.4 *Enforcing the LHC 125 GeV Higgs constraint*

Once the minima are found, one can compute the numerical value of $\Delta\chi^2_n = -2\ln\mathcal{L}_{tot} - \min(-2\ln\mathcal{L}_{tot})$ for a given set of 2HDM free parameters: using equations (3.38), (2.5) and (3.23) one can compute the numerical value of the total log-likelihood function and the minima are listed in tables 3.8 and 3.9.

From the numerical value of $\Delta\chi^2_n$ one is able to exclude or not the considered point.

Indeed, as explained in the last point of section 3.4.1, the point is excluded at 95% C.L. if $\Delta\chi^2_n > b^{2\sigma}_n$ with n the number of independent parameters – that is, $n = 4$ in $\mathcal{A}_1$, $n = 5$ in $\mathcal{A}_2$ and $\mathcal{A}_3$ and $n = 6$ in $\mathcal{A}_4$. The numerical values of $b^{2\sigma}_n$ are reminded in table 2.4.

We are therefore able to apply two sets of constraints: the 125 GeV Higgs constraints at 8 TeV and the 125 GeV Higgs constraints at 13 TeV.

Note that all the steps described above are performed by different subroutines of my own program.

3.4.1.5 *Check of the kappa trick consistency*

In the derivation of the signal strengths we have assumed that the 2HDM production cross-section in a production mode X could be obtained by a simple rescaling by a factor κ^2_X of the SM cross-section in the same production mode (see equation (3.38)). We called this approximation the *kappa trick*. In particular, we have in this approximation:

$$\sigma^{2HDM}_{gg\to h_{125}} \simeq \kappa^2_g \; \sigma^{SM}_{gg\to h_{125}}, \qquad \sigma^{2HDM}_{VBF,VH\to h_{125}} \simeq \kappa^2_V \; \sigma^{SM}_{VBF,VH\to h_{125}} \tag{3.40}$$

Although this approximation is quite good at LO in VBF and VH production modes as the process involves direct couplings between the 125 GeV Higgs boson and a pair of $W^{\pm}$ or Z^0 bosons, it may be quite incorrect in gluon fusion production mode as the process involves a loop of quarks and not a simple vertex between the 125 GeV Higgs boson and the two gluons.

In order to check the consistency of the *kappa trick* we tested the numerical value of the cross-section in gluon fusion production mode obtained with this method against the results given by `SusHi` v1.6.0 [61].

The `SusHi` program computes numerically the production cross-section of a neutral scalar or pseudoscalar Higgs boson in the 2HDM or MSSM framework using numerical Monte Carlo integration.

In the 2HDM case, `SusHi` takes as input a numerical value for each of the seven free parameters of the model and returns the production cross-section in gluon fusion mode and/or $b\bar{b}$ production mode.

The level of accuracy, from LO to N3LO in the QCD corrections and from LO to NLO for electroweak corrections, can be set by the user. As `2HDMC` includes some NLO QCD and electroweak corrections we decided to work at NLO with `SusHi` in order to have comparable results.

The parton distribution functions used in `SusHi` were `MMHT201468cl` for LO and `PDF4LHC15_mc` for NLO and NNLO [62]. The renormalization and factorization scales μ_R and μ_F for the gluon fusion process were set to $\mu_R = \mu_F = m_\phi/2$ with $\phi = \{h, H, A\}$ [63]. As we wanted to compare cross-sections in gluon fusion production mode, the computation in $b\bar{b}$ production mode proposed by `SusHi` was turned off.

One can also specify the value of some SM parameters. The values we used for both `SusHi` and `2HDMC` are summarized in table 3.10.

m_W (GeV)	Γ_W (GeV)	m_Z (GeV)	Γ_Z (GeV)	$\bar{m}_b(m_b)$ (GeV)	m_t(pole) (GeV)
80.385	2.085	91.1876	2.4952	4.18	174.2

m_c(pole) (GeV)	α_{EM}	α	α_s	G_F (GeV)$^{-2}$
1.76	1/127.934	1/137.0359991	0.118	1.16637×10^{-5}

TABLE 3.10: SM input parameters implemented in `SusHi` and `2HDMC` [10].

In order to compare the results obtained from the *kappa trick* and from `SusHi` we define the deviation between the two methods as:

$$\Delta \equiv \frac{\sigma^{kappa\ trick}_{gg\to h_{125}} - \sigma^{\texttt{SusHi}}_{gg\to h_{125}}}{\sigma^{\texttt{SusHi}}_{gg\to h_{125}}} \times 100 \tag{3.41}$$

◦ CHECK OF THE *kappa trick* CONSISTENCY FOR THE 125 GEV HIGGS BOSON

In order to check the consistency of the *kappa trick* approximation in the case of a 2HDM 125 GeV Higgs boson we computed the value of the gluon fusion production cross-section *via* `SusHi` and the *kappa trick* for the two separate cases $m_h = 125$ GeV and $m_H = 125$ GeV, the other six free parameters being set to a fixed arbitrary value. The results at 13 TeV for three different sets of parameters are written in table 3.11 for the $m_h = 125$ GeV case and table 3.12 for the $m_H = 125$ GeV case. The deviation between the two methods defined by equation (3.41) is written in the last column.

m_h (GeV)	m_H (GeV)	m_A (GeV)	$m_{H^\pm}$ (GeV)	m_{12} (GeV)	$s_{\beta-\alpha}$	$\tan\beta$	$\sigma^{kappa\ trick}_{gg\to h_{125}}$ (pb)	$\sigma^{\texttt{SusHi}}_{gg\to h_{125}}$ (pb)	Δ (%)
125	700	60	250	10	0.999	10	38.023	37.385	1.72
125	200	250	120	200	-0.999	20	37.521	36.887	1.72
125	300	800	800	0	0.999	2	39.396	38.729	1.72

TABLE 3.11: Comparison between the cross-section of the 2HDM 125 GeV Higgs boson in gluon production mode at 13 TeV obtained with the *kappa trick* and `SusHi`. The light Higgs boson h is here assimilated with the 125 GeV Higgs boson and the six other free parameters are fixed to a specific value. The deviation between the two methods is indicated in the last column.

m_h (GeV)	m_H (GeV)	m_A (GeV)	$m_{H^\pm}$ (GeV)	m_{12} (GeV)	$s_{\beta-\alpha}$	$\tan\beta$	$\sigma^{kappa\ trick}_{gg\to h_{125}}$ (pb)	$\sigma^{\texttt{SusHi}}_{gg\to h_{125}}$ (pb)	Δ (%)
80	125	60	250	10	-0.2	5	39.275	38.612	1.72
30	125	300	400	300	-0.4	20	33.123	32.563	1.72
110	125	130	70	0	-0.1	10	38.143	37.498	1.72

TABLE 3.12: Comparison between the cross-section of the 2HDM 125 GeV Higgs boson in gluon production mode at 13 TeV obtained with the *kappa trick* and `SusHi`. The heavy Higgs boson H is here assimilated with the 125 GeV Higgs boson and the six other free parameters are fixed to a specific value. The deviation between the two methods is indicated in the last column.

The deviation between the two methods for a production at 13 TeV are less than 2%,which is a very good result knowing that the uncertainty for such computations at NLO in the SM framework stands around 15-20% (see for instance [22]). Note that the deviation in the case of a production at 8 TeV is similar to the 13 TeV results.

These results hence validate the use of the *kappa trick* for gluon fusion production mode and, by extension, for $VBF + VH$ production mode for the 2HDM 125 GeV Higgs boson.

◦ CHECK OF THE *kappa trick* CONSISTENCY AT LOW AND HIGH MASS

The `SusHi` program computes with a good accuracy the cross-section production of a scalar or pseudoscalar Higgs boson in the 2HDM framework for gluon fusion production and $b\bar{b}$ production. However the $VBF + VH$ production mode, which is present in some ATLAS or CMS analyses on light or heavy additional scalars, are not available *via* this program.

The *kappa trick* may be a good way to obtain the cross-section in $VBF + VH$ production mode. In order to check the validity of the method, and as we do not have any program giving the cross-section production in $VBF + VH$ mode in the 2HDM framework, we performed again a check against `SusHi` results in gluon fusion production mode for the 2HDM non-125 GeV Higgs boson.

For this, we fixed the mass of one of the neutral scalar Higgs bosons at 125 GeV and let the mass of the other scalar vary freely. The five other free parameters are fixed to an arbitrary value.

In the case where $m_H = 125$ GeV the mass of the light Higgs boson is incremented, by steps of 2 GeV, from 20 GeV to 110 GeV. For each value of m_h, its production cross-section at 13 TeV in gluon fusion production mode is computed *via* the *kappa trick* – represented by the dashed blue curve in figure 3.6a – and `SusHi` – represented by the dashed red line. The deviation between the two results is represented by the solid green line.

The deviation between the two methods for a light Higgs – with $m_h < 110$ GeV – is less than 4%, which is very good. Hence, the *kappa trick* can be used in this mass range.

In the case where $m_h = 125$ GeV the mass of the heavy Higgs boson is incremented from 130 GeV to 1000 GeV, with a step of 10 GeV for $m_H < 500$ and 50 GeV elsewhere. As for the low-mass case, its production cross-section at 13 TeV in gluon fusion production mode is computed *via* the *kappa trick* – represented by the dashed blue curve in figure 3.6b – and `SusHi` – represented by the dashed red line. The deviation between the two results is represented by the solid green line.

This time the deviation is larger and goes up to 22% around $m_H \sim 300 - 400$ GeV. This is due to the QCD corrections which are taken in the top quark infinite mass approximation in the `2HDMC` program. This approximation, quite good at masses $m_H < m_t$, does not reflect any more the real corrections for intermediate masses, where the decay $H \to t\bar{t}$ becomes possible. However the approximation is still good for "low"-mass ranges – $m_H \gtrsim 125$ GeV – and high-mass ranges – $m_H > 700$ GeV.

Hence, the only solution to obtain the production cross-section in gluon-fusion mode with a good accuracy in the whole range of mass is to use `SusHi`.

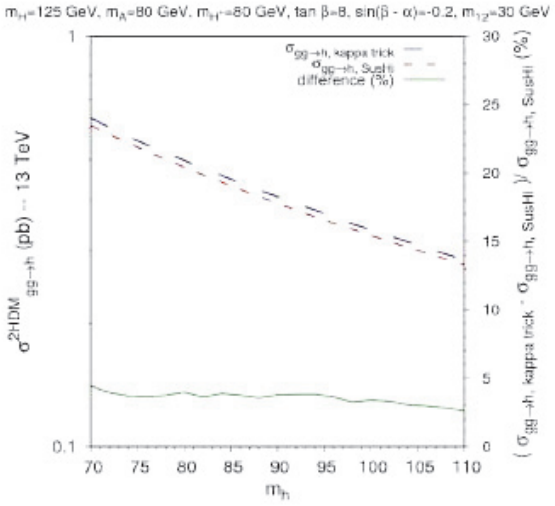

(A) Cross-section in gluon fusion production mode for the 2HDM light Higgs boson h depending on its mass, the six other 2HDM free parameters being fixed.

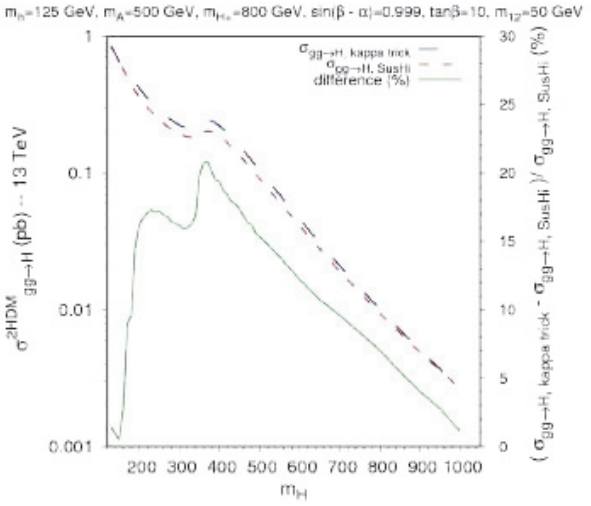

(B) Cross-section in gluon fusion production mode for the 2HDM heavy Higgs boson H depending on its mass, the six other 2HDM free parameters being fixed.

FIGURE 3.6: Comparison between the cross-section in gluon fusion production mode obtained using the *kappa trick* method and `SusHi`. The dashed blue lines correspond to the cross-section computed with the *kappa trick*, the dashed red lines correspond to those computed with `SusHi` and the solid green lines correspond to the deviation between the two methods. The value taken for the six free parameters are indicated above the graph.

3.4.2 LHC CONSTRAINTS ON OTHER SCALARS

In addition to the constraints on the 125 GeV Higgs boson coming from the LHC, one can also constrain the other particles of the Higgs sector using ATLAS and CMS studies, as explained in section 2.2.3.

The constraints are gathered in different subgroups that we enumerate below.

3.4.2.1 *Heavy Higgs constraints*

Heavy Higgs constraints gather upper limits on processes involving either heavy scalar Higgs bosons [64, 65, 66, 67, 68, 24, 69, 70, 71, 72, 73], both heavy scalar and pseudoscalar Higgs bosons [74, 75, 76, 77] or pseudoscalar Higgs bosons only [78, 79].

Experimental upper limits are given in terms of production cross-section of a scalar or pseudoscalar Higgs boson times its branching ratio in a specific decay channel. As we have seen above, we choose not to use the *kappa trick* at high masses; then the theoretical value of the scalar and pseudoscalar production cross-sections in the 2HDM framework is obtained using `SusHi`. The branching ratios are obtained with `2HDMC`. We will therefore restrict ourselves to processes involving gluon fusion and $b\bar{b}$ production modes.

These analyses, and in particular the following three, will be useful to constrain the 2HDM parameter space in the case where $m_h = 125$ GeV:

- ATLAS study at 13 TeV with 36.1 fb^{-1} of the process $\sigma(gg \to H) \times BR(H \to ZZ)$ [24],
- ATLAS study at 13 TeV with 36.1 fb^{-1} of the process $\sigma(gg \to A) \times BR(A \to \tau\tau)$ [77],
- ATLAS study at 13 TeV with 36.1 fb^{-1} of the process $\sigma(gg \to A) \times BR(A \to Zh) \times BR(h \to b\bar{b})$ [79], with h the 2HDM light Higgs.

Note that, in the case where both the scalar H and the pseudoscalar A can contribute to the process under study, we compute the cross-section times branching ratio values for both particles and check if they are both below the observed upper limit. However if the masses of the two particles are separated by less than 10 GeV, we also compare the sum of their cross-section times branching ratio to the experimental upper limit at a mass $m = \frac{m_H + m_A}{2}$.

3.4.2.2 *Light Higgs constraints*

Light Higgs constraints gather upper limits on processes involving direct production of light scalars or pseudoscalars [80] or production of a pair of light scalars or pseudoscalars through the decay of a 125 GeV Higgs boson [81, 82, 83].

When gluon fusion or $b\bar{b}$ production mode of the light scalar or pseudoscalar Higgs boson is involved we use `SusHi` to compute the production cross-section. When VBF production is under study we use the *kappa trick* to obtain the cross-section. Moreover, when the light scalar or pseudo scalar is produced through the decay of a 125 GeV Higgs boson, production cross-sections of the latter is also computed using the *kappa trick*, regardless its production mode.

As for the heavy Higgs case, when both the scalar h and the pseudoscalar A can contribute to the same process and if their masses differ from less than 10 GeV, then their cross-sections times branching ratios are summed before being checked against the experimental upper limit.

As this set of constraints includes light pseudoscalar Higgs it can usefully constrain both $m_h = 125$ GeV and $m_H = 125$ GeV cases.

3.4.2.3 *Charged Higgs constraints*

Charged Higgs constraints gather upper limits on processes involving the production and decay of a charged Higgs boson. The analysis can be made for two distinct ranges of masses: light charged Higgs masses, *i.e.* $m_{H^\pm} < m_t \simeq 173$ GeV, and heavy charged Higgs masses, *i.e.* $m_{H^\pm} > m_t$.

In the low-mass region, the charged Higgs boson is mainly produced through the decay of

a top quark. Then the experimental upper limits are given in terms of a product of branching ratios:

$$BR(t \to H^+ b) \times BR(H^+ \to \tau\nu) \tag{3.42}$$

This product can easily be computed theoretically using `2HDMC`.

Note that, so far, the 8 TeV [84, 85] and 13 TeV [86] upper limits are still equivalent.

In the high-mass region the charged Higgs boson is produced essentially through associated production with a top quark:

$$pp \to tH^+\bar{b} + X \tag{3.43}$$

Hence, experimental upper limits are given in terms of charged Higgs production cross-section $\sigma(pp \to tH^+\bar{b})$ times branching ratio for the decay $H^+ \to t\bar{b}$ or $H^+ \to \tau\nu$ [87, 88, 86].

The branching ratios can be obtained with `2HDMC`. However we cannot use `SusHi` to compute the charged Higgs production cross-section as it is available only for neutral scalars or pseudoscalars. However the LHC Higgs Cross-Section Working Group (LHCHXSWG) provides a table containing the heavy charged Higgs production cross-section values at NLO for 2HDM Type II in the range $m_{H^\pm} \in [200; 2000]$ GeV and $\tan\beta \in [0.1; 60]$. Hence, using an interpolation, we can compute the cross-section production of a charged Higgs in 2HDM Type II for any mass and any $\tan\beta$ value included in the ranges mentioned above.

In order to compute this quantity in the three other 2HDM types we followed the prescription described in [89]. We outline the idea in the following.

In the 2HDM the coupling between a charged Higgs boson, a top quark and a bottom quark is as follows:

$$g^{\text{Type II}}_{t\bar{b}H^-} = \sqrt{2}\left(\frac{m_t}{v}P_R \cot\beta + \frac{m_b}{v}P_L \tan\beta\right) = g^{\text{Flipped}}_{t\bar{b}H^-} \tag{3.44}$$

$$g^{\text{Type I}}_{t\bar{b}H^-} = \sqrt{2}\left(\frac{m_t}{v}P_R \cot\beta - \frac{m_b}{v}P_L \cot\beta\right) = g^{\text{Lepton-Specific}}_{t\bar{b}H^-} \tag{3.45}$$

with $P_{R/L} = \frac{1\pm\gamma^5}{2}$ the chirality projectors. Then we deduce that the charged Higgs cross-section production through the process (3.43) will be exactly the same in Type II and in Flipped type.

Moreover, in Type II, the m_t and m_b terms are enhanced respectively by a factor $\cot\beta$ and $\tan\beta$, whereas in Type I and Lepton-Specific type m_t and m_b terms have are both enhanced by the same $\cot\beta$ factor. Hence, as $m_b \ll m_t$, we have:

$$g^{\text{Type I}}_{t\bar{b}H^-} = g^{\text{Lepton-Specific}}_{t\bar{b}H^-} \simeq \sqrt{2}\frac{m_t}{v}P_R \cot\beta \tag{3.46}$$

Then we can approximate the production cross-section of the charged Higgs boson as:

$$\begin{aligned}
\sigma^{\text{Type II}}(pp \to \bar{t}H^+b)_{|\tan\beta=1} &\propto 2\frac{m_t^2}{v^2} \\
\sigma^{\text{Type I, Lepton-Specific}}(pp \to \bar{t}H^+b) &\propto 2\frac{m_t^2}{v^2}\cot^2\beta \\
&\simeq \sigma^{\text{Type II}}(pp \to \bar{t}H^+b)_{|\tan\beta=1}\cot^2\beta
\end{aligned} \tag{3.47}$$

This means that the charged Higgs production cross-section in Type I and Lepton-Specific type for a given pair $(m_{H^+}, \tan\beta)$ is simply the charged Higgs production cross-section in Type II for a pair $(m_{H^+}, 1)$ rescaled by a factor $\cot^2\beta$.

Then, using the cross-section values given by the LHCHXSWG, we can easily compute the charged Higgs production cross-section for a 2HDM Type I and Lepton-Specific type, and hence compare theoretical cross-section times branching ratio to experimental upper limits in the four different 2HDM type frameworks.

4 Study of the light Higgs h – $m_H = 125$ GeV

4.1 Introduction

The goal of this chapter is to constrain the 2HDM parameter space under the hypothesis that the heavy scalar Higgs boson H is assimilated to the 125 GeV particle discovered at the LHC. Therefore, for this whole chapter, we fix $m_H = 125$ GeV.

In order to visualize the effect of the different constraints listed in chapter 3 we allow the six free parameters to vary in a given range, summarized in table 4.1 and then generate a large amount of random "points", each "point" corresponding to a set of fixed values for the six free parameters of the model.

m_h (GeV)	m_H (GeV)	m_A (GeV)	$m_{H^\pm}$ (GeV)	$s_{\beta-\alpha}$	$\tan\beta$	m_{12}^2 (GeV)^2
[2 ; 110]	125	[2 ; 1000]	[43 ; 1000]	[-1 ; 1]	[0.5 ; 60]	[-(2000)^2 ; +(2000)^2]

Table 4.1: Range of variation for the free parameters used in the analysis.

Once the set of points is generated we check, for each of them, if they pass the different constraints listed in section 3.3.

We will study the influence of the different types of constraint on the parameter space in section 4.2. Then we will examine more specifically the light Higgs boson h in light of two analyses perfomed by CMS [80, 90] and study its possible detection at the LHC.

Note that, as the results obtained in the Lepton-Specific and Flipped type frameworks are very similar to ones obtained in Type I and Type II respectively, the figures for these two cases will not be presented in the main text of this thesis but can be found in Appendix D.

4.2 Influence of the different constraints

4.2.1 Theoretical constraints

We have seen in section 3.3.1 that we need to impose stability, unitarity and perturbativity constraints.

These constraints have a direct influence on the parameters λ_i present in the Lagrangian of the $\mathbb{Z}_2$-basis, imposing both a lower and an upper bound on them. This property is illustrated in figure 4.1a where the generated points are plotted in the plane m_A vs λ_1. The random points passing the unitarity constraint are drawn in violet, the ones passing, in addition, the perturbativity constraint are drawn in red and the ones passing, in addition, the stability constraint are drawn in orange.

We can see that, if we apply the three constraints of unitarity, perturbativity and stability, the parameter λ_1 is restricted to values between 0 and 10. The four other λ_i are constrained

in a similar way.

We can also note that, although the generated points used in figure 4.1 are generated in the Type I framework, the constraints on the λ_i – and hence on the free parameters of the physical basis – coming from the theoretical constraints are exactly the same in the four different 2HDM types.

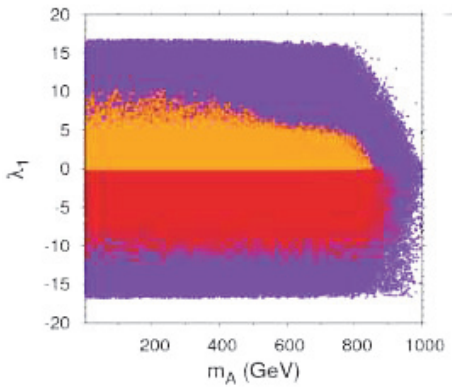

(A) Upper and lower bounds on λ_1 parameter due to the theoretical constraints.

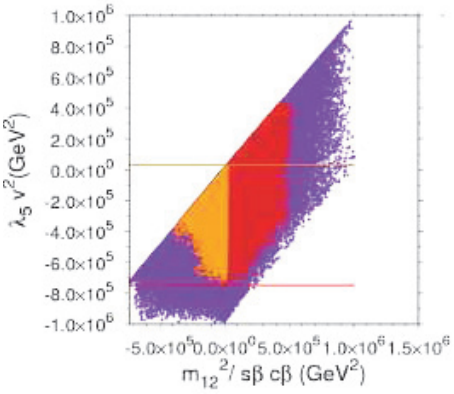

(B) Upper and lower bound on the $\bar{m}^2 \equiv \frac{m_{12}^2}{s_\beta c_\beta}$ parameter due to the theoretical constraints.

FIGURE 4.1: Theoretical constraints applied on the generated points. The points passing the unitarity constraint are drawn in violet, the ones passing, in addition, the perturbativity constraint are drawn in red and the ones passing, in addition, the stability constraint are drawn in orange.

The theoretical constraints also impose an upper bound on parameters m_A and $m_{H^\pm}$. In order to understand where this bound is coming from, we can look at figure 4.1b. The combination of the three theoretical constraints imposes an upper and a lower bound on $\bar{m}^2 = \frac{m_{12}^2}{s_\beta c_\beta}$. Moreover we have the following relations between the parameters of the physical basis and the $\mathbb{Z}_2$-basis:

$$m_A^2 = \bar{m}^2 - \lambda_5 v^2, \qquad m_{H^\pm}^2 = \bar{m}^2 - \frac{1}{2}v^2(\lambda_4 + \lambda_5), \qquad \bar{m}^2 = \frac{m_{12}^2}{s_\beta c_\beta} \tag{4.1}$$

As $\bar{m}^2$ is bounded from above – $\bar{m}^2 < 2.5\ 10^4$ GeV^2 – and λ_4 and λ_5 are bounded from below – $\lambda_4 v^2 > -1.4\ 10^6$ GeV^2 and $\lambda_5 v^2 > -7.5\ 10^5$ GeV^2 – hence m_A and $m_{H^\pm}$ are bounded from above. Using equation (4.1) and the estimate of the upper and lower bounds on $\bar{m}^2$, λ_4 and λ_5, one can find that $m_A < 880$ GeV and $m_{H^\pm} < 1000$ GeV, which is in agreement with the upper bounds visible on figure 4.2a.

Note that the lowest value allowed for $\bar{m}^2 - \lambda_5 v^2$ and $\bar{m}^2 - \frac{1}{2}v^2(\lambda_4 + \lambda_5)$ is negative; hence there is no lower bound on m_A and $m_{H^\pm}$.

One last effect of the theoretical constraints on the free parameters is the correlation which appears between m_A and $s_{\beta-\alpha}$ (see figure 4.2b). The highest m_A values are obtained for $|s_{\beta-\alpha}| \sim 0.7$.

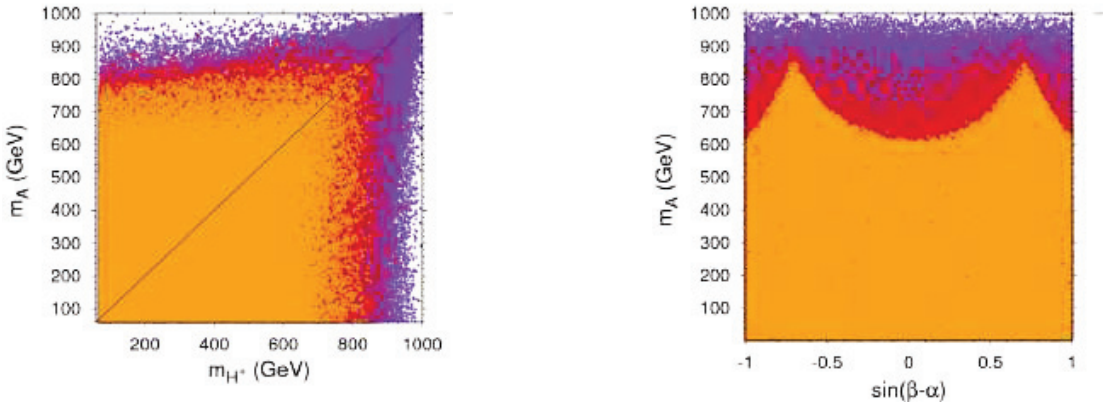

(A) Upper bounds on both m_A and $m_{H^\pm}$ due to the theoretical constraints.

(B) Correlation between m_A and $s_{\beta-\alpha}$ due to the theoretical constraints.

FIGURE 4.2: Theoretical constraints applied on the generated points. The color code is the same as in figure 4.1.

4.2.2 CONSTRAINTS FROM THE OBLIQUE PARAMETERS

In the following we will consider that all the generated points are at least passing the three theoretical constraints.

Enforcing oblique parameter constraints in the way described in section 3.3.2 has consequences on the generated points illustrated by figure 4.3. The points passing the theoretical constraints are drawn in pink and the points passing oblique parameter constraints are drawn in light blue. The solid black line corresponds to $m_{H^\pm} = m_A$.

Note that the points drawn in figure 4.3 have been generated in the Type I framework, but the results are exactly similar in the three other 2HDM types.

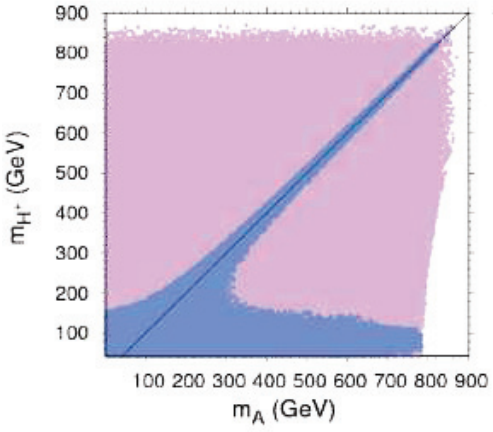

FIGURE 4.3: Influence of the oblique parameter constraints on the generated points in the plane $m_{H^\pm}$ vs m_A. The points passing the theoretical constraints are drawn in pink and the points passing, in addition, oblique parameter constraints are drawn in light blue. The solid black line corresponds to $m_{H^\pm} = m_A$. The oblique parameter constraints impose an important correlation between m_A and $m_{H^\pm}$.

We can see that oblique parameter constraints impose a strong correlation between the pseudoscalar mass m_A and the charged Higgs mass $m_{H^\pm}$. This is due to the T parameter which

is, as we have seen in section 3.3.2, sensitive to additional – heavy – particles in the Higgs sector. Hence, in order to keep the value of the T parameter around 0, the additional terms arising because of the presence of the pseudoscalar and the charged Higgs bosons need to cancel each other out, which is the case if the two particles have similar masses. This requirement is especially true when at least the charged Higgs boson is heavy but is relaxed when both the charged and pseudoscalar Higgs bosons are light.

4.2.3 Flavor constraints

First, in order to visualize the full influence of the flavor constraints, we will impose them on the random points passing the three theoretical constraints but not necessarily the oblique parameter constraints.

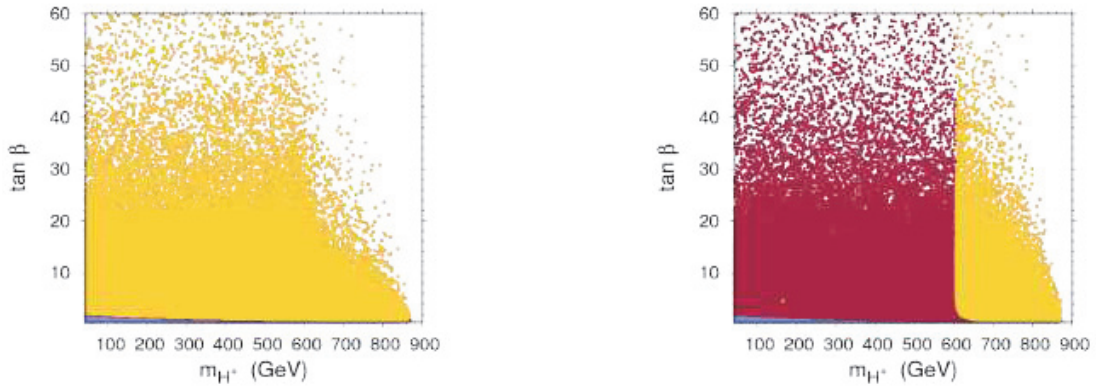

(A) Type I (B) Type II

FIGURE 4.4: Constraints due to flavor requirements in the plane $\tan\beta$ vs $m_{H^\pm}$. The points passing the theoretical constraints are drawn in pink, the ones passing, in addition, the isospin asymmetry constraint are drawn in light blue, the ones passing, in addition, the constraint on $BR(B_s \to \mu^+\mu^-)$ are drawn in dark red and the ones passing, in addition, the constraint on $BR(\bar{B} \to X_s\gamma)$ are drawn in yellow.

Contrary to the theoretical and oblique parameter constraints the influence of the flavor bounds on the parameter space will greatly depend on the 2HDM type considered. The results are drawn in the plane $\tan\beta$ vs $m_{H^\pm}$ in figure 4.4a for the Type I framework and figure 4.4b for the Type II framework. The figures illustrating the results for Flipped type and Lepton-Specific type can be found in Appendix D, in figures D.1a and D.1b respectively.

The points passing the theoretical constraints are drawn in pink, the ones passing, in addition, the isospin asymmetry constraint are drawn in light blue, the ones passing, in addition, the constraint on $BR(B_s \to \mu^+\mu^-)$ are drawn in dark red and the ones passing, in addition, the constraint on $BR(\bar{B} \to X_s\gamma)$ are drawn in yellow.

In Type I and Lepton-Specific type frameworks the flavor constraints have a very small influence on the available parameter space. They essentially impose a lower bound on $\tan\beta$ going from $\tan\beta_{min} \sim 0.6$ at high $m_{H^\pm}$ to $\tan\beta_{min} \sim 2$ at low $m_{H^\pm}$, but the rejected region is very small.

In Type II and Flipped type frameworks the constraint on $BR(B_s \to \mu^+\mu^-)$ rules out the low $\tan\beta$ values as in Type I and Lepton-Specific type; however the constraint on $BR(\bar{B} \to X_s\gamma)$ imposes a very strong constraint on $m_{H^\pm}$: the charged Higgs mass is bounded from below and,

for almost all $\tan\beta$ values, this lower bound is $m_{H^\pm,min} \simeq 610$ GeV.

The lower bound we obtain is higher than the one determined in [91], in which it is evaluated to $m_{H^\pm,min} = 583$ GeV for $\tan\beta > 2$ but it is coherent with the bound found in [92]. Note that this lower bound strongly depends on the evaluation of the theoretical uncertainties, which explains the discrepancy between the different papers.

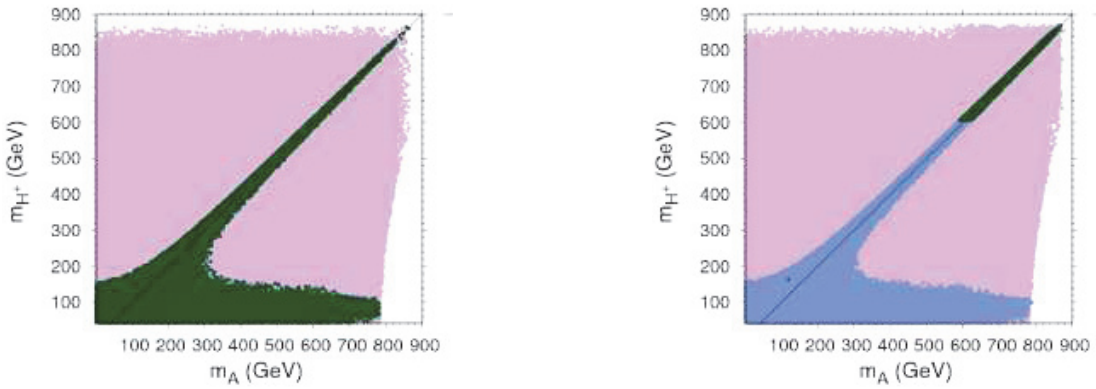

(A) Type I (B) Type II

FIGURE 4.5: Constraints on the parameter space due to theoretical, oblique parameter and flavor constraints. The points passing theoretical constraints are drawn in violet, the ones passing, in addition, oblique parameter constraints are drawn in light blue, and the ones passing, in addition, flavor constraints are drawn in dark green.

We show in figure 4.5 (and in Appendix figure D.2) the influence of the flavor constraints together with the theoretical constraints and the oblique parameter constraints.

In these figures the points passing theoretical constraints are drawn in pink, the ones passing, in addition, oblique parameter constraints are drawn in light blue and the ones passing, in addition, flavor constraints are drawn in dark green.

We can see that, in Type II and Flipped type, due to the correlation between m_A and $m_{H^\pm}$ imposed by the oblique parameter constraints, the application of both oblique parameter and flavor constraints imposes a lower bound on m_A of around 590 GeV. Hence in these two frameworks the pseudoscalar and charged Higgs masses are greatly constrained.

4.2.4 LEP CONSTRAINTS

LEP analyses [56, 93] have ruled out possible charged Higgs bosons with masses between 43 GeV $< m_{H^\pm} <$ 80 GeV in a 2HDM Type II framework and 43 GeV $< m_{H^\pm} <$ 72.5 GeV if $m_A > 12$ GeV in a 2HDM Type I framework. However these analyses had been made with the assumption that there were no neutral scalar Higgs boson with a mass below 82 GeV. Indeed the LEP excluded the possibility of such light neutral scalar Higgs boson in the SM framework but in other frameworks, such as a 2HDM with the heavy Higgs H assimilated with the 125 GeV Higgs boson, we will see that one can have a neutral scalar Higgs boson with mass $m_h < 82$ GeV which passes LEP constraints. Hence, the above lower bounds will not apply in this specific chapter.

First, in order to see the effect of LEP constraints on the parameter space, we will consider the set of points passing the theoretical constraints and check if they also pass LEP constraints.

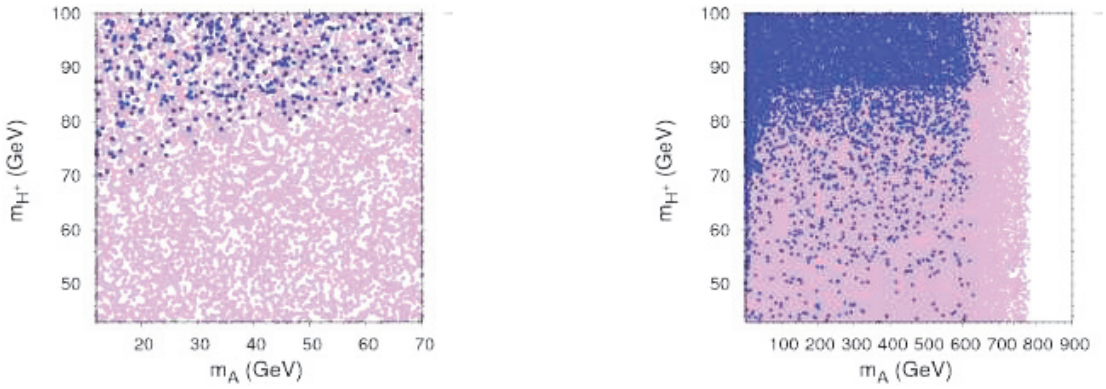

(A) Type I, $m_h > 83$ GeV.

(B) Type I, generic case.

FIGURE 4.6: Constraints on the parameter space due to LEP constraints. The points passing theoretical constraints are drawn in violet and the ones passing, in addition, LEP constraints, are drawn in blue.

The results are presented in figures 4.6a and 4.6b for 2HDM Type I. As LEP constraints at low $m_{H^\pm}$ are not relevant in Type II because this range of mass is already ruled out by flavor constraints, the results for Type II are only given in Appendix D (see figure D.3). In these figures the points passing theoretical constraints are drawn in violet and those passing, in addition, LEP constraints are drawn in blue.

In the left panel of figure 4.6 we follow reference [56] and hence require that the blue points check also the condition $m_h > 82$ GeV. Furthermore we focus on the region 12 GeV $< m_A <$ 70 GeV corresponding to the mass range used in [56]. In the right panel of figure 4.6, there is no mass restriction on the light scalar.

With the restriction $m_h > 82$ GeV on the light scalar mass the lower bound on $m_{H^\pm}$ obtained after the enforcement of LEP constraints is coherent with the LEP results [56] reminded at the beginning of this section. However, when this restriction is removed (see figure 4.6b) the LEP lower bound on $m_{H^\pm}$ is no longer valid.

Hence, in the case of a 2HDM Type I or Lepton-Specific type, it is important to notice that, under the assumption that $m_H = 125$ GeV, the limit given by LEP on the charged Higgs mass is not valid and that we need to take into account possible charged Higgs bosons with masses below 72.5 GeV. However, as there is no LEP analysis studying charged Higgs bosons with mass below 43 GeV we decided to impose in our study $m_{H^\pm} > 43$ GeV (see table 4.1) even though this last condition is not fully general.

When applying all the constraints up to LEP ones, the parameter space is greatly reduced. This is illustrated in figures 4.7 and 4.9 (and in Appendix D, figures D.4 and D.6) where green points pass theoretical, oblique parameter and flavor constraints and blue, red and orange points pass LEP constraints.

In figures 4.7 and D.4 one can see that important parts of the plane m_h vs $s_{\beta-\alpha}$ are now excluded, even though the full range of both m_h and $s_{\beta-\alpha}$ is still available in Type I and Lepton-Specific type. In Type II and Flipped type, the restriction is even better as the allowed range of $s_{\beta-\alpha}$ is reduced by LEP constraints.

In figure 4.9 and D.6 one can see that the area passing LEP constraints in the plane $m_{H^\pm}$ vs m_A is even more restricted, especially in Type I and Lepton-Specific type with the apparition of a lower bound on $m_{H^\pm}$ around 85 GeV for $m_A > 120$ GeV.

4.2.5 LHC constraints on 125 GeV Higgs boson

Now we look at the influence of the LHC 125 GeV Higgs boson constraints.

In the figures below, the points passing theoretical, oblique parameter and flavor constraints are drawn in green, the ones passing, in addition, LEP constraints, are drawn in blue, the ones passing, in addition, the 125 GeV Higgs constraints from 8 TeV data are drawn in red and the ones passing, in addition, the 125 GeV Higgs constraints from 13 TeV data are drawn in orange. Therefore, the most constrained points are those in orange.

We show the results in the plane m_h vs $s_{\beta-\alpha}$ in figures 4.7 and D.4, in the plane m_A vs $s_{\beta-\alpha}$ in figures 4.8 and D.5 and in the plane $m_{H^\pm}$ vs m_A in figures 4.9 and D.6.

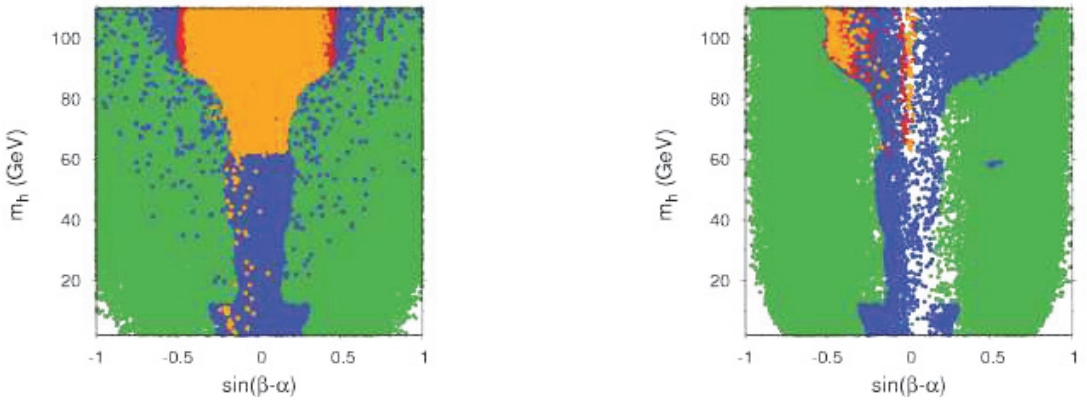

(A) Type I (B) Type II

FIGURE 4.7: Constraints on the parameter space due to LHC constraints. The points passing theoretical, oblique parameter and flavor constraints are drawn in green. The ones passing, in addition, LEP constraints, are drawn in blue. The ones passing, in addition, the 125 GeV Higgs constraints at 8 TeV are drawn in red and the ones passing, in addition, the 125 GeV Higgs constraints at 13 TeV, are drawn in orange.

We can see in figure 4.7 that the range of the $s_{\beta-\alpha}$ parameter is greatly reduced by the 125 GeV Higgs constraints. These constraints impose $s_{\beta-\alpha} \in [-0.5; 0.5]$ in Type I and $s_{\beta-\alpha} \in [-0.4; 0.25]$ in Lepton-Specific type. In Type II and Flipped type the positive values of $s_{\beta-\alpha}$ are almost entirely ruled out and $s_{\beta-\alpha} \in [-0.55; 0.05]$.

Moreover we can see that very few points with $m_h < 62.5$ GeV pass the 125 GeV Higgs constraints. This is due to the fact that the decay channel $H \to hh$ is open for $m_h < 62.5$ GeV, which contributes to the signal strength computation (see equation (3.37)). Hence, the signal strength value moves away from the SM expectation value, increasing the log-likelihood. This increase is too important to be counterbalanced by the increase of the upper bound $b_n^{2\sigma}$ due to the additional degree of freedom gained by the chi-squared function. This explains why most of the points in this area are ruled out by the 125 GeV Higgs constraints.

Note that, in the Type II case, as very few generated points pass LHC 125 GeV Higgs constraints, the apparent lower bound on m_h can be due to a lack of statistics, thus, with a finer scan, some points with $m_h < 62.5$ GeV may be able to pass these constraints.

The same phenomenon happens for the pseudoscalar in Type I and Lepton-Specific type, illustrated by figures 4.8a and D.5. Once again, for $m_A < 62.5$ GeV, the decay $H \to AA$ is possible. For the same reasons as in the light scalar case, most of the points with $m_A < 62.5$ GeV

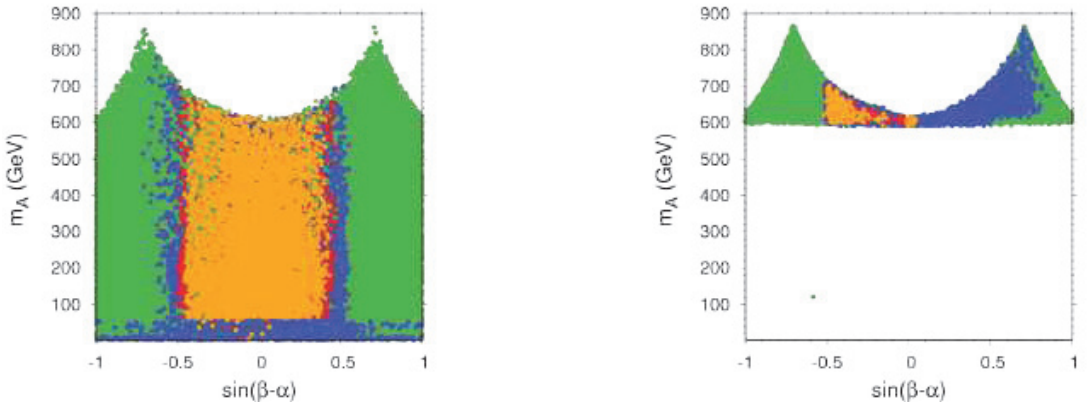

(A) Type I (B) Type II

FIGURE 4.8: Constraints on the parameter space due to LHC constraints. The color code is the same as in figure 4.7.

are hence excluded.

We can also see that, due to the 125 GeV Higgs constraints on the parameter $s_{\beta-\alpha}$ and the particular shape of the allowed points in the plane m_A vs $s_{\beta-\alpha}$ due to theoretical constraints, m_A has an upper bound around 700 GeV in Type I, 720 GeV in Type II and Flipped type and 550 GeV in Lepton-Specific type. Moreover, if future and more constraining results on 125 GeV Higgs bosons stay around SM values, then the allowed range of $s_{\beta-\alpha}$ will be even more reduced near 0, leading to the lowering of the upper bound on m_A. This can be particularly interesting in the case of Type II and Flipped type as the allowed range for m_A is already considerably reduced.

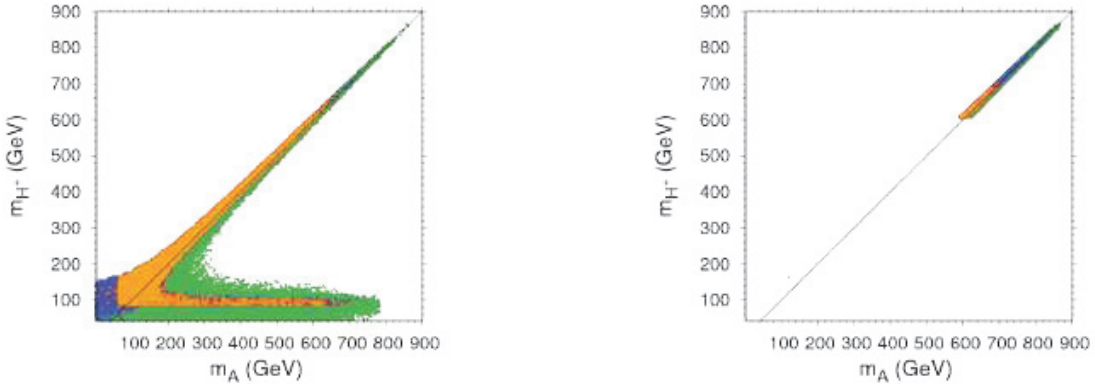

(A) Type I (B) Type II

FIGURE 4.9: Constraints on the parameter space due to LHC constraints. The color code is the same as in figure 4.7.

We can also note that the upper bound on m_A also leads to an upper bound on $m_{H^\pm}$ as the two masses are strongly correlated (see figure 4.9 and D.6).

4.2.6 LHC constraints on other hypothetical scalars

We have listed in section 3.4.2 the different constraints on other hypothetical scalars we considered. We will briefly summarize the consequences of each set of constraints.

4.2.6.1 *Heavy Higgs constraints*

The only analysis involving a neutral scalar or pseudoscalar able to constrain the generated points is the ATLAS analysis at 13 TeV giving an upper limit on the process $gg \to A \to Zh_{125} \to Zb\bar{b}$ [79] – with, in this chapter, $h_{125} = H$. In figures 4.10 and D.7 the generated points passing all the constraints up to 125 GeV Higgs constraints at 13 GeV are drawn in orange against the observed upper limit (solid black line). The points passing heavy Higgs constraints are drawn in violet.

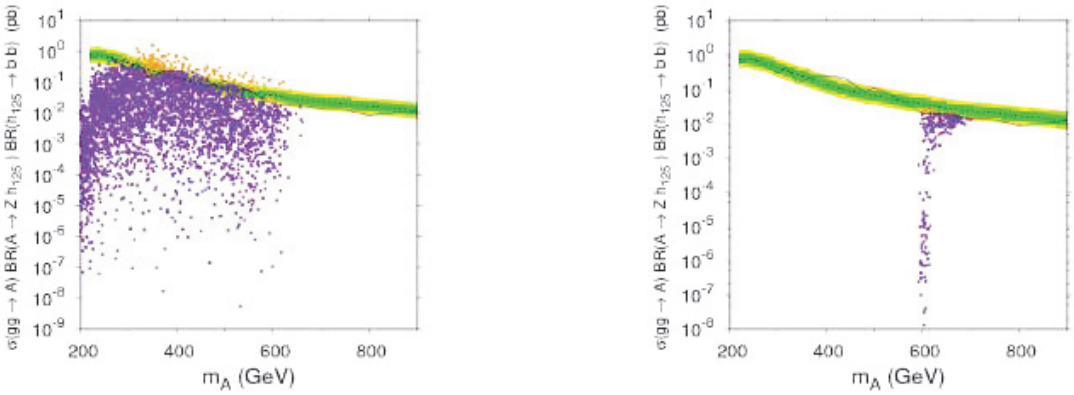

(A) Type I (B) Type II

FIGURE 4.10: Comparison between the generated 2HDM points passing all the constraints up to 125 GeV Higgs boson constraints at 13 TeV (orange points) and the observed upper limit on the process $gg \to A \to Zh_{125} \to Zb\bar{b}$ at 13 TeV [79] (solid black line). The points also passing heavy Higgs constraints are drawn in violet.

The constraint essentially excludes points with low $\tan\beta$ in both Type I and Type II (see figures 4.11 and D.8). If this behavior is not theoretically obvious in Type I, it is easier to understand in the Type II case: considering C_{bb} given in equation (3.33) and knowing that the available $s_{\beta-\alpha}$ values are mainly negative, C_{bb} – and consequently the decay width – is enhanced for low values of $\tan\beta$, leading to an enhancement of the exclusion in the low $\tan\beta$ region.

4.2.6.2 *Light Higgs constraints*

Here we briefly mention the light Higgs constraints, knowing that we focus here only on the processes involving the production of a pair of light scalar or pseudoscalar Higgs bosons. The analyses implying the direct production of light scalar or pseudoscalar Higgs bosons [80, 90] will be used in a more detailed study developped in section 4.3.

For the moment the observed upper limits provided by the ATLAS and CMS collaborations are far from being able to constrain the 2HDM-generated points. Hence we will not elaborate any further on these constraints.

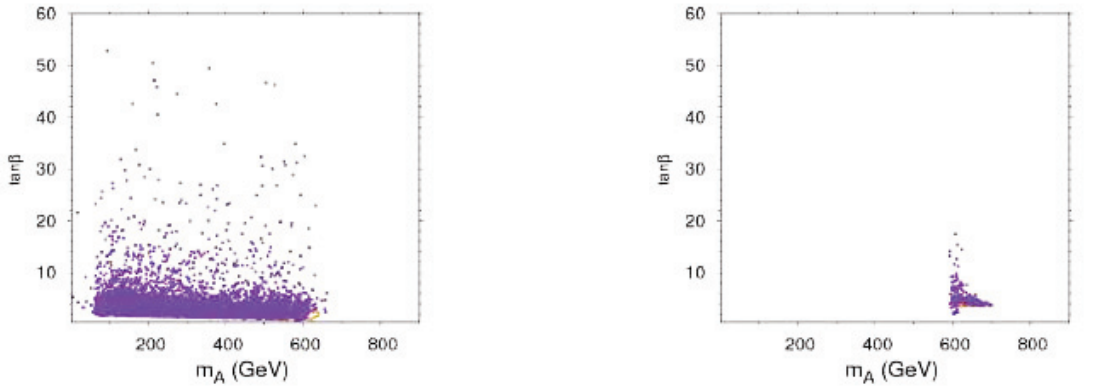

(A) Type I (B) Type II

FIGURE 4.11: Constraints on the parameter space due to heavy Higgs constraints. Same color code as in figure 4.10.

4.2.6.3 *Charged Higgs constraints*

The charged Higgs constraints are split into two categories: one where the search is performed at low $m_{H^\pm}$ and one where the search is done for high $m_{H^\pm}$ – respectively below and above the top mass. Note that, as low $m_{H^\pm}$ values are ruled out by flavor constraints in Type II and Flipped type frameworks, the first category of analyses cannot constrain them.

The three analyses at low $m_{H^\pm}$ [84, 85, 86] allow the suppression of a great number of generated points. Figures 4.12a and D.9a show the generated points passing all the constraints up to 125 GeV Higgs constraints at 13 TeV in orange together with the more constraining experimental upper limit, that is, the one given by CMS with 8 TeV data [85] (solid black line). Points passing, in addition, all the charged Higgs constraints, are drawn in light blue.

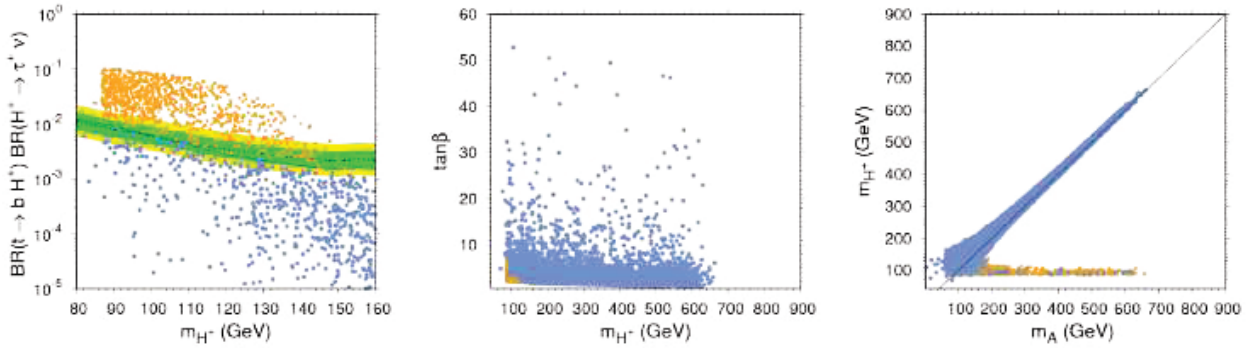

(A) Comparison between the 2HDM points generated in Type I framework and the observed upper limit on the process $t \to bH^+ \to b\tau\nu_\tau$ at 8 TeV [85] (solid black line).

(B) Consequences of the charged Higgs constraints in the plane $m_{H^\pm}$ vs $\tan\beta$.

(C) Consequences of the charged Higgs constraints in the plane $m_{H^\pm}$ vs m_A.

FIGURE 4.12: Charged Higgs constraints in the 2HDM Type I framework. The points passing all the implemented constraints up to the LHC 125 GeV Higgs boson constraints at 13 TeV are drawn in orange and the points passing, in addition, all the charged Higgs constraints are drawn in light blue.

In 2HDM Type I and Lepton-Specific type, the points suppressed by the low-mass charged

Higgs constraints have mainly low $\tan\beta$ values (see figures 4.12b and D.9b). Indeed the couplings of charged Higgs bosons to t and b quarks and to τ and ν_τ are both proportional to $\cot\beta$ in Type I and Lepton-Specific type (see equation (3.45)). Hence, the process $t \to bH^+ \to b\tau\nu_\tau$ is enhanced by low $\tan\beta$ values.

Light charged Higgs constraints also have an influence on available m_A values. Figures 4.12c and D.9c show the generated points in the plane $m_{H^\pm}$ vs m_A with the same color code as figure 4.12a. We can see in these plots that, in Type I, as many points with low $m_{H^\pm}$ are ruled out, the "lower leg" visible for 43 GeV $< m_{H^\pm} <$ 150 GeV is depopulated. This effect is even more visible for Lepton-Specific type. Hence, when upper limits on the process $t \to bH^+ \to b\tau\nu_\tau$ improve, we should be able to rule out the entire lower leg.

For the moment the analyses at high $m_{H^\pm}$ are still far from being able to constrain 2HDM parameter space. Hence, if charged Higgs constraints have consequences in Type I and Lepton-Specific type using the low-mass analyses, they have no influence at all on Type II and Flipped type frameworks.

4.2.6.4 *Summary on the LHC constraints on other scalars*

In order to illustrate the consequences on the 2HDM parameter space of the enforcement of the constraints listed in section 3.4.2 and described individually above, we drew the generated points in different planes. In these figures (figures 4.13, 4.14, D.10 and D.11) the points passing all the constraints up to 125 GeV Higgs boson at 13 TeV are drawn in orange and the ones passing, in addition, the LHC constraints on other scalars are drawn in dark green.

The whole parameter space is greatly reduced compared to the one we implemented initially (see table 4.1). We can then define the range of variation for the 2HDM free parameters still allowed by the constraints we imposed. They are summarized in table 4.2. The values written in red correspond to bounds that have been modified with respect to table 4.1 due to the application of the constraints.

Note that light scalars and pseudoscalars below 62.5 GeV are almost entirely ruled out by LHC constraints on 125 GeV Higgs bosons. Updates on 13 TeV data, especially with the publication of log-likelihood exclusion limits for WW, bb and $\tau\tau$ decay channels may constrain this region and even more maybe rule it out entirely.

	m_h (GeV)	m_H (GeV)	m_A (GeV)	$m_{H^\pm}$ (GeV)	$s_{\beta-\alpha}$	$\tan\beta$	m_{12}^2 (GeV)^2
Type I	[2 ; 110]	125	[2 ; 700]	[43 ; 700]	[-0.5 ; 0.5]	[0.5 ; 60]	[-(400)^2 ; +(150)^2]
Type II	[2 ; 110]	125	[580 ; 710]	[610 ; 720]	[-0.55 ; 0.05]	[0.5 ; 60]	[-(80)^2 ; +(100)^2]
Flipped	[2 ; 110]	125	[580 ; 700]	[610 ; 720]	[-0.5 ; 0.05]	[0.5 ; 60]	[-(80)^2 ; +(80)^2]
Lepton-Specific	[2 ; 110]	125	[2 ; 650]	[43 ; 650]	[-0.35 ; 0.2]	[0.5 ; 60]	[-(400)^2 ; +(150)^2]

TABLE 4.2: Reduced range of variation for the free parameters obtained after enforcing the constraints.

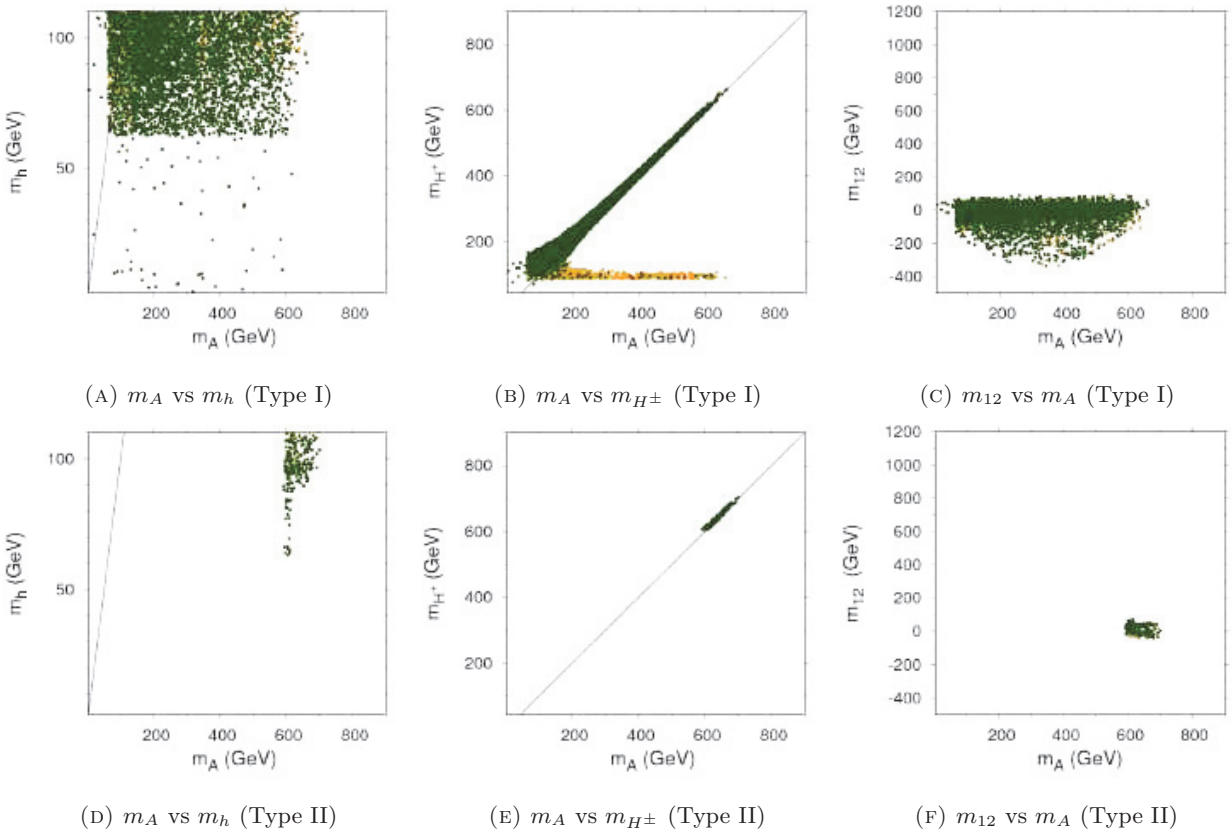

(A) m_A vs m_h (Type I) (B) m_A vs $m_{H^\pm}$ (Type I) (C) m_{12} vs m_A (Type I)

(D) m_A vs m_h (Type II) (E) m_A vs $m_{H^\pm}$ (Type II) (F) m_{12} vs m_A (Type II)

FIGURE 4.13: Points passing all the constraints up to 125 GeV Higgs constraints at 13 TeV (orange) and points passing, in addition, the LHC constraints on other hypothetical scalars (green) in different planes in the Type I (upper panel) and Type II (lower panel) frameworks.

4.3 STUDY OF A LIGHT NEUTRAL SCALAR h

Most research on additional neutral scalars is made in the heavy-mass range, *i.e.* at masses above 125 GeV. The search for a possible light Higgs with a mass below 125 GeV has lost its appeal since the ruling-out of SM Higgs bosons below 107.9 GeV by LEP [18]. However, as we have seen above, if the light scalar under study does not have the same couplings as those of the SM Higgs boson, it can easily pass LEP constraints. Hence, models such as 2HDM with H assimilated to the 125 GeV Higgs boson and h a light Higgs of unknown mass, are still viable.

One important question remains. If the model with a light Higgs boson h is not ruled out, would it be possible to detect this light particle at LHC or would it be totally out of reach?

We answered this question in a previous paper [94] based on a CMS study of a possible light resonance in the diphoton decay channel at 8 TeV [80]. As the same analysis using 13 TeV data has been published since then [90] this question will be answered in this thesis using these two analyses.

The CMS analysis at 13 TeV [90] presents a small local excess of 2.9 σ around 95.3 GeV. Even though the excess is very small, it can be the hint of the presence of a new particle with

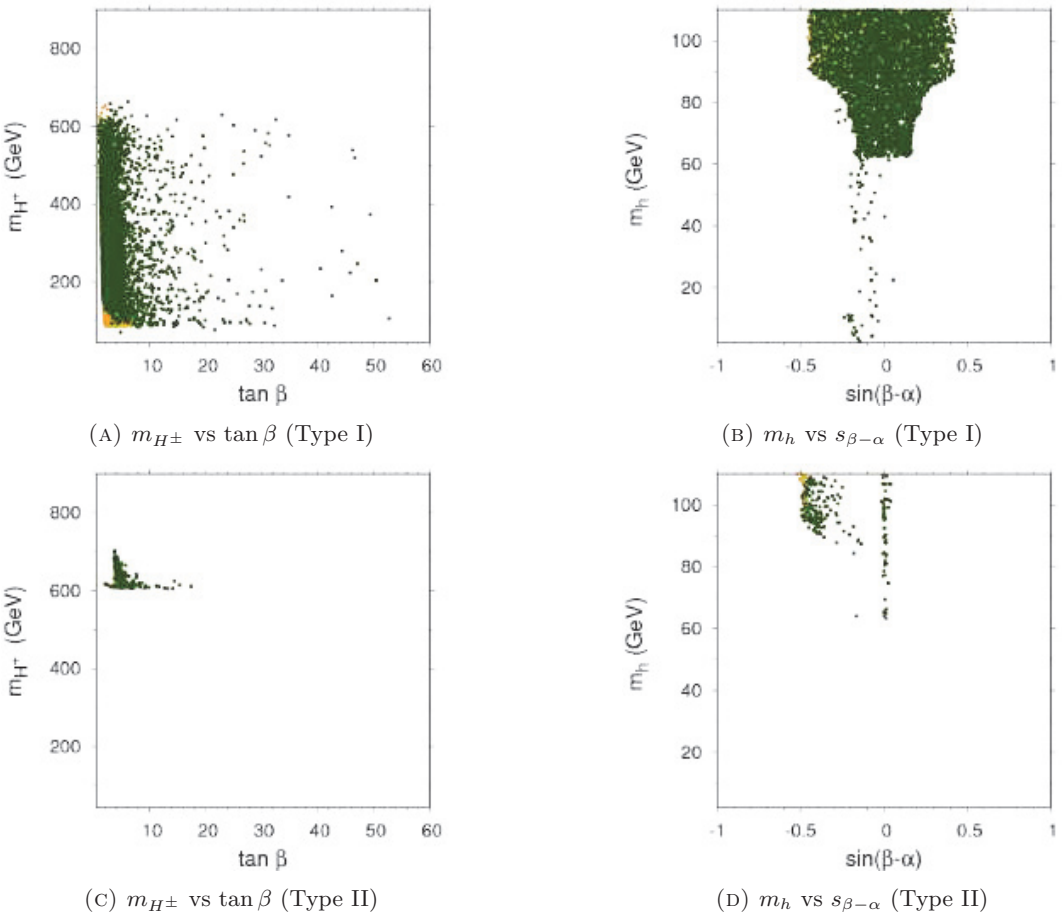

(A) $m_{H^\pm}$ vs $\tan\beta$ (Type I)

(B) m_h vs $s_{\beta-\alpha}$ (Type I)

(C) $m_{H^\pm}$ vs $\tan\beta$ (Type II)

(D) m_h vs $s_{\beta-\alpha}$ (Type II)

FIGURE 4.14: Same as figure 4.13.

mass $m_h \approx 95.3$ GeV decaying into two photons. Hence I will assume in a second analysis that this excess corresponds to a light scalar particle and will study the possibility that a 2HDM light Higgs h is able to explain such an excess.

4.3.1 Search for a possible resonance in the $\gamma\gamma$ decay channel

In this section we study the possibility that a 2HDM light Higgs boson h may be detected at LHC. For this, we used CMS analyses on a light scalar with mass between 70 GeV and 110 GeV decaying into two photons based on 8 TeV data [80] and 13 TeV data [90].

The CMS analyses provide upper limits on cross-section times branching ratio in $ggH + ttH$ production mode and $VBF + VH$ production mode, both in diphoton decay channel. We then need to compute the cross-section of the light Higgs boson h in the 2HDM framework for these two production modes.

The SM cross-section production of a Higgs in ttH production mode is around two orders of magnitude lower than the one in ggH production mode. Moreover the scaling factor κ_t of the light Higgs h cannot compensate the difference in a 2HDM: indeed it is approximately $\cot\beta$ (see equation (3.32)), whose value is bounded from above due to flavor constraints ($\cot\beta < 1.7$,

see section 4.2.3). Then the 2HDM production cross-section in tth production mode can be neglected compared to the one in ggH production mode.

The cross-section in ggH production mode is computed with `SusHi` and the one in $VBF + VH$ production mode is computed using the *kappa trick* (see right formula of equation (3.40)).

Using the set of random points generated for the study developped in section 4.2, we found that the cross-section times branching ratio in both Type II, Flipped type and Lepton-Specific type frameworks are extremely low compared to the CMS upper limit in both ggH and $VBF + VH$ production modes, and this for both 8 TeV and 13 TeV cases (see figures D.12, D.13 and D.14). Therefore **we will only study 2HDM Type I in the following**.

We generated a new set of random points using the bounds on the free parameters found in the analysis performed in section 4.2 and imposed in addition the restriction $m_h \in [70\ ;\ 110]$ GeV in order to stay within the mass range studied by CMS.

We study two different cases: a generic one, which we call the *general case*, where the only restrictions on the free parameters are the ones found in the previous study, and a second one where the light scalar h and the pseudoscalar A are assumed to be degenerate. In this latter case, the pseudoscalar's mass is allowed to vary within the interval $[m_h - 0.5\ ;\ m_h + 0.5]$ GeV.

The available range of variation for the 2HDM free parameters are recalled in tables 4.3 and 4.4 for the general case and the degenerate case respectively. Note that, due to the restriction on the range of variation of m_A and the correlation between m_A and $m_{H^\pm}$ because of the oblique parameters, the upper bound on $m_{H^\pm}$ in the degenerate case is lower than in the general case (see middle panel of figure 4.13 for instance).

m_h (GeV)	m_H (GeV)	m_A (GeV)	$m_{H^\pm}$ (GeV)	$s_{\beta-\alpha}$	$\tan\beta$	m_{12}^2 (GeV)^2
[70 ; 110]	125	[2 ; 700]	[43 ; 700]	[-0.5 ; 0.5]	[0.5 ; 60]	[-(400)^2 ; +(150)^2]

TABLE 4.3: Reduced range of variation of the 2HDM free parameters used in the general case.

m_h (GeV)	m_H (GeV)	m_A (GeV)	$m_{H^\pm}$ (GeV)	$s_{\beta-\alpha}$	$\tan\beta$	m_{12}^2 (GeV)^2
[70 ; 110]	125	$[m_h - 0.5\ ;\ m_h + 0.5]$	[43 ; 220]	[-0.5 ; 0.5]	[0.5 ; 60]	[-(400)^2 ; +(150)^2]

TABLE 4.4: Reduced range of variation of the 2HDM free parameters used in the degenerate case.

One can find the detailed results for 8 TeV data in [94]. As the main difference between the analyses at 8 TeV and 13 TeV is that the 2HDM cross-section times branching ratio is higher and that the experimental limit is slightly lower in the 13 TeV case than in the 8 TeV case, we will show here only the results for 13 TeV data.

In the following figures the generated points passing all the constraints we implemented are drawn in dark green and the ones passing, in addition, the CMS light Higgs constraints at both 8 TeV and 13 TeV are drawn in pink.

4.3.1.1 *General case*

We present in this section the results obtained using the general scan (see table 4.3 for details on the allowed range for the 2HDM free parameters).

The generated points drawn against the experimental upper limit on $\sigma_{gg\to s} \times BR_{s\to\gamma\gamma}$, $s = \{h,\ A\}$, and $\sigma_{VBF,VH\to h} \times BR_{h\to\gamma\gamma}$ are shown in figures 4.15a, 4.15b and 4.15c respec-

tively.

Note that, as the 2HDM pseudoscalar A does not have tree-level coupling to W^+W^- nor Z^0Z^0 we consider that the A production through $VBF + VH$ production is negligible. Hence only the light scalar h will be studied in the $VBF + VH$ production case.

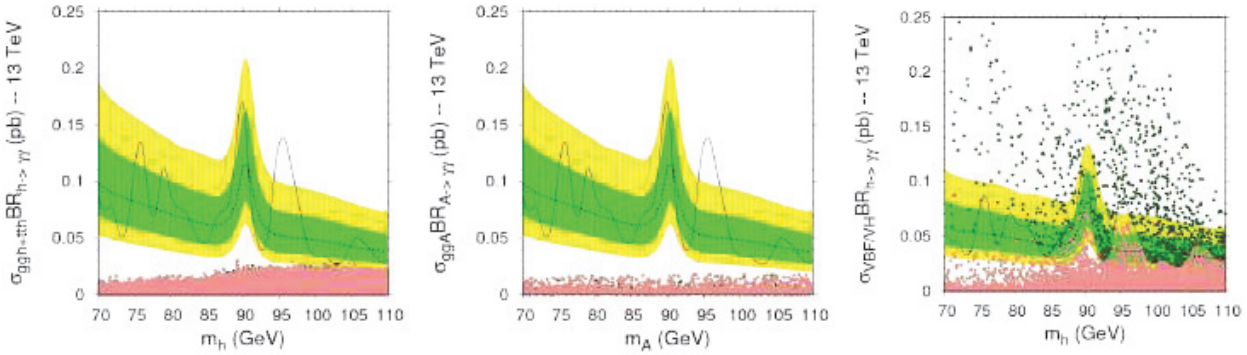

(A) Light h case in gluon fusion production mode.

(B) Light A case in gluon fusion production mode.

(C) Light h case in $VBF + VH$ production mode.

FIGURE 4.15: Comparison between the generated 2HDM points and the observed upper limit on the process $pp \to h/A \to \gamma\gamma$ at 13 TeV [90] (solid black line). The points passing all the implemented constraints are drawn in dark green, the ones passing in addition CMS light Higgs constraints at both 8 TeV and 13 TeV are drawn in pink.

Looking first at figures 4.15a and 4.15b we can see that the production cross-section in gluon fusion times branching ratio is higher in the h case than the A case. Moreover the generated points passing all the constraints we implemented are very close to the observed upper limit obtained in the gluon fusion production mode. First, this means that, if a light Higgs similar to a 2HDM h in Type I actually exists, then it begins to reach the sensitivity of the CMS detector and thus could be detected. This also means that, if no excess is observed, then the analysis in gluon fusion production mode is close to be able to constrain the 2HDM parameter space. These two positive conclusions are a real improvement compared to the ones obtained using only 8 TeV data [94].

Also note that, although the production cross-section times branching ratio of the pseudoscalar A is closer to the 13 TeV upper limit than to the 8 TeV one [94], it is still too low to hope for a possible detection by the CMS detector.

Turning now to the $VBF + VH$ production mode (see figure 4.15c) we can see that the CMS detector is already fully sensitive to a possible light 2HDM Higgs boson h. Once again, this can lead to a potential discovery if such a light particle exists and, if not, it leads to the deletion of a great number of generated points.

Considering that the analyses do not present any excess, we can use the observed upper limit to constrain the 2HDM generated points. This leads to a small restriction in the plane $\tan\beta$ vs $s_{\beta-\alpha}$ and m_{12} vs $s_{\beta-\alpha}$ (see figure 4.16).

Moreover, for some parameters we can identify ranges where the cross-section times branching ratio is higher than in other regions. Note that, as A is not yet reachable by the CMS detector, we will only look at the light scalar h cross-section times BR.

First of all, there is no privileged value of m_A nor $m_{H^\pm}$ where the cross-section times branching ratio values are higher than elsewhere, and this for both gluon fusion and $VBF + VH$ production modes. However this is not the case for the three other free parameters $s_{\beta-\alpha}$, $\tan\beta$

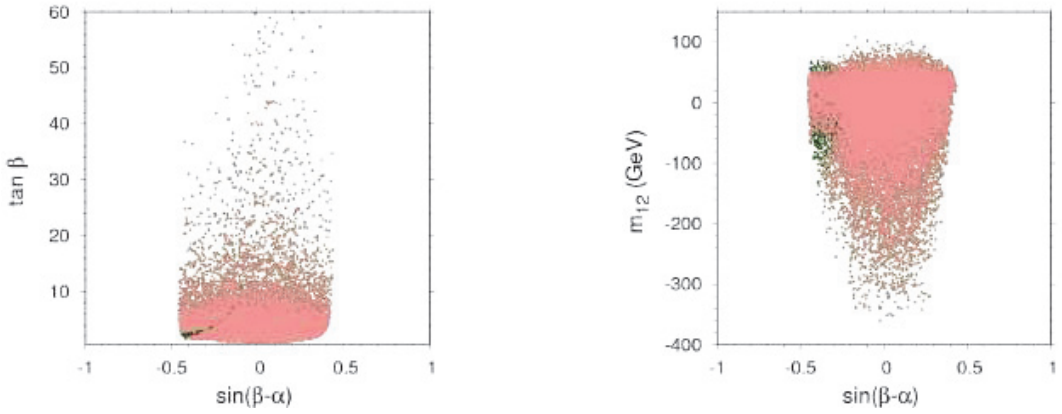

(A) $\tan\beta$ vs $s_{\beta-\alpha}$. (B) m_{12} vs $s_{\beta-\alpha}$.

FIGURE 4.16: Restriction of the parameter space due to the CMS light Higgs constraints in the general case. Same color code as in figure 4.15.

and m_{12}.

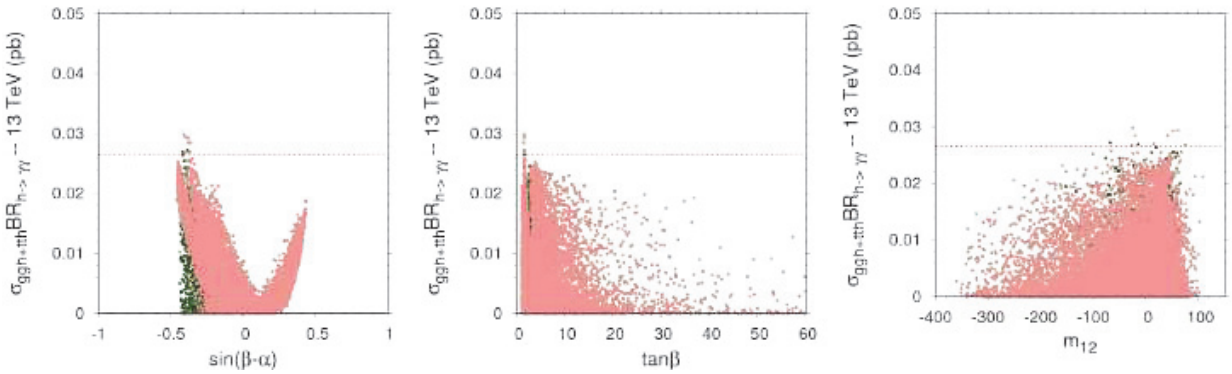

(A) Influence of $s_{\beta-\alpha}$. (B) Influence of $\tan\beta$. (C) Influence of m_{12}.

FIGURE 4.17: Value of $\sigma_{gg\to h} \times BR_{h\to\gamma\gamma}$ at 13 TeV as a function of different 2HDM free parameters in the general case. The dashed red line corresponds to the lowest value of the observed upper limit in gluon fusion production mode. The color code is the same as in figure 4.15.

Figures 4.17 and 4.18 show the cross-section times branching ratio values, for gluon fusion and $VBF+VH$ production mode respectively, of the generated points depending on $s_{\beta-\alpha}$ (left panel), $\tan\beta$ (middle panel) and m_{12} (right panel). The color code is the same as the one in figure 4.15. The dashed red line corresponds to the lowest $\sigma \times BR$ value of the observed upper limit. Hence, although the points above this line are not systematically excluded by CMS analysis, the line can nevertheless be used as a landmark representing a very rough approximation of the observed upper limit.

We can clearly see that the high values of $\sigma \times BR$ are obtained for specific ranges of both $s_{\beta-\alpha}$, $\tan\beta$ and m_{12}. These regions are more pronounced in the case of the $VBF + VH$ production mode.

We will come back to these results in section 4.3.2.

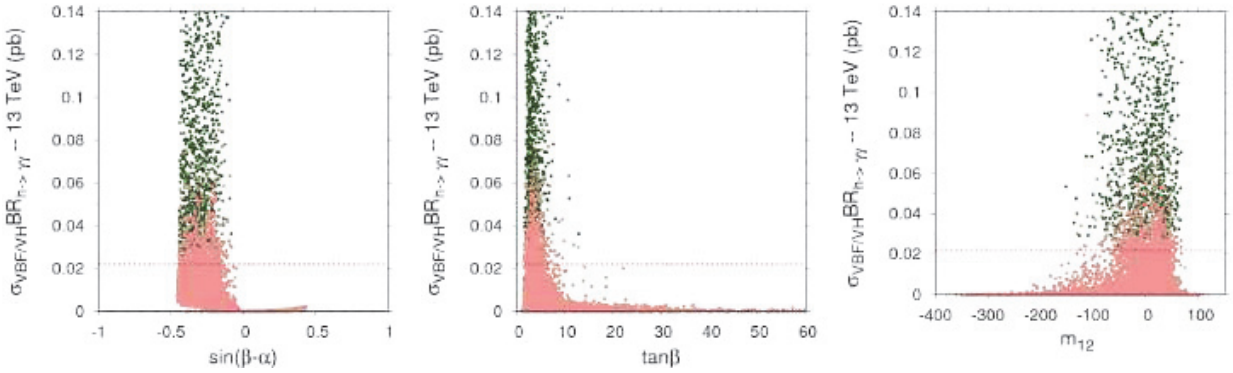

(A) Influence of $s_{\beta-\alpha}$. (B) Influence of $\tan\beta$. (C) Influence of m_{12}.

FIGURE 4.18: Value of $\sigma_{VBF,VH\to h} \times BR_{h\to\gamma\gamma}$ at 13 TeV as a function of different 2HDM free parameters in the general case. The dashed red line corresponds to the lowest value of the observed upper limit in $VBF + VH$ production mode. The color code is the same as in figure 4.15.

4.3.1.2 *Degenerate case*

Now we turn to a specific case where we assume that A and h are degenerated (see table 4.4 for details on the allowed range for the 2HDM free parameters).

In the $\gamma\gamma$ decay channel we are not able to identify the scalar or pseudoscalar nature of the decaying particle. Hence, if both h and A are degenerated, that is, if $m_h \simeq m_A$, the experimental number of measured events will be approximately the sum of the events produced by the h decay and those produced by the A decay.

Note that, as production and decay modes are identical for both A and h particles in gluon fusion production mode, interferences between decays involving A or h can happen in the term of the total decay amplitude. We here make the naive assumption that the interference term is zero and that we can simply add the two squared amplitudes – and hence sum the two $\sigma \times BR$. If interferences actually occur, a specific processing has to be performed. This will not be developed in this thesis.

We therefore compute a total $\sigma_{gg,tot} \times BR_{\gamma\gamma}$ as:

$$\sigma_{gg,tot} \times BR_{\gamma\gamma} = \sigma_{gg\to h} \times BR_{h\to\gamma\gamma} + \sigma_{gg\to A} \times BR_{A\to\gamma\gamma} \tag{4.2}$$

We also assume that we can compare the total cross-section times branching ratio to the observed upper limit taken at a mass $m = \frac{m_h+m_A}{2}$.

Note that, as the pseudoscalar production via $VBF + VH$ mode is negligible compared to the scalar production, the cross-section times branching ratio in this production mode will simply be the one corresponding to the scalar h.

The results are drawn in figure 4.19. As in the previous case, the $\sigma \times BR$ values in gluon fusion production mode are very close to the observed upper limit and some generated points can already be eliminated by experimental analysis. The $\sigma \times BR$ are higher than in the general case due to the degeneracy of h and A, increasing the chance to detect them in the CMS detector.

In the case of a $VBF + VH$ production mode many points are well above the experimental upper limit, leading to the elimination of a large amount of generated points.

As in the general case, some exclusion in the parameter space can be performed in the plane

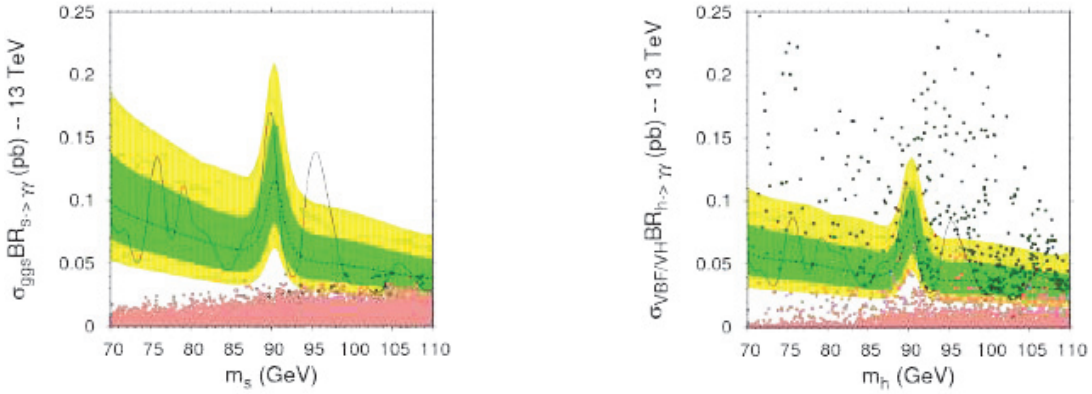

(A) $\sigma_{gg,tot} \times BR_{\gamma\gamma}$ as a function of $\frac{m_h+m_A}{2}$.

(B) $\sigma_{VBF,VH\to h} \times BR_{\gamma\gamma}$ as a function of m_h.

FIGURE 4.19: Comparison between the generated 2HDM points and the observed upper limit on the process $pp \to h/A \to \gamma\gamma$ at 13 TeV [90] (solid black line) in the degenerated hypothesis. The color code is the same as in figure 4.15.

$\tan\beta$ vs $s_{\beta-\alpha}$ and m_{12} vs $s_{\beta-\alpha}$ (see figure 4.20). We can also identify regions with high values of $\sigma \times BR$ for some specific ranges of $s_{\beta-\alpha}$, $\tan\beta$ and m_{12} (see respectively figures 4.21a, 4.21b and 4.21c for the gluon fusion production case and 4.22a, 4.22b and 4.22c for the $VBF + VH$ production case).

4.3.1.3 *Summary of the two analyses*

The two studies show that a light Higgs boson h may be within reach of the LHC. In particular, the degenerate case where $m_A \sim m_h$ presents an enhancement of the total $\sigma \times BR$ in the gluon fusion production mode compared to the one in the general case, making a potential discovery more likely in this scenario.

In both cases, the 13 TeV data are able to constrain the generated points in 2HDM Type I. Although this was already the case with the 8 TeV data in the $VBF + VH$ production mode, this was not true for the gluon fusion production mode. This is very promising and shows that the effort on the experimental side in the low-mass regions needs to continue.

4.3.2 The 2.9σ (local) excess in the $\gamma\gamma$ decay channel

One important change between the 8 TeV and 13 TeV CMS analyses is that a small excess appears in the 13 TeV data. Combining both 8 TeV and 13 TeV data, the excess has a local (global) significance of 2.9σ (1.47σ) [90] at a hypothetical mass of $m_h = 95.3$ GeV.

This excess is very small and will probably disappear after more data collection, as many other excesses did in the past. Note however that a broad excess was already found at LEP when combining the results of the four detectors, with a local significance of 2.3σ around $m_h \approx 98$ GeV [95].

In this section we will assume that the excess corresponds actually to the presence of a new scalar (or pseudoscalar) particle with a mass of around $m_h = 95$ GeV decaying into two photons. Hence, the goal of this section is to see if a 2HDM Type I would be able to explain such an excess.

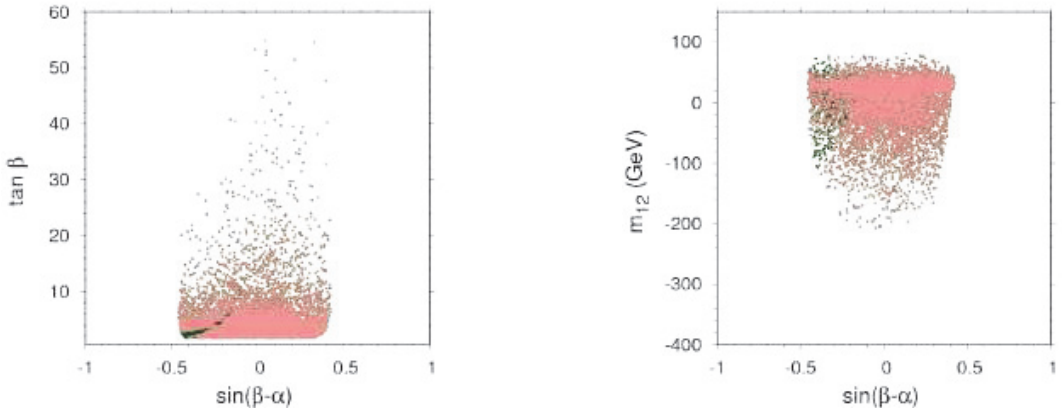

(A) $\tan\beta$ vs $s_{\beta-\alpha}$. (B) m_{12} vs $s_{\beta-\alpha}$.

FIGURE 4.20: Restriction of the parameter space due to the CMS light Higgs constraints in the degenerate case. Same color code as in figure 4.15.

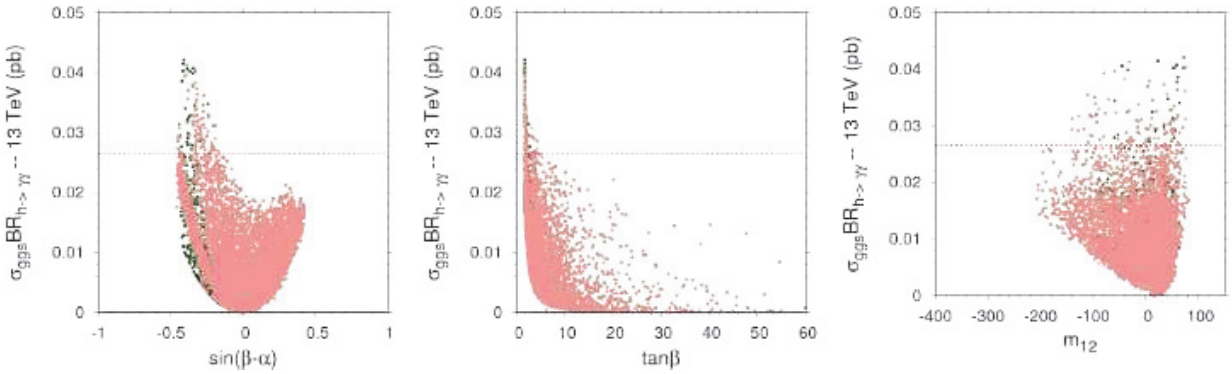

(A) Influence of $s_{\beta-\alpha}$. (B) Influence of $\tan\beta$. (C) Influence of m_{12}.

FIGURE 4.21: Value of $\sigma_{gg\to h} \times BR_{h\to\gamma\gamma}$ at 13 TeV as a function of different 2HDM free parameters in the degenerate case. The dashed red line corresponds to the lowest value of the observed upper limit in gluon fusion production mode. The color code is the same as in figure 4.15.

As we have seen in the previous section, the 2HDM Type I can generate points with sufficiently high $\sigma_{VBF,VH\to h} \times BR_{h\to\gamma\gamma}$ values to be consistent with the excess. However high values of $\sigma_{gg\to h} \times BR_{h\to\gamma\gamma}$ are harder to generate in this framework. Figures 4.15 and 4.19 do not show any generated points consistent with the excess in the gluon fusion production mode for both the degenerate case and the general case, but the scans performed are quite broad. Another scan focused on the region of interest, with the parameters $s_{\beta-\alpha}$, $\tan\beta$ and m_{12} restricted to the region where the $\sigma \times BR$ via gluon fusion is high (see figures 4.17 and 4.21) may generate rarer points with potentially even higher values of $\sigma \times BR$.

For this, and using figures 4.17 and 4.21 to constrain the parameters $s_{\beta-\alpha}$, $\tan\beta$ and m_{12} adequately, we define new ranges of variation for the 2HDM free parameters in table 4.5. Once again, we split the analysis into two cases: the general case and the degenerated one.

As in the previous section we apply the constraints we implemented and compare the resulting points with the observed CMS upper limit. The results are drawn in figure 4.23 for the

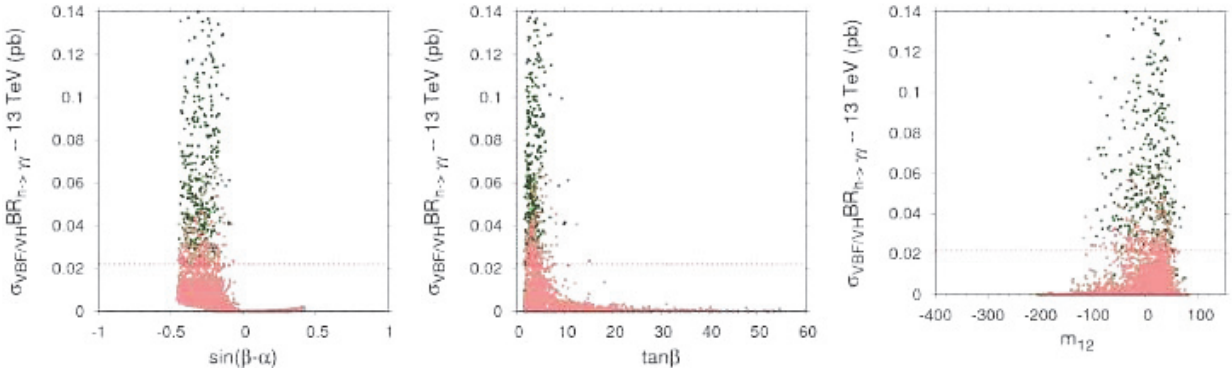

(A) Influence of $s_{\beta-\alpha}$. (B) Influence of $\tan\beta$. (C) Influence of m_{12}.

FIGURE 4.22: Value of $\sigma_{VBF,VH\to h}\times BR_{h\to\gamma\gamma}$ at 13 TeV as a function of different 2HDM free parameters in the degenerate case. The dashed red line corresponds to the lowest value of the observed upper limit in $VBF+VH$ production mode. The color code is the same as in figure 4.15.

m_h (GeV)	m_H (GeV)	m_A (GeV)	$m_{H^\pm}$ (GeV)	$s_{\beta-\alpha}$	$\tan\beta$	m_{12}^2 (GeV)^2
[92 ; 100]	125	[2 ; 700]	[43 ; 700]	[-0.47 ; -0.27]	[0.5 ; 2]	[-(180)^2 ; +(100)^2]
[92 ; 100]	125	$[m_h-0.5\ ;\ m_h+0.5]$	[43 ; 220]	[-0.5 ; -0.1]	[0.5 ; 2]	[-(160)^2 ; +(90)^2]

TABLE 4.5: Reduced range of variation of the 2HDM free parameters used in the general case (first line) and the degenerate case (second line) when searching for a resonance around 95 GeV.

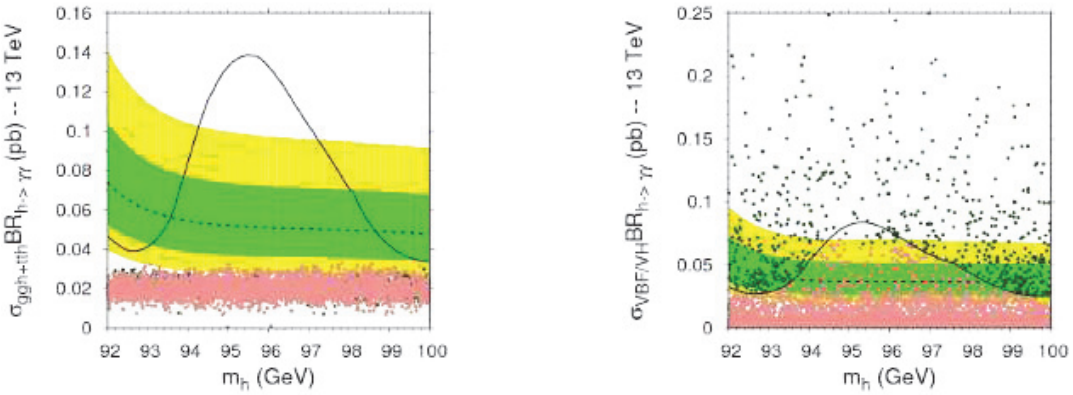

(A) $\sigma_{gg\to h}\times BR_{h\to\gamma\gamma}$ as a function of m_h. (B) $\sigma_{VBF+VH\to h}\times BR_{h\to\gamma\gamma}$ as a function of m_h.

FIGURE 4.23: Comparison between the generated 2HDM points generated around $m_h = 95.3$ GeV in the general case and the observed upper limit on the process $pp\to h/A\to\gamma\gamma$ at 13 TeV [90] (solid black line). Same color code as in figure 4.15.

general case and figure 4.24 for the degenerate case.

We can see that, if the slight excess present in the CMS data in the $VBF+VH$ production mode can easily be explained by a 2HDM light h in Type I framework, this is not the case for the gluon fusion production mode where no generated point has sufficiently high $\sigma_{gg\to h}\times BR_{h\to\gamma\gamma}$ values, even in the degenerate case. Hence, if the excess is confirmed by future analyses, the four types of 2HDM would be excluded.

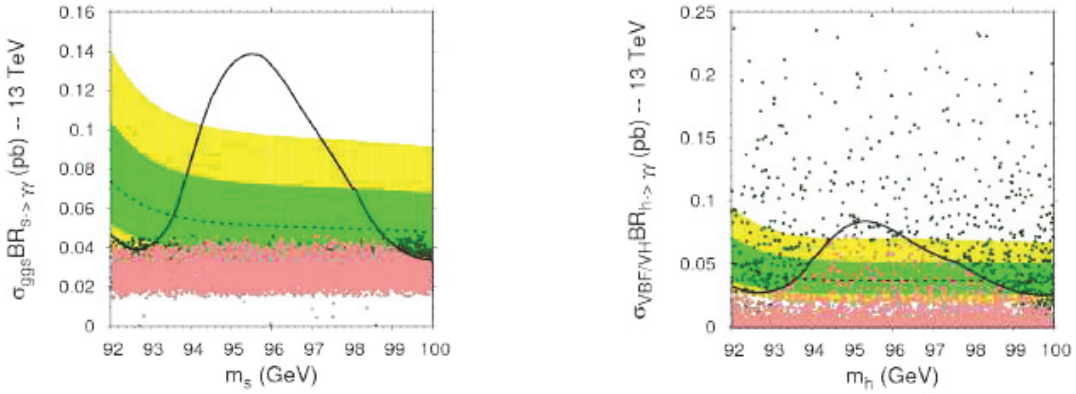

(A) $\sigma_{gg,tot} \times BR_{\gamma\gamma}$ as a function of $\frac{m_h+m_A}{2}$.

(B) $\sigma_{VBF+VH\to h} \times BR_{h\to\gamma\gamma}$ as a function of m_h.

FIGURE 4.24: Comparison between the generated 2HDM points generated with a mass of around $m_h = 95.3$ GeV in the degenerate case and the observed upper limit on the process $pp \to h \to \gamma\gamma$ at 13 TeV [90] (solid black line). Same color code as in figure 4.15.

4.4 Conclusion

In this part I have studied the four possible CP-conserving types of 2HDM under the hypothesis that the heavier Higgs H is assimilated to the 125 GeV Higgs boson discovered at the LHC. With this assumption, the mass of the 2HDM light Higgs boson h is lower than 125 GeV.

Such a light particle is often thought to have been ruled out by LEP analyses; however, if LEP experiment has excluded SM Higgs boson below 107.9 GeV [18], a light scalar with couplings different from those of the SM Higgs boson can still pass LEP constraints successfully. Hence, it is still very interesting to probe the low-mass region as light scalars could still exist there.

I have shown carefully the influence of each constraint listed in section 3.3 on the allowed parameter space, including LHC constraints on 125 GeV Higgs boson and on other hypothetical scalars. These constraints, taken together, provide an important restriction on the free parameters of the model.

Figures 4.13 and 4.14 show, in dark green, the parameter space still allowed in 2HDM Type I and II after imposing the constraints. The allowed regions are drastically reduced, especially in Type II which is very sensitive to flavor constraints. The region where h and A are simultaneously very light – below $m_{h,A} = \frac{125}{2}$ GeV – is extremely constrained by LHC 125 GeV Higgs constraints and may be entirely ruled out by the end of LHC Run II.

In a second part I have studied specifically the constraints on the light Higgs h using two CMS studies [80, 90] working on the process $pp \to h, A \to \gamma\gamma$ for light h or A. For this I worked in two different scenarios: the first one, called general case, where h has to be light but A does not have to be, and a second one, called degenerate case, where h is light and the mass of A is within ± 0.5 GeV around the mass of h such that the two particles are degenerated.

We have seen that the currently observed upper limits are unable to constrain either 2HDM Type II, Flipped or Lepton-Specific types. However, in Type I only, the 13 TeV analysis is able to constrain the parameter space in both ggh and $VBF + VH$ production mode. This is a great improvement as, with the 8 TeV data, only the analysis performed in the $VBF + VH$

production mode was able to constrain the generated points. This also means that a light 2HDM scalar or pseudoscalar is now within the reach of the LHC and that such a particle, if it exists, can possibly be detected.

Still using the CMS study at 13 TeV [90] I assumed next that the small excess present in the data was the sign of a new particle with a mass of around 95.3 GeV and checked if a light scalar h and/or a light pseudoscalar A in a 2HDM Type I framework were able to produce such a signal. I performed this study in the two scenarios – general and degenerate cases – described above.

I have shown that such an excess around 95.3 GeV can be produced in the $VBF + VH$ production mode but not in the gluon fusion production mode. Hence, if such a particle is confirmed, the 2HDM would not be able to produce a suitable candidate and would be ruled out.

5 Study of the heavy Higgs H – $m_h = 125$ GeV

5.1 Introduction

The goal of this chapter is to constrain the 2HDM parameter space under the hypothesis that the light scalar Higgs boson h is assimilated to the 125 GeV particle discovered at LHC. Therefore, in this whole chapter, we fix $m_h = 125$ GeV.

In addition we will work during all this chapter in the **alignment limit**, defined as the assumption that the couplings of the 2HDM 125 GeV Higgs boson have to be SM-like within 1% uncertainty. As a consequence, the parameter $s_{\beta-\alpha}$ has to be very close to unity: $|s_{\beta-\alpha}| \in [0.99; 1]$.

The framework of alignment limit, although not totally general, gathers most of the valid 2HDM points as the LHC constraints on 125 GeV Higgs boson impose that the couplings of the 2HDM neutral scalar assimilated to the 125 GeV Higgs boson have couplings close to the SM Higgs boson ones.

As in the previous chapter we allow the 2HDM free parameters to vary inside a given range (see table 5.1). We generate a large amount of random points before applying the different constraints listed in section 3.3.

Only Type I and Type II 2HDM frameworks will be studied in this chapter as we have seen in chapter 4 that the Lepton-Specific and Flipped types are similar to Type I and Type II respectively.

m_h (GeV)	m_H (GeV)	m_A (GeV)	$m_{H^\pm}$ (GeV)	$\lvert\sin(\beta-\alpha)\rvert$	$\tan\beta$	m_{12}^2 (GeV)^2
125	[129;2000]	[2;2000]	[min^*;2000]	[0.99;1]	[0.5;60]	[-(2000)^2;+(2000)^2]

Table 5.1: Allowed range of variation for the free parameters in the alignment limit. The min^* is taken to 70 GeV for Type I and 580 GeV for Type II.

Note that, under the assumption that $m_h = 125$ GeV, the decoupling limit, *i.e.* the limit where $m_H, m_A, m_{H^\pm} \to \infty$, is reachable [96, 97], contrary to the case where $m_H = 125$ GeV, as we have seen in the previous chapter. Hence, the available parameter space is much larger. We choose to impose an upper bound of 2000 GeV on both m_H, m_A and $m_{H^\pm}$ as we have to work with finite ranges to generate random points, but this bound is arbitrary and could be set to a higher value.

In order to generate points everywhere in the parameter space, especially in the high-mass regions, we decided to split the parameter space into five subregions. The allowed ranges of variation for the 2HDM free parameters in each of these regions are summarized in table 5.2.

The minimum value for $m_{H^\pm}$ is taken to $min^* = 70$ GeV for Type I and $min^* = 580$ GeV for Type II. The lower bound in Type I is a consequence of LEP constraints (see section 5.2.4)

whereas the one for Type II is due to flavor constraints and is taken according to [91] (see section 5.2.3 for further informations). The different allowed ranges, especially for m_{12}^2, will be justified in the following sections.

We will remind quickly the influence of the theoretical, oblique, flavor and LEP constraints on the parameter space as they have broadly the same effect as in the $m_H = 125$ GeV hypothesis developped in chapter 4. Then we will study in more details the consequences of the LHC constraints, both due to the 125 GeV Higgs boson and to additional hypothetical scalars. Finally we will summarize the effects of all these constraints in section 5.2.7.

no	m_h (GeV)	m_H (GeV)	m_A (GeV)	$m_{H^\pm}$ (GeV)	$\lvert s_{\beta-\alpha}\rvert$	$\tan\beta$	m_{12}^2 (GeV)^2
0	125	[129;700]	[2;62.5]	[min*;640]	[0.99;1]	[0.5;60]	$\begin{cases}[-(500)^2;+(200)^2], & \text{Type I}\\ [-200;200], & \text{Type II}\end{cases}$
1		[129;750]	[62.5;400]	[min^*;750]			$\begin{cases}[-(500)^2;+(0.706\ m_A+94)^2], & \text{Type I}\\ [-(200)^2;+(0.706\ m_A+94)^2, & \text{Type II}\end{cases}$
2		[129;1000]	[400;750]	[min^*;1000]			$\begin{cases}[-(500)^2;+(0.706\ m_A+94)^2], & \text{Type I}\\ [-(200)^2;+(0.706\ m_A+94)^2, & \text{Type II}\end{cases}$
3		$m_A \pm 350$	[750;1000]	$m_A \pm 350$			$[(0.706\ m_A-506)^2\,;(0.706\ m_A+94)^2]$
4		$m_A \pm 250$	[1000;2000]	$m_A \pm 250$			$[(0.706\ m_A-506)^2\,;(0.706\ m_A+94)^2]$

TABLE 5.2: The different scans actually used to probe the parameter space. The min^* is taken to 70 GeV for Type I and 580 GeV for Type II.

5.2 Influence of the different constraints

5.2.1 Theoretical constraints

As in the previous chapter the theoretical constraints impose lower and upper bounds on the λ_i present in the Lagrangian of the $\mathbb{Z}_2$-basis. However, contrary to the $m_H = 125$ GeV hypothesis, the decoupling limit where $m_H, m_A, m_{H^\pm} \to \infty$ is not ruled out [96, 97].

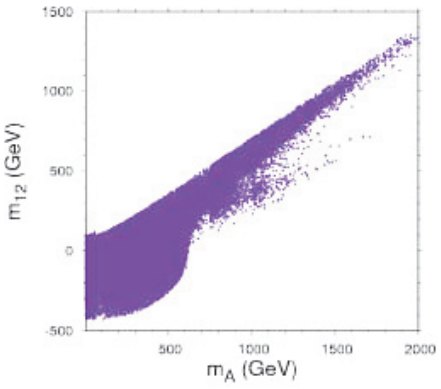

FIGURE 5.1: Points passing the three theoretical constraints in the plane m_{12} vs m_A.

The theoretical constraints also impose a correlation between m_A and m_{12}^2 due to equation (4.1), which is also a new consequence compared to the $m_H = 125$ GeV hypothesis. This

behaviour can be visualize in figure 5.1 where points passing theoretical constraints are drawn in violet. We can see that, as m_A grows, available m_{12} value grows as well.

Indeed, as $m_A^2 = \bar{m}^2 - \lambda_5 v^2$ and as λ_5 is bounded from below, high values of m_A require high values of $\bar{m}$. Moreover, we have:

$$\bar{m}^2 \equiv \frac{m_{12}^2}{s_\beta c_\beta} = m_{12}^2 \times \frac{1+\tan^2\beta}{\tan\beta} \tag{5.1}$$

As $\tan\beta$ will be bounded from below due to flavor constraints (see section 5.2.3), hence high $\bar{m}^2$ values imply either large $\tan\beta$ with positive m_{12} values or smaller $\tan\beta$ with large (positive) m_{12} values. This reasoning explains the rise of the available m_{12} values for increasing m_A which can be seen in figure 5.1.

Moreover, for a given value of m_A, the fact that λ_5 is bounded from above and below due to theoretical constraints implies, *via* equations (4.1) and (5.1) that m_{12} is bounded from above and below as well. Using these results and with the help of figure 5.1 we are able to estimate the upper and lower bounds on m_{12} as a function of m_A. The result is summarized in the last column of table 5.2.

5.2.2 Constraints from the oblique parameters

As in chapter 4 the oblique parameter constraints impose strong correlations between the masses of the different Higgs bosons. However, in the $m_h = 125$ GeV hypothesis, H can also be heavy, not just A and $H^\pm$.

Hence, the oblique parameters, in addition to enforcing a correlation between m_A and $m_{H^\pm}$, also impose a correlation between m_H and the masses of the pseudoscalar and charged Higgs bosons.

This behavior is shown in figure 5.2 where the points drawn in the plane m_H vs m_A pass both theoretical and oblique parameter constraints. Note that this last constraint does not depend on the 2HDM type but, as the lower bound on $m_{H^\pm}$ due to flavor constraints in 2HDM Type II is implemented directly in the scans (see table 5.1) we show the results for both Type I – left panel of figure 5.2 – and Type II – right panel.

The color of the points in figure 5.2 depends on the value of $m_{H^\pm}$. One can see that m_A and m_H are strongly correlated, with $m_H - m_A \to 0$ for high-mass values, and that, as m_H and m_A grow, the allowed $m_{H^\pm}$ values grow as well.

5.2.3 Flavor constraints

The influence of flavor constraints in Type I and II is exactly similar to the one obtained in section 4.2.3 in the $m_H = 125$ GeV hypothesis.

However the constraint due to the $\bar{B} \to X_s\gamma$ process, besides imposing a lower bound on $m_{H^\pm}$ in 2HDM Type II, also rules out a very large amount of points spread out in the whole parameter space without suppressing a precise region. For that reason, it becomes technically difficult to work with a representative amount of points after the imposition of the flavor constraint.

One solution would be to generate more points initially in order to still have a substantial random set after imposing flavor constraints, but it would be too time-consuming.

We choose instead not to use `SuperIso` to impose the constraints due to the $\bar{B} \to X_s\gamma$ process but instead to impose in Type II a fixed lower bound on $m_{H^\pm}$ set to 580 GeV according

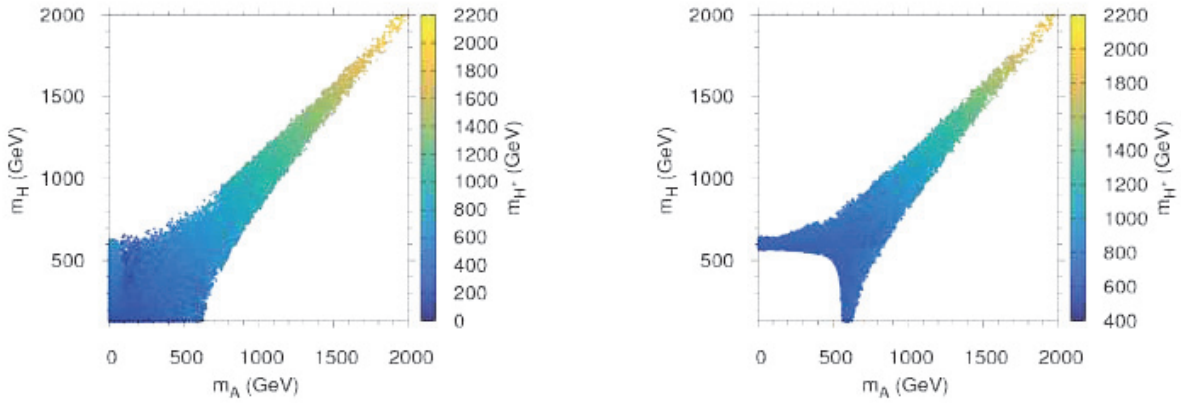

(A) Type I

(B) Type II

FIGURE 5.2: Points passing the theoretical and oblique parameter constraints in the plane m_H vs m_A. The color depends on the $m_{H^\pm}$ value.

to [91]. This value will not be very accurate in the low $\tan\beta$ region as the lower bound increases drastically (see figure 4.4b), but still makes it possible to roughly take into account this important bound.

5.2.4 LEP CONSTRAINTS

LEP constraints in the $m_h = 125$ GeV hypothesis are still important to constrain both possible light pseudoscalar A and light charged Higgs $H^\pm$. Note that, under this hypothesis, no CP-even scalar can have a mass below 82 GeV. Hence, LEP constraints given on $m_{H^\pm}$, that is, $m_{H^\pm} > 72.5$ GeV if $m_A > 12$ GeV in 2HDM Type I, are actually verified. This justifies the lower bound chosen for $m_{H^\pm}$ in Type I scans (see table 5.1).

5.2.5 LHC CONSTRAINTS ON THE 125 GEV HIGGS BOSON

In the following we show a selection of figures illustrating the effect of the 125 GeV Higgs constraints at 8 and 13 TeV on the parameter space.

The points passing all the constraints up to LEP ones are drawn in dark blue, the ones passing, in addition, LHC constraints on the 125 GeV Higgs boson at 8 TeV (and 13 TeV) are drawn in red (orange).

The main effect of these constraints is to greatly constrain the pseudoscalar at low mass – $m_A < 62.5$ GeV and to reduce significantly the available range of negative $s_{\beta-\alpha}$ in 2HDM Type II.

The first effect is visible in figure 5.3 which shows the generated points in the plane m_{12} vs m_A. The explanation for this phenomenon is the same as in chapter 4: the $h \to AA$ decay is open for $m_A < 62.5$ GeV, which moves the signal strength value away from 1. Hence, the log-likelihood increases, leading to a larger deletion of the generated points in this area.

The second effect is illustrated in figure 5.4 where the points generated in the 2HDM Type II framework are drawn in the plane m_H vs $s_{\beta-\alpha}$. The similar plots in Type I framework are in

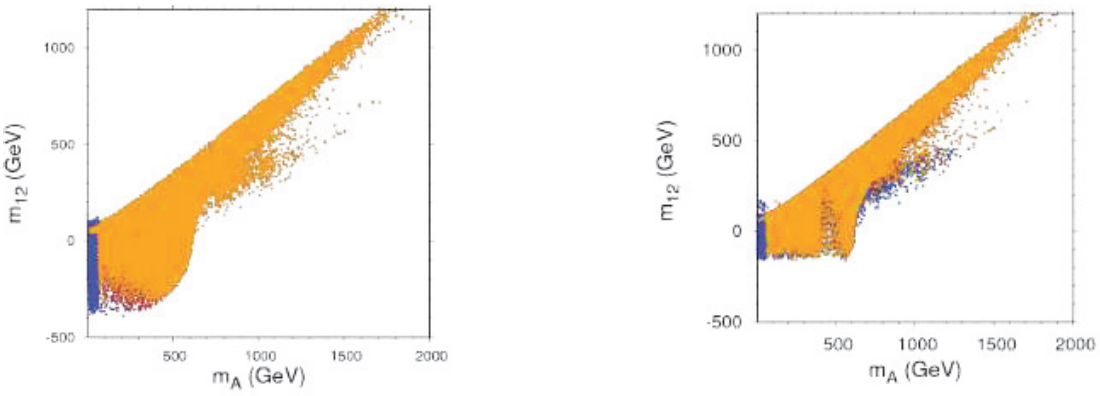

(A) Type I (B) Type II

FIGURE 5.3: Generated points in the plane m_{12} vs m_A. The points passing all the constraints up to LEP ones are drawn in blue. The ones passing, in addition, the LHC 125 GeV Higgs constraints at 8 TeV are drawn in red and the ones passing, in addition, the LHC 125 GeV Higgs constraints at 13 TeV are drawn in orange.

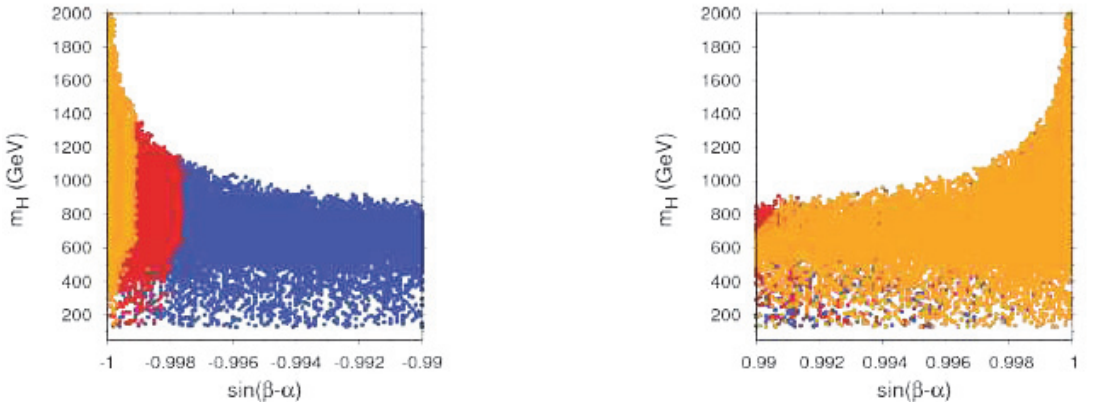

(A) Type II, negative $s_{\beta-\alpha}$ values. (B) Type II, positive $s_{\beta-\alpha}$ values.

FIGURE 5.4: Generated points in the plane m_H vs $s_{\beta-\alpha}$. The color code is the same as in figure 5.3.

Appendix E, figure E.1. Note that, if the sign of $s_{\beta-\alpha}$ has no influence on κ_V^2 and hence on the computation of $\sigma^{2HDM}_{VBF,VH\to h_{125}}$ in the *kappa trick* approximation (see equation (3.40)), it will however influence the computation of C_{tt} and C_{bb} (see equation (3.32)) and, by extension, the loop amplitudes and branching ratios for the decays $h_{125} \to \gamma\gamma$ and $h_{125} \to gg$ (see equation (C.1)).

5.2.6 LHC CONSTRAINTS ON OTHER HYPOTHETICAL SCALARS

5.2.6.1 *Heavy Higgs constraints*

We have seen in section 3.4.2.1 the different constraints on heavy scalar and pseudoscalar Higgs bosons coming from ATLAS and CMS collaborations that we apply on the generated set of points. The most constraining ones are [24, 77, 79]. We show as an example the generated

points passing all the constraints up to 125 GeV Higgs bosons at 13 TeV in orange together with the observed upper limit on the process $gg \to A \to \tau\tau$ coming from [77] in figure 5.5. Violet points are passing in addition all the heavy Higgs constraints.

Note that the figures for the two other analyses mentioned above are shown in appendix E, figures E.2 and E.3. We used the same color code as in figure 5.5.

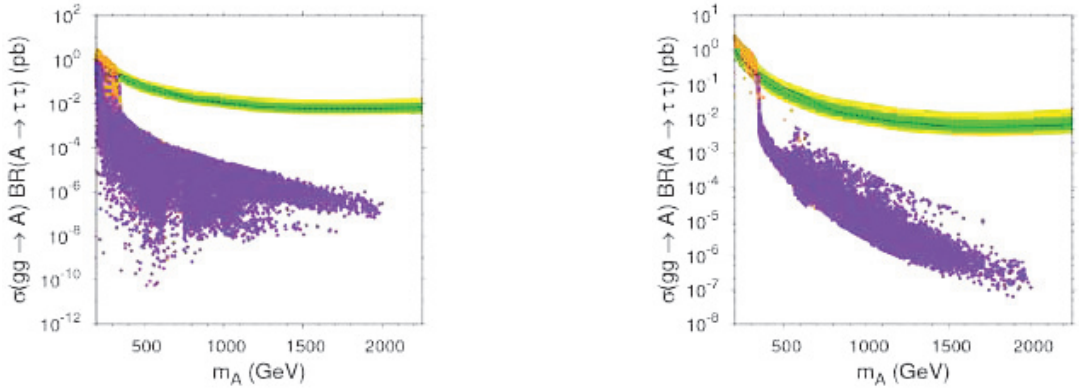

(A) Type I (B) Type II

FIGURE 5.5: Comparison between generated 2HDM points and ATLAS observed upper limit on the process $\sigma(gg \to A) \times BR(A \to \tau\tau)$ [77] (black solid line). Orange points are passing all the constraints up to 125 GeV Higgs boson constraints at 13 TeV. Violet point are passing, in addition, all the heavy Higgs constraints.

Figure 5.6 shows the 2HDM generated points in the plane m_H vs m_A and the consequences of heavy Higgs constraints in this plane. The color code is the same as in figure 5.5.

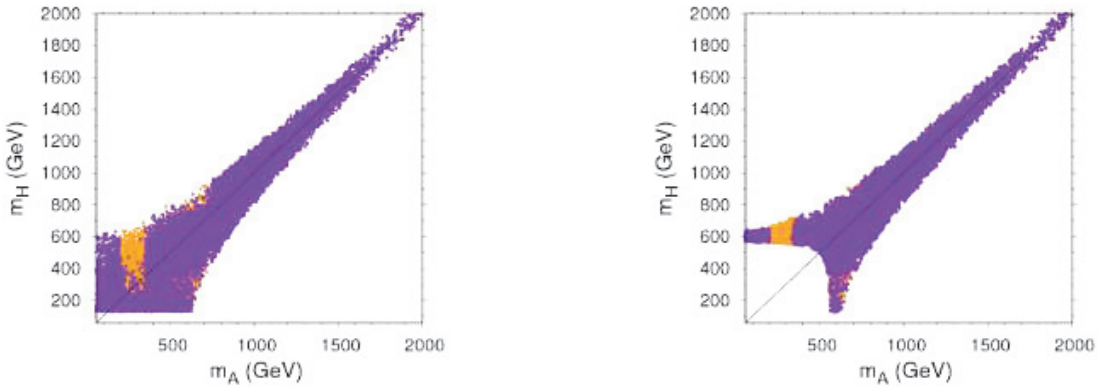

(A) Type I (B) Type II

FIGURE 5.6: Constraints on the parameter space due to heavy Higgs constraints. The color code is the same as in figure 5.5.

We can see that heavy Higgs constraints provide important cuts in the m_H vs m_A plane, in particular in Type II (see figure 5.6b): the range $m_A \in [200; 330]$ GeV is totally excluded by heavy Higgs constraints. This exclusion is essentially due to the upper limit on the process $gg \to A \to \tau\tau$ [77] (see figure 5.5b).

5.2.6.2 *Light Higgs constraints*

As in chapter 4 the constraints coming from the study of di-scalar or pseudoscalar production is unable to constrain the generated points. However the CMS studies on direct production of a light scalar or pseudoscalar [80, 90] are able to do so.

As h is assumed to have a mass of 125 GeV, only the pseudoscalar A can be light. Figure 5.7 shows the comparison between the generated points passing all the constraints up to LHC 125 GeV Higgs constraints at 13 TeV in orange and the observed upper limit at 13 TeV in gluon fusion production mode (solid black line) [90]. Points passing in addition all the light Higgs constraints are drawn in dark red.

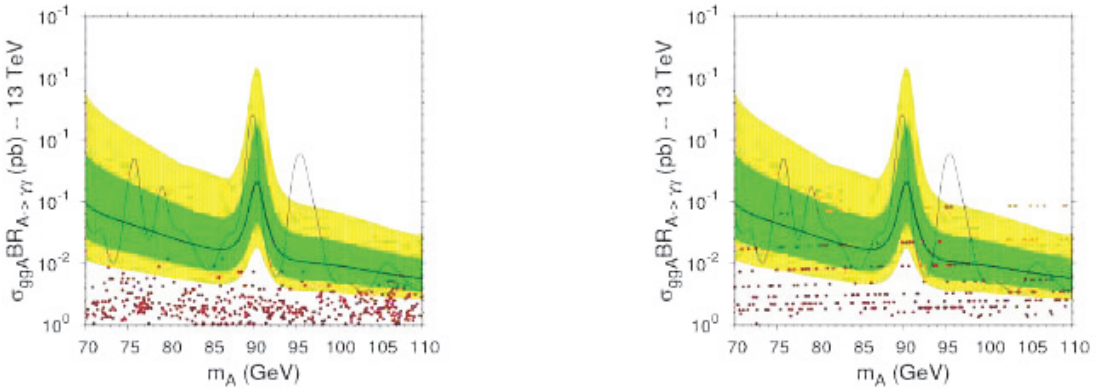

(A) Type I (B) Type II

FIGURE 5.7: Comparison between generated 2HDM points and CMS observed upper limit on the process $\sigma(gg \to A) \times BR(A \to \gamma\gamma)$ [90] (black solid line). Orange points are passing all the constraints up to 125 GeV Higgs boson constraints at 13 TeV. Dark red point are passing, in addition, all the light Higgs constraints.

Contrary to the $m_H = 125$ GeV hypothesis the light pseudoscalar A can have values of $\sigma_{gg\to A} \times BR_{A\to\gamma\gamma}$ sufficiently high to be above the observed upper limit in both Type I and Type II. The CMS analysis [90] is then able to suppress some points.

In chapter 4 we made the assumption that the slight excess observed in CMS 13 TeV data in both gluon fusion and $VBF + VH$ production mode could be due to a spin-0 particle decaying into two photons and we studied whether the 2HDM light Higgs h could explain it. However, in the $m_h = 125$ GeV hypothesis only the pseudoscalar A can be light and, if figure 5.7 shows that the pseudoscalar may be a good candidate to explain the excess in gluon fusion production mode, especially in Type II, the absence of VBF or VH production at tree level prevents A from explaining the excess in the $VBF + VH$ channel. Hence we will not reproduce the study performed in section 4.3.2.

5.2.6.3 *Charged Higgs constraints*

The current constraints on charged Higgs bosons only constrain 2HDM at low $m_{H^\pm}$ and hence only in 2HDM Type I. Figure 5.8a shows the most constraining observed upper limit [85] together with the generated points. The points passing all the constraints up to 125 GeV Higgs boson constraints at 13 TeV are drawn in orange and the ones passing, in addition, charged Higgs constraints are drawn in light blue. Note that heavy Higgs and light Higgs constraints are not applied in this plot.

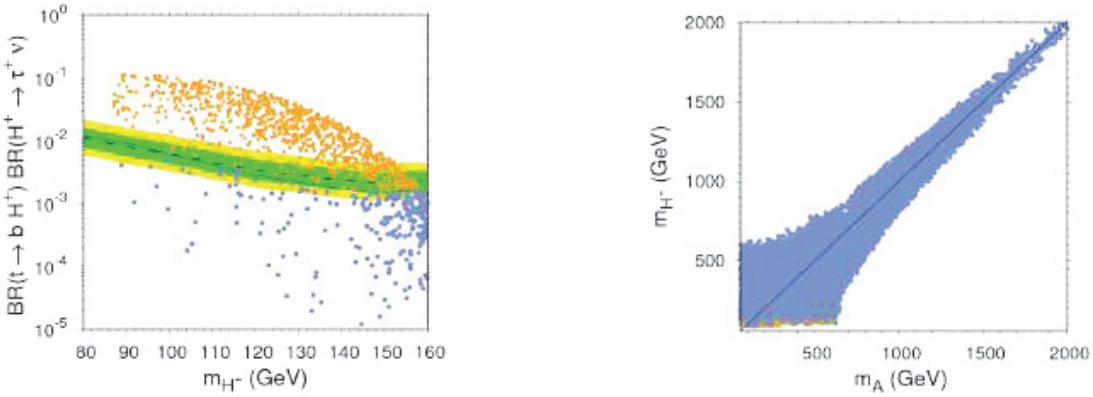

(A) Comparison between the 2HDM points generated in Type I framework and the observed upper limit on the process $t \to bH^+ \to b\tau\nu_\tau$ at 8 TeV [85] (solid black line).

(B) Consequences of the charged Higgs constraints in a 2HDM Type I.

FIGURE 5.8: Charged Higgs constraints in Type I. Orange points are passing all the constraints up to 125 GeV Higgs boson constraints at 13 TeV. Blue points are passing, in addition, the light charged Higgs constraints.

Although analyses at high $m_{H^\pm}$ are still not able to exclude points in 2HDM Type I and II, the upper limit is very close to the generated points, especially in the channel $pp \to H^+ \to t\bar{b}$ (see figure 5.9). It is hence very important to continue to study these channels as, with more luminosity, they will probably be able to constrain the 2HDM parameter space.

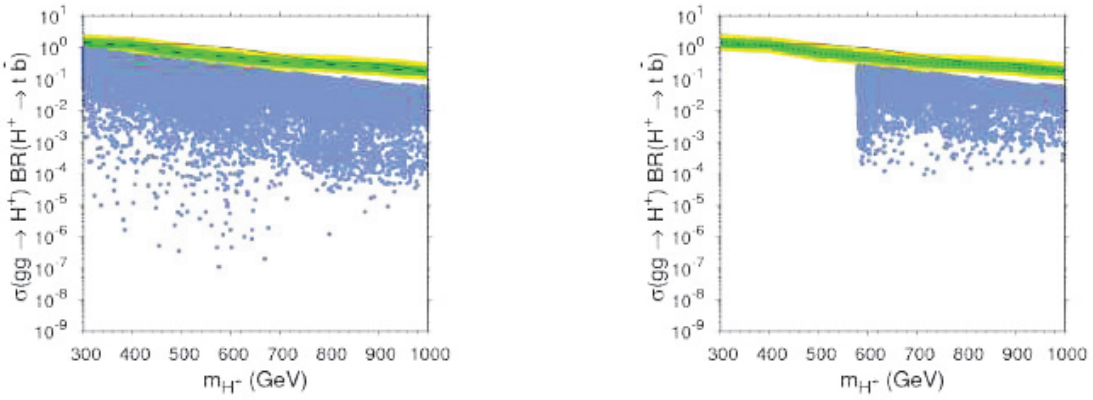

(A) Type I

(B) Type II

FIGURE 5.9: Constraints on a heavy 2HDM charged Higgs together with the upper limit coming from [87]. The color code is the same as figure 5.8a.

We can summarize this section by saying that the charged Higgs constraints have no influence on 2HDM Type II and only slightly constrain the 2HDM parameter space in Type I, reducing the number of available points with low charged Higgs mass. Figure 5.8b summarize this property by showing the generated points in 2HDM Type I in the plane $m_{H^\pm}$ vs m_A. The color code is the same as in figure 5.8a.

5.2.7 Summary of the constraints

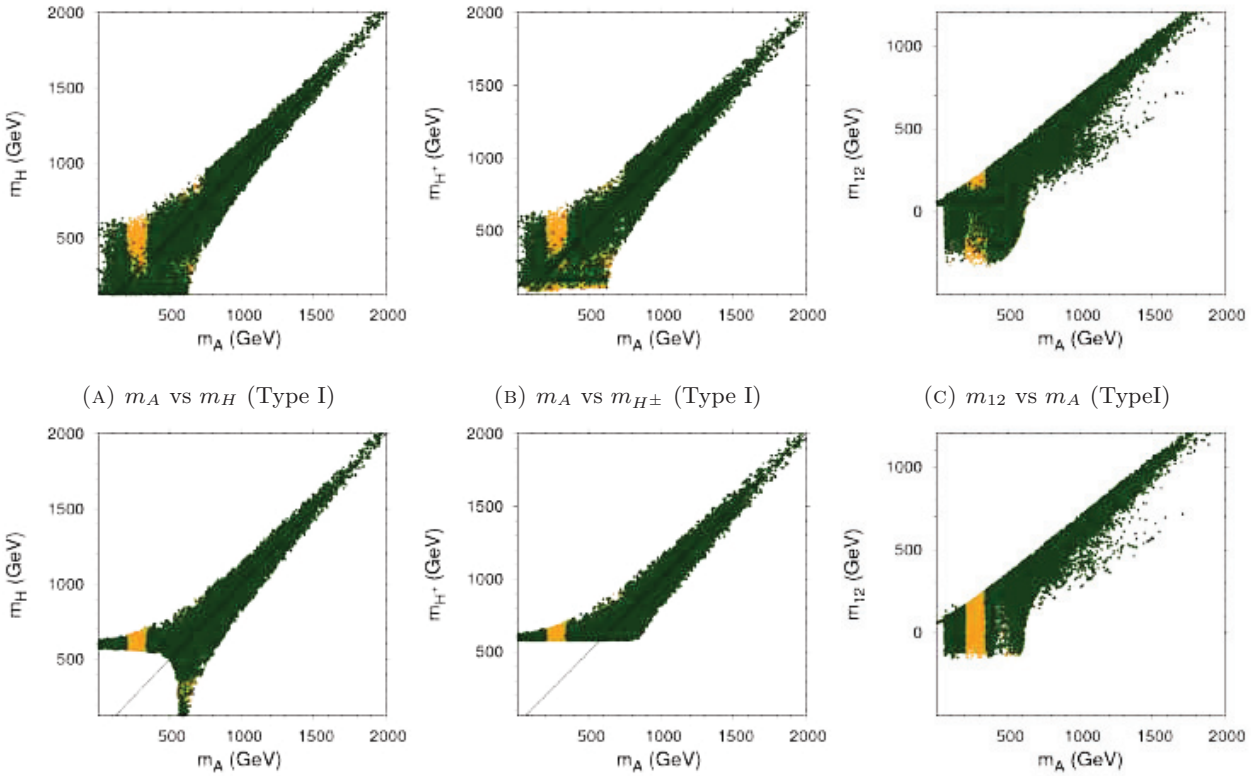

(A) m_A vs m_H (Type I) (B) m_A vs $m_{H^\pm}$ (Type I) (C) m_{12} vs m_A (TypeI)

(D) m_A vs m_H (Type II) (E) m_A vs $m_{H^\pm}$ (Type II) (F) m_{12} vs m_A (Type II)

FIGURE 5.10: Points passing all the constraints up to 125 GeV Higgs constraints at 13 TeV (orange) and points passing, in addition, the LHC constraints on other hypothetical scalars (green) in different planes in the Type I (upper panel) and Type II (lower panel) frameworks.

So far we have studied the influence of the different sets of constraints. In this section we will apply all the constraints together and summarize their influence on the parameter space.

We present figures in different planes, showing for both of them the points passing all the constraints up to LHC 125 GeV Higgs constraints at 13 TeV in orange and the ones passing, in addition, the LHC constraints on other hypothetical scalars in dark green.

The parameter $s_{\beta-\alpha}$ in 2HDM Type II is the most affected by these constraints. Indeed, due to LHC 125 GeV Higgs constraints at 13 TeV, the parameter is restricted to $s_{\beta-\alpha} \in [-1; -0.999]$ in the negative region.

Furthermore entire mass regions in both Type I and Type II are ruled out by the different constraints. This is particularly true in Type II, where the possible existence of a pseudoscalar with mass $m_A \in [200; 325]$ GeV is totally eliminated.

Up to now studies on light di-Higgs production and heavy charged Higgs have been unable to constrain the 2HDM parameter space, but we hope that, with more luminosity, at least the upper limits on processes including heavy charged Higgs bosons will be relevant to put harder exclusions on it.

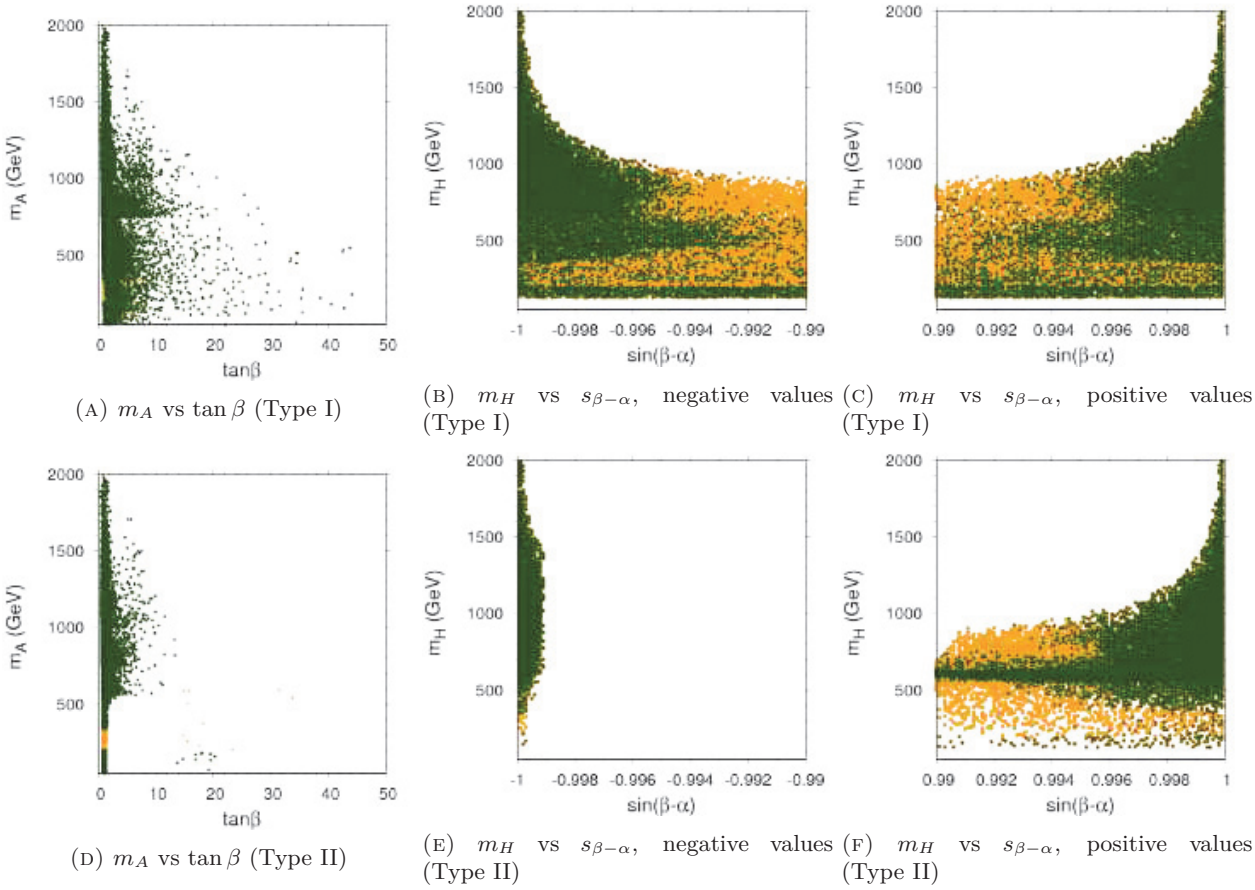

(A) m_A vs $\tan\beta$ (Type I)

(B) m_H vs $s_{\beta-\alpha}$, negative values (Type I)

(C) m_H vs $s_{\beta-\alpha}$, positive values (Type I)

(D) m_A vs $\tan\beta$ (Type II)

(E) m_H vs $s_{\beta-\alpha}$, negative values (Type II)

(F) m_H vs $s_{\beta-\alpha}$, positive values (Type II)

FIGURE 5.11: Same as figure 5.10.

5.3 CONCLUSION

In this chapter I have studied the CP-conserving 2HDM Type I and II under the hypothesis that the lighter Higgs h is assimilated to the 125 GeV Higgs boson discovered at the LHC and in the alignment limit framework, that is, the assumption that the couplings of the 125 GeV 2HDM Higgs boson are the same as those of the SM Higgs boson within a deviation of less than 1%.

I have shown the influence of the different constraints on the parameter space, in particular the LHC 125 GeV Higgs boson constraints at 8 and 13 TeV which significantly restrict the free parameters, and particularly the $s_{\beta-\alpha}$ parameter in 2HDM Type II.

I have also shown that the heavy Higgs constraints, and particularly the one on the process $gg \to A \to \tau\tau$, are very efficient at ruling out entire parts of the parameter space in the plane m_H vs m_A (see figure 5.6).

The charged Higgs constraints are currently only giving poor restrictions on the model: only the light charged Higgs studies are able to constrain the generated points, whereas the upper limits involving heavy charged Higgs bosons are still too high to rule out any point.

The parameter space is however greatly reduced by all the constraints and 13 TeV results on both 125 GeV Higgs boson and other possible additional scalar resonances have greatly improved the restrictions.

Part III:

Composite Higgs model

The Two-Higgs Doublet model studied in the previous part of this thesis is a theory beyond the Standard Model of particle physics but that does not answer the issues that have been raised in section 1.3. Its main interest is that it can be taken as an effective model describing the Higgs sector of larger and more comprehensive theories.

In this part we will study another model called Fundamental Composite Dynamics (FCD), based on the combination of Technicolor and Composite Higgs theories. Both of them postulate that a new strongly coupled interaction is acting at high energy. New gauge bosons – the so called technigluons – and fermions – called techniquarks – come with it. Inspired by the chiral symmetry breaking mechanism which occurs in QCD, the FCD theory assumes that, below a certain scale Λ_{FCD}, the global symmetry acting on the techniquarks breaks due to a condensate, leading to the emergence of composite (pseudo-) Goldstone bosons – similar to the QCD pions – and to heavier composite particles corresponding to the QCD mesons and baryons.

In a first part we will recall the main properties and mechanisms of both Technicolor and Composite Higgs theories and show how one can combine them into a more general FCD theory. Then we will study the specific symmetry breaking pattern $SU(4) \to Sp(4)$, which corresponds to the minimal FCD symmetry breaking pattern.

This breaking gives rise to two scalar particles h_1 and h_2 and a pseudoscalar η. We will study the phenomenology of the model and test it against oblique parameter constraints and LHC measurements assuming the light scalar state h_1 being the 125 GeV Higgs boson and the heavier state h_2 being a heavy Higgs.

6 Fundamental Composite Electroweak Dynamics

6.1 Introduction to Technicolor and Composite Higgs theories

We have seen in section 1.3 that the SM has pitfalls and that a complete theory of particle physics would be needed to solve them.

The first model we studied, the Two-Higgs Doublet Model, is an extension of the SM that has to be taken as an effective model which should ultimately be part of a more comprehensive model. In this part we will work in the framework of one such theory that intends to address some of the limitations of the SM.

We will study a combination of two theories, namely Technicolor (TC) and Composite Higgs models. These two theories, based on the assumption that a new strongly coupling interaction exists at high energy beyond the SM, have both been developed in order to solve the hierarchy problem and to provide a dynamical explanation to electroweak symmetry breaking. They operate on very similar principles – in particular, if all TC theories do not admit a Composite Higgs limit, the reverse is true – explaining why their unification is so easy.

In this section we will briefly review the generic construction and behavior of both TC and Composite Higgs models. The implementation of their combination in a specific symmetry breaking pattern will be exposed in section 6.2 and the phenomenology of such a breaking will be developed in section 6.3.

6.1.1 Technicolor

The TC theory was introduced by Weinberg [98] and Susskind [99] in the late 1970's [100]. At that time the heaviest known fermion was the b quark, with a mass of around 4.18 GeV. The $W^{\pm}$ and Z^0 bosons were still not discovered but their masses were predicted to be around 80 GeV and 90 GeV respectively.

At that time one of the challenges was to find a theory able to generate massive gauge bosons. One possible solution was found to be the Higgs mechanism. Another one, called TC, postulates the existence of an additional strong interaction at high energy associated with new gauge bosons and fermions. The global flavor symmetry of these new fermions is assumed to break at low energy in a similar way as QCD.

As SM fermions seemed almost massless at that time compared to the expected mass of $W^{\pm}$ and Z^0 gauge bosons – the top was not yet discovered – they could be reasonably let out of the mass generation mechanism. The question of generating large masses of fermions, such as the top one, in TC models came later.

The idea behind TC theories is to consider a new strongly interacting gauge theory associated with a gauge group $G_{TC} = SU(N_T)_{TC}$ hence providing $N_T^2 - 1$ new *technigluons*. Then one can introduce new chiral fermions, called *techniquarks*, sensitive to this new strongly coupled

interaction and transforming under a specific flavor symmetry G_f which contains at least the electroweak symmetry $SU(2)_L \times U(1)_Y$. Ordinary fermions are assumed to be singlets under G_{TC} but not necessarily under G_f.

In analogy with QCD [101] a technifermion condensate can appear, breaking the initial flavor symmetry G_f into a subgroup $H \subset G_f$ which has to preserve $U(1)_{em}$ but not $SU(2)_L \times U(1)_Y$.

According to the Goldstone theorem, this breaking generates $n = \dim(G_f) - \dim(H)$ Goldstone bosons. Three of them remain massless and are absorbed by the $W^\pm$ and Z^0 gauge bosons to give them masses. The others can remain massless or acquire a mass – and hence become pseudo-Goldstone bosons, or pGBs – *via* corrections due to explicit breaking terms in the Lagrangian of the theory.

A first pitfall of the theory is that without any additional condition it leads to corrections to the ρ parameter – $\rho \equiv \frac{m_W^2}{c_W^2 m_Z^2}$ – that move drastically away from its measured value $\rho = 1.00037 \pm 0.00023$ [10].

In order to preserve the ρ parameter the model needs to contain a custodial symmetry, that is, the flavor symmetry G_f must contain $SU(2)_L \times SU(2)_R$ which breaks to $SU(2)_V \subset H$.

The flavor symmetry breaking gives rise to numerous composite particles composed of techniquarks and/or anti-techniquarks. In analogy with QCD, we will call them *technimesons* for integer-spin particles and *technibaryons* for half-interger-spin particles. All these particles have masses M of the order of the symmetry breaking scale Λ_{TC}: $M \sim \frac{\Lambda_{TC}}{4\pi}$. The exact particle spectrum of a given TC theory is usually found using extensive lattice computations.

In such models scalar particle singlets under H arise after symmetry breaking. The lightest one is assimilated to the Higgs boson discovered at the LHC. We will call it σ, in analogy with the $\sigma/f_0(500)$ from QCD.

The main problem with this particle is that it is rather heavy – as we have seen above, $M_\sigma \sim \frac{\Lambda_{TC}}{4\pi}$. As we now know, the Higgs boson is very light compared to the TC scale, and hence the theory needs additional corrections to M_σ in order to lower it down to 125 GeV. However the appropriate corrections are difficult to obtain, often requiring important fine-tuning.

Although gauge boson masses are generated in TC theories by the dynamical electroweak symmetry breaking, ordinary quarks and leptons are still massless and TC needs to supply a reliable mechanism to replace the Yukawa terms of the SM Lagrangian.

One solution is to introduce, in a scenario called extended Technicolor (ETC), an additional broken gauge interaction which allows couplings between the technifermions and the ordinary fermions. Hence, at low energy, this interaction can be viewed as a local four-fermion interaction of the form [102, 103]:

$$\frac{g_{ETC}^2}{M_{ETC}^2}(\bar{Q}Q)(\bar{\psi}\psi) \tag{6.1}$$

with Q a technifermion, ψ an ordinary fermion, g_{ETC} the ETC coupling strength and M_{ETC} the characteristic mass of an ETC gauge boson. Note that the above formula is assumed to be at low energy compared to M_{ETC}.

TC breaking leads to a non-zero value of the condensate term $\left\langle \bar{Q}Q \right\rangle$, giving rise to a fermion mass term:

$$m_f \approx \frac{g_{ETC}^2}{M_{ETC}^2} \left\langle \bar{Q}Q \right\rangle_{ETC} \tag{6.2}$$

where $\left\langle \bar{Q}Q \right\rangle_{ETC}$ is the value of the technifermion condensate evaluated at the ETC scale $\sim M_{ETC}$.

In such a scenario, the different mass scales of each fermion generation would be due to multiple breakings of the ETC gauge group, each one generating the mass of one generation of fermions. Hence ETC would provide a dynamical explanation to the fermion masses and to the mass splitting between generations.

However ETC theories encounter a number of shortcomings, including the cause of the different breakings of the ETC and TC flavor symmetries, the derivation of the exact condensate spectrum after TC breaking and the deletion of possible Flavor-Changing Neutral Currents (FCNC) naturally arising in every ETC theory.

These FCNC are difficult to avoid or reduce. One solution to solve this problem is called *walking Technicolor*, in which the evolution of the coupling constant α_{TC} of the TC theory depending on the energy is almost flat for a large range of energy before decreasing to zero in the UV regime (see figure 10 in [103]).

There are obviously more requirements to obtain viable ETC/TC theories but we will not go into further detail here. For more information on the subject, see for instance [102, 103, 104].

The TC theory was very attractive during many decades as it was able to give a dynamical explanation to the electroweak symmetry breaking and to the gauge boson masses.

In the meantime the Higgs boson has been discovered at LHC at a mass of 125 GeV, which is very light compared to the mass of the condensates predicted by TC theories. Lattice results predict masses around the TeV scale for the lightest resonances [105], meaning that the theory needs important fine-tuning to include a viable Higgs candidate with a mass comparable to the one of the discovered Higgs boson. Hence, the initial theory has known many modifications in order to adjust to experimental results. One of the possible modifications is to unify it with Composite Higgs models by creating a continuous link between pure TC models and Composite ones (see in particular section 6.2.2).

6.1.2 Composite Higgs theory

Another approach close to the TC theories is the Composite Higgs models. In these theories a strongly interacting gauge symmetry associated with a global flavor symmetry G_f acting on the new fermion sector also acts at high energy. The flavor symmetry G_f is broken at a scale Λ down to a subgroup H which, contrary to TC, includes the electroweak symmetry $SU(2)_L \times U(1)_Y$.

The symmetry breaking gives rise to $n = \dim(G_f) - \dim(H)$ Goldstone bosons. The Composite Higgs theory requires there be at least one $SU(2)_L$ doublet amongst them that can be identified with the SM Higgs doublet. Then another mechanism is required to break the electroweak symmetry, giving rise to massive gauge bosons in a similar way as in the SM.

In such models additional terms break the global symmetry G_f at tree or loop level, leading to the generation of a mass for the Goldstone bosons, and in particular for the Higgs candidate.

The great advantage of identifying the Higgs boson discovered at the LHC with a pGB is that the pGBs are naturally light compared to the technimeson and technibaryon condensates – which also emerge in Composite Higgs theory in a similar way as in TC – allowing the Higgs candidate to have a mass of around 125 GeV without fine-tuning. Moreover the hierarchy problem is also solved as corrections to the pGB Higgs candidate can only go up to the Λ scale and no longer up to the Planck scale as it is the case for the SM Higgs boson. Hence, the corrections to the Higgs mass are much smaller than in the SM case.

In Composite Higgs theory the fermion masses are often obtained through partial compositness [106], where SM fermions mix with the new heavy fermions – which we will call techniquarks in analogy with TC. At energy scales below Λ the techniquarks condense, giving rise to the fermion mass terms. The hierarchy between the generations is obtained varying the degree of coupling: light fermions will be essentially elementary whereas the heavy fermions of the third generation will be obtained through a strong mixing with the heavy techniquark states.

Note however that, although ETC-like and partial compositness mechanisms are the most popular fermion mass generation mechanisms for TC and Composite Higgs frameworks respectively, both ETC-like and partial compositness mechanisms can be used for either TC or Composite Higgs theories.

6.1.3 Combining the two theories

We have seen that both TC and Composite Higgs theories are based on a strongly coupled interaction with new particles, called *techniquarks*, transforming under a global flavor symmetry G_f. This symmetry breaks at a specific scale Λ, producing *technimesons* and *technihadrons* resulting from the condensation of the techniquarks. The symmetry breaking also generates Goldstone bosons which can acquire a mass, albeit small compared to other condensates.

There are two main differences between these theories. First, in TC, the electroweak symmetry is entirely broken during the breaking of G_f whereas in Composite Higgs models, the electroweak symmetry is preserved after G_f breaking, and another mechanism needs to be responsible for the $SU(2)_L \times U(1)_Y$ breaking. Second, the Higgs candidate is assimilated to the lightest neutral scalar condensate in the TC theories and to a neutral scalar pGB being part of a doublet of $SU(2)_L$ in the Composite Higgs theories.

A simple way to combine these two theories at an effective level is to consider a ground state – or, equivalently, a vacuum – Σ_0 which is a mixing between the TC ground state(s) Σ_{TC} and the Composite Higgs ground state(s) Σ_C. Hence, the most general vacuum Σ_0 will partially break the electroweak symmetry. One also needs to impose that the Goldstone bosons resulting from the G_f breaking contain a $SU(2)_L$ doublet.

Hence, in such unified theories the Higgs candidate will be a mixing between the pGB candidate arising from the Composite Higgs part of the theory and the lightest neutral scalar condensate, called σ, inherited from the TC theory.

6.2 The $SU(4) \to Sp(4)$ breaking: set up

We have exposed in the previous section the main aspects of the general theory we will be working with. Now we will expose with more details the mechanism and phenomenology of the combined theory, called Fundamental Composite Dynamics (FCD), for the specific global flavor symmetry breaking $SU(4) \to Sp(4)$. This breaking is the minimal possible pattern.

We will assume that a condensate breaking the initial $SU(4)$ symmetry actually exists – which is confirmed by lattice computations [108] – but, as we keep an effective approach in the following, we will not consider details about the initial strongly coupled interaction nor its extensions allowing the generation of fermion masses.

6.2.1 Preliminaries

We assume that the model relies on a strongly coupled gauge group $SU(2)_{FCD}$ with just two Dirac techniquarks U and D transforming according to the fundamental representation of the underlying gauge group. In this case the representation is pseudo-real [109], which means that each new fermion can be described as two Weyl fermions: $Q^i = (U_L, D_L, U_R, D_R)$. Hence, the technifermion sector in the vanishing mass limit has a SU(4) global symmetry.

The Lagrangian underlying the new sector reads (see sections 1.2.2.1 and 1.2.2.2):

$$\mathcal{L} = -\frac{1}{4} F^a_{\mu\nu} F^{a\mu\nu} + \bar{Q}_j \left(i\gamma^\mu D_\mu\right) Q_j - M^{ij}_Q Q_i Q_j \tag{6.3}$$

with $F^a_{\mu\nu}$ the field strength of the new gauge bosons associated with the $SU(2)_{FCD}$ gauge group, D_μ the appropriate covariant derivative and M^{ij}_Q a general mass matrix.

Lattice computations [108] confirm that a condensate forms in the chiral limit, breaking the global symmetry $SU(4)$ down to $Sp(4)$. Then, using group theory [110], one can show that, as the technifermions transform in the fundamental representation of $SU(4)$, that is, acting as a $\mathbf{4}_{SU(4)}$, then the vacuum $\langle Q^i Q^j \rangle$ breaking the symmetry acts as a $\mathbf{6}_{SU(4)}$. After symmetry breaking, it acts as $\mathbf{5}_{Sp(4)} \oplus \mathbf{1}_{Sp(4)}$. The $\mathbf{5}_{Sp(4)}$ corresponds to the five Goldstone bosons arising from the breaking.

Note that the σ condensate issued from the TC part of the theory is a singlet under $Sp(4)$ and hence may be assimilated to the $\mathbf{1}_{Sp(4)}$ obtained above. However there are many ways to obtain scalar singlets in FCD theories, for instance by considering condensates of the form $\left\langle Q^i Q^j Q^k Q^l \right\rangle$, and only lattice computations can settle which one will corresponds to the lightest one.

In order to embed the electroweak sector in the largest $SU(4)$ symmetry we choose to assign the first two Weyl fermions U_L and D_L to a doublet of $SU(2)_L$ and the other two U_R and D_R to a doublet of $SU(2)_R$.

The resulting quantum numbers of the techniquarks and SM fermions under $SU(2)_{FCD}$ and the SM gauge group $SU(3)_c \times SU(2)_L \times U(1)_Y$ are summarized in table 6.1.

	$SU(2)_{FCD}$	$SU(3)_c$	$SU(2)_L$	Q_Y $(U(1)_Y)$
$Q^{TC}_L = (U_L, D_L)$	$\mathbf{2}$	$\mathbf{1}$	$\mathbf{2}$	0
U_R	$\bar{\mathbf{2}}$	$\mathbf{1}$	$\mathbf{1}$	-1
D_R	$\bar{\mathbf{2}}$	$\mathbf{1}$	$\mathbf{1}$	1
$Q^{SM}_L = (u_L, d_L)$	$\mathbf{1}$	$\mathbf{3}$	$\mathbf{2}$	1/3
u_R	$\mathbf{1}$	$\bar{\mathbf{3}}$	$\mathbf{1}$	-4/3
d_R	$\mathbf{1}$	$\bar{\mathbf{3}}$	$\mathbf{1}$	2/3

Table 6.1: Quantum numbers of the FCD techniquarks and the SM quarks under the new gauge group $SU(2)_{FCD}$ and the SM gauge group.

6.2.2 Vacua and generators

Now that the electroweak symmetry is embedded into $SU(4)$ we can define two distinct vacua breaking the $SU(4)$ global symmetry but preserving a $Sp(4)$ symmetry, namely:

$$\Sigma_C = \begin{pmatrix} i\sigma_2 & 0 \\ 0 & -i\sigma_2 \end{pmatrix}, \qquad \Sigma_{TC} = \begin{pmatrix} 0 & \mathbb{1} \\ -\mathbb{1} & 0 \end{pmatrix} \tag{6.4}$$

with Σ_C the vacuum leaving the electroweak symmetry unbroken, hence related to the Composite Higgs theory, and Σ_{TC} fully breaking the electroweak symmetry and hence related to the TC models. The two matrices are therefore two viable vacua for the symmetry breaking, each one preserving a different $Sp(4)$ subgroup of the initial $SU(4)$ flavor symmetry.

Moreover, group theory tells us that the unbroken generators T^a of $SU(4)$ for a given vacuum Σ must obey the following equation:

$$T^a \cdot \Sigma + \Sigma \cdot (T^a)^T = 0 \tag{6.5}$$

which is exactly the definition of an $Sp(4)$ Lie algebra. This relation allows the determination of the explicit expression of the unbroken generators associated with the chosen vacuum Σ.

The unbroken generators associated with the Σ_C vacuum are [109]:

$$S^{i=1,2,3} = \frac{1}{2}\begin{pmatrix} \sigma_i & 0 \\ 0 & 0 \end{pmatrix}, \qquad S^{i=4,5,6} = \frac{1}{2}\begin{pmatrix} 0 & 0 \\ 0 & -\sigma_{i-3}^T \end{pmatrix} \tag{6.6}$$

$$S^{i=7,8,9} = \frac{1}{2\sqrt{2}}\begin{pmatrix} 0 & i\sigma_{i-6} \\ -i\sigma_{i-6} & 0 \end{pmatrix}, \qquad S^{10} = \frac{1}{2\sqrt{2}}\begin{pmatrix} 0 & 1 \\ 1 & 0 \end{pmatrix} \tag{6.7}$$

and the broken ones are:

$$X^1 = \frac{1}{2\sqrt{2}}\begin{pmatrix} 0 & \sigma_3 \\ \sigma_3 & 0 \end{pmatrix}, \qquad X^2 = \frac{1}{2\sqrt{2}}\begin{pmatrix} 0 & i\mathbb{1}_2 \\ -i\mathbb{1}_2 & 0 \end{pmatrix}, \qquad X^3 = \frac{1}{2\sqrt{2}}\begin{pmatrix} 0 & \sigma_1 \\ \sigma_1 & 0 \end{pmatrix}, \tag{6.8}$$

$$X^4 = \frac{1}{2\sqrt{2}}\begin{pmatrix} 0 & \sigma_2 \\ \sigma_2 & 0 \end{pmatrix}, \qquad X^5 = \frac{1}{2\sqrt{2}}\begin{pmatrix} \mathbb{1}_2 & 0 \\ 0 & -\mathbb{1}_2 \end{pmatrix} \tag{6.9}$$

The first three unbroken matrices can be thought of as the generators of the embedded $SU(2)_L$ and the following three can be assimilated to the $SU(2)_R$ generators with, in particular, S^6 the generator of $U(1)_Y$. Hence, the electroweak symmetry is not broken, as expected in a Composite Higgs framework, and the custodial symmetry due to the presence of an initial $SU(2)_L \times SU(2)_R$ symmetry is preserved.

Note that, in this case, the five Goldstone bosons act under $SU(2)_L \times SU(2)_R \subset Sp(4)$ as a singlet and a bi-doublet [111]. The bi-doublet can be assimilated to the SM Higgs doublet containing the Composite Higgs candidate h and three other fields which are absorbed by the $W^\pm$ and Z^0 bosons after electroweak symmetry breaking. The singlet is a pseudoscalar state which we will call η and which can be seen as a possible DM candidate (see section 6.3.5 for more details).

The unbroken generators associated with the Σ_{TC} vacuum are:

$$S^1 + S^4, \qquad S^2 + S^5, \qquad S^3 + S^6, \qquad S^{7,9,10}, \qquad X^{1,2,3,5} \tag{6.10}$$

and the broken ones are:

$$S^1 - S^4, \qquad S^2 - S^5, \qquad S^3 - S^6, \qquad S^8, \qquad X^4 \tag{6.11}$$

This time, as S^i, $i \in \{1, ..., 6\}$, are not preserved, the electroweak symmetry $SU(2)_L \times U(1)_Y$ is broken but the charge generator $Q \equiv I_3 + \frac{Q_Y}{2} = S^3 + S^6$ is still unbroken. Hence, the symmetry breaking preserves $U(1)_{em}$ as expected.

In order to unify Composite and TC approaches we define the general vacuum Σ_0 as a superposition of the two vacua above:

$$\Sigma_0 = \cos\theta \; \Sigma_C + \sin\theta \; \Sigma_{TC} \tag{6.12}$$

Angle $\theta \in [0; \frac{\pi}{2}]$ represents the mixing between the two theories and is a free parameter of this FCD model. Hence, the model is similar to a Composite Higgs theory when $\theta \to 0$ and to a TC one if $\theta \to \frac{\pi}{2}$.

The broken generators associated with the general vacuum Σ_0 are therefore:

$$Y^1 = c_\theta X^1 - s_\theta \frac{S^1 - S^4}{\sqrt{2}}, \qquad Y^2 = c_\theta X^2 + s_\theta \frac{S^2 - S^5}{\sqrt{2}}, \qquad Y^3 = c_\theta X^3 + s_\theta \frac{S^3 - S^6}{\sqrt{2}}, \tag{6.13}$$
$$Y^4 = X^4, \qquad Y^5 = c_\theta X^5 - s_\theta S^8$$

with $c_\theta \equiv \cos\theta$ and $s_\theta = \sin\theta$.

These matrices will be used to derive the dynamical behavior of the Goldstone bosons.

6.2.3 Effective Lagrangian

The dynamical behavior of the Goldstone bosons can be obtained using the Callan-Coleman-Wess-Zumino (CCWZ) formalism [112, 113]. For this we need to define the Σ field containing the Goldstone boson fields:

$$\Sigma = e^{\frac{i}{f}\sum_{j=1}^{5} \phi_j Y^j} \cdot \Sigma_0 \tag{6.14}$$

with ϕ_j, $j \in \{1, ..., 5\}$, the Goldstone boson fields associated with the broken generators Y^i and f the decay constant of the Goldstone bosons, similar to the decay constant f_π of the pion in QCD.

Hence, the dynamical part of the Goldstone boson Lagrangian at the lowest order in the chiral expansion is given by:

$$\mathcal{L}_{dyn} = f^2 \mathrm{Tr}[(D_\mu \Sigma)^\dagger D^\mu \Sigma] \tag{6.15}$$

with D_μ the covariant derivative:

$$D_\mu \Sigma = \partial_\mu \Sigma - \left[i g W_\mu^a (S^a \Sigma + \Sigma S^{aT}) + i g' B_\mu (S^6 \Sigma + \Sigma S^{6T}) \right] \tag{6.16}$$

with S^a, $a = 1...3$ and S^6 the generators associated with $SU(2)_L$ and $U(1)_Y$ respectively.

Developing the above Lagrangian and performing the appropriate rotation as in the SM case make it possible to get rid of the first three Goldstone fields $\phi_{1,2,3}$ which are absorbed by the $W^\pm$ and Z^0 bosons to give them mass.

We are then left with only two physical fields: the Higgs candidate h which comes from the bi-doublet of the broken $SU(2)_L \times SU(2)_R$ symmetry and the pseudoscalar η, singlet under the broken $SU(2)_L \times SU(2)_R$. The Lagrangian (6.15) thus reads:

$$\begin{aligned}\mathcal{L}_{dyn} =& \frac{1}{2}(\partial_\mu h)^2 + \frac{1}{2}(\partial_\mu \eta)^2 \\ & - \frac{1}{48f^2}(h\partial_\mu \eta - \eta \partial_\mu h)^2 + \mathcal{O}(f^{-3}) \\ & + \left(2g^2 W_\mu^+ W^{-\mu} + (g^2 + g'^2) Z_\mu Z^\mu\right) \left[f^2 s_\theta^2 + \frac{s_{2\theta} f}{2\sqrt{2}} h \left(1 - \frac{1}{12f^2}(h^2+\eta^2)\right) \right. \\ & \left. + \frac{1}{8}(c_{2\theta} h^2 - s_\theta^2 \eta^2) \left(1 - \frac{1}{24f^2}(h^2+\eta^2)\right) + \mathcal{O}(f^{-3}) \right] \end{aligned} \tag{6.17}$$

In the above Lagrangian one can see that mass terms and couplings to the h and η particles arise for the $W^\pm$ and Z^0 gauge bosons.

As we work in an effective theory and hence do not have an established theory of flavor to work with, the mass terms and couplings to the Goldstone bosons for the SM fermions are harder to implement. We will however assume, following [109], that the fermion masses are generated via the following effective Yukawa interactions:

$$\mathcal{L}_{yuk} = f \left(y'_u{}^{i,j} (Q_{L,i} \tilde{u}_{R,j})^\dagger_\alpha + y'_d{}^{i,j} (Q_{L,i} \tilde{d}_{R,j})_\alpha + y'_l{}^{i,j} (L_{L,i} \tilde{l}_{R,j})^\dagger_\alpha \right) \mathrm{Tr}[P^\alpha \Sigma] + h.c. \tag{6.18}$$

with $\alpha = \{1,2\}$ an $SU(2)_L$ index, $i,j \in \{1,2,3\}$ generation indexes, $\tilde{u}_{R,j}$ the charged conjugate of the SM up-type quarks, $Q_{L,i}$ and $L_{L,i}$ the SM quark and lepton left doublets respectively and P^α 4×4 matrices that project out of Σ the components acting as a doublet of $SU(2)_L$.

Note that this term comes from a hypothetical four-fermion interaction term such as the one introduced in equation (6.1).

Developing the Lagrangian (6.18) in the top sector, one finds:

$$f y'_t (Q_L \tilde{t}_R)^\dagger_\alpha \mathrm{Tr}[P^\alpha \Sigma] \sim -y'_t \left(f s_\theta + \frac{1}{2\sqrt{2}} c_\theta h - \frac{1}{16f} s_\theta (h^2 + \eta^2) + ... \right) t_L \tilde{t}_R \tag{6.19}$$

which contains, as expected, a mass term in addition to terms describing the top couplings to the scalar h and pseudoscalar η.

We have now almost all the pieces of the new Yukawa and Higgs Lagrangian. However, until now, we have only focused on the Goldstone bosons coming from the $SU(4)$ symmetry breaking. We also have to consider the influence of the neutral composite scalar called σ, singlet under $Sp(4)$, that emerges naturally [114], on the above Lagrangians (6.15) and (6.18). For this, as σ is a singlet, we simply add its kinetic term and an appropriate factor $\xi(\sigma)$ depending on the σ field in front of each term of the above Lagrangians.

Finally one can write the full Lagrangian as:

$$\begin{aligned}\mathcal{L} = & \xi_G(\sigma) f^2 \mathrm{Tr}[(\mathcal{D}_\mu \Sigma)^\dagger \mathcal{D}^\mu \Sigma] \\ & + \frac{1}{2}\partial_\mu \sigma \partial^\mu \sigma - \frac{1}{2} M^2 \xi_M(\sigma) \sigma^2 \\ & + f\left(\xi_t(\sigma) y'^{\,i,j}_u (Q_{L,i} \tilde{u}_{R,j})^\dagger_\alpha + \xi_d(\sigma) y'^{\,i,j}_d (Q_{L,i} \tilde{d}_{R,j})_\alpha + \xi_l(\sigma) y'^{\,i,j}_l (L_{L,i} \tilde{l}_{R,j})^\dagger_\alpha\right) \mathrm{Tr}[P^\alpha \Sigma] + h.c.\end{aligned} \tag{6.20}$$

The first line corresponds to the kinetic term of the Goldstone bosons together with the $\xi_G(\sigma)$ correction coming from the scalar singlet σ. This term gives rise to the $W^\pm$ and Z^0 mass terms, to couplings between h, η, σ and a pair of gauge bosons W^+W^- or Z^0Z^0 and to trilinear (dynamical) couplings between the three scalars.

The second line corresponds to the kinetic and dynamical mass term of the σ field.

Finally, the last line gives rise to the fermion mass terms and to couplings between h, η, σ and a pair of fermions. Note that, as all the Yukawa terms have the same 4-fermion origin, one may expect that $\xi_t(\sigma) = \xi_b(\sigma) = \xi_l(\sigma)$. We will assume this hypothesis to be true in the remainder of this thesis.

The $\xi(\sigma)$ functions introduced in the Lagrangian (6.20) can be obtained theoretically by performing extensive lattice computations. These results do not exist yet but one can expand the ξ functions as follows [109]:

$$\xi_{G,M,t}(\sigma) \simeq 1 + \frac{\xi^{(1)}_{G,M,t}}{4\pi f}\sigma + \frac{1}{2}\frac{\xi^{(2)}_{G,M,t}}{(4\pi f)^2}\sigma^2 + ... \tag{6.21}$$

with $\xi^{(1)}$, $\xi^{(2)}$, additional unknown constant parameters of order unity and f the Goldstone boson decay constant already introduced.

Hence, using the different equations developed above, one can expand the Lagrangian (6.20) in order to obtain the gauge and fermion masses [109]:

$$m_W^2 = 2g^2 f^2 s_\theta^2, \qquad m_Z^2 = \frac{m_W^2}{\cos^2\theta_W}, \tag{6.22}$$

$$\frac{y_f v}{\sqrt{2}} \equiv m_f = y'_f f s_\theta \qquad \Rightarrow y_f = \frac{y'_f}{2} \tag{6.23}$$

with y_f the SM Yukawa couplings.

Note that the expression of m_W leads to a relation between the SM vev $v = 245$ GeV and the Goldstone bosons decay constant f:

$$v \equiv \frac{2m_W}{g} = 2\sqrt{2} f s_\theta \tag{6.24}$$

The development of Lagrangian (6.20) also gives us access to the explicit expression of the couplings involving at least one h, η or σ particle [109]. These couplings normalized to their SM values are summarized in table 6.2.

Using the results in table 6.2, we can note that the η cannot decay at tree level into a pair of gauge bosons nor into a pair of fermions. Indeed we can see that the full Lagrangian (6.20) is invariant under the symmetry:

$$\eta \to -\eta \tag{6.25}$$

which prevents the η particle from decaying. It is then stable and can potentially be a DM candidate. We will further study this hypothesis in section 6.3.5.

	$VV = WW, ZZ$	$f\bar{f}$
h	c_θ	c_θ
σ	$\tilde{\xi}_G s_\theta \equiv \frac{\xi_G^{(1)}}{2\sqrt{2}\pi} s_\theta$	$\tilde{\xi}_f s_\theta \equiv \frac{\xi_f^{(1)}}{\sqrt{2}\pi} s_\theta$
η	-	-

TABLE 6.2: Coupling of h, σ and η to the gauge bosons and fermions normalized to the SM value.

6.2.4 Mass generation of the pseudo-Goldstone bosons

We have established how the $W^\pm$ and Z^0 gauge bosons and the SM fermions acquire a mass and found the tree-level coupling between the scalars of the theory and the gauge bosons and fermions. However we still need to look at how the Goldstone bosons h and η acquire a mass and hence become pGBs.

We have seen that the initial $SU(4)$ symmetry is dynamically broken down to $Sp(4)$ by the appearance of a condensate, as in QCD. However there are terms in the Lagrangian which break explicitly the $SU(4)$ symmetry. The corrections coming from these terms will generate a small mass for the two pGBs and modify the mass of the σ which was initially a pure dynamical M term.

The most obvious explicit symmetry breaking term comes from the techniquark mass term $-M_Q^{ij} Q_i Q_j$ (see equation (6.3)) if the mass M_Q is aligned with the vacuum Σ_C: $M_Q \propto \Sigma_C$. Performing an infinitesimal $SU(4)$ transformation, one can check that the mass term stays invariant if and only if the $SU(4)$ generators check equation (6.5), that is, if they are unbroken under the $Sp(4)$ symmetry related to the Σ vacuum [109]. The other generators are thus broken by this term.

Corrections will also arise due to the embedding of the partially broken $SU(2)_L \times U(1)_Y$ symmetry and to top couplings to the vacuum [109].

The potential term which needs to be added to the Lagrangian in order to take into account these corrections is of the form:

$$V_{corr} = \xi_G(\sigma) V_{gauge} + \xi_t^2(\sigma) V_{top} + \xi_m(\sigma) V_m \tag{6.26}$$

where the $\xi(\sigma)$ factors have been added to take into account the influence of the σ particle.

As the corrections coming from the gauge sector are small compared to the ones from the top sector [109] we will neglect the V_{gauge} term in the following.

Based on the formalism developed in [115] one can deduce the expression of the resulting radiative corrections. Their general shapes have been computed in [116, 117] and developed in our notations in [109]:

$$\begin{aligned} \xi_t^2(\sigma) V_{top} &\sim -\xi_t^2(\sigma) C_t y_t'^2 \left(f^4 s_\theta^2 + \frac{1}{\sqrt{2}} f^3 c_\theta s_\theta h + \frac{1}{8} f^2 (c_{2\theta} h^2 - s_\theta^2 \eta^2) + ... \right) \\ \xi_m(\sigma) V_m &\sim \xi_m(\sigma) C_m \left(-4 f^4 c_\theta + \sqrt{2} f^3 s_\theta h + \frac{1}{4} f^2 c_\theta (h^2 + \eta^2) + ... \right) \end{aligned} \tag{6.27}$$

with C_t and C_m order 1 coefficients determined by the dynamics.

Using the two above equations and setting all fields to zero, one can deduce that the mini-

mization condition of the potential $V_{corr}(\theta)$ writes:

$$\cos\theta_{|min} = \frac{2C_m}{y_t'^2 C_t}, \qquad y_t'^2 C_t > 2|C_m| \tag{6.28}$$

This condition allows the substitution of C_m in the expression of V_{corr}.

From equation (6.27) one can deduce the mass of the pseudoscalar η:

$$m_\eta^2 = \frac{y_t'^2 C_t f^2}{4} \tag{6.29}$$

We can also see that, due to the $\xi(\sigma)$ factors added to the loop corrections the scalar h is not a mass eigenstate and mixes with the σ field. Hence we introduce the mass eigenstates h_1 and h_2, with $m_{h_1} < m_{h_2}$, defined as the rotation by an angle α of composite states h and σ:

$$\begin{pmatrix} h_1 \\ h_2 \end{pmatrix} = \begin{pmatrix} c_\alpha & s_\alpha \\ -s_\alpha & c_\alpha \end{pmatrix} \begin{pmatrix} h \\ \sigma \end{pmatrix} \tag{6.30}$$

The mass matrix in the (h, σ) basis writes [109]:

$$\begin{gathered} \mathcal{M} = \begin{pmatrix} m_h^2 & m_{h\sigma}^2 \\ m_{h\sigma}^2 & m_\sigma^2 \end{pmatrix}, \\ m_h^2 = m_\eta^2 s_\theta^2, \qquad m_\sigma^2 = M^2 - m_\eta^2 \left[\left(\tilde{\xi}_t^2 + \tilde{\xi}_t^{(2)} \right) s_\theta^2 + \tilde{\xi}_m^{(2)} c_\theta^2 \right] \\ m_{h\sigma}^2 = -\frac{1}{2} m_\eta^2 s_{2\theta} \left(2\tilde{\xi}_t - \tilde{\xi}_m \right) \end{gathered} \tag{6.31}$$

with the $\tilde{\xi}$ defined for simplicity as:

$$\begin{aligned} \tilde{\xi}_G &= \frac{\xi_G^{(1)}}{2\sqrt{2}\pi}, & \tilde{\xi}_t &= \frac{\xi_t^{(1)}}{\sqrt{2}\pi}, & \tilde{\xi}_m &= \frac{\xi_m^{(1)}}{\sqrt{2}\pi}, \\ \tilde{\xi}_G^{(2)} &= \frac{\xi_G^{(2)}}{4\pi^2}, & \tilde{\xi}_t^{(2)} &= \frac{\xi_t^{(2)}}{2\pi^2}, & \tilde{\xi}_m^{(2)} &= \frac{\xi_m^{(2)}}{2\pi^2} \end{aligned} \tag{6.32}$$

From the above equations we can deduce the mass eigenvalues m_{h_1} and m_{h_2} [109]:

$$\begin{aligned} m_{h_{1,2}}^2 =& \frac{1}{2} \Big[M^2 - m_\eta^2 \left(\tilde{\xi}_m^{(2)} c_\theta^2 + (\tilde{\xi}_t^2 + \tilde{\xi}_t^{(2)} - 1) s_\theta^2 \right) \\ & \mp \sqrt{\left[M^2 - m_\eta^2 \left(\tilde{\xi}_m^{(2)} c_\theta^2 + (\tilde{\xi}_t^2 + \tilde{\xi}_t^{(2)} + 1) s_\theta^2 \right) \right]^2 + m_\eta^4 s_{2\theta}^2 (2\tilde{\xi}_t - \tilde{\xi}_m)^2} \Big] \end{aligned} \tag{6.33}$$

constructed such that $m_{h_1} < m_{h_2}$. In addition, one can show [109] that the following bound stands:

$$m_{h_1} \leq m_\eta s_\theta \tag{6.34}$$

Hence, the light Higgs h_1, which will be assimilated to the 125 GeV Higgs, will be lighter than η. Therefore, there will not be any new decay such as $h_1 \to \eta\eta$ nor $h_1 \to h_2 h_2$.

6.2.4.1 *Scalar trilinear couplings*

The potential term V_{corr} together with the Lagrangian (6.20) allow the extraction of the tree-level trilinear couplings between the scalars h, η and σ. In particular one can find:

$$g_{\sigma hh} = -\frac{m_h^2}{v s_\theta}\left(\tilde{\xi}_m c_\theta^2 - 2\tilde{\xi}_t c_{2\theta}\right) - \frac{\tilde{\xi}_G s_\theta}{v} m_\sigma^2 \left(1 - \frac{2m_h^2}{m_\sigma^2}\right) \tag{6.35}$$

$$g_{\sigma\eta\eta} = -\frac{m_h^2}{v s_\theta}\left(\tilde{\xi}_m c_\theta^2 + 2\tilde{\xi}_t s_\theta^2\right) - \frac{\tilde{\xi}_G s_\theta}{v} m_\sigma^2 \left(1 - \frac{2m_\eta^2}{m_\sigma^2}\right) \tag{6.36}$$

The first term in equations (6.35) and (6.36) comes from V_{corr}. We will call it the potential part of the coupling. The second term of these equations comes from the Lagrangian (6.20) itself, and more precisely from the dynamical term $\xi_G(\sigma)\mathcal{L}_{dyn}$ (see equations (6.17) and (6.20)) where a term $\frac{\xi_G^{(1)}}{4\pi f}\sigma\left(\frac{1}{2}(\partial_\mu h)^2 + \frac{1}{2}(\partial_\mu \eta)^2\right)$ arises. This last term will be called the dynamical part of the coupling.

These relations will be useful when studying the heavy Higgs h_2 in the limit $\alpha \to 0$ in section 6.3.4.

6.3 $SU(4) \to Sp(4)$ BREAKING: PHENOMENOLOGY

6.3.1 PARTICLES AND FREE PARAMETERS

We have seen in section 6.2.1 that the breaking pattern $SU(4) \to Sp(4)$ leads to the emergence of pGB scalar and pseudoscalar h and η respectively and heavier condensates similar to the QCD mesons and baryons. One of them, the scalar singlet σ, can be sufficiently light to be a 125 GeV Higgs boson candidate.

As the h and σ have the same quantum numbers they mix and give rise to the mass eigenstates h_1 and h_2, with, by definition, $m_{h_1} < m_{h_2}$. The lightest state h_1 is assimilated to the 125 GeV Higgs boson and the heaviest h_2 to an additional heavy Higgs boson.

Even with only three additional particles compared to the SM case, the FCD model has ten free and unknown parameters, namely:

$$m_{h_1} = 125 \text{ GeV}, \quad m_{h_2}, \quad M, \quad \theta, \quad \alpha, \quad \tilde{\xi}_t, \quad \tilde{\xi}_t^{(2)}, \quad \tilde{\xi}_G, \quad \tilde{\xi}_G^{(2)}, \quad \tilde{\xi}_m, \quad \tilde{\xi}_m^{(2)} \tag{6.37}$$

However they do not play simultaneously a role in the different constraints we will impose on the FCD model. We then need to carefully specify which parameters influence each constraint.

6.3.2 CONSTRAINTS ON THE MODEL

In order to constrain the model we take into account the constraints coming from oblique parameters and the ones coming from LHC experiments, both on the 125 GeV Higgs boson and a possible heavy Higgs.

Note that, as we have seen in section 6.1.1, the implementation of a comprehensive theory of flavor without FCNC is not an easy task, so we will not consider any flavor constraints in the following. Moreover the LEP constraints do not have any influence on this FCD model since h_1, the lightest particle of the model, is set at $m_{h_1} = 125$ GeV, hence far beyond the reach of LEP data.

6.3.2.1 *Oblique parameters in FCD*

The precise determination of the oblique parameters in FCD models is a very delicate problem. The first issue is to identify precisely which contribution comes from the SM and which one comes from the strong dynamics. Then one needs to compute the latter numerically, through lattice computations for instance.

Such lattice results are not yet available but one can however roughly approximate the S and T parameters by [94]:

$$\begin{aligned} S &= \frac{1}{6\pi}\left[(1-k_{h_1}^2)\ln\frac{\Lambda}{m_{h_1}} - k_{h_2}^2\ln\frac{\Lambda}{m_{h_2}} + N_D s_\theta^2\right] \\ T &= -\frac{3}{8\pi\cos^2\theta_W}\left[(1-k_{h_1}^2)\ln\frac{\Lambda}{m_{h_1}} - k_{h_2}^2\ln\frac{\Lambda}{m_{h_2}}\right] \end{aligned} \tag{6.38}$$

with N_D the number of technifermion doublets – here, $N_D = 2$ – k_{h_1} and k_{h_2} the h_1 and h_2 couplings to $W^\pm$ and Z^0 gauge bosons normalized to the SM coupling:

$$k_{h_1} = \frac{g^{FCD}_{h_1VV}}{g^{SM}_{h_{125}VV}} = c_{\theta-\alpha} + (\tilde{\xi}_G - 1)s_\theta s_\alpha, \qquad k_{h_2} = \frac{g^{FCD}_{h_2VV}}{g^{SM}_{hVV}(m_{h_2})} = s_{\theta-\alpha} + (\tilde{\xi}_G - 1)s_\theta c_\alpha \tag{6.39}$$

and Λ the physical cutoff of the order of the mass of the spin-1 resonances, that is:

$$\Lambda \sim 4\pi f = \frac{\sqrt{2}\pi v}{s_\theta} \tag{6.40}$$

The terms $(1-k_{h_i}^2)\ln\frac{\Lambda}{m_{h_i}}$, $i = \{1,2\}$, stand for the contribution of the scalars h and σ respectively and the term $N_D s_\theta^2$ stands for the contribution of the fundamental fermions to the oblique parameters.

As FCD models do not change the U parameter, we used the data coming from [11] in the two-dimensional case, where U is assumed to be zero. These values are given in table 6.3.

	Experimental best fit	Uncertainty σ_i
$\widehat{S}_{\|U=0}$	0.06	0.09
$\widehat{T}_{\|U=0}$	0.10	0.07

$$\text{C}=\begin{array}{c} \begin{matrix} S & T \end{matrix} \\ \begin{pmatrix} 1 & 0.91 \\ 0.91 & 1 \end{pmatrix} \end{array} \begin{matrix} S \\ T \end{matrix}$$

TABLE 6.3: Experimental values of the S and T oblique parameters with 1σ uncertainty and their correlation matrix C [11].

Hence, one can compute the chi-squared function associated with the oblique parameters:

$$\chi^2_{S,T} = \begin{pmatrix} S - \widehat{S}_{|U=0} \\ T - \widehat{T}_{|U=0} \end{pmatrix}^T \cdot V^{-1} \cdot \begin{pmatrix} S - \widehat{S}_{|U=0} \\ T - \widehat{T}_{|U=0} \end{pmatrix} \tag{6.41}$$

with $\widehat{S}_{|U=0}$ and $\widehat{T}_{|U=0}$ the experimental best fit values of the S and T parameters assuming $U = 0$ and V^{-1} the inverse of their 2×2 covariant matrix defined by:

$$V_{ij} = C_{ij}\sigma_i\sigma_j, \qquad i,j \in \{1,2,3\} \tag{6.42}$$

with C the 2×2 correlation matrix between the oblique parameters and σ_i their corresponding uncertainty.

Looking at equation (6.38) we deduce that the S and T parameters depend on the independent parameters θ, α, $\tilde{\xi}_G$ and m_{h_2} – as m_{h_1} is fixed at 125 GeV. Hence, the chi-squared function related to the oblique parameters will rely on these four degrees of freedom:

$$\chi^2_{S,T} = f(\theta, \alpha, \tilde{\xi}_G, m_{h_2}) \tag{6.43}$$

6.3.2.2 *LHC 125 GeV Higgs constraints on FCD*

The light Higgs h_1 emerging in the FCD model is assimilated to the 125 GeV Higgs boson discovered at LHC. We can hence apply the LHC 125 GeV Higgs constraints in a similar way as in the 2HDM case.

One first needs to compute the signal strength of h_1 in the gluon fusion and $VBF + VH$ production modes for different decay channels YY. As all the new particles are heavier than the 125 GeV Higgs boson h_1 no additional channels will be open compared to the SM case. Hence we can use equation (3.28) and apply it to the FCD case:

$$\mu_{XX \to h_1 \to YY} = \kappa_X^2 \kappa_Y^2 \times \frac{1}{\sum\limits_Z \kappa_Z^2 BR^{SM}_{h_{125} \to ZZ}}, \qquad \kappa_X \equiv \frac{g^{FCD}_{h_1 XX}}{g^{SM}_{h_{125} XX}} \tag{6.44}$$

Here the κ factors are assimilated to the reduced couplings instead of the scaling factors as in the 2HDM case (see section 3.4.1.1), but the approach is entirely similar.

The κ related to both $W^\pm$, Z^0 boson and fermion couplings can be easily obtained using table 6.2 and knowing that, due to the mixing between h and σ, we have:

$$g^{FCD}_{h_1 XX} = c_\alpha \; g^{FCD}_{hXX} + s_\alpha \; g^{FCD}_{\sigma XX} \tag{6.45}$$

with $g^{FCD}_{h_1 XX}$ the couping between h_1 and two bosons or fermions and similarly for g^{FCD}_{hXX} and $g^{FCD}_{\sigma XX}$. Hence, the κ factors will depend on θ, α, $\tilde{\xi}_G$ and $\tilde{\xi}_t$ (see table 6.2).

The κ involving loop processes and hence which can only be defined by $\kappa_X^2 = \frac{\Gamma^{FCD}_{h_1 \to XX}}{\Gamma^{SM}_{h_{125} \to XX}}$ are more difficult to compute. We used the analytic expression of the decay width at one-loop level for the processes $h_1 \to gg$, $\gamma\gamma$ or $Z\gamma$ (see equation (C.1) in Appendix C with the amplitude due to a possible charged Higgs boson set to zero). These κ factors will depend on κ_t, κ_b, κ_τ and κ_V defined above, and hence will have the same dependence on the model's free parameters.

Then, using the ellipse parameters found using LHC 8 TeV data (see table 2.5) and 13 TeV data (see table 2.6), one can compute the total log-likelihood for each of these two data sets. Hence, one has to minimize the log-likelihood function and to determine the number of free parameters in order to impose the LHC constraints on 125 GeV Higgs boson.

We have shown that the κ factors depend on θ, α, $\tilde{\xi}_G$ and $\tilde{\xi}_t$. Hence, the LHC log-likelihood function will depend on these four independent parameters:

$$\chi^2_{LHC} = -2 \log \mathcal{L}_{tot} - \min\left(-2 \log \mathcal{L}_{tot}\right) = f(\theta, \alpha, \tilde{\xi}_G, \tilde{\xi}_t) \tag{6.46}$$

6.3.2.3 *LHC heavy Higgs constraints*

The last type of constraints we impose in our study is the constraints coming from LHC studies on possible heavy Higgs bosons. We will illustrate their influence by picking the most constraining ones, namely the two CMS studies on di-Higgs production through the decay of a heavier Higgs $pp \to h_2 \to h_{125}h_{125} \to b\bar{b}\tau\tau$ [68] and $pp \to h_2 \to h_{125}h_{125} \to b\bar{b}\gamma\gamma$ [70] and the ATLAS study on a heavy Higgs boson produced through gluon fusion and decaying into a pair of Z^0 bosons [24]. In order to use them one needs to compute the cross-section and branching ratios of the heavy Higgs h_2.

- Decay width computation

Knowing the tree-level coupling g_{h_2YY} of h_2 to two other particles YY one can easily compute the tree-level decay width for this specific decay channel cited above using the tree-level two-body decay formula:

$$d\Gamma_{h2\to YY} = \frac{1}{32\pi^2}|\mathcal{M}_{h_2YY}|^2\frac{|\overrightarrow{p_{h_2}}|}{m_{h_2}^2}d\Omega \tag{6.47}$$

with $|\mathcal{M}_{h_2YY}|^2$ the squared matrix element computed using the tree-level Feynman diagram of the $h_2 \to YY$ decay, $|\overrightarrow{p_{h_2}}|$ the norm of the three-vector momentum of h_2 and $d\Omega$ the solid angle associated with h_2.

This formula allows the computation of decays such as $h_2 \to h_1h_1$ or $h_2 \to \eta\eta$ that do not exist in the SM.

- Production cross-section computation

We choose to use the *kappa trick* method developed in section 3.4.1.5 to compute the production cross-section of the heavy Higgs boson h_2. We have seen that the method is not very accurate at intermediate masses, especially around twice the top mass, but it makes it possible to obtain a rough estimate of the production cross-section.

In this approximation we have, for any production mode XX:

$$\sigma^{FCD}_{XX\to h_2} \simeq \kappa_X^2\sigma^{SM}_{XX\to h_2}(m_{h_2}) \tag{6.48}$$

with $\sigma^{SM}_{XX\to h_2}(m_{h_2})$ the SM production cross-section value taken at a mass equal to m_{h_2} and κ_X the κ factor associated with the production mode – κ_V in the VBF or VH production mode, κ_g in the gluon fusion production mode.

As in section 6.3.2.2 we can define the κ of tree-level processes as the ratio between FCD coupling and SM coupling taken at the same m_{h_2} mass. Hence, for VBF or VH production modes, we find:

$$\kappa_V = \frac{g^{FCD}_{h_2WW}}{g^{SM}_{hWW}(m_{h_2})} = k_{h_2} \tag{6.49}$$

In the gluon fusion production case, the κ_g factor has to be computed using the analytic expression of the width at loop level (see equation (C.1) in Appendix C with the amplitude due to a possible charged Higgs boson set to zero) and is hence defined as:

$$\kappa_g^2 = \frac{\Gamma^{FCD}_{h_2\to gg}}{\Gamma^{SM}_{h\to gg}(m_{h_2})} \tag{6.50}$$

With the above definitions we are able to compute the cross-section times branching ratios of the heavy Higgs h_2. We will specify in section 6.3.4 which free parameters they rely on.

6.3.3 Constraints on the light Higgs state h_1

In this section we will only consider the oblique parameter constraints and the LHC 125 GeV Higgs constraints. The influence of the heavy Higgs constraints will be treated in section 6.3.4.

We will first look at two limiting scenarios: the Composite pGB limit, where $\alpha \to 0$ and $h_1 \to h$, and the TC limit, where $\alpha \to \frac{\pi}{2}$ and $h_1 \to \sigma$.

Finally we will look at a more general case where both α and θ are left free and hence, where the 125 GeV Higgs boson is a mixing between the h and the σ states.

Note that the following results are an update of the ones published in [118]. Hence, all the results implying LHC studies at 13 TeV are performed with the latest results and are entirely new.

6.3.3.1 *Composite pseudo-Goldstone boson limit*

The Composite pseudo-Goldstone boson limit corresponds to the case where the σ particle totally decouples, that is, where $\alpha = 0$ and $\tilde{\xi}_G = \tilde{\xi}_t = 0$. Under this assumption the Higgs candidate h_1 is assimilated to the pGB h and h_2 to the σ particle.

Moreover σ – or equivalently h_2 – is assumed to be heavy compared to h_1 in the decoupling limit. We will hence fix $m_{h_2} \sim 1$ TeV. However the value of m_{h_2} will have no influence at all as the LHC log-likelihood function depends only on h_1 and, under the hypotheses $\alpha = 0$ and $\tilde{\xi}_G = 0$ the $h_2 = \sigma$ does not couple to gauge bosons and hence, does not contribute to S and T.

Looking at equations (6.43) and (6.46), one can see that, under the pGB limit hypothesis, the oblique parameters S and T and the LHC log-likelihood function depend only on θ. Hence, both oblique parameter and LHC constraints will provide an upper bound at 3σ on θ, given by the condition that $\chi^2_{S,T}(\theta), \chi^2_{LHC}(\theta) < b_1^{3\sigma}$ – with $b_1^{3\sigma}$ the 3σ bound for a chi-squared function with one degree of freedom (see table 2.4).

The upper bounds at 3σ on θ are summarized in table 6.4.

	LHC (8 TeV data)	LHC (13 TeV data)	Oblique parameters
θ upper bound	0.46	0.39	0.25

Table 6.4: Upper bound on θ obtained in the pGB limit using LHC 125 GeV Higgs constraints at 8 TeV and 13 TeV and using oblique parameter constraints.

We can see that the oblique parameter constraints set a more restrictive bound on θ than the LHC constraints. However the bound coming from the 13 TeV LHC data is significantly lower than the one obtained with 8 TeV data. We can expect that, by the end of LHC Run II, this bound will be even lower and may be very close to the one coming from oblique parameter constraints.

One can imagine a situation where $\alpha \sim 0$, *i.e.* where we still have $h_1 = h$, but where $\tilde{\xi}_G \neq 0$, that is, where σ is not totally decoupled. Although this will not affect the LHC log-likelihood function, which is only influenced by the 125 GeV Higgs boson h_1, it will modify the oblique parameters as S and T are both sensitive to scalar Higgs-type particles coupling to a pair of $W^\pm$ or Z^0 bosons.

Therefore, for a fixed non-zero $\tilde{\xi}_G$ value, we can derive an upper bound at 3σ on θ depending on $m_\sigma = m_{h_2}$, given by the condition that $\chi^2_{S,T}(\theta, m_{h_2}) < b_2^{3\sigma}$.

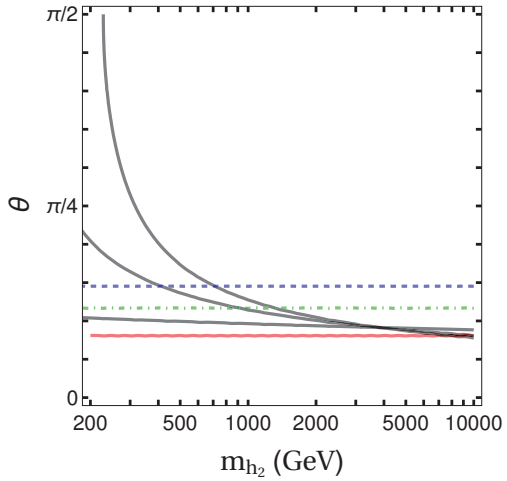

FIGURE 6.1: Upper bound on θ as a function of the mass $m_\sigma = m_{h_2}$ in the pGB hypothesis $\alpha \to 0$ with partial σ decoupling. The red solid line corresponds to the bound coming from oblique parameter constraints at 3σ in the total decoupling limit – $\tilde{\xi}_G = \tilde{\xi}_t = 0$ – the black solid lines correspond to partial decoupling cases with $\tilde{\xi}_G$=0.5, 1 and 1.2 and the dashed blue (dotted dashed green) line corresponds to the upper limit due to LHC 125 GeV Higgs constraints at 8 TeV (13 TeV).

These upper bounds are drawn in figure 6.1. The bound coming from the oblique parameter constraints in the total decoupling hypothesis is drawn as a red solid line, the ones obtained in the partial decoupling hypothesis are drawn as black solid lines – bottom from top: $\tilde{\xi}_G = 0.5,\ 1,\ 1.2$ – and the bound coming from LHC 125 GeV Higgs constraints at 8 TeV (13 TeV) is drawn as a dashed blue (dotted dashed green) line.

We can see that when the decoupling hypothesis is partially lifted the upper bound on θ coming from oblique parameter constraints is relaxed, especially for low m_{h_2} values. In this region, and depending on the $\tilde{\xi}_G$ value, the LHC constraints can become more restrictive than the oblique parameter ones.

Note that additional constraints can arise from heavy Higgs LHC analyses. This will be studied in section 6.3.4.

6.3.3.2 *Technicolor limit*

Another interesting limit is the case where the Higgs candidate corresponds to the σ particle. This may be achieved *via* cancellations between the dynamical mass M, of the order of a TeV, and loop contributions from explicit breaking of the global flavor symmetry, such as top loops [119].

In this limit $\theta = \frac{\pi}{2}$ and $\alpha = \frac{\pi}{2}$, which means that $h_1 = \sigma$ and $h_2 = h$. Moreover, due to the $\theta = \frac{\pi}{2}$ hypothesis, the pGB h does not couple any more to pairs of $W^\pm$, Z^0 bosons nor to pairs of fermions (see table 6.2). Hence in this limit the scalar h and the pseudoscalar η are

degenerate and can both play the role of a DM candidate [109] with a mass:

$$m_{DM}^2 = m_h^2 = m_\eta^2 = \frac{C_t y_t'^2 f^2}{4} \tag{6.51}$$

As h does not couple any more to pairs of weak bosons, oblique parameters will no longer depend on it. This intuition can be checked mathematically. Indeed the parameters k_{h_1} and k_{h_2} involved in the computation of the oblique parameters become in the Technicolor limit:

$$k_{h_1} = \tilde{\xi}_G, \qquad k_{h_2} = 0 \tag{6.52}$$

Hence, the S and T parameters will only depend on $\tilde{\xi}_G$ and the related limit at 3σ will be given by the condition $\chi^2_{S,T}(\tilde{\xi}_G) < b_1^{3\sigma}$.

As the LHC log-likelihood function depends on $\tilde{\xi}_G$ and $\tilde{\xi}_t$ in this limit, then the LHC 125 GeV Higgs boson constraints will be given by the condition $\chi^2_{LHC}(\tilde{\xi}_G, \tilde{\xi}_t) < b_2^{n\sigma}$, leading to exclusion contours at $n\sigma$ on these two parameters.

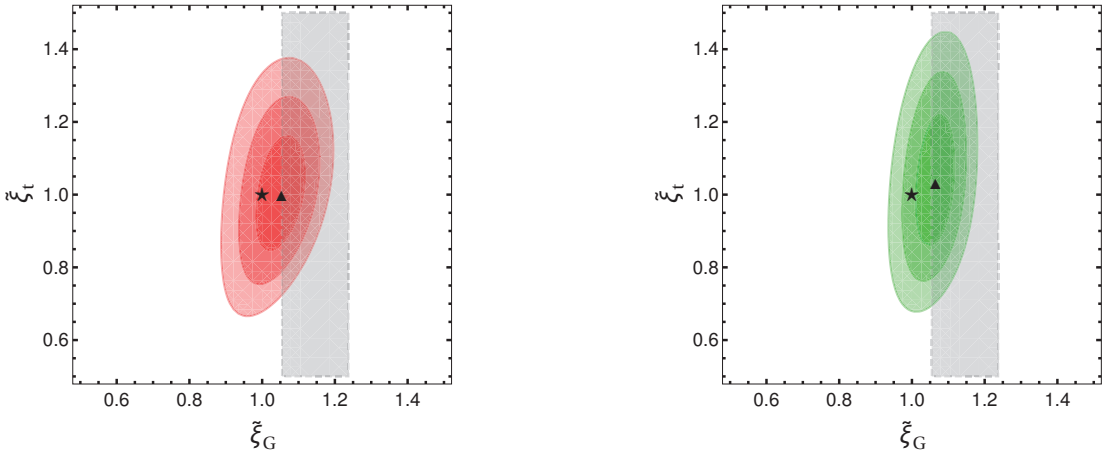

(A) 8 TeV data

(B) 13 TeV data.

FIGURE 6.2: Exclusion contours obtained from the LHC 125 GeV Higgs constraints in the TC limit – $\theta = \alpha = \frac{\pi}{2}$ – at 1, 2 and 3σ. The black triangle corresponds to the LHC log-likelihood best-fit whereas the star corresponds to the SM value. The light grey area represents the region not excluded by oblique parameter constraints at 3σ.

The exclusion contours at 1, 2 and 3σ obtained using the LHC 125 GeV Higgs constraints are drawn in figure 6.2 using 8 TeV data (left panel) and 13 TeV data (right panel). That obtained at 3σ with oblique parameter constraints is drawn in light gray. The colored areas correspond to the regions that are not excluded.

We can see that a large region around the SM value – $\tilde{\xi}_G = \tilde{\xi}_t = 1$, represented in the figures by a black star – is still not excluded by LHC data. Moreover the overlap between the region allowed by oblique parameter constraints and the ones allowed by LHC at both 8 TeV and 13 TeV is quite large.

It shows that, provided that such light composite state σ exists, the Technicolor limit is not yet excluded.

6.3.3.3 *General case*

We now consider the general case where the values of θ and α are not determined. Hence, the physical 125 GeV Higgs boson will be a mix between the Composite Higgs particle h and the TC condensate σ.

In order to reduce the number of unknown parameters we are working with, we decide to fix $\tilde{\xi}_G = \tilde{\xi}_t \equiv \tilde{\xi}$. Moreover we fix the mass of the heavy Higgs h_2 at $m_{h_2} = 1$ TeV. Note that m_{h_2} will only affect the limit given by the oblique parameter constraints and its exact value has little influence on the exclusion bound at 3σ.

In this case both the oblique parameter constraints and the LHC constraints depend on two degrees of freedom, namely θ and α. Hence, the bounds are given by:

$$\chi^2_{S,T}(\theta,\alpha) < b_2^{3\sigma}, \qquad \chi^2_{LHC}(\theta,\alpha) < b_2^{n\sigma}, \qquad n = 1,2,3 \tag{6.53}$$

We show the exclusions obtained for three different values of $\tilde{\xi}$: $\tilde{\xi} = 1$ (figure 6.3), $\tilde{\xi} = 1.1$ (figure 6.4) and $\tilde{\xi} = 0.8$ (figure 6.5). The colored areas correspond to the not-excluded zones at 1, 2 and 3σ using 8 TeV LHC data (left panel) or 13 TeV LHC data (right panel). The dashed grey contour corresponds to the exclusion contour at 3σ due to the oblique parameter constraints.

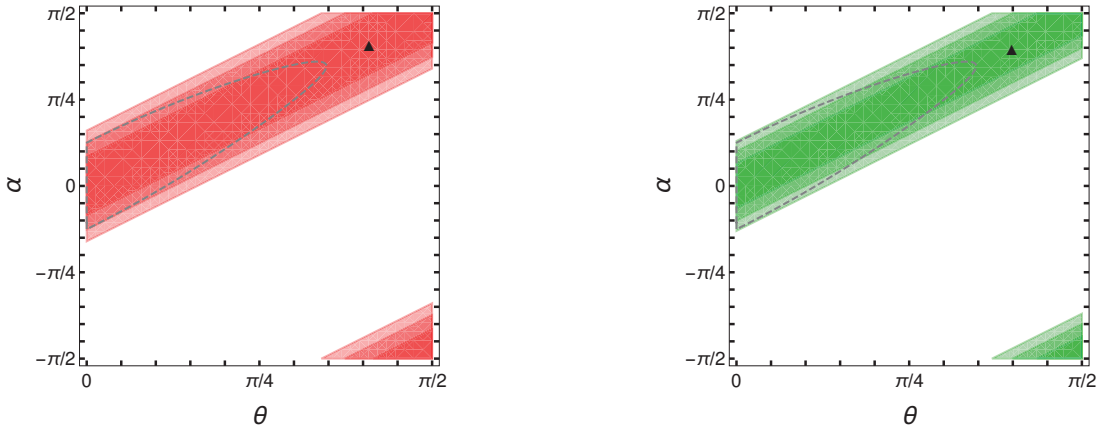

(A) 8 TeV data

(B) 13 TeV data.

FIGURE 6.3: Exclusion contours obtained from the LHC 125 GeV constraints at 1, 2 and 3σ assuming $\tilde{\xi}_G = \tilde{\xi}_t = 1$ and using 8 TeV data (left panel) and 13 TeV data (right panel). The triangle corresponds to the LHC log-likelihood best-fit. The inside of the dashed grey contour represents the not-excluded region by oblique parameter constraints at 3σ.

In figure 6.3 the region allowed by LHC constraints is around the line $\alpha = \theta$. Indeed, looking at table 6.2, and under the hypothesis that $\tilde{\xi}_G = \tilde{\xi}_t = \tilde{\xi}$, one can see that the coupling g_{h_1XX} between h_1 and two gauge bosons or a pair of fermions writes:

$$g_{h_1XX} = k_{h_1} g^{SM}_{h_{125}XX} = \left(c_{\theta-\alpha} + (\tilde{\xi}-1)s_\theta s_\alpha\right) g_{h_{125}XX} \tag{6.54}$$

Hence, if $\tilde{\xi} = 1$, the second term disappears and we are left with:

$$g_{h_1XX} = c_{\theta-\alpha} g_{h_{125}XX} \tag{6.55}$$

As LHC constraints favor $g_{h_1XX} \sim g_{h_{125}XX}$ this leads to $\theta \sim \alpha$.

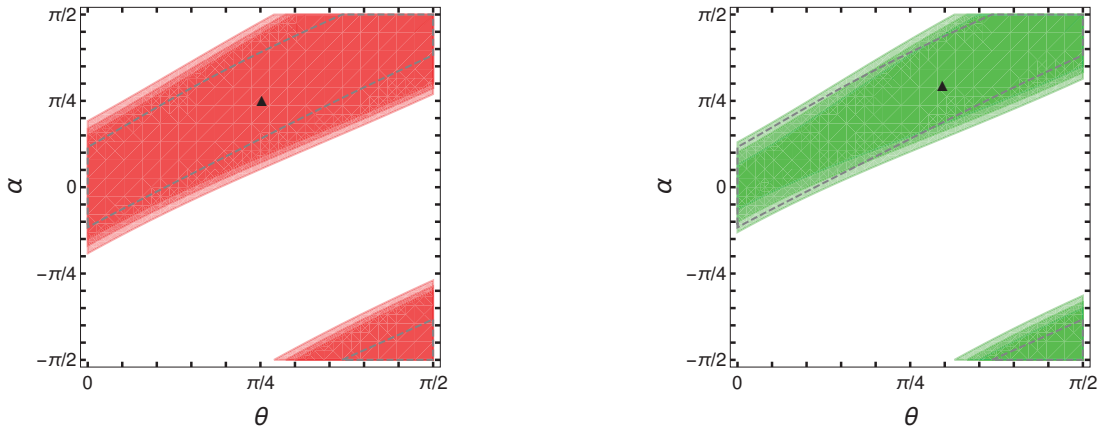

(A) 8 TeV data

(B) 13 TeV data.

FIGURE 6.4: Same as figure 6.3 with $\tilde{\xi}_G = \tilde{\xi}_t = 1.1$.

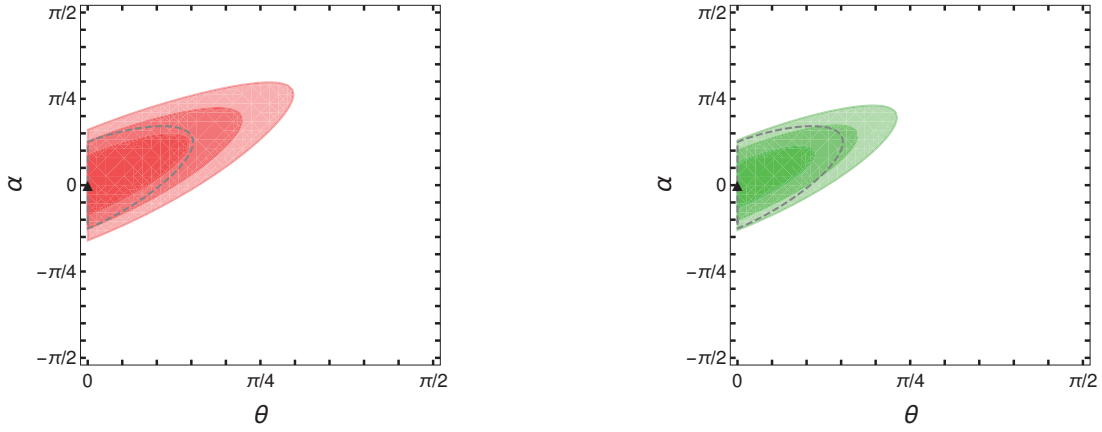

(A) 8 TeV data

(B) 13 TeV data.

FIGURE 6.5: Same as figure 6.3 with $\tilde{\xi}_G = \tilde{\xi}_t = 0.8$.

In the case where $\tilde{\xi} \neq 1$ the $\alpha \sim \theta$ condition is no longer true. If $\tilde{\xi} > 1$ (see figure 6.4) then the second term in equation (6.54) – $(\tilde{\xi} - 1)s_\theta s_\alpha$ – is positive for $\alpha > 0$ and can compensate a decrease of the first term due to a divergence between α and θ values. The higher α and θ are, the larger the divergence between them can be. This behavior is visible in figure 6.4.

If $\tilde{\xi} < 1$ (see figure 6.5), as $\theta \in [0; 2\pi]$ by definition, the second term can be positive only if $\alpha < 0$. Hence, at large – positive – value of θ and α, a decrease of $c_{\theta-\alpha}$ cannot be counterbalanced by an increase of the second term. That is why the region at high θ and α is excluded in this case.

Note that the exclusions obtained using 8 TeV and 13 TeV data are quite similar. The allowed area is simply shrunk around the $\alpha = \theta$ line in the 13 TeV case compared to the 8 TeV one.

Also note that the 3σ exclusion contour due to oblique parameter constraints is consistent with those due to the LHC constraints. Although it is still the most constraining, the LHC

exclusions at 13 TeV data are very close to it. By the end of LHC Run II they can be expect to be more constraining than the oblique parameter constraints.

6.3.4 Constraints on the heavy Higgs state h_2

Although we have used LHC data constraining the 125 GeV Higgs boson h_1 until now we have not considered yet LHC constraints on the heavier Higgs boson h_2. This will be the goal of this section.

In order to simplify the analysis we will restrict ourselves to the case where $\alpha \to 0$. Hence h_1 corresponds to the Composite Higgs h and h_2 corresponds to the σ particle.

Under this hypothesis h_2 will decay essentially into a pair of $W^{\pm}$ or Z^0 bosons or into $t\bar{t}$, h_1h_1 or $\eta\eta$. The decays into other fermions or into a pair of gluons or photons via loop processes are negligible compared to the ones cited above.

Using table 6.2 and equations (6.35), (6.36) and (6.47), one can compute the tree-level decay width for the five decay channels cited above.

As the decay channels other than those cited above are negligible, we can assume that the total decay width $\Gamma^{h_2}_{tot}$ is essentially:

$$\Gamma^{h_2}_{tot} \simeq \Gamma_{h_2\to W^+W^-} + \Gamma_{h_2\to Z^0Z^0} + \Gamma_{h_2\to t\bar{t}} + \Gamma_{h_2\to h_1h_1} + \Gamma_{h_2\to\eta\eta} \tag{6.56}$$

Hence we can deduce the value of the branching ratio for the five main decay channels.

Using table 6.2 and equations (6.35) and (6.36), and knowing that $\alpha \approx 0$, $m_h = m_{h_1} = 125$ GeV, $m_\sigma = m_{h_2}$ and $m_\eta = \frac{m_h}{s_\theta}$, we can deduce the dependence of the total decay width, and hence of the branching ratios, on the free parameters of the model:

$$\Gamma^{h_2}_{tot}, BR_{h_2\to YY} = f(\theta, \tilde{\xi}_G, \tilde{\xi}_t, \tilde{\xi}_m, m_{h_2}) \tag{6.57}$$

We show a typical plot of the branching ratios in figure 6.6. We set $\theta = 0.2$, $\tilde{\xi}_G = \tilde{\xi}_t = 1$ and $\tilde{\xi}_m = 0$ and compute the value of the different branching ratios as a function of m_{h_2}.

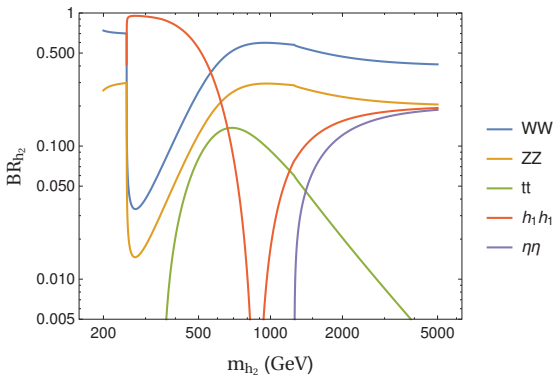

Figure 6.6: Branching ratios of h_2 as a function of its mass in the limit $\alpha \to 0$. We have chosen $\theta = 0.2$, $\tilde{\xi}_G = \tilde{\xi}_t = 1$ and $\tilde{\xi}_m = 0$.

The variation of the four fixed parameters has little influence on the shape of the figure. We can notice that the branching ratio of $h_2 \to h_1h_1$ process goes to zero for a specific value of m_{h_2}. This is due to the cancellation between the potential part and the dynamical part of

the $g_{\sigma hh}$ coupling (see equation (6.35)). This cancellation will be present as long as $\tilde{\xi}_G \neq 0$ and will occur at a precise value of m_{h_2} which depends on the value chosen for $\tilde{\xi}_G$, $\tilde{\xi}_t$, $\tilde{\xi}_m$ and θ.

We can also note that the value of the branching ratios in the W^+W^-, Z^0Z^0, h_1h_1 and $\eta\eta$ decay channels stabilize at high m_{h_2} around 40% for W^+W^- and 20% for the others. This is due to the fact that, in the high-mass limit, the σ couples essentially to the Goldstone bosons, and this in a similar way. Hence, the σ will decay into h_1h_1, $\eta\eta$ and Z^0Z^0 with the same amount – as the coupling to Z^0Z^0 involves the Z^0 longitudinal component, which is one of the five original Goldstone bosons – and into W^+W^- with a ratio of 2 with respect to the ZZ decay – as the W^+ and W^- involve two Goldston bosons instead of one. Hence the W^+W^- decay width is $\frac{2}{5}$ of the total decay width and the Z^0Z^0, h_1h_1 and $\eta\eta$ are all $\frac{1}{5}$ of the total decay width. This behavior is visible in figure 6.6.

A mathematical development of the above explanation is performed in Appendix F.

The method for computing the production cross-section has been described in section 6.3.2.3. Hence, using the production cross-section and the branching ratio computations described above we can now constrain the FCD model using heavy Higgs constraints. We have listed the three analyses which impose the most severe constraints in section 6.3.2.3. Note that the selected studies are different from those used in our published paper [118] as I used for this thesis the latest LHC results at 13 TeV, which are more constraining than the ones at 8 TeV used in [118].

In order to simplify the study, we will fix the value of $\tilde{\xi}_G$, $\tilde{\xi}_t$ and $\tilde{\xi}_m$ and draw the upper limit on θ depending on m_{h_2} obtained using the heavy Higgs constraints, in a similar way to what was done in section 6.3.3.1.

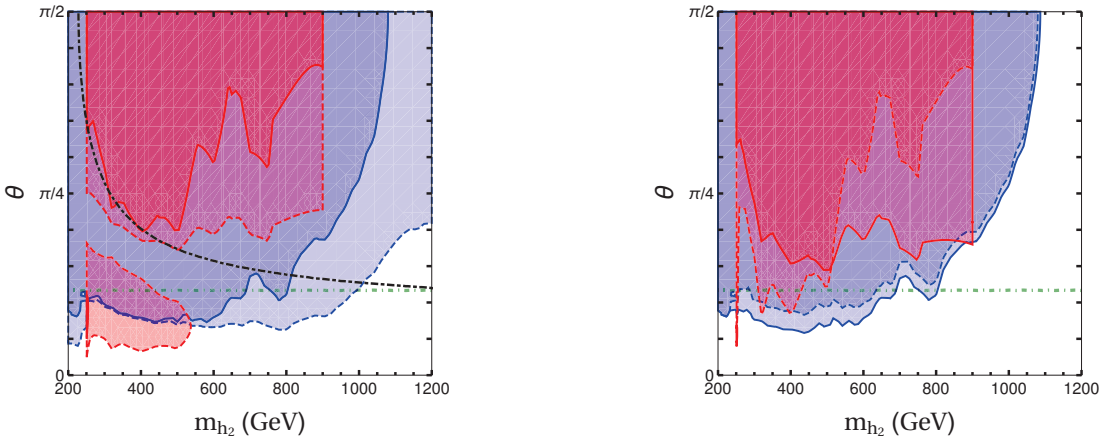

(A) $\tilde{\xi}_G = 1.2$, $\tilde{\xi}_m = 0$; $\tilde{\xi}_t = 1$ (solid lines), $\tilde{\xi}_t = 2$ (dashed lines).

(B) $\tilde{\xi}_t = 1$; $\tilde{\xi}_G = 3$, $\tilde{\xi}_m = 0$ (solid lines), $\tilde{\xi}_G = 1.2$, $\tilde{\xi}_m = 3$ (dashed lines).

FIGURE 6.7: Upper bound on θ due to heavy Higgs constraints. The colored areas are excluded at 2σ using the process $h_2 \to h_1h_1$ [68, 70] (red areas) and $h_2 \to ZZ$ [24] (blue areas). The dashed black line in the left panel corresponds to the upper limit on θ using oblique parameter constraints with $\tilde{\xi}_G = 1.2$. The dotted dashed green line corresponds to the upper limit on θ given by the LHC 125 GeV Higgs boson constraints at 3σ.

The upper bounds on θ depending on m_{h_2} are shown in figure 6.7, where the colored areas are, this time, excluded at 2σ by the heavy Higgs constraints. The red zones are excluded by $h_2 \to h_1h_1$ studies [68, 70] whereas the blue ones are excluded by $h_2 \to ZZ$ study [24].

Also included in the same figure as a dashed black line is the upper limit on θ obtained using

the oblique parameter constraints in the same way as in section 6.3.3.1 – where $\chi^2_{S,T}$, once $\tilde{\xi}_G$ is fixed, depends only on θ and m_{h_2}.

As we have seen in section 6.3.3.1, in the limit $\alpha \to 0$, the LHC log-likelihood function depends only on θ. Hence, the upper bound obtained using the LHC 125 GeV Higgs boson constraints at 13 TeV is drawn in figure 6.7 as a horizontal dotted dashed green line.

In figure 6.7a the parameters are set to $\tilde{\xi}_G = 1.2$ and $\tilde{\xi}_m = 0$ for the four curves but $\tilde{\xi}_t = 1$ for the solid lines and $\tilde{\xi}_t = 2$ for the dashed lines. In figure 6.7b the parameters are set to $\tilde{\xi}_t = 1$ for the four curves and $\tilde{\xi}_G = 3$, $\tilde{\xi}_m = 0$ for the solid lines and $\tilde{\xi}_G = 1.2$, $\tilde{\xi}_m = 3$ for the dashed lines.

We can see that the heavy Higgs constraint on the process $h_2 \to ZZ$, represented by the blue lines, is very competitive compared to both oblique parameter and 125 GeV Higgs constraints, especially in the case $\tilde{\xi}_t = 2$ (see dashed blue line of figure 6.7a). This is less true above 1 TeV, where the bound on θ increases a lot.

The upper bound on θ obtained using the process $h_2 \to h_1 h_1$ is essentially less constraining than the others but is still interesting as an excluded island appears in the low-mass region of figure 6.7a. The island in the case $\tilde{\xi}_t = 1$ (solid red line) is barely visible and excludes $\theta \in [\frac{\pi}{16}; \frac{\pi}{8}]$ around $m_{h_2} \sim 250$ GeV. The island for $\tilde{\xi}_t = 2$ (dashed red line) is much larger.

The influence of the $\tilde{\xi}_t$ parameter can be seen on figure 6.7a. The upper bound on θ lowers for both $h_2 \to ZZ$ and $h_2 \to h_1 h_1$ when $\tilde{\xi}_t$ grows.

We can see that the $\tilde{\xi}_G$ parameter has little influence on the upper limit on θ by comparing the solid lines of figure 6.7b to the solid lines of figure 6.7a. The upper bound at low m_{h_2} is slightly lower when $\tilde{\xi}_G$ increases, but the influence is quite small.

The influence of $\tilde{\xi}_m$ is much more important: comparing the dashed lines from figure 6.7b and the solid lines from figure 6.7a one can see that the upper bound on θ given by $h_2 \to h_1 h_1$ process is much lower when $\tilde{\xi}_m$ increases. The upper limit given by $h_2 \to ZZ$ process is however slightly higher than in the case $\tilde{\xi}_m = 0$.

We can conclude that the heavy Higgs constraints are very useful to constrain FCD models as they are very competitive with the other constraints, and, depending on the value of the $\tilde{\xi}$ parameters, can even be better than oblique parameter and 125 GeV Higgs constraints.

6.3.5 Study of the pseudoscalar η

In the naive development of the effective Lagrangian performed in sections 6.2.3 and 6.2.4 we have seen that it is invariant under the symmetry $\eta \to -\eta$, thus preserving η to decay.

However this property is no longer true in the fermionic sector if one looks at higher-order operators: one can show [118] that η has tree-level couplings to pairs of fermions. Note that, as it is not part of my own work, I will not go into details and just summarize the concept.

The main idea of this development is to construct invariant operators under $SU(4)$ symmetry using the spurions already introduced such as the techniquark mass M_Q, the projectors P^α ($\alpha = \{1, 2\}$) or the S^i generators ($i \in \{1, 2, 3, 6\}$) associated with the SM gauge bosons. Then, developing these operators – as done in equation (6.19) for instance – terms involving one η and a pair of fermions appear. Some of these terms can be set to zero by a simple rotation with no physical meaning, but others cannot be canceled, thus allowing the η to decay into pairs of

fermions.

Although the η does not couple to a pair of gauge bosons at tree level, the coupling can be generated through the Wess-Zumino-Witten anomaly term [120, 121]. Computing it in the FCD framework, one can show that the couplings to a pair of gluons or photons are canceled but the couplings to W^+W^-, ZZ or $Z\gamma$ are non-zero [117]. Note however that the gluon gluon and gamma gamma couplings are probably non-zero when looking at higher-order operators, in a similar way to what was done in the fermion case.

Using all these results one can compute the width and the branching ratios of the η particle (see figure 2 in [117]). The conclusion is that, regardless of the mass of η, it is always able to decay into at least $Z\gamma$. Hence this is not a viable DM candidate as the latter is assumed to be stable.

In [118] the production cross-section of η in a pp collider is computed in order to estimate if it can be detected at the LHC. The simulation is made using `Madgraph` [122] with the MSTW2008NLO PDF set [123]. The production cross-section is unfortunately very low – at most 1 fb – and decreases as m_η increases. Hence it would be very difficult to detect it at the LHC.

For completeness [118] also calculated the production cross-section at a linear electron-positron collider such as the ILC. They are also very low – at most $\sim 10^{-3}$ fb – meaning that discovering this particle would require an enormous amount of luminosity.

We can conclude that the η particle is neither a good DM candidate nor a useful particle to probe this FCD model in existing accelerators. However it may have a sizable production rate if produced from the decay of heavier resonances, such as spin-1 or spin-$\frac{1}{2}$ condensates (see for instance [124]).

6.4 Conclusion

We have exposed in this part the mechanism of Technicolor and Composite Higgs theories, both relying on a new strongly coupled interaction and on related new fermions, called techniquarks. In both theories, the global flavor symmetry occurring in the techniquark sector is broken at low energy by the presence of a condensate, leading to the appearance of Goldstone bosons and heavy condensates similar to the QCD pions and heavier hadrons respectively.

We have seen how these two theories could be gathered into an intermediate one, called Fundamental Composite Dynamics, and have studied the phenomenology of the specific symmetry breaking $SU(4) \to Sp(4)$ under this unified theory.

The $SU(4) \to Sp(4)$ breaking gives rise to two pseudo-Goldstone bosons, the scalar h and pseudo-scalar η. Moreover heavy condensates appear after the breaking. In our study we consider the lightest scalar state singlet under the $Sp(4)$ symmetry, called σ. As its quantum numbers are identical to those of the h, the two particles will mix and form the two mass eigenstates h_1 and h_2. The lightest one, h_1, is assumed to be the 125 GeV Higgs boson discovered at LHC.

We have shown that, using at the same time rough estimate of oblique parameter constraints, LHC 125 GeV Higgs boson constraints and LHC heavy Higgs constraints, we are able to suppress large parts of the parameter space. In particular, the heavy Higgs constraints on the processes $h_2 \to ZZ$ and $h_2 \to h_1 h_1$ at 13 TeV are very competitive with the oblique parameter constraints.

More generally, the 13 TeV results substantially improve the constraints on the different free parameters but this FCD model is still viable, even when confronted with experimental data.

For completeness we also mentioned the phenomenological study of the pseudoscalar η performed in [118]. As the particle is eventually always able to decay into $Z\gamma$ through anomaly diagrams, the particle is not a viable candidate for DM. Moreover its production cross-section in pp colliders such as LHC or e^+e^- colliders such as ILC is lower than 1 fb; hence its possible study in colliders seems very unlikely.

The $SU(4) \to Sp(4)$ breaking is the minimal symmetry breaking pattern which can occur in a FCD scenario. Many other symmetry breakings can be chosen, such as $SU(6) \to Sp(6)$. Other breakings will provide additional Goldstone bosons, making the phenomenology of the model richer, with the possible appearance of charged scalars for instance.

In this study we have only focused on scalar particles. However one can also study non-scalar resonances – spin-one condensates for instance. This is done *via* lattice computation in [108, 125].

General conclusion

In this thesis I have exposed my work on the scalar sector of two distinct theories beyond the Standard Model.

The study of the first theory, the CP-conserving Two-Higgs Doublet Model, was performed in two different frameworks: the first one assuming the heavier Higgs boson of the theory to be the 125 GeV Higgs boson discovered at the LHC, and the second one assuming the lighter Higgs boson to be the 125 GeV Higgs boson. In this latter case I assumed in addition to be in the alignment limit, *i.e.* that the couplings of the light Higgs boson deviate from those of the SM Higgs boson with less than 1%.

For both frameworks I have checked the model against different theoretical and experimental constraints. I exposed carefully the influence of each constraint on the parameter space before showing the parameter space finally available after having applied all constraints.

This work has been done in the four different available CP-conserving 2HDM types – types I, II, Flipped and Lepton-Specific – for the $m_H = 125$ GeV hypothesis. I have been able to conclude that Lepton-Specific and Flipped types were very similar to Type I and II respectively. Hence, the similar study has only been done in Type I and II for the $m_h = 125$ GeV hypothesis.

The constraints applied on the model proved very efficient at reducing the available parameter space, yet not excluding the model. The free parameters still have large ranges of variation but the possible masses of the scalars have been considerably narrowed.

Up to now the most effective constraints have been the ones coming from the signal strengths on the 125 GeV Higgs boson. Some studies on additional scalars are beginning to be useful for constraining the parameters, such as studies on light Higgs boson for the $m_H = 125$ GeV hypothesis and studies on heavy Higgs boson for the $m_h = 125$ GeV hypothesis, but others like heavy charged Higgs boson studies or light di-Higgs production are still unable to constrain the parameter space. The increase in luminosity by the end of LHC Run II should help improve these constraints.

In the $m_H = 125$ GeV hypothesis I also looked at the possibility for the 2HDM light h to be detected at the LHC. This study was first performed [94] using 8 TeV data [80] and was updated with the latest CMS results using 13 TeV data [90]. I have shown that only 2HDM Type I can generate points reaching the sensitivity of the CMS detector. Furthermore, assuming the existence of a 2HDM Type I light h, this particle would be easier to detect in the $VBF + VH$ production channel; but at 13 TeV the CMS detector begins to be sensitive to such a particle even in the gluon fusion production mode.

As the CMS analysis at 13 TeV [90] presents a very small excess around a mass of 95.3 GeV in both gluon fusion and $VBF + VH$ production mode I performed a quick study to see, assuming that the excess was confirmed and a new neutral scalar particle discovered at this mass range, if the 2HDM Type I was able to explain such an excess. Unfortunately, if it provides plenty of suitable particles to explain an excess in the $VBF + VH$ production mode, the model cannot reproduce an excess in gluon fusion production mode. Hence, if such a light particle were to be discovered, it would rule out the four CP-conserving 2HDM types.

I worked on a second theory, called Fundamental Composite Dynamics, based on the combination of Technicolor and Composite Higgs theories. I focused on the $SU(4) \to Sp(4)$ flavor symmetry breaking, where three neutral scalars emerge: two pseudo-Goldstone bosons – a CP-even h and a CP-odd η – and a condensate σ. The h and σ mix together to give the two mass eigenstates h_1 and h_2, with $m_{h_1} < m_{h_2}$.

I performed the phenomenological study of this model using both constraints coming from the oblique parameters and constraints from scalar studies from the LHC.

I have shown that the 13 TeV constraints on 125 GeV Higgs boson were very efficient at constraining the free parameters and that the derived upper limits were very close to – but still above – those given by the oblique parameter constraints. Moreover some studies on additional scalars, in particular the study on a possible heavy Higgs boson decaying into two Z^0 bosons and the one on a possible heavy Higgs boson decaying into two 125 GeV Higgs bosons are very constraining and, depending on the value of the different free parameters of the model, can be more efficient than both the oblique parameter and the 125 GeV Higgs constraints.

We have seen that, despite the efficiency of the constraints, the model is still not ruled out. In particular the limits giving back either the Technicolor or the Composite Higgs frameworks are not ruled out by the current constraints.

We have also briefly seen that the pseudoscalar η present in the theory is not a good Dark Matter candidate as it is able to decay, and has too low a production cross-section to be detected in current proton-proton or positron-electron accelerators.

I have worked on two different BSM theories but many other models are being developed and are just as viable in light of the latest experimental studies. Hence, despite the growing efficiency of experimental analyses to constrain BSM theories, no model is clearly favored. We are hoping for the discovery of a new particle which could help rule out many BSM models and accelerate the development of a viable extension of the Standard Model.

Appendix

A Pauli, Dirac and Gell-Mann matrices

A.1 Pauli matrices

The Pauli matrices are a set of three 2×2 complex matrices which are hermitian, unitary and traceless:

$$\sigma_x = \begin{pmatrix} 0 & 1 \\ 1 & 0 \end{pmatrix}, \qquad \sigma_y = \begin{pmatrix} 0 & -i \\ i & 0 \end{pmatrix}, \qquad \sigma_z = \begin{pmatrix} 1 & 0 \\ 0 & -1 \end{pmatrix} \tag{A.1}$$

The matrices $i\sigma_x$, $i\sigma_y$, $i\sigma_z$ form a basis of the $su(2)$ Lie algebra of the $SU(2)$ symmetry group.

They obey to the following commutation and anticommutation relations:

$$[\sigma_i, \sigma_j] = 2i\epsilon_{ijk}\sigma_k, \qquad \{\sigma_i, \sigma_j\} = 2\delta_{ij}\mathbb{1}_2 \tag{A.2}$$

The Levi-Civita tensor ϵ_{ijk} corresponds to the structure constant of the group.

A.2 Gamma matrices

The Gamma matrices, also known as the Dirac matrices, are a set of four 4×4 complex matrices with specific commutation rules. Different representations of these matrices exist. We only mention here the Dirac representation:

$$\gamma^0 = \begin{pmatrix} \mathbb{1}_2 & 0 \\ 0 & -\mathbb{1}_2 \end{pmatrix}, \qquad \gamma^i = \begin{pmatrix} 0 & \sigma^i \\ -\sigma^i & 0 \end{pmatrix} \tag{A.3}$$

with σ^i, i=1,2,3, the three Pauli matrices.

They have the following properties:

$$\begin{aligned} \{\gamma^\mu, \gamma^\nu\} &= 2g^{\mu\nu}\mathbb{1}_4, \\ (\gamma^0)^\dagger = \gamma^0, &\qquad (\gamma^0)^2 = \mathbb{1}_4, \\ (\gamma^k)^\dagger = -\gamma^k, &\qquad (\gamma^k)^2 = -\mathbb{1}_4 \end{aligned} \tag{A.4}$$

with k=1,2,3.

In addition one can construct a fifth Gamma matrix:

$$\gamma^5 \equiv i\gamma^0\gamma^1\gamma^2\gamma^3 = \begin{pmatrix} 0 & \mathbb{1}_2 \\ \mathbb{1}_2 & 0 \end{pmatrix}, \qquad (\gamma^5)^\dagger = \gamma^5, \qquad (\gamma^5)^2 = \mathbb{1}_4 \tag{A.5}$$

A.3 Gell-Mann matrices

The Gell-Mann matrices are a set of eight 3×3 complex matrices which are hermitian and traceless:

$$\lambda_1 = \begin{pmatrix} 0 & 1 & 0 \\ 1 & 0 & 0 \\ 0 & 0 & 0 \end{pmatrix}, \qquad \lambda_2 = \begin{pmatrix} 0 & -i & 0 \\ i & 0 & 0 \\ 0 & 0 & 0 \end{pmatrix}, \qquad \lambda_3 = \begin{pmatrix} 1 & 0 & 0 \\ 0 & -1 & 0 \\ 0 & 0 & 0 \end{pmatrix}, \tag{A.6}$$

$$\lambda_4 = \begin{pmatrix} 0 & 0 & 1 \\ 0 & 0 & 0 \\ 1 & 0 & 0 \end{pmatrix}, \qquad \lambda_5 = \begin{pmatrix} 0 & 0 & -i \\ 0 & 0 & 0 \\ i & 0 & 0 \end{pmatrix}, \tag{A.7}$$

$$\lambda_6 = \begin{pmatrix} 0 & 0 & 0 \\ 0 & 0 & 1 \\ 0 & 1 & 0 \end{pmatrix}, \qquad \lambda_7 = \begin{pmatrix} 0 & 0 & 0 \\ 0 & 0 & -i \\ 0 & i & 0 \end{pmatrix}, \qquad \lambda_8 = \frac{1}{\sqrt{3}} \begin{pmatrix} 1 & 0 & 0 \\ 0 & 1 & 0 \\ 0 & 0 & -2 \end{pmatrix} \tag{A.8}$$

They form a basis of the $su(3)$ Lie algebra of the $SU(3)$ symmetry group. They obey to the following commutation relations:

$$[\lambda_i, \lambda_j] = 2i f_{ijk} \lambda_k \tag{A.9}$$

where f_{ijk} is the structure constant of the group.

B Complementary material on statistics

This appendix presents a quick overview of the basic tools in statistics useful for particle physics. For a more comprehensive review, see for instance [25, 26, 126, 127].

B.1 Frequentist and bayesian approaches

There are different ways of interpreting a probability. There are two main approaches: the frequentist and the bayesian interpretations.

In the frequentist approach, the probability of an event A is, basically, the fraction of times the event A occurs in a set of N trials, assuming $N \to \infty$:

$$P(A) = \lim_{N\to\infty} \frac{\text{Number of times A occurs}}{N} \tag{B.1}$$

This interpretation is then well suited for repeatable observations, but is not well adapted for hypotheses such as "Is this theory true?", which is either true or false, no matter the number of times you test it.

In the bayesian approach, the probability of an assertion A represents the degree of belief that A is true. Coming back to the hypothesis "Is this theory true?", the related bayesian probability $P(A)$ will not account for whether this assertion is true or false but how seriously one can think it is true or false.

In the following we will work essentially in the frequentist framework.

B.2 Probability density functions

Considering a discrete *random variable* X, that is, the outcome x of a repeatable experiment which can take different possible values x_1, ..., x_n. For each possible value x_i there is a probability $P(x_i)$ of getting the x_i value as outcome of the experiment.

If the random variable is continuous then, assuming that the possible outcome values take place inside an interval $[x_i; x_f]$, one can introduce the *probability density function* (PDF) $f(x)$ defined on the interval $[x_i; x_f]$. Hence, the probability to get an outcome value between x_a and x_b, $\forall x_a, x_b \in [x_i; x_f]$, is:

$$P([x_a; x_b]) = \int_{x_a}^{x_b} f(x)dx \tag{B.2}$$

Particularly, $P([x_i; x_f]) = 1$ and $\forall x \in [x_i; x_f]$, $P(x) = 0$.

The PDF function $f(x)$ can have various forms depending on the problem we are looking for. Here we will present only two different PDF, the Gaussian and the Poissonian distributions, as they are very useful in particle physics; but many other distributions exist (see for instance [26]).

B.2.1 Poissonian distribution

A Poissonian distribution is used when we know exactly how much times an event is supposed to occur in a given period of time – for instance the average number λ of photon pairs supposed to be produced by a SM mechanism at the LHC during a fixed time Δt.

Then the probability to actually measure exactly n events during the period Δt is given by the Poissonian distribution:

$$P(n;\lambda) = \frac{\lambda^n}{n!} e^{-\lambda} \tag{B.3}$$

One can show that λ corresponds to both the average and the standard deviation of the distribution. The shape of the distributions for $\lambda = 2$ and 5 are shown in figure B.1.

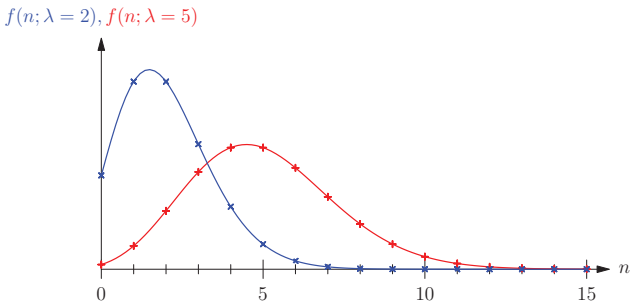

Figure B.1: Poissonian distribution with $\lambda = 2$ (in blue) and $\lambda = 5$ (in red).

This distribution is very often used in particle physics as the number of events λ expected to be detected in an accelerator is well determined by theory and must be compared to the number of events n actually observed.

Note that, for large λ – that is, for a large number of expected events – the Poissonian distribution with parameter λ tends to a Gaussian distribution with mean value $\mu = \lambda$ and standard deviation $\sigma = \sqrt{\lambda}$. Many other PDF also tend to the Gaussian distribution, hence the usefulness of this distribution.

B.2.2 Gaussian distribution

The PDF of a continuous random variable x following a Gaussian – or Normal – distribution with parameters μ and σ reads:

$$f(x;\mu,\sigma) = \frac{1}{\sqrt{2\pi}\sigma} e^{-\frac{(x-\mu)^2}{2\sigma^2}} \tag{B.4}$$

One can show that μ corresponds to the mean value of the distribution and σ to its standard deviation. The shape of the PDF is shown in figure B.2.

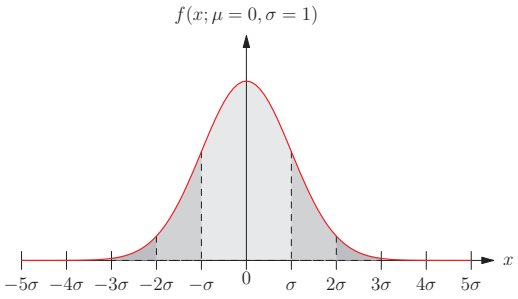

FIGURE B.2: Gaussian distribution with $\mu = 0$, $\sigma = 1$. The grey areas correspond to the confidence level said at 1, 2 or 3σ, which corresponds to the integrated probability covering respectively 65.3%, 95.5% and 99.7% of the distribution.

B.3 Determination of unknown parameters

In particle physics we use statistics to come back to unknown parameters θ that we hope to determine with the help of experiments.

We say that the parameter θ has a true value θ_0, which is its real value we are looking for, but which we cannot access directly. However the parameter θ will influence the value of the PDF function. Hence, using experimental results and choosing a PDF distribution well-suited to the experimental data, one can infer an *estimate* of the θ value, also called central value or best fit and usually denotted $\hat{\theta}$.

This estimate is always given together with an uncertainty $\delta\theta$, which corresponds to a confidence level: we assume that the true value θ is within the interval $[\hat{\theta} - \delta\theta; \hat{\theta} + \delta\theta]$ with 65.3% of probability.

There are different methods to infer the estimate of the relevant unknown parameters. We will only expose here the method called maximum likelihood method.

B.3.1 The maximum likelihood method

For a given set $\vec{x} = (x_1, ..., x_n)$ of n random variables depending on m unknown parameters $\vec{\theta} = (\theta_1, ..., \theta_m)$, the likelihood function is defined as:

$$\mathcal{L}(x_1, ..., x_n; \theta_1, ..., \theta_m) = f(x_1, ..., x_n; \theta_1, ..., \theta_m) \tag{B.5}$$

with f the PDF of the random variable $\vec{x}$.

For N independent measurements $\vec{x}^1$, ..., $\vec{x}^N$ of the random variable $\vec{x}$, the total likelihood reads:

$$\mathcal{L}_{tot}(\theta_1, ...\theta_m) = \prod_{i=1}^{N} f(x_1^i, ..., x_n^i; \theta_1, ..., \theta_m) \tag{B.6}$$

Then the best estimate of the parameter $\vec{\theta}$ corresponds to the value of $\vec{\theta}$ maximizing the total likelihood $\mathcal{L}_{tot}$.

An equivalent method is to use the log-likelihood function. In this case, the best fit of $\vec{\theta}$ is found by minimizing the function $-2 \ln \mathcal{L}_{tot}$.

We have mentioned before that many PDF distributions tend to the Gaussian distribution when the number of measurements is high. Hence, considering a random variable x following a Gaussian distribution which depends on the unknown parameter $\vec{\theta}$ and N independent measurements x^1, ..., x^N of this random variable, one finds:

$$-2\ln\mathcal{L}_{tot} = \underbrace{\sum_{i=1}^{N}\frac{(x^i-\mu(\vec{\theta}))^2}{\sigma^2}}_{=\chi^2(\vec{\theta})} + N\ln(2\pi) + 2N\ln\sigma \tag{B.7}$$

The first term corresponds to what is called a chi-square distribution, denoted χ^2. Hence, maximizing $\mathcal{L}_{tot}$ with respect to $\vec{\theta}$ is equivalent to minimizing the χ^2 function with respect to $\vec{\theta}$.

Note that the above formula is obtained considering only one random variable at play. A more generic formula for the χ^2 function with n random variables is:

$$\chi^2 = \sum_{i=1}^{N}(\vec{x}^i - \vec{\mu}(\vec{\theta}))^T \cdot V^{-1} \cdot (\vec{x}^i - \vec{\mu}(\vec{\theta})) \tag{B.8}$$

with $\vec{x}^i = (x_1^i, ..., x_n^i)$ the values of the n random variables for the i^{th} measurement and V their $n \times n$ covariant matrix.

B.3.2 Confidence level and confidence intervals

Once we have extracted an estimator $\hat{\theta}$ of the true value θ_0, we still need to estimate a *confidence interval* on $\hat{\theta}$. The idea is to find an interval $[\theta_a;\theta_b]$ around $\hat{\theta}$ in which $P([\theta_a \leq \theta_0 \leq \theta_b]) = \beta$, that is, an interval $[\theta_a;\theta_b]$ in which we have a probability β to find the true value.

The β parameter is a fixed number called the *confidence level* and often taken to 68.3% or 95.5% – values often said at 1 and 2σ respectively in reference to the Gaussian distribution. The corresponding interval $[\theta_a;\theta_b]$ is called the *confidence interval*.

Hence, we can write:

$$\theta_0 = \hat{\theta}^{+\theta_b-\hat{\theta}}_{-(\hat{\theta}-\theta_a)} \tag{B.9}$$

There are different methods to determine the confidence interval at a given confidence level β depending on the PDF used.

In the case of the Gaussian distribution, one can show that there is a bound $b_d^{n\sigma}$, depending only on the number of degrees of freedom d of the related χ^2 function and on the chosen confidence level $n\sigma$, which defines completely the confidence interval:

$$P(\chi^2(\vec{\theta}) \leq b_d^{n\sigma}) = \beta \tag{B.10}$$

That is, $\vec{\theta}$ is in the confidence interval if and only if $\chi^2(\vec{\theta}) \leq b_d^{n\sigma}$.

The numerical values of the $b_d^{n\sigma}$ bounds are summarized in table 2.4.

The area where $\chi^2(\vec{\theta}) \leq b_d^{n\sigma}$ is an hyperellipsoid in dimension d. The line or (hyper)surface defined by $\chi^2(\vec{\theta}) = b_d^{n\sigma}$ corresponds to the upper bound on $\vec{\theta}$ at a confidence level of $n\sigma$.

B.4 Hypothesis testing and p-value

Another challenge in experimental particle physics is to test an hypothesis against data in order to check if it is rejected or not by the experiment. This is essential to test the validity of an excess and hence, whether claiming a discovery.

The idea is to look at the expected distribution of the random variable $\vec{x}$ under study, which is assumed, under an hypothesis H_0, to follow a given PDF $f(\vec{x})$.

Once the experiment is done we have access to the experimental value $\vec{x}_{obs}$ of the random variable $\vec{x}$.

In order to test the hypothesis H_0 in light of the experimental observation $\vec{x}_{obs}$ one will define an appropriate region, called *critical region*, where the values of $\vec{x}$ have, under the hypothesis H_0, an equal or greater incompatibility with the observed data $\vec{x}_{obs}$.

Then one can compute the p-value of H_0, which is the probability, under H_0, to find data in this critical region. Hence, the lower the p-value is, the less compatible are the observed data $\vec{x}_{obs}$ with the H_0 hypothesis.

The p-value is compared to a pre-defined bound α – often taken such that $1-\alpha$=65.3% or 95.5%. If $p < \alpha$ then the H_0 hypothesis is rejected.

We can also convert the p-value into significance Z, based on an analogy with the Gaussian distribution:

$$Z = \Phi^{-1}(1-p) \tag{B.11}$$

with Φ the cumulative standard Gaussian distribution – with zero mean value and unit variance. The conversion between the two is shown in figure B.3.

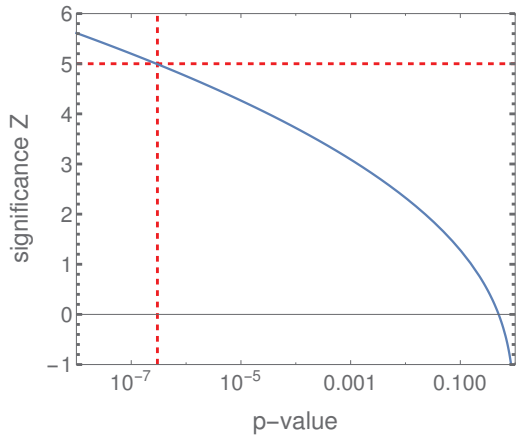

FIGURE B.3: Correspondence between the p-value and the significance Z defined in equation (B.11). The 5σ value and its corresponding p-value, often taken to claim a discovery, are highlighted by the dashed red lines.

C Complementary material on the 125 GeV Higgs boson decays through loop processes

The decay of a SM Higgs boson with mass m_h into a pair of gluons, photons or in $Z^0\gamma$ only takes place at loop level. Different particles may run into the loops – quarks, fermions or $W^\pm$ gauge bosons depending on which decay we are looking for (see figure C.1).

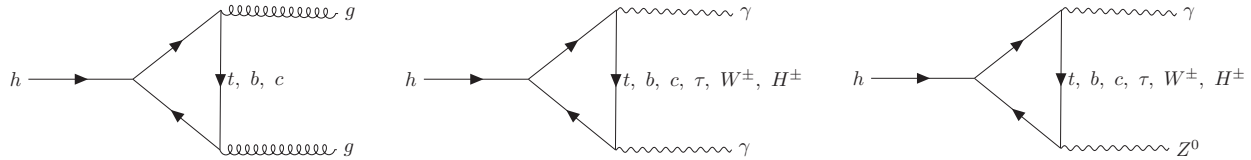

FIGURE C.1: Decay of a SM Higgs boson into a pair of gluons (left), a pair of photons (middle) and into $Z^0\gamma$ (right) with the appropriate particles running in the loop. The contribution of the charged Higgs boson from the 2HDM is also mentioned.

The analytical expression of the widths is well known at one-loop level and includes amplitude terms A_X taking into account the effect of the different X particles which may contribute.

Assuming a BSM Higgs boson, that is, a neutral scalar particle with couplings to a pair XX of SM fermions or gauge bosons rescaled by a factor C_{XX} compared to those of the SM Higgs boson, one can deduce the analytical expression of its decay width at loop level by simply rescaling the amplitudes A_X by the appropriate factor C_{XX} and by adding the missing amplitudes A_Y involving non-SM Y particles.

In the case of the 2HDM, besides the SM particle contributions, only the charged Higgs bosons $H^\pm$ can contribute to the $h \to \gamma\gamma$ and $h \to Z\gamma$ processes.

We can hence deduce the expression of the scaling factors κ_g and κ_γ whose squared values are, by definition, the ratio of the 2HDM width over the SM width for the decay considered [128, 41]:

$$\kappa_g^2 = \frac{\Gamma^{2HDM}_{h\to gg}}{\Gamma^{SM}_{h\to gg}} = \frac{\left|\sum\limits_{f=t,b,c} C_{ff} A_{\frac{1}{2}}(\tau_f)\right|^2}{\left|\sum\limits_{f=t,b,c} A_{\frac{1}{2}}(\tau_f)\right|^2}$$

$$\kappa_\gamma^2 = \frac{\Gamma^{2HDM}_{h\to\gamma\gamma}}{\Gamma^{SM}_{h\to\gamma\gamma}} = \frac{\left|\sum\limits_{f=t,b,c,\tau} N_{c,f} Q_f^2 C_{ff} A_{\frac{1}{2}}(\tau_f) + C_{WW} A_1(\tau_W) - C_{H^+} A_0(\tau_{H^+})\right|^2}{\left|\sum\limits_{f=t,b,c,\tau} N_{c,f} Q_f^2 A_{\frac{1}{2}}(\tau_f) + A_1(\tau_W)\right|^2} \tag{C.1}$$

with $\tau_x = \frac{m_h^2}{4m_x^2}$, m_x the mass of the x particle, N_c the number of colors of the fermion considered, Q_f its charge, and $A(\tau_x)$ the different amplitude terms depending on the nature of the x particle

running in the loop:

$$\begin{aligned} A_{\frac{1}{2}}(\tau) &= \frac{2}{\tau^2}(\tau + (\tau-1)f(\tau)) \\ A_1(\tau) &= -\frac{1}{\tau^2}(2\tau^2 + 3\tau + 3(2\tau-1)f(\tau)) \\ A_0(\tau) &= \frac{1}{\tau^2}(f(\tau) - \tau) \end{aligned} \tag{C.2}$$

and the $f(\tau)$ function:

$$f(\tau) = \begin{cases} \arcsin^2(\sqrt{\tau}), & \tau \leq 1 \\ -\frac{1}{4}\left[\log\left(\frac{1+\sqrt{1-1/\tau}}{1-\sqrt{1-1/\tau}}\right) - i\pi\right]^2, & \tau > 1 \end{cases} \tag{C.3}$$

The expression for the third scaling factor $\kappa_{Z\gamma}$ is slightly more complicated [129]:

$$\kappa_{Z\gamma} = \frac{\Gamma^{2HDM}_{h\to Z\gamma}}{\Gamma^{SM}_{h\to Z\gamma}} = \frac{\left|\sum\limits_{f=t,b,c,\tau} C_{ff} A^{Z\gamma}_{\frac{1}{2}}(\tau_f,\lambda_f) + C_{WW} A^{Z\gamma}_1(\tau_W,\lambda_W) + C_{H^+} A^{Z\gamma}_0(\tau_{H^+},\lambda_{H^+})\right|^2}{\left|\sum\limits_{f=t,b,c,\tau} A^{Z\gamma}_{\frac{1}{2}}(\tau_f,\lambda_f) + A^{Z\gamma}_1(\tau_W,\lambda_W)\right|^2} \tag{C.4}$$

with, again, $\tau_x = \frac{m_h^2}{4m_x^2}$, m_x the mass of the x particle, $\lambda_x = \frac{m_Z^2}{4m_x^2}$ and $A^{Z\gamma}(\tau_x,\lambda_x)$ the different amplitude terms depending on the nature of the x particle running in the loop and specific to the $h \to Z\gamma$ decay:

$$\begin{aligned} A^{Z\gamma}_{\frac{1}{2}}(\tau_f,\lambda_f) &= 2N_c Q_f \frac{I_{3f} - 2s^2_{\theta w} Q_f}{c_{\theta w}} \times \left[I_1\left(\frac{1}{\tau_f},\frac{1}{\lambda_f}\right) - I_2\left(\frac{1}{\tau_f},\frac{1}{\lambda_f}\right)\right] \\ A^{Z\gamma}_1(\tau_W,\lambda_W) &= -c_{\theta w}\left[4\left(3 - \frac{s^2_{\theta w}}{c^2_{\theta w}}\right) I_2\left(\frac{1}{\tau_W},\frac{1}{\lambda_W}\right) + \left\{(1+2\tau_W)\frac{s^2_{\theta w}}{c^2_{\theta w}} - (5+2\tau_W)\right\} I_1\left(\frac{1}{\tau_W},\frac{1}{\lambda_W}\right)\right] \\ A^{Z\gamma}_0 &= -\left(2c_{\theta w} - \frac{1}{c_{\theta w}}\right) I_1\left(\frac{1}{\tau_{H^+}},\frac{1}{\lambda_{H^+}}\right) \end{aligned} \tag{C.5}$$

with $s_{\theta w} \equiv \sin(\theta_w)$, N_c the number of colors of the fermion considered, Q_f its charge, I_{3f} its weak isospin and the I_1 and I_2 functions defined as:

$$I_1(\alpha,\beta) = \frac{\alpha\beta}{2(\alpha-\beta)} + \frac{\alpha^2\beta^2}{2(\alpha-\beta)^2}\left[f\left(\frac{1}{\alpha}\right) - f\left(\frac{1}{\beta}\right)\right] + \frac{\alpha^2\beta}{(\alpha-\beta)^2}\left[g\left(\frac{1}{\alpha}\right) - g\left(\frac{1}{\beta}\right)\right] \tag{C.6}$$

$$I_2(\alpha,\beta) = -\frac{\alpha\beta}{2(\alpha-\beta)}\left[f\left(\frac{1}{\alpha}\right) - f\left(\frac{1}{\beta}\right)\right] \tag{C.7}$$

with $f(\tau)$ defined above and $g(\tau)$:

$$g(\tau) = \begin{cases} \sqrt{1/\tau - 1}\arcsin(\sqrt{\tau}), & \tau \leq 1 \\ \frac{1}{2}\sqrt{1-1/\tau}\left[\log\left(\frac{1+\sqrt{1-1/\tau}}{1-\sqrt{1-1/\tau}}\right) - i\pi\right], & \tau > 1 \end{cases} \tag{C.8}$$

D Complementary material on the study of the light Higgs boson – figures for Flipped and Lepton-Specific types

This section contains the figures completing the ones of chapter 4.

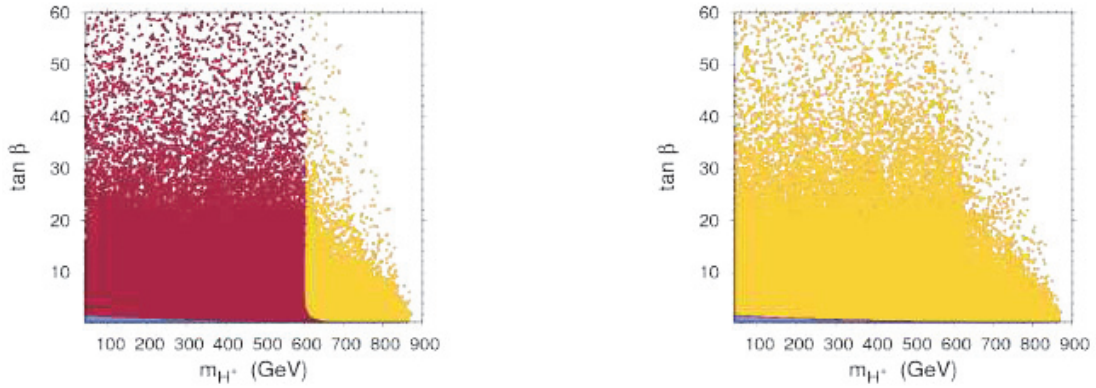

(A) Flipped type (B) Lepton-Specific type

FIGURE D.1: Constraints due to flavor requirements in the plane $\tan\beta$ vs $m_{H^\pm}$. Same color code as in figure 4.4.

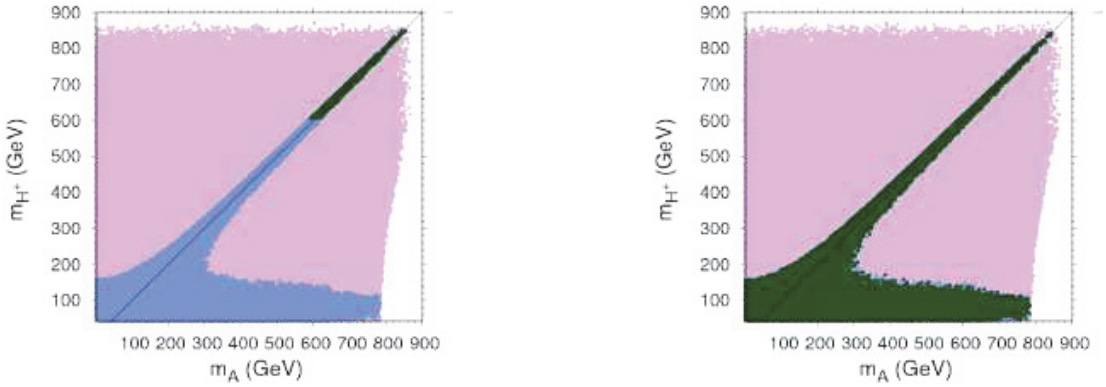

(A) Flipped type (B) Lepton-Specific type

FIGURE D.2: Constraints on the parameter space due to theoretical, oblique parameters and flavor constraints. Same color code as in figure 4.5.

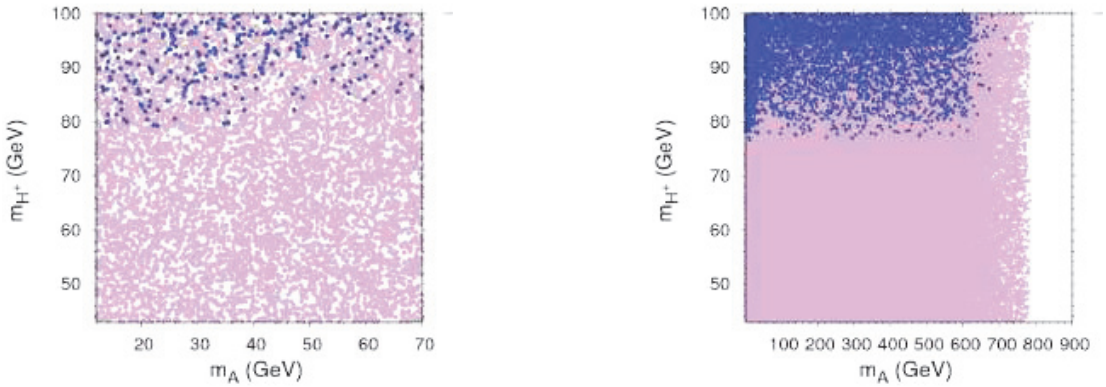

(A) Type II, $m_h > 83$ GeV. (B) Type II, generic case.

FIGURE D.3: Constraints on the parameter space due to LEP constraints in 2HDM Type II. Same color code as in figure 4.6.

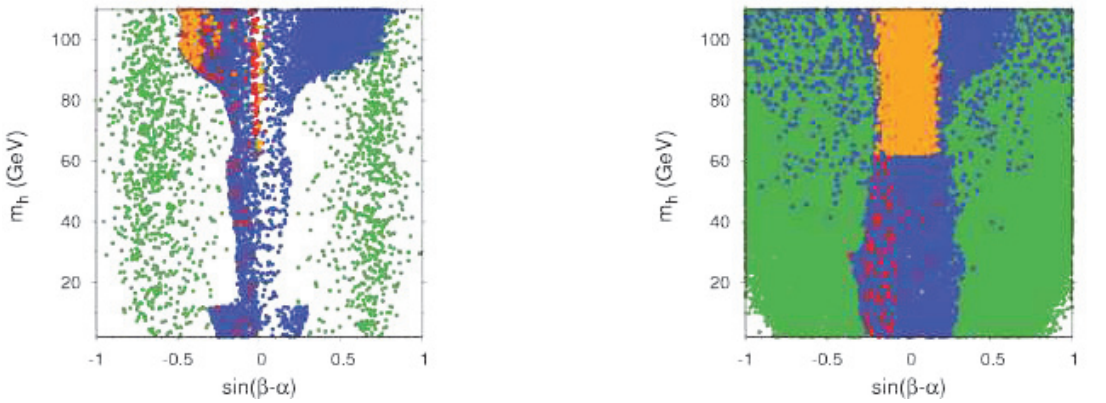

(A) Flipped type (B) Lepton-Specific type

FIGURE D.4: Constraints on the parameter space due to LHC constraints. Same color code as in figure 4.7.

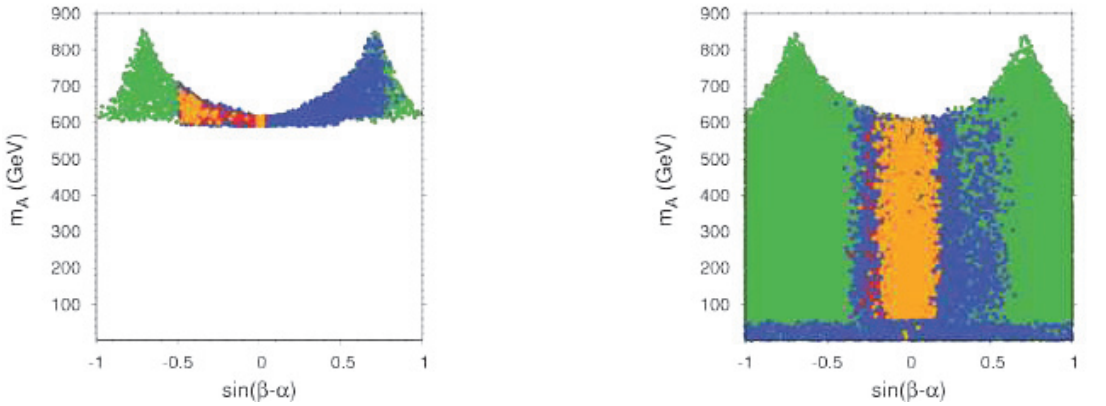

(A) Flipped type (B) Lepton-Specific type

FIGURE D.5: Constraints on the parameter space due to LHC constraints. Same color code as in figure 4.7.

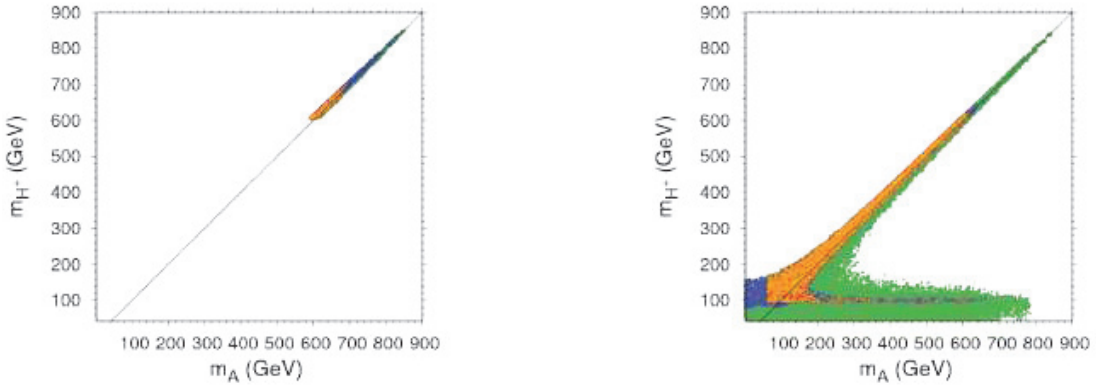

(A) Flipped type (B) Lepton-Specific type

FIGURE D.6: Constraints on the parameter space due to LHC constraints. Same color code as in figure 4.7.

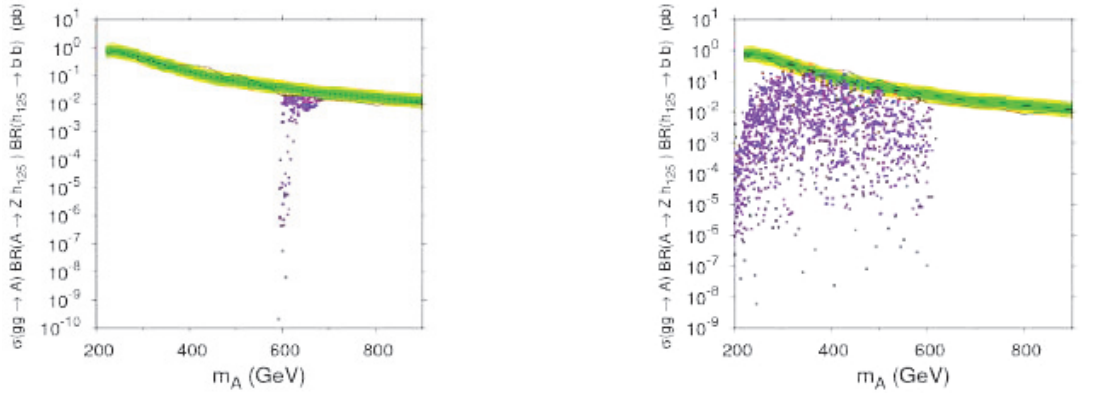

(A) Flipped type (B) Lepton-Specific type

FIGURE D.7: Constraints on the parameter space due to heavy Higgs constraints. Same color code as in figure 4.10.

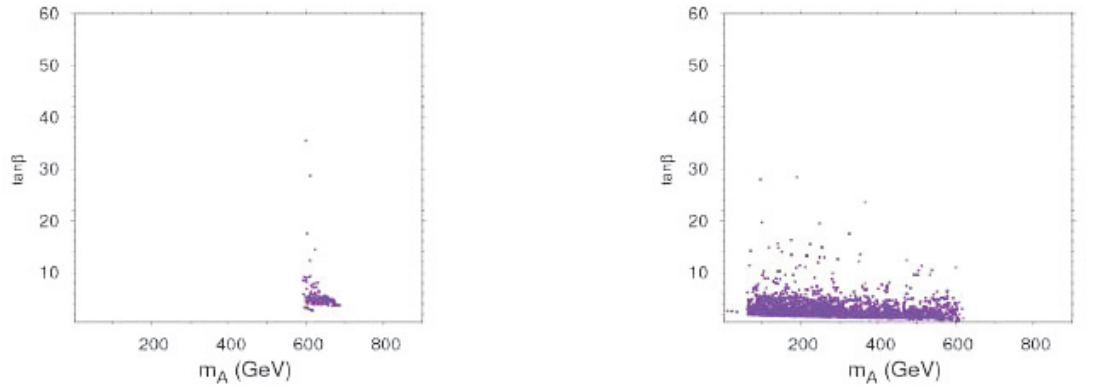

(A) Flipped type (B) Lepton-Specific type

FIGURE D.8: Constraints on the parameter space due to heavy Higgs constraints. Same color code as in figure 4.10.

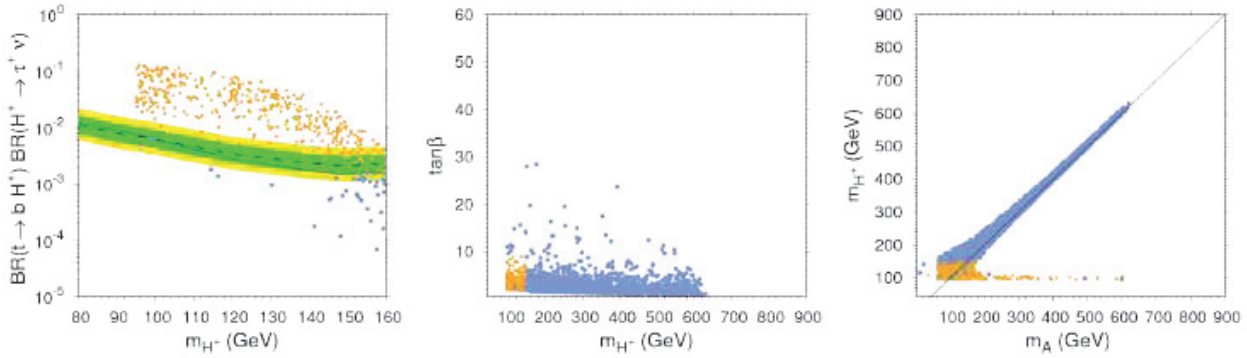

(A) Comparison with the process $t \to bH^+ \to b\tau\nu_\tau$ at 8 TeV [85].

(B) $m_{H^\pm}$ vs $\tan\beta$.

(C) $m_{H^\pm}$ vs m_A.

FIGURE D.9: Constraints on the parameter space due to charged Higgs constraints for the Lepton-Specific type. Same color code as in figure 4.12.

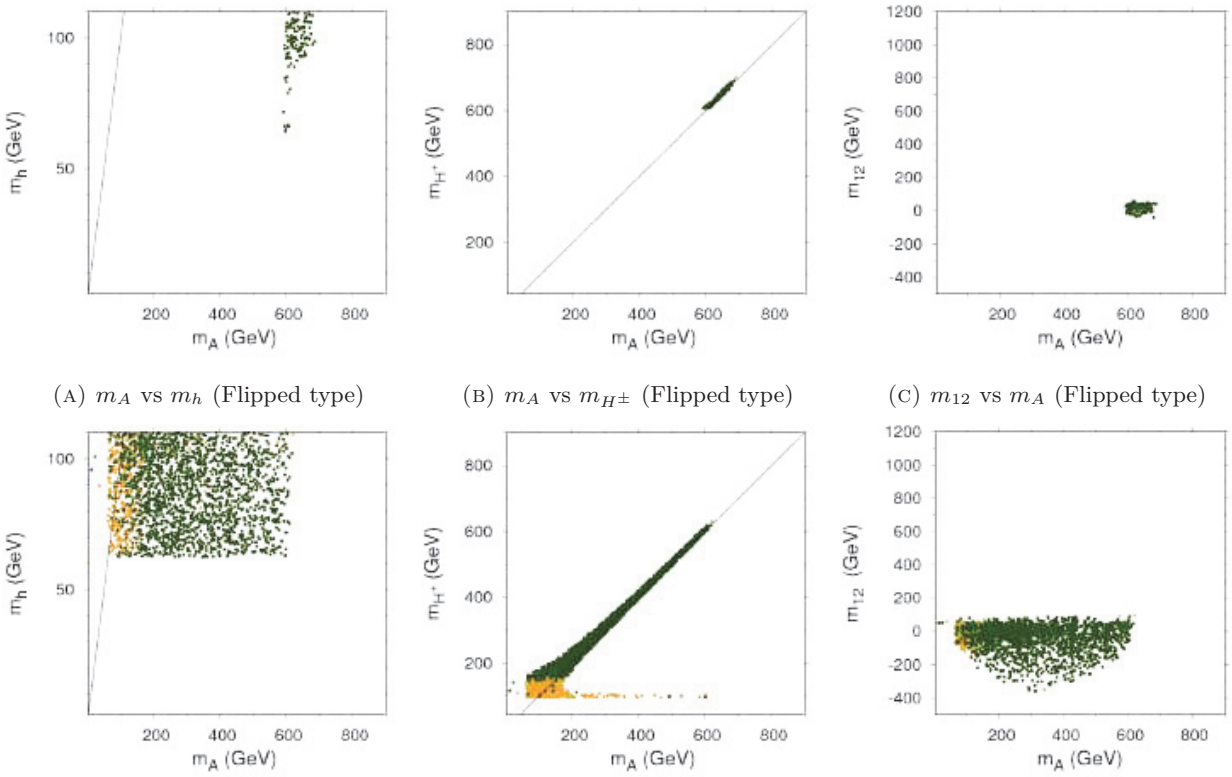

(A) m_A vs m_h (Flipped type)

(B) m_A vs $m_{H^\pm}$ (Flipped type)

(C) m_{12} vs m_A (Flipped type)

(D) m_A vs m_h (Lepton-Specific type)

(E) m_A vs $m_{H^\pm}$ (Lepton-Specific type)

(F) m_{12} vs m_A (Lepton-Specific type)

FIGURE D.10: Consequences of all the constraints in the Flipped type (upper panel) and Lepton-Specific type (lower panel) frameworks. Same color code as in figure 4.13.

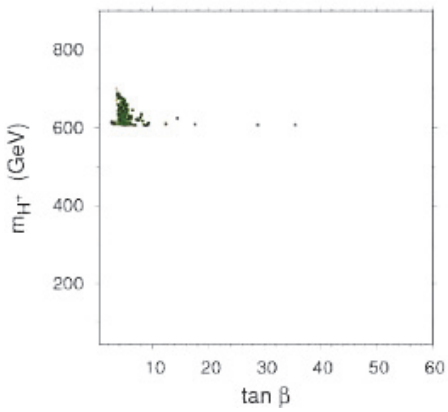

(A) $m_{H^\pm}$ vs $\tan\beta$ (Flipped type)

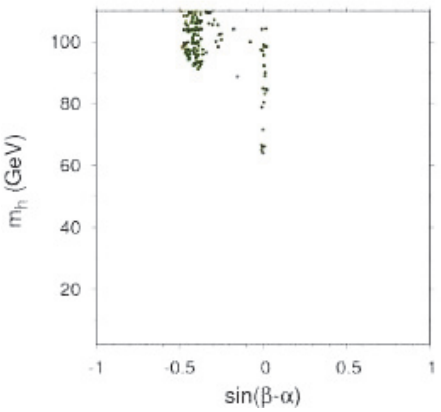

(B) m_h vs $s_{\beta-\alpha}$ (Flipped type)

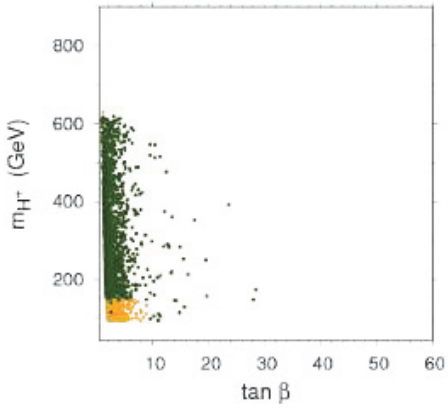

(C) $m_{H^\pm}$ vs $\tan\beta$ (Lepton-Specific type)

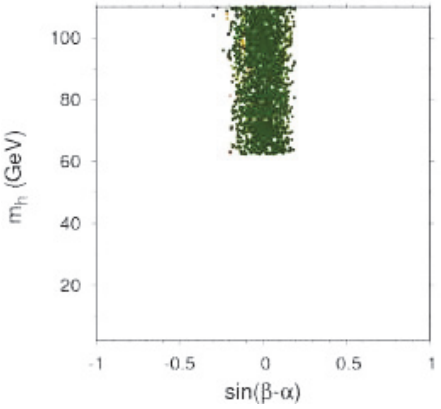

(D) m_h vs $s_{\beta-\alpha}$ (Lepton-Specific type)

FIGURE D.11: Same as figure D.10.

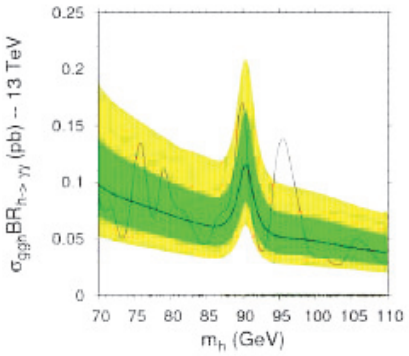

(A) Light h case in gluon fusion production mode.

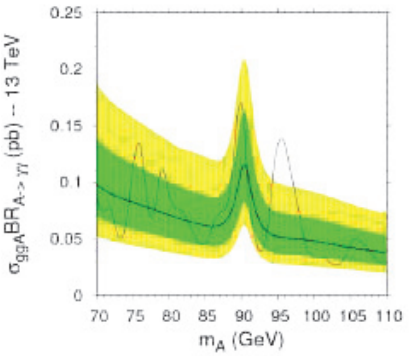

(B) Light A case in gluon fusion production mode.

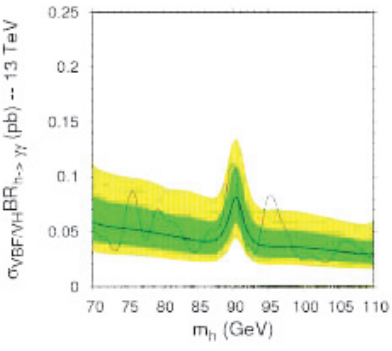

(C) Light h case in $VBF + VH$ production mode.

FIGURE D.12: Comparison between the generated 2HDM points in Type II framework and the observed upper limit on the process $pp \to h/A \to \gamma\gamma$ at 13 TeV [90] (solid black line). Same color code as in figure 4.13.

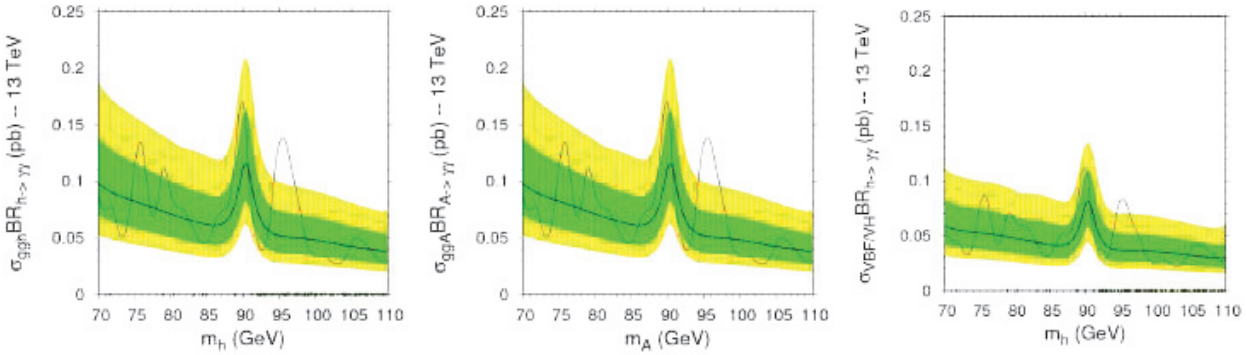

(A) Light h case in gluon fusion production mode.

(B) Light A case in gluon fusion production mode.

(C) Light h case in $VBF + VH$ production mode.

FIGURE D.13: Same as figure D.12 in the Flipped type framework.

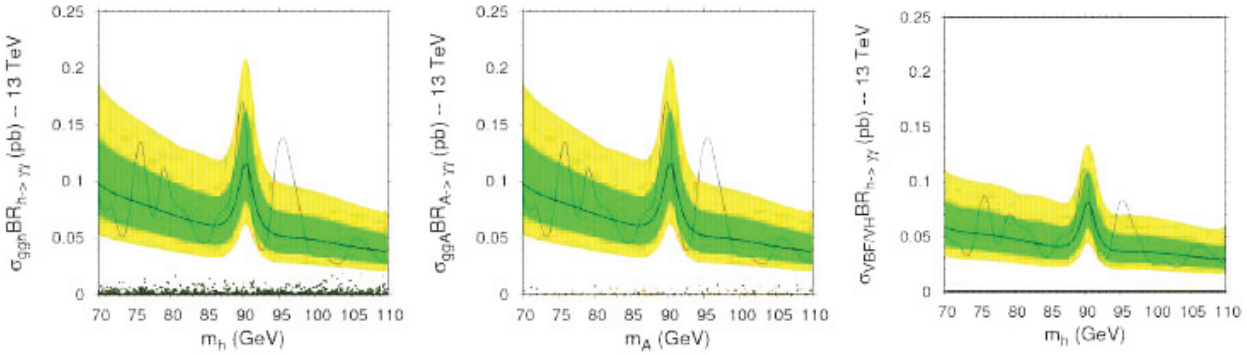

(A) Light h case in gluon fusion production mode.

(B) Light A case in gluon fusion production mode.

(C) Light h case in $VBF + VH$ production mode.

FIGURE D.14: Same as figure D.12 in the Lepton-Specific type framework.

E Complementary material on the study of the heavy Higgs boson

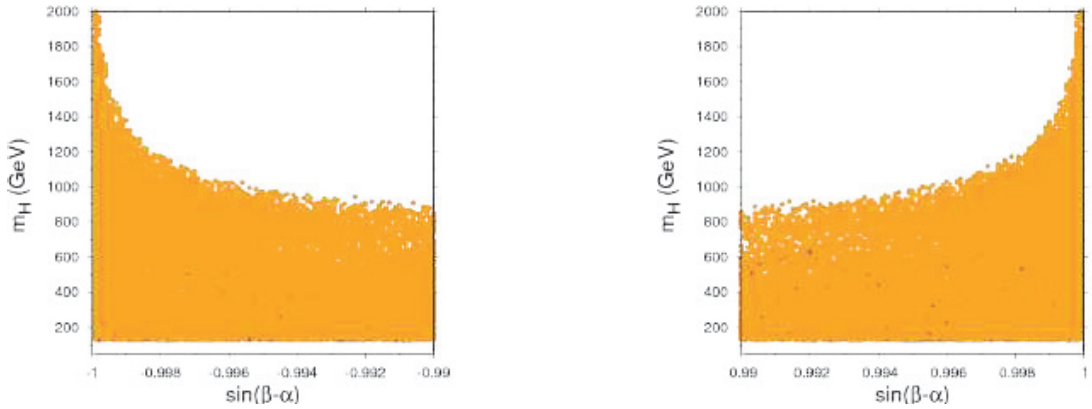

(A) Type I, negative $s_{\beta-\alpha}$ values.

(B) Type I, positive $s_{\beta-\alpha}$ values.

FIGURE E.1: Generated points in the plane m_H vs $s_{\beta-\alpha}$. Same color code as in figure 5.3.

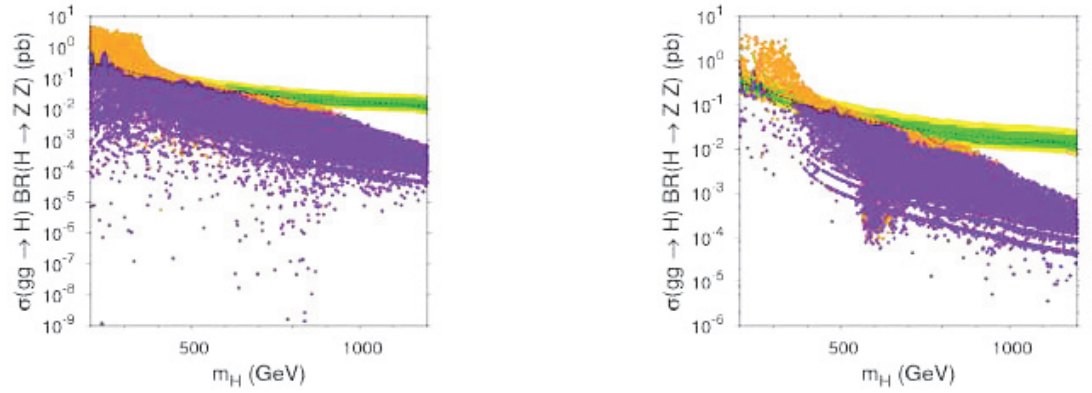

(A) Type I

(B) Type II

FIGURE E.2: Comparison between generated 2HDM points and ATLAS observed upper limit on the process $\sigma(gg \to H) \times BR(H \to ZZ)$ [24] (black solid line). Same color code as in figure 5.5

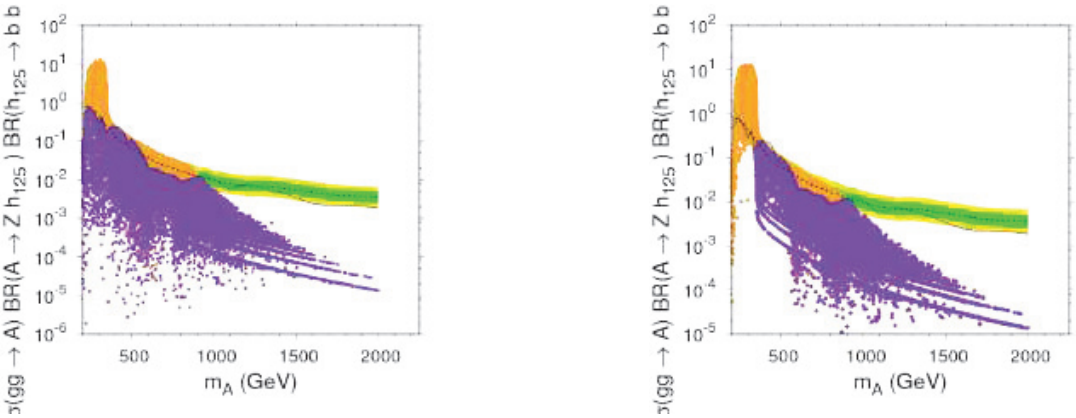

(A) Type I (B) Type II

FIGURE E.3: Comparison between generated 2HDM points and ATLAS observed upper limit on the process $\sigma(gg \to A) \times BR(A \to Zh) \times BR(h \to b\bar{b})$ [79] (black solid line). Same color code as figure 5.5.

F The σ decay width in the FCD model

We summarize in this appendix the obtention of the decay widths of the σ particle in the FCD model based on the breaking $SU(4) \to Sp(4)$.

F.1 W^+W^- and ZZ decays

The couplings at tree level of the σ particle with a pair of $W^\pm$ gauge bosons is $g_{\sigma WW} = \tilde{\xi}_G \; s_\theta \; g^{SM}_{hWW}$ with g^{SM}_{hWW} the coupling of a SM Higgs boson with mass $m_h = m_\sigma$ with a pair of $W^\pm$ gauge bosons (see table 6.2).

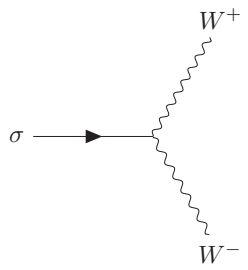

Figure F.1: Feynman diagram of the tree-level decay of the σ particle into a pair of $W^\pm$ gauge bosons. The decay into a pair of Z^0, h, η or fermions has a similar Feynman diagram.

Using the tree-level Feynman diagram (see figure F.1) one can derive the expression of the squared matrix element averaged on the possible $W^\pm$ polarizations:

$$\sum_{\text{polarizations}} |\mathcal{M}_{\sigma W^+W^-}|^2 = g^2_{\sigma WW} \times \left[3 + \frac{m^4_\sigma}{4m^4_W} - \frac{m^2_\sigma}{m^2_W}\right] \tag{F.1}$$

Using the two-body decay formulas reminded in equation (6.47) and integrating over the solid angle $d\Omega$ one finds:

$$\Gamma_{\sigma \to W^+W^-} = \frac{g^2_{\sigma WW}}{16\pi m_\sigma} \left[3 + \frac{m^4_\sigma}{4m^4_W} - \frac{m^2_\sigma}{m^2_W}\right] \sqrt{1 - \frac{4m^2_W}{m^2_\sigma}} \tag{F.2}$$

The derivation of the partial width for the decay $\sigma \to ZZ$ is exactly similar except for the

additional $\frac{1}{2}$ factor as the two Z^0 bosons are indiscernible:

$$\Gamma_{\sigma\to W^+W^-} = \frac{g_{\sigma ZZ}^2}{32\pi m_\sigma}\left[3+\frac{m_\sigma^4}{4m_Z^4}-\frac{m_\sigma^2}{m_Z^2}\right]\sqrt{1-\frac{4m_Z^2}{m_\sigma^2}} \tag{F.3}$$

F.2 Fermionic decays

The coupling between the σ particle and a pair of fermions $f\bar{f}$ with mass m_f is $g_{\sigma ff} = \tilde{\xi}_f s_\theta g_{hff}^{SM}$ with g_{hff}^{SM} the coupling of a SM Higgs boson with mass $m_h = m_\sigma$ with a pair of fermions $f\bar{f}$.

We first compute the squared matrix element for the decay $\sigma \to f\bar{f}$ – for a SM fermion f with mass m_f – averaged on the possible spin states. One finds:

$$\sum_{\text{spin}} |\mathcal{M}_{\sigma f\bar{f}}|^2 = g_{\sigma f\bar{f}}^2 \times 2N_c m_\sigma^2\left[1-\frac{4m_f^2}{m_\sigma^2}\right] \tag{F.4}$$

with N_c the number of colors ($N_c = 1$ for leptons, $N_c = 3$ for quarks).

Using the partial width formula for two-body decays and integrating on the solid angle $d\Omega$ one finds:

$$\Gamma_{\sigma\to f\bar{f}} = g_{\sigma f\bar{f}}^2 \frac{N_c m_\sigma}{8\pi}\left(1-\frac{4m_f^2}{m_\sigma^2}\right)^{3/2} \tag{F.5}$$

F.3 Decay into hh and $\eta\eta$

The couplings between the σ particle and a pair of pseudo-Goldstone bosons – either hh or $\eta\eta$ – are (see equations (6.35) and (6.36)):

$$\begin{aligned} g_{\sigma hh} &= -\frac{m_h^2}{v s_\theta}\left(\tilde{\xi}_m c_\theta^2 - 2\tilde{\xi}_t c_{2\theta}\right) - \frac{\tilde{\xi}_G s_\theta}{v} m_\sigma^2\left(1-\frac{2m_h^2}{m_\sigma^2}\right) \\ g_{\sigma\eta\eta} &= -\frac{m_h^2}{v s_\theta}\left(\tilde{\xi}_m c_\theta^2 + 2\tilde{\xi}_t s_\theta^2\right) - \frac{\tilde{\xi}_G s_\theta}{v} m_\sigma^2\left(1-\frac{2m_\eta^2}{m_\sigma^2}\right) \end{aligned}$$

As both h, σ and η are scalars we can deduce directly the partial decay widths:

$$\Gamma_{\sigma\to hh} = \frac{1}{32\pi}\frac{g_{\sigma hh}^2}{m_\sigma}\sqrt{1-\frac{4m_h^2}{m_\sigma^2}}, \quad \Gamma_{\sigma\to\eta\eta} = \frac{1}{32\pi}\frac{g_{\sigma\eta\eta}^2}{m_\sigma}\sqrt{1-\frac{4m_\eta^2}{m_\sigma^2}} \tag{F.6}$$

F.4 Decay widths in the limit $m_\sigma \to \infty$

Using the formulas derived above one can derive the expression of the different partial decay width in the limit $m_\sigma \to \infty$:

$$\Gamma_{\sigma\to W^+W^-} \xrightarrow[m_\sigma\to\infty]{} \frac{g^2_{\sigma WW}}{16\pi} \times \frac{m^3_\sigma}{4m^4_W} = \left(\frac{\tilde{\xi}_G s_\theta}{v}\right)^2 \times \frac{m^3_\sigma}{16\pi} \tag{F.7}$$

$$\Gamma_{\sigma\to ZZ} \xrightarrow[m_\sigma\to\infty]{} \frac{g^2_{\sigma ZZ}}{32\pi} \times \frac{m^3_\sigma}{4m^4_Z} = \left(\frac{\tilde{\xi}_G s_\theta}{v}\right)^2 \times \frac{m^3_\sigma}{32\pi} = \frac{1}{2}\Gamma_{\sigma\to W^+W^-} \tag{F.8}$$

$$\Gamma_{\sigma\to f\bar{f}} \xrightarrow[m_\sigma\to\infty]{} g^2_{\sigma ff} \times \frac{N_c m_\sigma}{8\pi} \ll \Gamma_{\sigma\to W^+W^-} \tag{F.9}$$

For the decays into hh and $\eta\eta$ one needs first to obtain the limit of the couplings:

$$g_{\sigma hh} \xrightarrow[m_\sigma\to\infty]{} -\frac{\tilde{\xi}_G s_\theta}{v} m^2_\sigma, \qquad g_{\sigma\eta\eta} \xrightarrow[m_\sigma\to\infty]{} -\frac{\tilde{\xi}_G s_\theta}{v} m^2_\sigma \tag{F.10}$$

Hence, we deduce:

$$\Gamma_{\sigma\to hh} \xrightarrow[m_\sigma\to\infty]{} \left(\frac{\tilde{\xi}_G s_\theta}{v}\right)^2 \times \frac{m^3_\sigma}{32\pi} = \frac{1}{2}\Gamma_{\sigma\to W^+W^-}, \tag{F.11}$$

$$\Gamma_{\sigma\to \eta\eta} \xrightarrow[m_\sigma\to\infty]{} \left(\frac{\tilde{\xi}_G s_\theta}{v}\right)^2 \times \frac{m^3_\sigma}{32\pi} = \frac{1}{2}\Gamma_{\sigma\to W^+W^-} \tag{F.12}$$

These results represent a mathematical proof of the discussion on the heavy Higgs branching ratios at the beginning of section 6.3.4.

Bibliography

[1] T. W. B. Kibble, "The Standard Model of Particle Physics," 2014. arXiv:1412.4094 [physics.hist-ph]. https://inspirehep.net/record/1334156/files/arXiv:1412.4094.pdf.

[2] D. Griffiths, *Introduction to Elementary Particles*. Wiley-VCH, 2nd ed., 2008.

[3] H. Leutwyler, "On the history of the strong interaction," *Mod. Phys. Lett.* **A29** (2014) 1430023, arXiv:1211.6777 [physics.hist-ph]. [,29(2014)].

[4] L. Maiani, "The GIM Mechanism: origin, predictions and recent uses," in *Proceedings, 48th Rencontres de Moriond on Electroweak Interactions and Unified Theories: La Thuile, Italy, March 2-9, 2013*, pp. 3–16. 2013. arXiv:1303.6154 [hep-ph]. https://inspirehep.net/record/1225307/files/arXiv:1303.6154.pdf.

[5] S. S. Schweber, *QED And The Men Who Made It: Dyson, Feynman, Schwinger And Tomonaga*. Princeton University Press, 1994.

[6] **ATLAS** Collaboration, G. Aad *et al.*, "Observation of a new particle in the search for the Standard Model Higgs boson with the ATLAS detector at the LHC," *Phys. Lett.* **B716** (2012) 1–29, arXiv:1207.7214 [hep-ex].

[7] **CMS** Collaboration, S. Chatrchyan *et al.*, "Observation of a new boson at a mass of 125 GeV with the CMS experiment at the LHC," *Phys. Lett.* **B716** (2012) 30–61, arXiv:1207.7235 [hep-ex].

[8] CPEP, "Cpep, contemporary physics educational project," 2017. http://www.cpepphysics.org/.

[9] A. D. m. Francis Halzen, *Quarks & leptons: an introductory course in moder particle physics*. John Wiley & Sons, 1984.

[10] **Particle Data Group** Collaboration, C. Patrignani *et al.*, "Review of Particle Physics," *Chin. Phys.* **C40** no. 10, (2016) 100001.

[11] **Gfitter Group** Collaboration, M. Baak, J. CÃžth, J. Haller, A. Hoecker, R. Kogler, K. MÃűnig, M. Schott, and J. Stelzer, "The global electroweak fit at NNLO and prospects for the LHC and ILC," *Eur. Phys. J.* **C74** (2014) 3046, arXiv:1407.3792 [hep-ph].

[12] A. Djouadi, "The Higgs particles in the MSSM," tech. rep., Ecole de GIF 2001, LAPP Annecy, 2001.

[13] Q. Arnaud, *Direct detection of dark matter with the EDELWEISS-III experiment : signals induced by charge trapping, data analysis and characterization of cryogenic detector sensitivity to low-mass WIMPs*. Theses, Université Claude Bernard - Lyon I, Nov., 2015. https://tel.archives-ouvertes.fr/tel-01273303.

[14] **Planck** Collaboration, P. A. R. Ade *et al.*, "Planck 2015 results. XIII. Cosmological parameters," *Astron. Astrophys.* **594** (2016) A13, arXiv:1502.01589 [astro-ph.CO].

[15] S. M. Bilenky, "Neutrino oscillations: brief history and present status," in *Proceedings,*

22nd International Baldin Seminar on High Energy Physics Problems, Relativistic Nuclear Physics and Quantum Chromodynamics, (ISHEPP 2014): Dubna, Russia, September 15-20, 2014. 2014. arXiv:1408.2864 [hep-ph]. https://inspirehep.net/record/1310742/files/arXiv:1408.2864.pdf.

[16] P. Minkowski, "$\mu \to e\gamma$ at a Rate of One Out of 10^9 Muon Decays?," *Phys. Lett.* **B67** (1977) 421–428.

[17] L. Canetti, M. Drewes, and M. Shaposhnikov, "Matter and Antimatter in the Universe," *New J. Phys.* **14** (2012) 095012, arXiv:1204.4186 [hep-ph].

[18] S. L. Wu, "Brief history for the search and discovery of the Higgs particle – A personal perspective," *Mod. Phys. Lett.* **A29** no. 09, (2014) 1330027, arXiv:1403.4425 [hep-ex].

[19] D. Barney, "CMS Detector Slice." CMS Collection., Jan, 2016.

[20] **ATLAS, CMS** Collaboration, G. Aad *et al.*, "Measurements of the Higgs boson production and decay rates and constraints on its couplings from a combined ATLAS and CMS analysis of the LHC pp collision data at $\sqrt{s} = 7$ and 8 TeV," *JHEP* **08** (2016) 045, arXiv:1606.02266 [hep-ex].

[21] **ATLAS, CMS** Collaboration, G. Aad *et al.*, "Combined Measurement of the Higgs Boson Mass in *pp* Collisions at $\sqrt{s} = 7$ and 8 TeV with the ATLAS and CMS Experiments," *Phys. Rev. Lett.* **114** (2015) 191803, arXiv:1503.07589 [hep-ex].

[22] LHC Higgs Cross Section Working Group, S. Heinemeyer, C. Mariotti, G. Passarino, and R. Tanaka (Eds.), "Handbook of LHC Higgs Cross Sections: 3. Higgs Properties," *CERN-2013-004* (CERN, Geneva, 2013) , arXiv:1307.1347 [hep-ph].

[23] B. Mellado Garcia, P. Musella, M. Grazzini, and R. Harlander, "CERN Report 4: Part I Standard Model Predictions,". https://cds.cern.ch/record/2150771.

[24] **ATLAS** Collaboration, T. A. collaboration, "Search for heavy ZZ resonances in the $\ell^+\ell^-\ell^+\ell^-$ and $\ell^+\ell^-\nu\bar{\nu}$ final states using proton–proton collisions at $\sqrt{s} = 13$ TeV with the ATLAS detector,".

[25] G. Cowan, "Topics in statistical data analysis for high-energy physics," in *High-energy physics. Proceedings, 17th European School, ESHEP 2009, Bautzen, Germany, June 14-27, 2009*, pp. 197–218. 2013. arXiv:1012.3589 [physics.data-an]. https://inspirehep.net/record/881668/files/arXiv:1012.3589.pdf. [,207(2013)].

[26] L. Lista, "Statistical Methods for Data Analysis in Particle Physics," *Lect. Notes Phys.* **909** (2016) pp.1–172.

[27] **ATLAS** Collaboration, T. A. collaboration, "Measurement of the Higgs boson coupling properties in the $H \to ZZ^* \to 4\ell$ decay channel at $\sqrt{s} = 13$ TeV with the ATLAS detector,".

[28] **CMS** Collaboration, A. M. Sirunyan *et al.*, "Measurements of properties of the Higgs boson decaying into the four-lepton final state in pp collisions at sqrt(s) = 13 TeV," arXiv:1706.09936 [hep-ex].

[29] **ATLAS** Collaboration, T. A. collaboration, "Measurements of Higgs boson properties in the diphoton decay channel with 36.1 $\text{fb}^{\hat{a}\acute{L}\check{S}1}$ *pp* collision data at the center-of-mass energy of 13 TeV with the ATLAS detector,".

[30] **CMS** Collaboration, C. Collaboration, "Measurements of properties of the Higgs boson

in the diphoton decay channel with the full 2016 data set,".

[31] **CMS** Collaboration, C. Collaboration, "Higgs to WW measurements with 15.2 fb^{-1} of 13 TeV proton-proton collisions,".

[32] **CMS** Collaboration, C. Collaboration, "Observation of the SM scalar boson decaying to a pair of τ leptons with the CMS experiment at the LHC,".

[33] P. Binétruy, *Supersymmetry : Theory, Experiment, and Cosmology*. Oxford Graduate Texts. Oxford University Press, 2006. ISBN:9780198509547.

[34] M. Drees, R. Godbole, and P. Roy, *Theory and phenomenology of sparticles: An account of four-dimensional N=1 supersymmetry in high energy physics*. 2004.

[35] J. F. Gunion and H. E. Haber, "Conditions for CP-violation in the general two-Higgs-doublet model," *Phys. Rev.* **D72** (2005) 095002, arXiv:hep-ph/0506227 [hep-ph].

[36] L. Fromme, S. J. Huber, and M. Seniuch, "Baryogenesis in the two-Higgs doublet model," *JHEP* **11** (2006) 038, arXiv:hep-ph/0605242 [hep-ph].

[37] G. C. Branco, P. M. Ferreira, L. Lavoura, M. N. Rebelo, M. Sher, and J. P. Silva, "Theory and phenomenology of two-Higgs-doublet models," *Phys. Rept.* **516** (2012) 1–102, arXiv:1106.0034 [hep-ph].

[38] D. M. Asner *et al.*, "ILC Higgs White Paper," in *Proceedings, 2013 Community Summer Study on the Future of U.S. Particle Physics: Snowmass on the Mississippi (CSS2013): Minneapolis, MN, USA, July 29-August 6, 2013*. 2013. arXiv:1310.0763 [hep-ph]. https://inspirehep.net/record/1256491/files/arXiv:1310.0763.pdf.

[39] J. F. Gunion, H. E. Haber, G. L. Kane, and S. Dawson, "The Higgs Hunter's Guide," *Front. Phys.* **80** (2000) 1–404.

[40] C. B. Braeuninger, "Flavour changing neutral currents in two higgs doublet models with yukawa alignment," *Journal of Physics: Conference Series* **259** no. 1, (2010) 012073. http://stacks.iop.org/1742-6596/259/i=1/a=012073.

[41] D. Eriksson, J. Rathsman, and O. Stal, "2HDMC: Two-Higgs-Doublet Model Calculator Physics and Manual," *Comput. Phys. Commun.* **181** (2010) 189–205, arXiv:0902.0851 [hep-ph].

[42] I. F. Ginzburg and I. P. Ivanov, "Tree-level unitarity constraints in the most general 2HDM," *Phys. Rev.* **D72** (2005) 115010, arXiv:hep-ph/0508020 [hep-ph].

[43] J. Horejsi and M. Kladiva, "Tree-unitarity bounds for THDM Higgs masses revisited," *Eur. Phys. J.* **C46** (2006) 81–91, arXiv:hep-ph/0510154 [hep-ph].

[44] O. Eberhardt, U. Nierste, and M. Wiebusch, "Status of the two-Higgs-doublet model of type II," *JHEP* **07** (2013) 118, arXiv:1305.1649 [hep-ph].

[45] J. D. Wells, "TASI lecture notes: Introduction to precision electroweak analysis," in *Physics in D >= 4. Proceedings, Theoretical Advanced Study Institute in elementary particle physics, TASI 2004, Boulder, USA, June 6-July 2, 2004*, pp. 41–64. 2005. arXiv:hep-ph/0512342 [hep-ph].

[46] M. D. Schwartz, *Quantum Field Theory and the Standard Model*. Cambridge University Press, 2014. http://www.cambridge.org/us/academic/subjects/physics/theoretical-physics-and-mathematical-physics/quantum-field-theory-and-standard-model.

[47] M. E. Peskin and T. Takeuchi, "New constraint on a strongly interacting higgs sector," *Phys. Rev. Lett.* **65** (Aug, 1990) 964–967. https://link.aps.org/doi/10.1103/PhysRevLett.65.964.

[48] M. E. Peskin and T. Takeuchi, "Estimation of oblique electroweak corrections," *Phys. Rev. D* **46** (Jul, 1992) 381–409. https://link.aps.org/doi/10.1103/PhysRevD.46.381.

[49] F. Mahmoudi, "SuperIso: A Program for calculating the isospin asymmetry of B —> K* gamma in the MSSM," *Comput. Phys. Commun.* **178** (2008) 745–754, arXiv:0710.2067 [hep-ph].

[50] F. Mahmoudi, "SuperIso v2.3: A Program for calculating flavor physics observables in Supersymmetry," *Comput. Phys. Commun.* **180** (2009) 1579–1613, arXiv:0808.3144 [hep-ph].

[51] Y. Amhis *et al.*, "Averages of b-hadron, c-hadron, and τ-lepton properties as of summer 2016," arXiv:1612.07233 [hep-ex].

[52] M. Misiak *et al.*, "Updated NNLO QCD predictions for the weak radiative B-meson decays," *Phys. Rev. Lett.* **114** no. 22, (2015) 221801, arXiv:1503.01789 [hep-ph].

[53] **LHCb** Collaboration, R. Aaij *et al.*, "Measurement of the $B_s^0 \to \mu^+\mu^-$ branching fraction and search for $B^0 \to \mu^+\mu^-$ decays at the LHCb experiment," *Phys. Rev. Lett.* **111** (2013) 101805, arXiv:1307.5024 [hep-ex].

[54] **LHCb, CMS** Collaboration, V. Khachatryan *et al.*, "Observation of the rare $B_s^0 \to \mu^+\mu^-$ decay from the combined analysis of CMS and LHCb data," *Nature* **522** (2015) 68–72, arXiv:1411.4413 [hep-ex].

[55] T. Hurth, F. Mahmoudi, and S. Neshatpour, "On the anomalies in the latest LHCb data," *Nucl. Phys.* **B909** (2016) 737–777, arXiv:1603.00865 [hep-ph].

[56] **LEP, DELPHI, OPAL, ALEPH, L3** Collaboration, G. Abbiendi *et al.*, "Search for Charged Higgs bosons: Combined Results Using LEP Data," *Eur. Phys. J.* **C73** (2013) 2463, arXiv:1301.6065 [hep-ex].

[57] P. Bechtle, O. Brein, S. Heinemeyer, G. Weiglein, and K. E. Williams, "HiggsBounds: Confronting Arbitrary Higgs Sectors with Exclusion Bounds from LEP and the Tevatron," *Comput. Phys. Commun.* **181** (2010) 138–167, arXiv:0811.4169 [hep-ph].

[58] P. Bechtle, O. Brein, S. Heinemeyer, G. Weiglein, and K. E. Williams, "HiggsBounds 2.0.0: Confronting Neutral and Charged Higgs Sector Predictions with Exclusion Bounds from LEP and the Tevatron," *Comput. Phys. Commun.* **182** (2011) 2605–2631, arXiv:1102.1898 [hep-ph].

[59] P. Bechtle *et al.*, "Recent Developments in HiggsBounds and a Preview of HiggsSignals," *PoS* **CHARGED2012** (2012) 024, arXiv:1301.2345 [hep-ph].

[60] P. Bechtle *et al.*, "HiggsBounds-4: Improved Tests of Extended Higgs Sectors against Exclusion Bounds from LEP, the Tevatron and the LHC," *Eur. Phys. J.* **C74** (2014) 2693, arXiv:1311.0055 [hep-ph].

[61] R. V. Harlander, S. Liebler, and H. Mantler, "SusHi Bento: Beyond NNLO and the heavy-top limit," arXiv:1605.03190 [hep-ph].

[62] J. Butterworth *et al.*, "PDF4LHC recommendations for LHC Run II," *J. Phys.* **G43** (2016) 023001, arXiv:1510.03865 [hep-ph].

[63] R. Harlander, M. MÃijhlleitner, J. Rathsman, M. Spira, and O. StÃěl, "Interim recommendations for the evaluation of Higgs production cross sections and branching ratios at the LHC in the Two-Higgs-Doublet Model," arXiv:1312.5571 [hep-ph].

[64] **ATLAS** Collaboration, T. A. collaboration, "Search for new resonances decaying to a Z boson and a photon in 13.3 fb^{-1} of pp collisions at $\sqrt{s} = 13$ TeV with the ATLAS detector,".

[65] **ATLAS** Collaboration, T. A. collaboration, "Study of the Higgs boson properties and search for high-mass scalar resonances in the $H \to ZZ^* \to 4\ell$ decay channel at $\sqrt{s} = 13$ TeV with the ATLAS detector,".

[66] **ATLAS** Collaboration, T. A. collaboration, "Searches for heavy ZZ and ZW resonances in the llqq and vvqq final states in pp collisions at sqrt(s) = 13 TeV with the ATLAS detector,".

[67] **ATLAS** Collaboration, T. A. collaboration, "Search for a high-mass Higgs boson decaying to a pair of W bosons in pp collisions at $\sqrt{s}$=13 TeV with the ATLAS detector,".

[68] **CMS** Collaboration, A. M. Sirunyan *et al.*, "Search for Higgs boson pair production in events with two bottom quarks and two tau leptons in proton-proton collisions at sqrt(s) = 13 TeV," arXiv:1707.02909 [hep-ex].

[69] **ATLAS** Collaboration, T. A. collaboration, "Search for WW/WZ resonance production in $\ell\nu qq$ final states in pp collisions at $\sqrt{s} = 13$ TeV with the ATLAS detector,".

[70] **CMS** Collaboration, C. Collaboration, "Search for Higgs boson pair production in the final state containing two photons and two bottom quarks in proton-proton collisions at $\sqrt{s} = 13$ TeV,".

[71] **CMS** Collaboration, C. Collaboration, "Search for new diboson resonances in the dilepton + jets final state at $\sqrt{s} = 13$ TeV with 2016 data,".

[72] **CMS** Collaboration, C. Collaboration, "Search for heavy resonances decaying to a pair of Higgs bosons in the four b quark final state in proton-proton collisions at $\sqrt{s} = 13$ TeV,".

[73] **CMS** Collaboration, C. Collaboration, "Search for resonant and non-resonant Higgs boson pair production in the $\mathrm{b\bar{b}l\nu l\nu}$ final state at $\sqrt{s} = 13$ TeV,".

[74] **ATLAS** Collaboration, T. A. collaboration, "Search for Minimal Supersymmetric Standard Model Higgs Bosons H/A in the $\tau\tau$ final state in up to 13.3 fb$^{\hat{a}\acute{L}\check{S}1}$ of pp collisions at $\sqrt{s}$= 13 TeV with the ATLAS Detector,".

[75] **CMS** Collaboration, C. Collaboration, "Search for a neutral MSSM Higgs boson decaying into $\tau\tau$ with 12.9 fb^{-1} of data at $\sqrt{s} = 13$ TeV,".

[76] **CMS** Collaboration, C. Collaboration, "Search for a narrow heavy decaying to bottom quark pairs in the 13 TeV data sample,".

[77] **ATLAS** Collaboration, T. A. collaboration, "Search for additional heavy neutral Higgs and gauge bosons in the ditau final state produced in 36.1 fb^{-1} of pp collisions at $\sqrt{s} =$ 13 TeV with the ATLAS detector,".

[78] T. A. collaboration, "Search for a CP-odd Higgs boson decaying to Zh in pp collisions at âĹŽs = 13 TeV with the ATLAS detector,".

[79] **ATLAS** Collaboration, T. A. collaboration, "Search for heavy resonances decaying to a W or Z boson and a Higgs boson in final states with leptons and b-jets in 36.1 fb^{-1} of pp collision data at $\sqrt{s} = 13$ TeV with the ATLAS detector,".

[80] **CMS** Collaboration, "Search for new resonances in the diphoton final state in the mass range between 80 and 110 GeV in pp collisions at $\sqrt{s} = 8$ TeV," Tech. Rep. CMS-PAS-HIG-14-037, CERN, Geneva, 2015. http://cds.cern.ch/record/2063739.

[81] **ATLAS** Collaboration, M. Aaboud *et al.*, "Search for the Higgs boson produced in association with a W boson and decaying to four b-quarks via two spin-zero particles in pp collisions at 13 TeV with the ATLAS detector," *Eur. Phys. J.* **C76** no. 11, (2016) 605, arXiv:1606.08391 [hep-ex].

[82] **ATLAS** Collaboration, G. Aad *et al.*, "Search for Higgs bosons decaying to aa in the $\mu\mu\tau\tau$ final state in pp collisions at $\sqrt{s} = 8$ TeV with the ATLAS experiment," *Phys. Rev.* **D92** no. 5, (2015) 052002, arXiv:1505.01609 [hep-ex].

[83] **CMS** Collaboration, V. Khachatryan *et al.*, "Search for light bosons in decays of the 125 GeV Higgs boson in proton-proton collisions at $\sqrt{s} = 8$ TeV," arXiv:1701.02032 [hep-ex].

[84] **ATLAS** Collaboration, G. Aad *et al.*, "Search for charged Higgs bosons decaying via $H^{\pm} \to \tau^{\pm}\nu$ in fully hadronic final states using pp collision data at $\sqrt{s} = 8$ TeV with the ATLAS detector," *JHEP* **03** (2015) 088, arXiv:1412.6663 [hep-ex].

[85] **CMS** Collaboration, V. Khachatryan *et al.*, "Search for a charged Higgs boson in pp collisions at $\sqrt{s} = 8$ TeV," *JHEP* **11** (2015) 018, arXiv:1508.07774 [hep-ex].

[86] **CMS** Collaboration, C. Collaboration, "Search for charged Higgs bosons with the $H^{\pm} \to \tau^{\pm}\nu_{\tau}$ decay channel in the fully hadronic final state at $\sqrt{s} = 13$ TeV,".

[87] **ATLAS Collaboration** Collaboration, "Search for charged Higgs bosons in the $H^{\pm} \to tb$ decay channel in pp collisions at $\sqrt{s} = 13$ TeV using the ATLAS detector," Tech. Rep. ATLAS-CONF-2016-089, CERN, Geneva, Aug, 2016. https://cds.cern.ch/record/2206809.

[88] **ATLAS** Collaboration, T. A. collaboration, "Search for charged Higgs bosons in the ĬĎ+jets final state using 14.7 fbâĹŠ1 of pp collision data recorded at sâĹŽ=13 TeV with the ATLAS experiment,".

[89] M. Flechl, R. Klees, M. Kramer, M. Spira, and M. Ubiali, "Improved cross-section predictions for heavy charged Higgs boson production at the LHC," *Phys. Rev.* **D91** no. 7, (2015) 075015, arXiv:1409.5615 [hep-ph].

[90] **CMS Collaboration** Collaboration, "Search for new resonances in the diphoton final state in the mass range between 70 and 110 GeV in pp collisions at $\sqrt{s} = 8$ and 13 TeV," Tech. Rep. CMS-PAS-HIG-17-013, CERN, Geneva, 2017. https://cds.cern.ch/record/2285326.

[91] M. Misiak and M. Steinhauser, "Weak radiative decays of the B meson and bounds on $M_{H^{\pm}}$ in the Two-Higgs-Doublet Model," *Eur. Phys. J.* **C77** no. 3, (2017) 201, arXiv:1702.04571 [hep-ph].

[92] A. Arbey, F. Mahmoudi, O. Stal, and T. Stefaniak, "Status of the Charged Higgs Boson in Two Higgs Doublet Models," arXiv:1706.07414 [hep-ph].

[93] **OPAL** Collaboration, G. Abbiendi *et al.*, "Decay mode independent searches for new

scalar bosons with the OPAL detector at LEP," *Eur. Phys. J.* **C27** (2003) 311–329, arXiv:hep-ex/0206022 [hep-ex].

[94] G. Cacciapaglia, A. Deandrea, S. Gascon-Shotkin, S. Le Corre, M. Lethuillier, and J. Tao, "Search for a lighter Higgs boson in Two Higgs Doublet Models," *JHEP* **12** (2016) 068, arXiv:1607.08653 [hep-ph].

[95] **OPAL, DELPHI, LEP Working Group for Higgs boson searches, ALEPH, L3** Collaboration, R. Barate *et al.*, "Search for the standard model Higgs boson at LEP," *Phys. Lett.* **B565** (2003) 61–75, arXiv:hep-ex/0306033 [hep-ex].

[96] J. F. Gunion and H. E. Haber, "The CP conserving two Higgs doublet model: The Approach to the decoupling limit," *Phys. Rev.* **D67** (2003) 075019, arXiv:hep-ph/0207010 [hep-ph].

[97] J. Bernon, J. F. Gunion, H. E. Haber, Y. Jiang, and S. Kraml, "Scrutinizing the alignment limit in two-Higgs-doublet models: m_h=125âĂŁâĂŁGeV," *Phys. Rev.* **D92** no. 7, (2015) 075004, arXiv:1507.00933 [hep-ph].

[98] S. Weinberg, "Implications of dynamical symmetry breaking," *Phys. Rev. D* **13** (Feb, 1976) 974–996. https://link.aps.org/doi/10.1103/PhysRevD.13.974.

[99] L. Susskind, "Dynamics of spontaneous symmetry breaking in the weinberg-salam theory," *Phys. Rev. D* **20** (Nov, 1979) 2619–2625. https://link.aps.org/doi/10.1103/PhysRevD.20.2619.

[100] C. T. Hill and E. H. Simmons, "Strong dynamics and electroweak symmetry breaking," *Phys. Rept.* **381** (2003) 235–402, arXiv:hep-ph/0203079 [hep-ph]. [Erratum: Phys. Rept.390,553(2004)].

[101] S. Scherer, "Introduction to chiral perturbation theory," *Adv. Nucl. Phys.* **27** (2003) 277, arXiv:hep-ph/0210398 [hep-ph].

[102] R. S. Chivukula, "Lectures on technicolor and compositeness," in *Flavor physics for the millennium. Proceedings, Theoretical Advanced Study Institute in elementary particle physics, TASI 2000, Boulder, USA, June 4-30, 2000*, pp. 731–772. 2000. arXiv:hep-ph/0011264 [hep-ph].

[103] J. R. Andersen *et al.*, "Discovering Technicolor," *Eur. Phys. J. Plus* **126** (2011) 81, arXiv:1104.1255 [hep-ph].

[104] E. Farhi and L. Susskind, "Technicolor," *Phys. Rept.* **74** (1981) 277.

[105] F. Sannino, "Conformal Dynamics for TeV Physics and Cosmology," *Acta Phys. Polon.* **B40** (2009) 3533–3743, arXiv:0911.0931 [hep-ph].

[106] D. B. Kaplan, "Flavor at SSC energies: A New mechanism for dynamically generated fermion masses," *Nucl. Phys.* **B365** (1991) 259–278.

[107] K. Agashe, R. Contino, and A. Pomarol, "The Minimal composite Higgs model," *Nucl. Phys.* **B719** (2005) 165–187, arXiv:hep-ph/0412089 [hep-ph].

[108] A. Hietanen, R. Lewis, C. Pica, and F. Sannino, "Fundamental Composite Higgs Dynamics on the Lattice: SU(2) with Two Flavors," *JHEP* **07** (2014) 116, arXiv:1404.2794 [hep-lat].

[109] G. Cacciapaglia and F. Sannino, "Fundamental Composite (Goldstone) Higgs Dynamics," *JHEP* **04** (2014) 111, arXiv:1402.0233 [hep-ph].

[110] R. Slansky, "Group Theory for Unified Model Building," *Phys. Rept.* **79** (1981) 1–128.

[111] B. Gripaios, A. Pomarol, F. Riva, and J. Serra, "Beyond the Minimal Composite Higgs Model," *JHEP* **04** (2009) 070, arXiv:0902.1483 [hep-ph].

[112] S. R. Coleman, J. Wess, and B. Zumino, "Structure of phenomenological Lagrangians. 1.," *Phys. Rev.* **177** (1969) 2239–2247.

[113] C. G. Callan, Jr., S. R. Coleman, J. Wess, and B. Zumino, "Structure of phenomenological Lagrangians. 2.," *Phys. Rev.* **177** (1969) 2247–2250.

[114] T. A. Ryttov and F. Sannino, "Ultra Minimal Technicolor and its Dark Matter TIMP," *Phys. Rev.* **D78** (2008) 115010, arXiv:0809.0713 [hep-ph].

[115] E. J. Weinberg, *Radiative corrections as the origin of spontaneous symmetry breaking*. PhD thesis, Harvard U., 1973. arXiv:hep-th/0507214 [hep-th]. https://inspirehep.net/record/85345/files/arXiv:hep-th_0507214.pdf.

[116] E. Katz, A. E. Nelson, and D. G. E. Walker, "The Intermediate Higgs," *JHEP* **08** (2005) 074, arXiv:hep-ph/0504252 [hep-ph].

[117] J. Galloway, J. A. Evans, M. A. Luty, and R. A. Tacchi, "Minimal Conformal Technicolor and Precision Electroweak Tests," *JHEP* **10** (2010) 086, arXiv:1001.1361 [hep-ph].

[118] A. Arbey, G. Cacciapaglia, H. Cai, A. Deandrea, S. Le Corre, and F. Sannino, "Fundamental Composite Electroweak Dynamics: Status at the LHC," *Phys. Rev.* **D95** no. 1, (2017) 015028, arXiv:1502.04718 [hep-ph].

[119] R. Foadi, M. T. Frandsen, and F. Sannino, "125 GeV Higgs boson from a not so light technicolor scalar," *Phys. Rev.* **D87** no. 9, (2013) 095001, arXiv:1211.1083 [hep-ph].

[120] S. Dimopoulos, S. Raby, and G. L. Kane, "Experimental Predictions from Technicolor Theories," *Nucl. Phys.* **B182** (1981) 77–103.

[121] J. R. Ellis, M. K. Gaillard, D. V. Nanopoulos, and P. Sikivie, "Can One Tell Technicolor from a Hole in the Ground?," *Nucl. Phys.* **B182** (1981) 529–545.

[122] J. Alwall, M. Herquet, F. Maltoni, O. Mattelaer, and T. Stelzer, "MadGraph 5 : Going Beyond," *JHEP* **06** (2011) 128, arXiv:1106.0522 [hep-ph].

[123] A. D. Martin, W. J. Stirling, R. S. Thorne, and G. Watt, "Parton distributions for the LHC," *Eur. Phys. J.* **C63** (2009) 189–285, arXiv:0901.0002 [hep-ph].

[124] J. Serra, "Beyond the Minimal Top Partner Decay," *JHEP* **09** (2015) 176, arXiv:1506.05110 [hep-ph].

[125] R. Arthur, V. Drach, M. Hansen, A. Hietanen, C. Pica, and F. Sannino, "SU(2) gauge theory with two fundamental flavors: A minimal template for model building," *Phys. Rev.* **D94** no. 9, (2016) 094507, arXiv:1602.06559 [hep-lat].

[126] G. Cowan, "Statistics for Searches at the LHC," in *Proceedings, 69th Scottish Universities Summer School in Physics : LHC Phenomenology (SUSSP69): St.Andrews, Scotland, August 19-September 1, 2012*, pp. 321–355. 2013. arXiv:1307.2487 [hep-ex]. https://inspirehep.net/record/1242009/files/arXiv:1307.2487.pdf.

[127] F. James, *Statistical methods in experimental physics*. 2006.

[128] G. Cacciapaglia, A. Deandrea, and J. Llodra-Perez, "Higgs —> Gamma Gamma beyond the Standard Model," *JHEP* **06** (2009) 054, arXiv:0901.0927 [hep-ph].

[129] A. Djouadi, V. Driesen, W. Hollik, and A. Kraft, "The Higgs photon - Z boson coupling revisited," *Eur. Phys. J.* **C1** (1998) 163–175, arXiv:hep-ph/9701342 [hep-ph].